Design for Additive Manufacturing: Topology Optimization of Structures under Design-Dependent Loads and Manufacturing Constraints

by

Osezua Obehi Ibhadode

A thesis

presented to the University of Waterloo

in fulfillment of the

thesis requirement for the degree of

Doctor of Philosophy

in

Mechanical and Mechatronics Engineering

Waterloo, Ontario, Canada, 2021

Examining Committee Membership

The following served on the Examining Committee for this thesis. The decision of the Examining Committee is by majority vote.

External Examiner: Prof. Jill Urbanic

Dept. of Mechanical, Automotive, and Materials Engineering

University of Windsor

Supervisor: Prof. Ehsan Toyserkani

Dept. of Mechanical and Mechatronics Engineering

University of Waterloo

Supervisor: Dr. Ali Bonakdar

Dept. of Mechanical and Mechatronics Engineering

University of Waterloo

Internal Member: Assis. Prof. Mihaela Vlasea

Dept. of Mechanical and Mechatronics Engineering

University of Waterloo

Internal Member: Assoc. Prof. Kaan Inal

Dept. of Mechanical and Mechatronics Engineering

University of Waterloo

Internal-External Member: Assoc. Prof. Shoja'eddin Chenouri

Dept. of Statistics and Actuarial Science

University of Waterloo

Author's Declaration

This thesis consists of material all of which I authored or co-authored: see Statement of Contributions included in the thesis. This is a true copy of the thesis, including any required final revisions, as accepted by my examiners.

I understand that my thesis may be made electronically available to the public.

Statement of Contributions

I want to acknowledge my co-authors and others who contributed to the research described in this thesis:

Prof. Ehsan Toyserkani: Supervising the research, providing the initial idea for the current thesis, editing papers, and providing lab facilities.

Dr. Ali Bonakdar: Co-supervising the research, managing the research project, providing valuable discussions, and editing papers.

Dr. Zhidong Brian: Providing valuable discussions and insights throughout the research process, editing and co-authoring journal papers.

Pouyan Rahnama: Providing valuable discussions especially for multiphysics topology optimization and providing validation results from Hypermesh for the Labyrinth seal case study, editing and co-authoring a journal paper.

Shahriar Imani Shahabad: Assisting with surface residual stress measurements using the XRD machine and providing meaningful discussions on residual stresses in LPBF.

Reza Esmaeilizadeh: Helping in measuring tensile and bending test results for the experimental validation of the post-topology optimization overhang elimination model

Chinedu Francis Dibia: Organizing the project, helping out with some prints, and providing valuable discussions.

Abstract

The advances in additive manufacturing (AM) have opened new possibilities in design and manufacturing that were not previously attainable. AM has found application in several industries such as aerospace, medical, automotive, power, and a host of others. Of its many unique selling points, one of the most appealing is the design freedom it offers due to its capability to produce structurally complex parts. In design for additive manufacturing (DfAM), one of the most common structural design tools is topology optimization. Topology optimization is a mathematical tool that obtains the optimal structural layout of a design for an objective, and together with additive manufacturing, optimal structural designs are possible with almost no manufacturability concern so long certain constraints are adhered to.

Many efforts have gone into topology optimization for design-independent loads such as point forces, restricted or design-independent pressure loads, torques, etc., including the considerations for additive manufacturing. However, fewer works exist for design-dependent loads, especially when multiple load cases are concerned. Furthermore, even fewer works have attempted to develop topology optimization models for design-dependent loads while considering manufacturability.

In this research, frameworks have been proposed to handle topology optimization of structures under design-dependent loads (thermal stress load – TSL, centrifugal loads, and design-dependent pressure loads) and AM constraints (overhang and feature size control). The first framework for design-dependent loads is achieved by introducing the Boundary Identification and Load Evolution (BILE) model, load thresholding, and sensitivity scaling in a weighted multiobjective topology optimization process. The BILE model, specifically for pressure loads, resulted in optimal designs under 80 seconds and 100 iterations for 5,000 to 13,000 design elements using a regular desktop computing power. Load thresholding applied to thermal stress loads for a threshold $\eta = 0.8$, resulted in a reasonably stable optimization process. Also, sensitivity scales were applied to sensitivity contributions from TSLs and centrifugal loads. This ensured that optimal solutions were obtained with fewer numerical instabilities while using simple optimizers at low optimization iterations. The second framework developed is a post-topology optimization process for overhang feature elimination. Aside from the fact that volume correction is possible in this framework, boundary identification and overhang elimination, being key stages in the model, consumed only 8% of the combined process of topology optimization and overhang feature control. Two design case studies were printed using Laser Powder Bed Fusion (LPBF) and Material Extrusion, known as Fused Deposition Modeling (FDM), for manufacturability validation. Additional performance validation studies to investigate the relationship between manufacturing

constraints, residual surface stresses and structural performance were carried out on the optimized LPBF parts. No meaningful effect of overhang and feature size control was discovered on the residual stresses formed for Hastelloy X parts. However, bending test results revealed a 30% decrease in the maximum load (and a 40% increase in compliance) when a 65° overhang angle constraint was placed on a Hastelloy X optimized part. Fortunately, the performances improve when smaller angles (45° or 50°) and feature size ($5a$) constraints are imposed. Finally, an image-based initialization and post-processing code for topology optimization is provided to aid research and teaching.

Acknowledgments

First and foremost, I express all thanks and glory to God, my Maker, and Redeemer, I will not be here but for Him. I greatly appreciate my supervisor Prof. Ehsan Toyserkani, who has been exceptionally wonderful all through my research. He hired me, gave me the initial idea for my research, guided me thoroughly, provided me with an enormous amount of assistance financially and otherwise. I have grown quite significantly in my career in every sense because of his excellent leadership and robust knowledge. I also appreciate my Co-supervisor, Dr. Ali Bonakdar who closely supervised and followed up with my research and progress. He also brought a lot of industry knowledge to aid my work and cause meaningful impacts.

My appreciation also goes to all my colleagues at the MultiScale Additive Manufacturing (MSAM) lab. I want to thank Prof. Mihaela Vlasea for providing very valuable discussions and inviting me as a guest presenter in ME739 on several occasions. I especially want to thank Dr. Zhidong Zhang, Dr. Esmat Sheydaeian, Dr. Usman Ali, Dr. Farzad Liravi, Pouyan Rahnama, Francis Dibia with whom I had meaningful discussions several times during my Ph.D.; they also provided a lot of assistance when I commenced my program. I thank my other colleagues in the collaborative Siemen's project: Shahriar, Reza, Ali, Katayoon, Ken, Dr. Ehsan Marzbanrad. I especially thank Shahriar and Reza for providing me with meaningful discussions and assisting me with various experiments at different times. I also thank Dr. Dyuti Sarker and Dr. Paola Russo for the meaningful discussions and exchange of knowledge during the times the Metal Additive Manufacturing book was being prepared. I am grateful for the help and advice from Jerry Ratthapakdee for the machine setup and post-processing of my prints. I thank Karl Rautenberg for helping to cut my printed samples. I thank Laurie Wilfong, Meghan Schmuck, Catherine Demers, Denise Porter, and Haley Staller for the help in financial management and others.

My warm appreciation also goes to that are in and out of the MME department at UW. I thank Dr. Behravesh for providing a lot of assistance and advice during my bending test experiments. I thank all my course lecturers for their wealth of knowledge and guidance in the courses: Prof. Adrian Gerlich, Prof. Grzegorz Glinka, Prof. Armaghan Salehian, and Prof. Mihaela Vlasea.

I thank my friends and brethren at the Waterloo Pentecostal Assembly: Tope and Ogo Balogun (they greatly assisted me when I just arrived in Canada for my program), Funmi and Yemi Onikan, Katie West, Promise Williams, Emmanuel Badewa, Emmanuel Ojogbo, Prof and Mrs. Oriowo, Pastor Chris Padiath, Pastor Kim Davies. I also thank other friends who found time to visit and encourage me

To God and family

Contents

List of Figures

xviii

List of Tables

List of Symbols

Unless otherwise stated, the following major symbols are defined as:

$a(u,v)$ Energy bilinear form for internal work for real and virtual displacement fields u and v

B_e Ratio of terms in the derivative of Lagrangian function

C   Compliance function

ϵ Strain

E   Young's Modulus

H_{ei} Weight factor in density or sensitivity filtering

K   Stiffness

l(v)   Load linear form for external work on virtual displacement v.

U   Displacement

F   External force

f   Volume fraction

N   Shape function

x Density design variable

Ω Design domain

Γ_t Surface function

D   Matrix of material properties

V   Volume of design domain

w_i Weight value of an *ith* objective function in a multi-objective optimization problem

λ Lagrangian multiplier

η Damping coefficient

η_e Interpolation function for an element

η_{SIMP}	SIMP Interpolation function
η_{RAMP}	RAMP Interpolation function
ρ_0	Material density
ω	Angular velocity
I_e	Moment of inertia for an element

Subscripts

c	Centrifugal load
e	Related to an element in a discretized domain
f	Force load
p	Pressure load
th	Thermal stress load

Superscripts

b	Related to the body of the part
c	Centrifugal load
e	Related to an element in a discretized domain
f	Force load
p	Penalty for SIMP
q	Penalty for RAMP
T	Transpose of a vector or matrix
th	Thermal stress load

Chapter 1. Introduction

1.1.   Motivation

Design and Manufacturing are key components of the development cycle of a product [1]. Manufacturability-based design (Design for manufacture) is a concept that considers the manufacturing technology for a product during the design process and is paramount for successful product development. As an overview of the design process for the development of any product by any manufacturing technology, the major steps include (1) Part selection, (2) conceptualization (3) detailed design (embodiment design, which will usually be justified by analysis/virtual testing), (4) manufacturing, (5) testing. Similarly, in design for additive manufacturing (DfAM), the major steps include (1) part selection and concept development, (2) topology optimization and result interpretation for AM, (3) design justification, (4) additive manufacturing and, (5) material verification and mechanical testing [2].

As opposed to subtractive and formative manufacturing, according to ASTM, Additive Manufacturing (AM) is defined as "the process of joining materials to make parts from 3D model data, usually, layer upon layer [3]. Due to the nature of typical AM processes, it affords engineers to idealize out of the box and optimize design solutions without being restricted by the structural complexity of the result. AM technologies have previously been deployed in producing prototypes but more recently, industries have become increasingly interested in extending these technologies to producing fully functional metal parts [4]. This is noticed in several recent works in aerospace and aeronautics [4]–[8], automotive [9]–[12], Medical [12]–[14], Space [2], [15], [16], Power ([17], [18]) and a host of others.

Within the workflow of DfAM is the use of a popular and robust tool for obtaining conceptual, in some cases working designs, known as topology optimization. Topology optimization is a type of structural optimization that suggests optimal placement of material for an efficient structure [19]. This mathematical tool helps for weight reduction in parts while maximizing performance (in many cases, stiffness); and this is a crucial criterion in the aerospace and automotive industries [20]. To obtain optimal results that are manufacturable by AM, some manufacturing restrictions such as overhanging members, minimum feature size, build-support structure, distortion/residual stresses, anisotropic material properties, surface finish, orientation/build direction, layering patterns, shrinkage, etc must be dealt with. This is made possible when these constraints are incorporated into the design cycle [19]. In the last decade, several studies have focused on AM constrained topology optimization based on structural loads, such as in [21]–[26] and others. Although parts under a pair of design-dependent and

1

design-independent loads such as temperature distribution and a force [27], [28], body loads and a force, or centrifugal loads and a force [29], etc, have been studied, there are only a few works on the combination of several design-dependent loads. Popular efforts to address design-dependent topology optimization have either been in thermo-mechanical problems without considering other design-dependent loads as in [30]–[33] or pure thermal-based problems optimizing for cooling as in [32], [33]. Moreover, the manufacturability of structural designs obtained from a multi-physics and multi-objective topology optimization model should be considered. Developing a framework for topology optimization of structures under design-dependent loads increases the spectrum of load cases that can be addressed in the DfAM workflow. Although introducing manufacturing constraints within topology optimization decreases structural efficiency to certain degrees, the designer is assured a more robust DfAM process. The main motivations of this research are as follows:

1. A multi-objective topology optimization process is vital to structurally design rotating parts under extreme temperature and pressure conditions. This is particularly important for optimally designing rotating turbine parts that operate close to the combustion chamber. The prevalent loads, in this case, are thermal stress loads (TSLs), centrifugal loads, and unrestricted or design-dependent pressure loads from fluid effects.

2. To facilitate the manufacturability of topologically optimized parts, a framework can be developed to control overhang features and their sizes. The development of a suitable methodology should be influenced by an easy and seamless integration or workflow with the complex multiphysics and multiobjective topology optimization model developed in 1.

3. Experimental validation of the framework in 2 is necessary, not for justification only, but to provide an understanding of the quantitative and qualitative relationships between manufacturing constraints and structural performance.

4. Most of the frameworks and processes are developed in 2D for ease of implementation, therefore, the provision of an initialization and post-processing algorithm for general 2D topology optimization is essential and can be made open source for research and educational purposes.

1.2. Aim and Objectives

The basis for this work is to address design for additive manufacturing by considering topology optimization of structures under design-dependent loads and manufacturing constraints. This research, therefore, aims to develop two major frameworks: one for multi-physics and multi-objective topology

optimization of structures under design-dependent loads and the other for topology optimization considering additive manufacturing constraints. The frameworks will come decoupled with one addressing topology optimization for design-dependent loads and the other handling additive manufacturing constraints in the topologically optimized parts. Notwithstanding, a seamless workflow is expected from the first to the second framework.

For the implementation of this aim, the following objectives will be followed:

1. Develop a computationally efficient 2D model for topology optimization of structures under design-dependent loads such as thermal stress loads from a temperature distribution, centrifugal forces, and design-dependent pressure loads.
2. Develop an efficient model to control overhang features and their sizes while ensuring compatibility with the model in 1.
3. Carry out experimental validation studies to investigate surface residual stress formation and structural performance for the model in 2.
4. Develop an initialization and post-processing algorithm for 2D topology optimization that will be beneficial for research and educational purposes.

1.3.   Outline

This thesis has been organized to address the aim and objectives as follows: **Chapter 2** reviews additive manufacturing, topology optimization of structures under design-independent and dependent loads, and topology optimization for additive manufacturing. **Chapter 3** presents the modeling of thermal stress and centrifugal loads while considering load thresholding. **Chapter 4** presents and elaborates on a new Boundary Identification and Load Evolution (BILE) model for topology optimization of structures under design-dependent pressure loads. **Chapter 5** presents a multiphysics and weighted multiobjective topology optimization model considering sensitivity scaling. **Chapter 6** elaborates on the development and implementation of a post-topology optimization process for overhang feature elimination in additive manufacturing. **Chapter 7** presents an experimental validation of the effects of overhang angle and feature size control on surface residual stress and structural performance. **Chapter 8** presents a new and open-source initialization and post-processing code for 2D topology optimization, finally, **Chapter 9** presents conclusions and recommendations for future work.

A graphical outline showing the organization of the chapters in this thesis is shown in Figure 1.1.
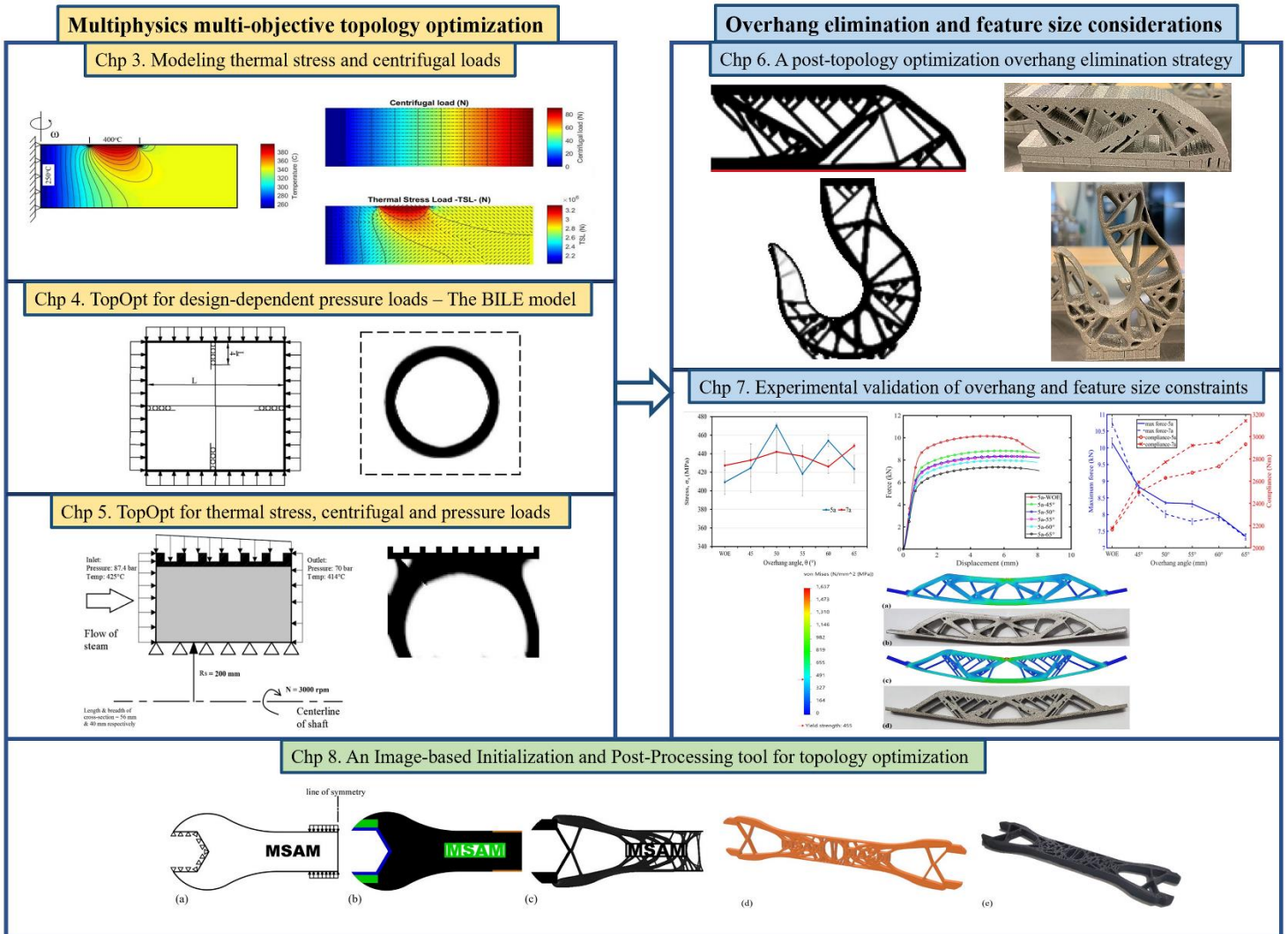
Figure 1.1: A graphical view of the thesis organization

Chapter 2: Literature Review

This chapter will first broadly review additive manufacturing, then go over design for additive manufacturing frameworks, and elaborate on the theoretical backgrounds for structural optimization with a focus on topology optimization. Thereafter, several efforts to develop topology optimization for additive manufacturing will be discussed. Finally, some efforts that have helped advance the use and knowledge transfer of topology optimization models will be presented.

2.1   Additive Manufacturing

According to ASTM [3], additive manufacturing (AM) is defined as "the process of joining materials to make parts from 3D model data, usually layer upon layer". There are several other terms used to describe AM technology such as 3-D printing, direct digital manufacturing (DDM), layered manufacturing, and additive fabrication [34]. It applies to a wide range of materials such as polymers, metals, concretes, rubbers, resins, glass, biomedical products, etc. [35], [34]. Unlike rapid prototyping, AM specifically looks at obtaining consumer products rather than mock-ups [35]. In a broad sense, For AM to be functional, it requires raw materials, supports, and utilities all controlled by a CAD file containing the geometry of the model and process parameters that can be as many as 150 different variables [36]. Figure 2.1 shows the essential requirements and representation of AM, while Figure 2.2 shows a typical Laser Powder Bed Fusion (LPBF) additive manufacturing technology.
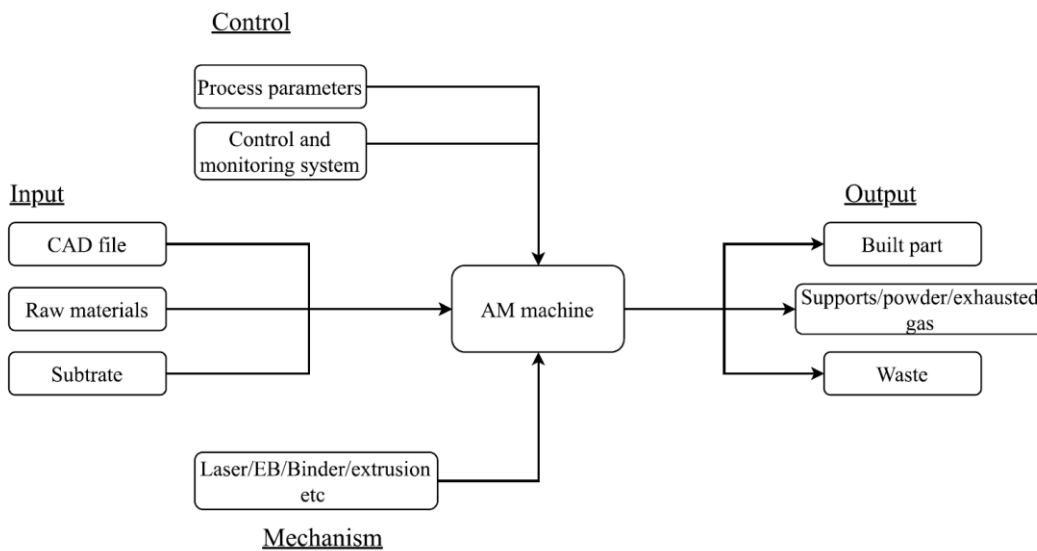
Figure 2.1: Basic representation of AM. Adapted and modified from [36]
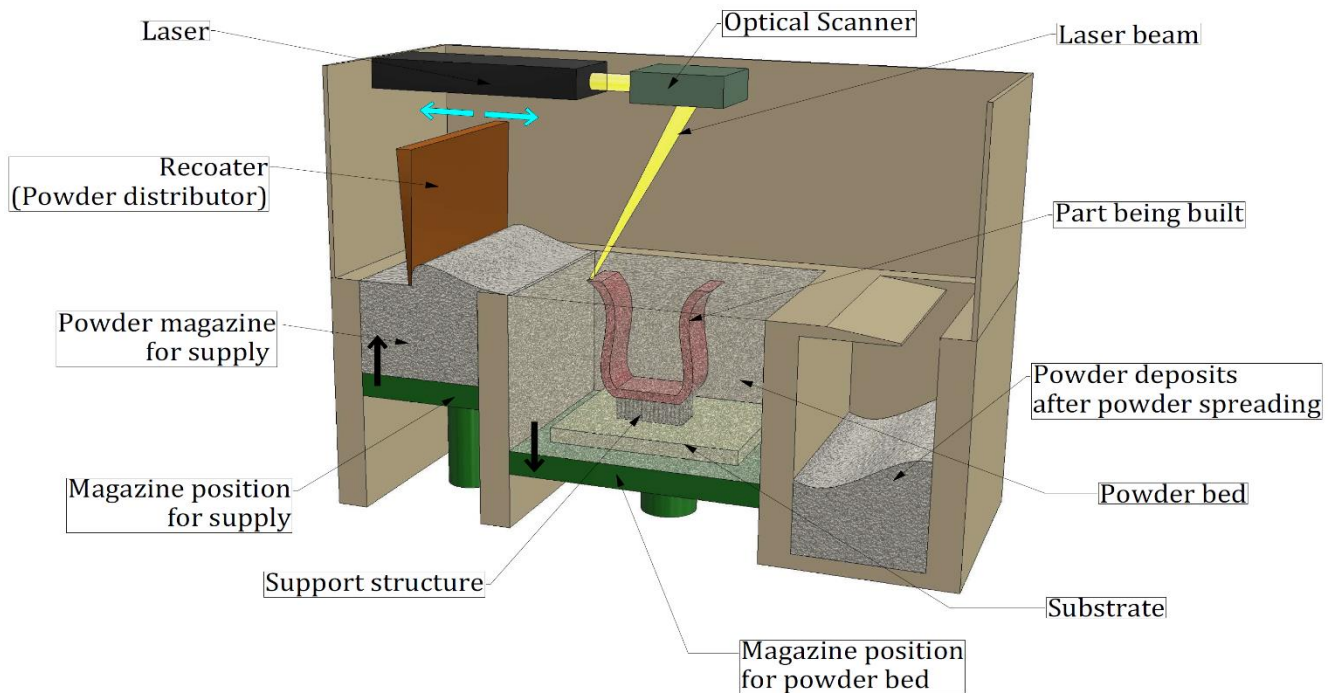
Figure 2.2: 3D schematic of a Laser Powder Bed Fusion AM

There are 7 broad AM technologies which consist of all different commercial variants of the technology [36] and [3]:

- Direct energy deposition: focused thermal energy is used to fuse materials by melting as they are being deposited.

- Powder Bed Fusion: thermal energy selectively fuses powders in a powder bed.

- Binder jetting: a liquid bond is used to join materials selectively in a powder bed.

- Material extrusion: the material is selectively dispensed through a nozzle or orifice.

- Material jetting: material droplets are selectively deposited to form a part.

- Sheet lamination: Sheets of material are joined to form an object.

- VAT photopolymer: liquid polymer in a vat is selectively cured by light-activated photopolymerization.

It is noteworthy that AM is possible because of other technologies such as computer-aided design (CAD), computer-aided manufacturing (CAM), and computer numerical control (CNC). These three technologies substantially metamorphosed into AM [37].

AM process usually commences with obtaining a set of 2D profiles such as those generated from CAD tools or Computed Tomography (CT) scans. These profiles are then transformed into digital data

6

(volume or facet models) using solid modeling or image reconstruction software. This data is usually checked for errors for correction if necessary and support structures may be added depending on the specific AM technology [38]. The lump sum of the object model and support structures is sliced into several "2D sections" with micron thickness along the proposed build direction using an AM-specific software such as Magics from Materialize. An AM machine builds the object in a layer-by-layer process based on the discretized model.

2.2. Design for Additive Manufacturing

It is popular that the development of a robust DfAM knowledge base consisting of tools, rules, processes, and methodologies has been particularly challenging owing to the lack of understanding, yet, of the application of DfAM [38]. DfAM aims at synthesizing shapes, sizes, geometric microstructures, and material compositions and microstructures to best utilize manufacturing process capabilities to achieve desired performance and other lifecycle objectives [39]. Several efforts have attempted to develop methodologies for an all-inclusive DfAM, such as in [39]–[46], etc. This review will take a closer look at the methods proposed by Yang and Zhao [46] and Kumke et al. [47].

Yang and Zhao [46] proposed a two-part process design methodology for an initial design model. The first process design is to analyze the initial CAD model and carry out part consolidation to conform to certain specified functional and performance requirements; they defined this step as functional integration. The second step is to carry out structural optimization to obtain either a lighter weight, better heat dissipation, or an improved dynamic response depending on performance requirements. Topology optimization is usually adopted during this stage due to its several attractive qualities we will discover in later sections. In both stages, there is interfacing with manufacturing, assembly, and standardization constraints. Figure 2.3 shows a flow chart of this design method.
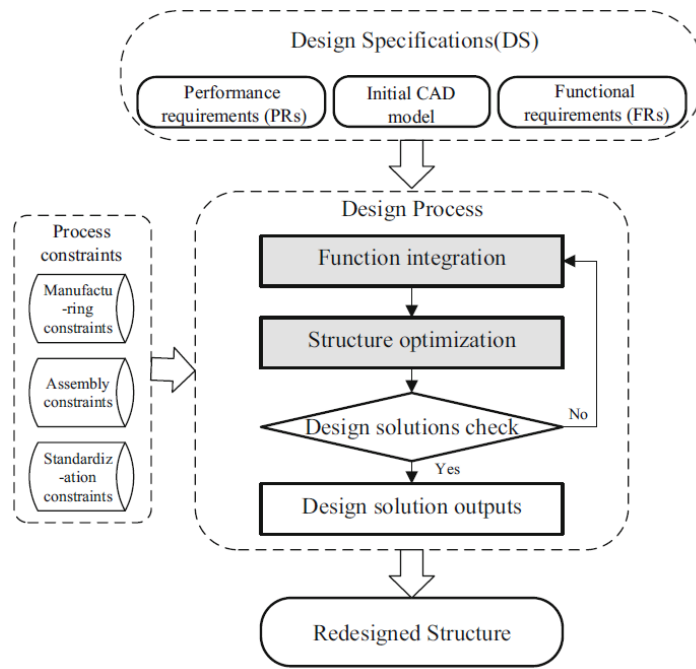
Figure 2.3: AM-enabled design methodology [46]

Kumke et al. [47] proposed a new design framework, which is an offshoot from the conventional VD12221 design methodology. They argued that their framework has advantages over previous methods for its comprehensiveness and modularity, which allow easy interfacing with existing DfAM tools and methods. They stated that with their method, integrating AM tools and methods could be done in the correct design phases as well as facilitate a goal-oriented utilization of AM design potentials. They also claimed that their framework ensures sufficient support and guidance notwithstanding the user's knowledge base or experience in AM. Their design framework is shown in Figure 2.4.

I — *Planning and clarifying the task*

1 Task clarification and definition of requirements

Requirements list

II — *Conceptual design*

2 Determination of functions and their structures

3 Development of basic solution ideas

| **a** AM-specific association aids | **b** Creativity techniques |
| **c** Design catalogues | . . . |

Concept evaluation

Conceptual model(s)

4 Dividing into realisable modules

5 Technical feasibility and (AM) process selection

6 Economic feasibility

Product's part(s) for AM

III — *Embodiment and detail design of AM part(s)*

7 Optimisation of specific product properties

| **a** Topology optimisation | **b** Flow optimisation |
| **c** Acoustics optimisation | . . . |

8 AM-conformal embodiment and detail design

| **a** Design rules for manuf. processes | **b** Standards and guidelines |
| **c** AM-specific CAD functions | . . . |

9 Simulation, design check, manufacturability analysis

| **a** Finite element analysis | **b** AM-specific CAD functions |
| **c** Process simulation | . . . |

Design evaluation

Design solution

Iterative forwards and backwards between previous and following phases/modules

F — Functional extension and parts consolidation

Figure 2.4: DfAM framework [47]

9

2.3.   Structural Optimization Methods

2.3.1.   Structural Optimization

Structural optimization attempts to obtain the most efficient structural layout of a model, part, component, or system. This form of optimization consists of three broad aspects: sizing optimization, shape optimization, and topology optimization. A typical sizing optimization solution finds the optimal thickness of member areas in a truss structure [48]. The thicknesses of the members become the design variables for the problem formulation and optimization of the structure's compliance, deflection, or peak stress is performed as dictated by performance requirements. The challenge inherent in sizing optimization is the fact that there has to be an already established structural layout that restricts design freedom. In shape optimization, the goal is to find the best shape for a prescribed domain; consequently, the shape of a solid or empty domain becomes the design variable that optimizes the structure's performance within a designable volume. Just as in sizing optimization, there is also restriction with design freedom because an *a priori* shape has to be established before the optimization is initialized. Topology optimization entails the determination of features such as the number and location of squares and the connectivity of the domain [48]. Figure 2.5 shows the different structural optimization methods.
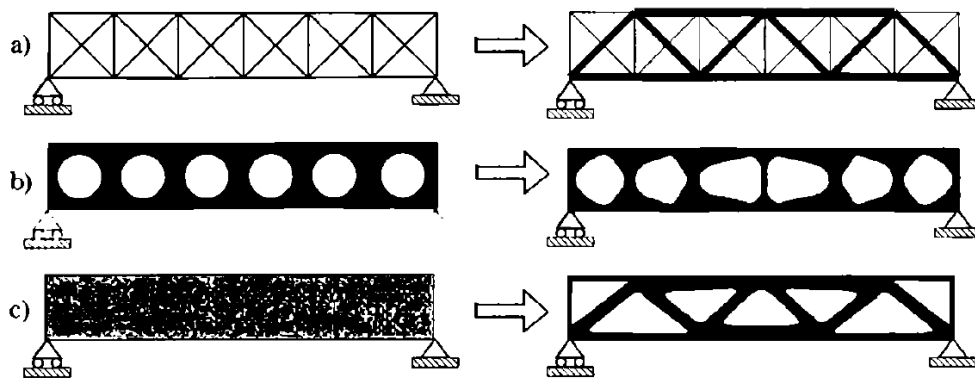
Figure 2.5: The three classifications of structural optimization. (a) Sizing optimization, (b) Shape optimization, (c) Topology optimization. Sizing and shape optimization initially start with a predefined structural layout with optimal thickness [48]

The definition of a general structural optimization (SO) problem follows [49]:

$$(SO) \begin{cases} \text{minimize } f(x,y) \text{ with} - \text{respect} - \text{to } x \text{ and } y \\\\ \text{subject to} \begin{cases} \text{behavioral constraints on } y \\\\ \text{design constraints on } x \\\\ \text{equilibrium constraint} \end{cases} \end{cases} \tag{2.1}$$

In this formulation, *x* and *y* are design and behavioral variables. Design constraints are constraints imposed on the design variable *x* while behavioral constraints are constraints on the state variable *y* and the combination of these constraints is possible. The equilibrium constraint is

$$\boldsymbol{K}(x)\boldsymbol{u} = \boldsymbol{F}(x) \tag{2.2}$$

Where $\boldsymbol{K}(x)$ is the stiffness matrix of the structure being a function of the design variable, $\boldsymbol{u}$ is the system's displacement vector and $\boldsymbol{F}(x)$ is the external or internal force vector (or combination of both) which may or may not be a function of the design variable. For a frequent case where the stiffness is invertible,

$$\boldsymbol{u} = \boldsymbol{u}(x) = \boldsymbol{K}(x)^{-1}\boldsymbol{F}(x) \tag{2.3}$$

The displacement vector in equation 2.3 can be treated as a state-space variable and substituted as a variable in the objective function

$$(SO) \begin{cases} \min\limits_{x} & f(x, \boldsymbol{u}(x)) \\\\ \text{s.t.} & g(x, \boldsymbol{u}(x)) \leq 0 \end{cases} \tag{2.4}$$

2.3.2.   Topology Optimization

Topology optimization aims at obtaining the optimal material distribution within a design space and usually does this by minimizing an objective function (e.g compliance) under constraints for a designable volume [43]. The first known paper on topology optimization was published by Michell, an Australian inventor, in 1904. He derived optimality criteria for the least weight layout of trusses [50]. Since then, there have been several efforts that have made topology optimization an attractive and efficient tool within a general design for manufacturing.

Currently, and amongst available classes, there are three popular general methods for topology optimization which are density-based, hard-kill, and level set methods. Solid Isotropic Material with Penalization (SIMP) and Rational Approximation of Material Properties (RAMP) are density-based methods with SIMP being the more popular scheme. In simple terms, SIMP applies a power-law

penalization to relate stiffness and density where the density variables for mesh elements have values between 0 and 1; 0 meaning void element and 1 full dense/solid element [51]. RAMP differs from SIMP by only the penalization or interpolation function which is a ratio of the density variable and a penalized density function. Hard-kill methods consist of Evolutionary Structural Optimization (ESO) and Bi-directional Evolutionary Structural Optimization (BESO) with BESO gaining more popularity. Both methods are similar in the fact that they iteratively add a finite amount of material within a given design space but BESO has the added advantage of removing material when necessary. In these methods, heuristic criteria are adopted and may or may not have strict dependence on the sensitivity information of the structure [52]. In the Level Set Method (LSM), Level Set Functions (LSF) are generated to determine the boundaries of a design and topologies change with change in the level set function [51]. The difference between a conventional design and a topology optimized version is shown in Figure 2.6.
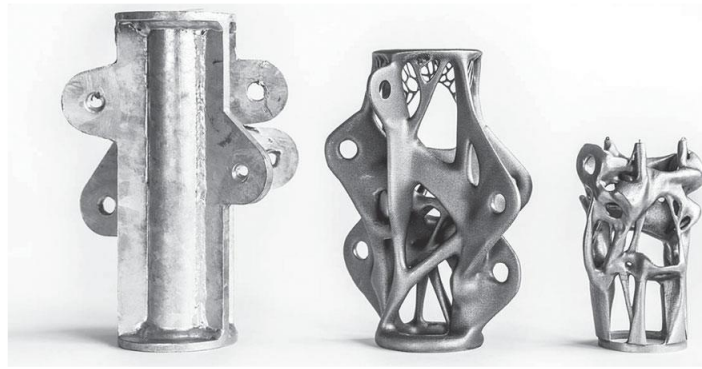
Figure 2.6: Original metal part (left-most part) and its topology optimized versions [52].

Topology optimization problem formulation is broadly discussed in Chapters 3 and 4 but briefly introduced here. If **u** and **v** are taken as displacement fields that define equilibrium of the elastic structure and kinematically admissible virtual displacement field respectively, for an elastic structure with a fixed boundary Γ_d, we have [53]

$$\int_{\Omega} \boldsymbol{\epsilon}^T(\boldsymbol{v})\big(\boldsymbol{D}\epsilon(\boldsymbol{u})\big)d\Omega = \int_{\Omega} \boldsymbol{f}^T\boldsymbol{v}d\Omega + \int_{\Gamma_t} \boldsymbol{t}^T\boldsymbol{v}d\Gamma \tag{2.5}$$

The left-hand side of 2.5 is the system's strain energy in the elastic domain which is a combination of work done by forces $\boldsymbol{f}$, applied on Ω and surface traction forces on Γ_t. By using notations from functional analysis and energy bilinear form for internal work and load linear form for external work,

$$a(\boldsymbol{u}, \boldsymbol{v}) = l(\boldsymbol{v}), \quad \forall \boldsymbol{v} \in \mathbf{V} \tag{2.6}$$

Where

$$a(\boldsymbol{u}, \boldsymbol{v}) = \int_{\Omega} \boldsymbol{\epsilon}^T (\boldsymbol{v}) \big(\boldsymbol{D}\epsilon(\boldsymbol{u}) \big) d\Omega \tag{2.7}$$

and

$$l(\boldsymbol{v}) = \int_{\Omega} \boldsymbol{f}^T \boldsymbol{v} d\Omega + \int_{\Gamma_t} \boldsymbol{t}^T \boldsymbol{v} d\Gamma \tag{2.8}$$

Topology optimization based on obtaining the stiffest structural layout means minimizing compliance or strain energy. It aims at ensuring the structural layout gives the least response possible to external loads and surface traction forces. Therefore, the structural problem by minimizing compliance $l(\mathbf{u})$ can be formulated thus:

$$
\begin{aligned}
&\text{Minimize} &&l(\mathbf{u}) \\
&\text{subject to} &&a(\boldsymbol{u}, \boldsymbol{v}) = l(\boldsymbol{v}), \quad \forall \boldsymbol{v} \in \mathbf{V} \\
&\text{and} &&design\ constraints
\end{aligned}
\tag{2.8}
$$

2.8 is subjected to the comparison of internal work, $a(\boldsymbol{u}, \boldsymbol{v})$ and external work, $l(\boldsymbol{v})$ on the system. This can be translated to the finite element equation

$$\boldsymbol{K}(x)\boldsymbol{U}(x) = \boldsymbol{F} \tag{2.9}$$

Where $\boldsymbol{K}$ and $\boldsymbol{U}$ are the stiffness matrix and displacement vector respectively due to the external load vector $\boldsymbol{F}$. With compliance $l(\mathbf{u}) = \boldsymbol{F}^T \boldsymbol{U}$ and volume constraint, the optimization problem in 2.8 transforms to:

$$
\begin{aligned}
&\text{min} &&c(x) = \boldsymbol{F}^T \boldsymbol{U}(x) \\
&\text{subject to:} &&\boldsymbol{K}(x)\boldsymbol{U}(x) = \boldsymbol{F} \\
& &&\frac{V(x)}{fV_0} \leq 1 \\
& &&0 \leq x \leq 1
\end{aligned}
\tag{2.10}
$$

To solve this non-linear optimization problem by the Optimality Criteria Method, the following functions are implemented:

OCM updates the design variables depending on the optimality conditions being met as follows [54]:

$$x_e^{\text{new}} = \begin{cases} \max(0, x_e - \text{m}) & \text{if } x_e B_e^\eta \leq \max(0, x_e - \text{m}) \\ \min(1, x_e + \text{m}) & \text{if } x_e B_e^\eta \geq \min(1, x_e - \text{m}) \\ x_e B_e^\eta & \text{otherwise} \end{cases} \qquad (2.11)$$

where m and η are move limits and numerical damping coefficient, respectively. The numerical damping coefficient is commonly given a value of ½ and B_e is obtained as

$$B_e = \frac{-\dfrac{\partial c}{\partial x_e}}{\lambda \dfrac{\partial V}{\partial x_e}} \qquad (2.12)$$

λ is a Langrangian multiplier whose value must be chosen so that the volume constraint is met. Usually, the appropriate value is found using the numerical bisection method [54].

To solve this non-linear optimization problem by the Globally Convergent Method of Moving Asymptotes, the problem statement in 2.10 can be compared to a general optimization problem [55]:

$$\text{Minimize:} \quad f_0(x) + a_0 z + \sum_{i=1}^{m} \left(c_i y_i + \frac{1}{2} d_i y_i^2 \right)$$

$$\text{subject to:} \ f_i(x) - a_i z - y_i \leq 0, \ \ i = 1 \ldots, m \qquad (2.13)$$

$$x \in X, y \geq 0, z \geq 0.$$

where x is the independent design variable and y, z are dependent state variables, also, the objective and constraint functions $f_0, f_1, \ldots \ldots, f_m$ must be differentiable. For Equations 10.10 and 10.13 to be equivalent, 2.13 must be written as

$$\text{Minimize} \quad f_0(x)$$

$$\text{subject to} \ f_i(x) \leq 0, \ \ i = 1 \ldots, m \qquad (2.14)$$

$$x \in X.$$

where $a_0 = 1, a_i = 0$ for all $i > 0, z = 0, d_i = 1$ and $c_i = $ "a large number". Subproblems are obtained for $f_i(x), i = 0,1, \ldots \ldots, m$ and solved by either of two methods: dual approach or primal-dual interior-point approach. The subproblem for GCMMA is given as [55]:

$$f_i^{(k,v)} = \sum_{j=1}^{n} \left(\frac{p_{ij}^{(k,v)}}{u_j^{(k)} - x_j} + \frac{q_{ij}^{(k,v)}}{x_j - u_j^{(k)}} \right) + r_i^{(k,v)}, \ \ i = 0,1, \ldots \ldots, m \qquad (2.15)$$

where p, q are coefficients of the convex subproblem, which are a function of the sensitivity information during the kth outer and "v^{th}" inner iterations where the sensitivity remains constant throughout v iterations in a *kth* iteration. r is the residual of the value of subproblem at the "*kth*" iteration subtracted

from the actual function's value. For an optimal solution of these sub-problems, the KKT optimality conditions are both necessary and sufficient.

When a sub-problem has been developed, an iterative solution step is taken to arrive at appropriate values of the design variables that give an optimum structure (minimum compliance in this case):

i. Step 0: Choose a starting point $\mathbf{x}^{(0)}$, and let the iteration index be $k = 0$.

ii. Step 1: Given an iteration point $\mathbf{x}^{(k)}$, calculate $f_i(\mathbf{x}^{(k)})$ and the gradients $\nabla f_i(\mathbf{x}^{(k)})$ for $i = 0, 1, \ldots\ldots, m$.

iii. Step 2: Generate a sub-problem $P^{(k)}$ by replacing in P, the (usually implicit) functions f_i by approximating explicit functions $f_i^{(k)}$, based on the calculations from step 1.

iv. Step 3: Solve $P^{(k)}$ and let the optimal solution of this subproblem be the next iteration point $\mathbf{x}^{(k+1)}$. Let $k = k + 1$ and go to step 1.

MMA is done such that each $f_i^{(k)}$ is obtained by a linearization of f_i in variables of the type $\frac{1}{x_i - L_i}$ or $\frac{1}{U_j - x_j}$ which are dependent on the signs of the derivatives of f_i at $\mathbf{x}^{(k)}$. The values of L_i and U_j are normally changed between the iterations and are popularly referred to as 'moving asymptotes'. Article by Prof Krister Svanberg [55] is recommended to the reader for more information on MMA and GCMMA.

2.3.3. Design-dependent topology optimization

Many studies on structural optimization, topology optimization particularly, have focused on point loads while some extensions have been made to uniformly distributed loads and pressure on non-designable regions. A challenging aspect of topology optimization is the presence of design-dependent loads in a structural design problem. In such a case, the loads depend on the material volume and/or layout over the design domain and are subject to changes during the optimization process [56]. Gao and Zhang [56] classified these into:

a. Transmissible or sliding force: This force maintains its magnitude but consistently changes its line of action as the topology changes during optimization.

b. Body load: This load is a result of the inertia load of the design. As material distribution changes within the optimization process, the magnitude and centroid of this load change. Centrifugal loads can come under this class because the force exerted on a rotating body largely depends on its weight then also on the position of the center of rotation and the rotational speed.

c. Surface pressure load: When the surface on which this load is supported is designable, then it can be defined as a design-dependent load case. Gao and Zhang [56] further classified this load into solid weight, hydrostatic, and snow weight pressure.

d. Thermo-elastic stress load: Thermal loads have gained more interest in recent times because of complications that arise from thermal stresses which depend not only on the changing topology but changing Young's Modulus and thermal expansivity. For this kind of load, a term called Thermal Stress Coefficient is usually introduced within thermo-structural topology optimization methodology to ensure simultaneous material interpolation and penalization of element stiffness and thermal stress load [56].

2.3.3.1. Thermo-mechanical Topology Optimization

There have been several interesting studies on design-dependent topology optimization especially related to thermo-mechanical problems. As early as 1995, Rodrigues and Fernandes [57] formulated a computational model for topology optimization based on the material distribution for a 2-D linear-elastic solid subjected to thermal loads. In their work, the temperature distribution was a uniform steady-state temperature independent of the design. Their study showed that even for simple models and at low-temperature changes, optimal topologies obtained strongly depend on these temperature effects. In 2006, Li, Steven, and Xie [31] proposed an evolutionary optimization procedure by thermo-elasticity to address varying temperature distribution throughout the design domain. Their model's iterative loop included transient heat analysis by conduction, finite element thermo-elastic analysis, and design modifications. Works that were done separately by Hou, Zhu, and Li [58] and Deaton, Grandhi [59] addressed thermo-mechanical topology optimization by stress-based criteria while maximizing stiffness. This is achieved by including a constraint of a global stress measure based on a p-norm function so that the number of stress constraints is reduced in topology optimization. Compliance minimization is the common objective function for most topology optimization approaches, however, in this case, a stress constraint in the form of the *p-norm* function is added to the usual volume constraint. It is worthy to note that Gao and Zhang [56] and Deaton and Grandhi [59] both concluded that the classical SIMP material interpolation function encountered numerical difficulties for thermo-mechanical topology optimization which is largely due to the existence of null values in the stiffness matrix for elements with zero design variables as this causes singularity issues. Also, the SIMP function significantly penalizes the stiffness values of intermediate density elements (which regularly occur in thermo-mechanical topology optimization) causing an undesirably high number of near-zero values in the stiffness matrix. They therefore suggested that the RAMP interpolation function is more efficient for design-dependent

topology optimization procedures. SIMP and RAMP interpolation functions are defined by the functions:

$$\text{SIMP:} \qquad E(x_e) = x_e^p E_0 \qquad (2.16)$$

$$\text{RAMP:} \qquad E(x_e) = \frac{x_e}{1 + p(1 - x_e)} E_0 \qquad (2.17)$$

For density values close to zero ($x_e \cong 0$), the interpolation schemes in the sensitivity function become

$$\text{SIMP:} \qquad \frac{dE(x_e \cong 0)}{dx_e} = p x_e^{p-1} E_0 \rightarrow 0 \qquad (2.18)$$

$$\text{RAMP:} \qquad \frac{dE(x_e \cong 0)}{dx_e} = \frac{1 + p(1 - x_e) + p x_e^2}{\left(1 + p(1 - x_e)\right)^2} E_0 \rightarrow \frac{1}{p+1} E_0 \qquad (2.19)$$

2.18 shows that SIMP neglects the significance of elements with design values close to zero but RAMP gives low-density elements with at the least, a factor of $\frac{1}{p+1}$ of the material property (Young's Modulus).

Figure 2.7 shows an L-shaped design case study carried out by Deaton and Grandhi [59]. Figure 2.8 shows the results of purely mechanical loads on the design for SIMP and RAMP. It is noticed that there is a considerable amount of intermediate elements left in the results from RAMP compared to that from SIMP. In Figure 2.9 the optimization of a combination of mechanical and thermal loads is presented and a slightly different structural layout is observed to enable the thermal expansion of structural members.
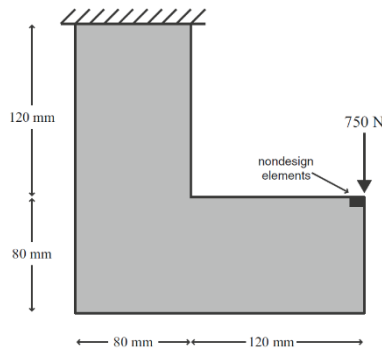
Figure 2.7: Design domain with loading and boundary conditions [59]

17

(a) SIMP - Density ρ_e, Material usage = 27.8% (b) RAMP - Density ρ_e, Material usage = 33.7%
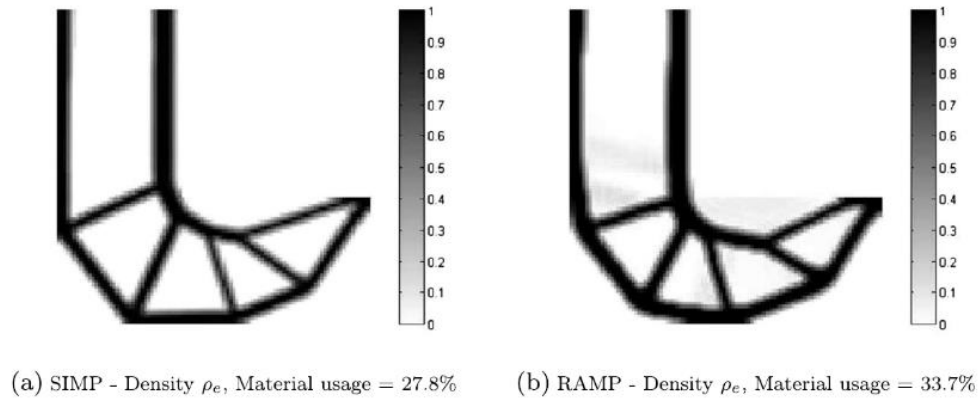
Figure 2.8: Topology optimized results for the L-shaped design in pure mechanical loading. Resulting topologies for (a) SIMP, (b) RAMP [59].
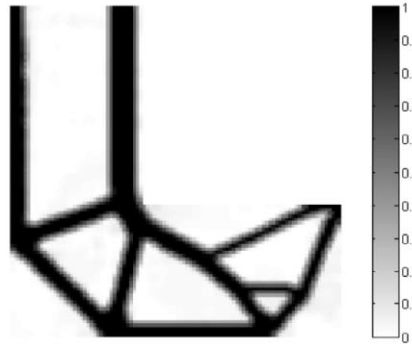
Figure 2.9: Topology optimized results for the same design in Figure 2.7 but under coupled thermal and mechanical loads of material usage = 33.2%. A constant temperature change of 20°C is applied [59].

From studies, it is common for thermo-mechanical optimization to produce results with significant gray/intermediate elements more so when lower penalty values are used. Since the structural interpretation of these gray elements is difficult, many research efforts have looked into using multi-material models to handle this problem as in the works by Vantyghem et. al. [60], Takezawa and Kobashi [61]. Applications of thermo-mechanical topology optimization have been extended to compliant actuators by Du et. al. [62] where they used mesh-free methods, additionally, thermal-actuated compliant, and electro-thermal complaint mechanisms were done by Ansola et. al. [63]. Jahan et. al [64] developed a topology optimization model for redesigning traditional injection molding tools. They aimed at minimizing compliance (while ensuring low weight considerations) and maximizing heat conduction which led to a multi-objective thermo-mechanical topology optimization based on compliance and heat conduction.

18

2.3.3.2. Topology Optimization considering centrifugal loads

Topology optimization considering loads arising from rotational effects, such as centrifugal loads, was analyzed by Enrico et. al [51] using a turbine disk. They utilized level set methods for optimization because they encountered numerical difficulties with density-based methods. They carried out a two-stage structural optimization with the first being topology optimization to generate a solution consisting of solid, void, and "*intermediate*" regions. The second stage was lattice structure optimization of the intermediate regions which involved obtaining optimized lattice structure parameters to transform the porous zones to an explicit lattice structure design shown in Figure 2.10.
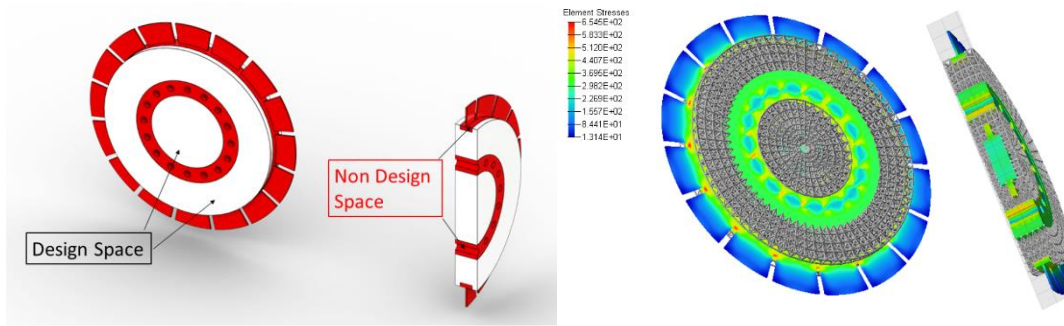
Figure 2.10: Design and non-design domain for turbine disk optimization (left) and stress distribution of optimized design (right) [51].

Zheng and Gea [29] also studied the effect of dynamical structures considering body loads. Using a rotating arm as a case study, they observed that their optimized results had more mass concentrated near the center of rotation as should be expected. An important design criterion was to minimize the moment of inertia which is directly proportional to the power required for rotation. Therefore, they formulated a multi-objective optimization of compliance and kinetic energy minimization using weight factors to ensure comparable magnitudes of the objective values. The problem is formulated as shown in equation 2.15 while Figure 2.11 shows results of topology optimization of the rotating arm.

$$\min \; \Pi = w_1 F^T U + w_2 \frac{1}{2} I \omega^2$$

$$\text{subject to:} \; KU = F_c$$

$$\frac{\sum_{e=1}^{n} V(x_e)}{f V_0} \leq 1 \qquad (2.15)$$

$$0 \leq x_e \leq 1$$

19

$$0 \leq E_{min} \leq E_e \leq E_0$$
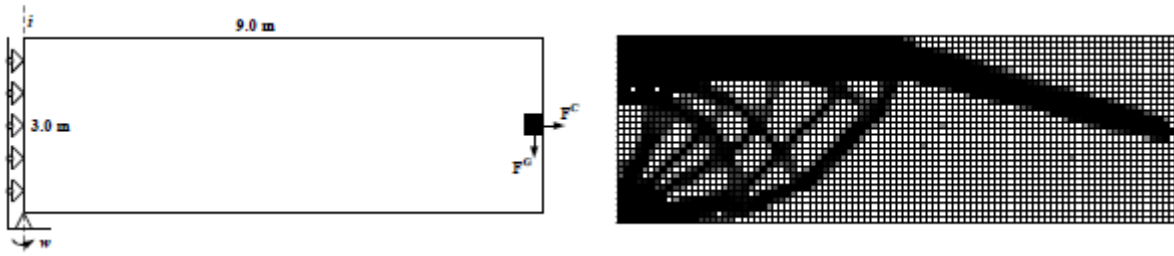
Figure 2.11: Free-body diagram of a rotating arm (left) and optimized design considering both gravitational and centrifugal forces from both structural and non-structural mass [29].

2.3.3.3. Topology optimization for design-dependent pressure loads

There have been several impressive works to address unconstrained pressure loads such as hydrostatic, snow weight, and solid pressure. Topology optimization of structures under pressure loads can be formulated either as design-independent or design-dependent subject to the nature of the design problem. For design-dependent pressure loads, as the optimization carries on, these loads might change in direction only or in both magnitude and direction depending on the methodology devised to update the changing pressure. If they change in magnitude, there will be a load sensitivity term in the sensitivity function that has to be calculated for and it is usually non-trivial.

A significant aspect of these problems is the identification of changing topological boundaries and several researchers have devised methods for this. Cheng and Kikuchi [65] applied a fictitious thermal load to simulate this dependent load, Niu et al [66] proposed a density threshold method to evaluate contact pressure value for elastic continuum structures in frictionless contact to improve the uniformity of contact pressures. Li et. al. [67] proposed a simple algorithm based on digital image processing and regional contour tracking technology which identified and generated the changing topological boundary on every iteration. Zheng et. al. [68] introduced a pseudo-equal-potential function while Wang et. al [69] employed an image segmentation technique based on Distance Regularized Level Set Evolution (DRLSE) for material boundary identification. Figure 2.12 shows the topology optimization of a structure under unidirectional design-dependent pressure loads for using the Optimality Criteria Method (OCM) and the Method of Moving Asymptotes (MMA).
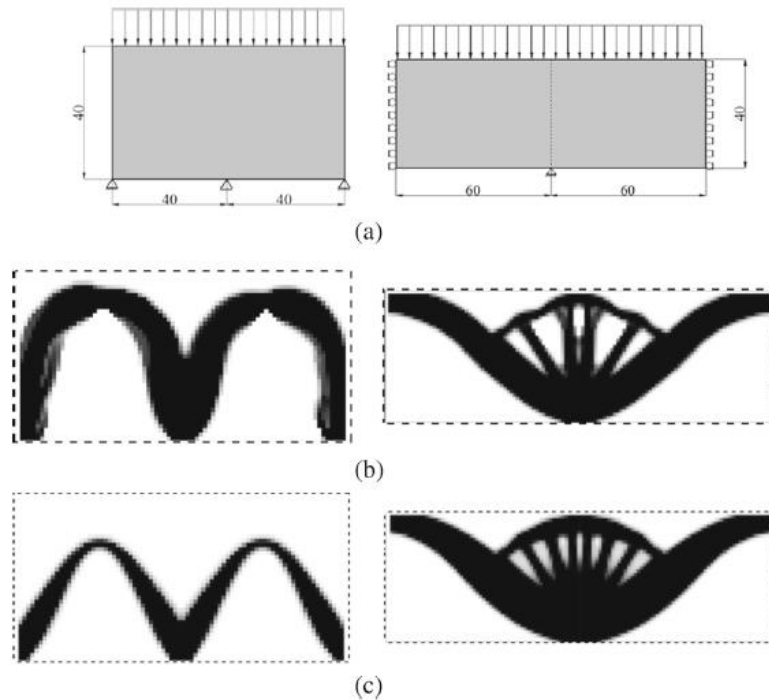
Figure 2.12: Optimization of different structures under unidirectional pressure load. (a) the design problems, (b) Optimized results using Optimality Criteria Method, (c) Optimized results using Method of Moving Asymptotes [67].

Lee and Martins [70] proposed a boundary identification scheme which with the help of some predefined void region, iteratively joined points of equal densities. They also pointed out that by using an iso-density line to define generated boundaries, no extra artificial variable might influence the final result required. Picelli et.al. [71] employed the BESO scheme while introducing a buoyancy inequality constraint to set a minimum required buoyancy effect which they measure by combined volumes of solid structure and voids. Hammer et.al. [72] used interpolation schemes to obtain a set of corner nodes. These nodes were fit by Bezier cubic splines to obtain load-carrying surfaces. Since these load-carrying surfaces are obtained from the nodes of finite elements, the loads were applied directly to boundary elements and the external load sensitivity was close to zero. This will avoid complex load sensitivity computations often carried out such as the finite difference method in [73]. More recently, Picelli et. al. [74] by level-set topology optimization utilized a coupled fluid-structure methodology which was solved by obtaining fluid pressure first, determining the fluid-structure interface next, and finally carrying out structural analysis. For both fluid and structural domains, they used bilinear elements and isoparametric mapping. Kumar et. al. [75] modeled design-dependent pressure loads on structures and compliant mechanisms

21

using Darcy's law coupled with a "drainage" term. The need for the drainage term was to ensure structural boundaries that are not in contact with the fluid domain were excluded from loading.

2.4. Topology Optimization for Additive Manufacturing

With design freedom as a major advantage of additive manufacturing, many industries and researchers have adopted topology optimization as an important tool in DfAM. For topology optimization to be successfully integrated into DfAM, the constraints posed by this manufacturing technology must be captured in the optimization algorithms. This section will examine several efforts by researchers to incorporate additive manufacturing constraints within topology optimization. Several of these constraints that have been captured are overhang minimization or elimination [22], [76]–[82], minimum feature thickness [83]–[87], self-supporting feature constraint (very similar to overhang feature control), void elimination [88]–[90], build orientation optimization [91]–[93], support structure minimization or elimination [94]–[96], residual stress or deformation reduction [93], [97], etc. Some of these constraints are discussed in the following sections.

2.4.1. Overhang Minimization and Elimination

Overhanging features of parts built by laser powder bed fusion AM cause a significant increase in cost and printing time because more sacrificial material is needed to support them. Overhangs are arguably the most studied AM constraint in topology optimization. An overhanging feature lacks sufficient supporting material beneath it in such a way that it is either perpendicular or at an angle subtended to the building direction; a well-supported element or feature is shown in Figure 2.13. Although several researchers have suggested 45º as the minimum self-supporting angle, the choice of the angle must be governed by the technicalities of the process [76]. Gaynor and Guest [76] included three more minimum overhang angle constraints which depended on the feature size thickness shown in Figure 2.14.
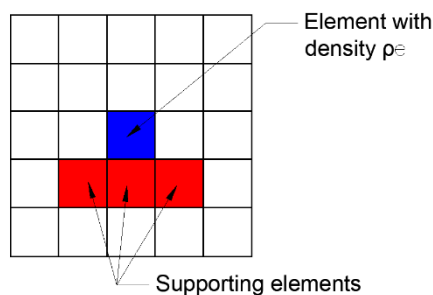
Figure 2.13:Element density with supporting elements in a 2D FE mesh
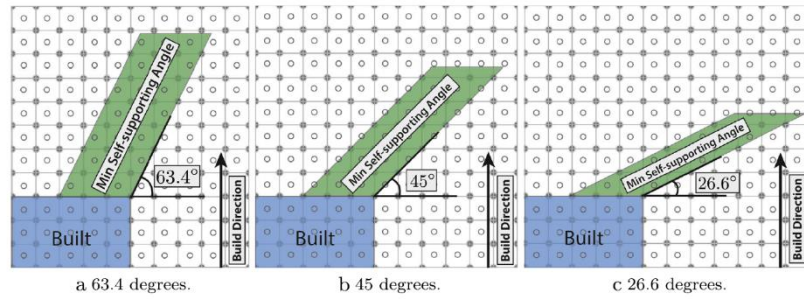
Figure 2.14: Different allowable minimum self-supporting angles for satisfying overhang constraints [78]

Typically, in defining or building up the overhang constraint, an evaluation of the contour for resulting topologies on every iteration should be done [98]. Several researchers have deployed different methodologies to identify edges and formulate an expression for overhang as a constraint within the optimization problem. Two common aspects in resolving overhanging features are predetermining a build direction or orientation and formulating an element overhang expression that can be coupled with the objective function or included as a constraint in the optimization problem statement. Overhang formulations solved as constraints in optimization problems can be seen in [98], [80]. Zhang et. al. [99] considered hanging features alongside overhang features shown in Figure 2.15, Xinyi et. al. [100] looked at overhang reduction by coupling normalized compliance and overhang expressions serving as the objective function for minimization.

(a) The optimum design without overhang constraint and hanging feature constraint.

(b) The optimum design subject to overhang angle constraint.

(c) The optimum design subject to overhang angle constraint and hanging feature constraint.
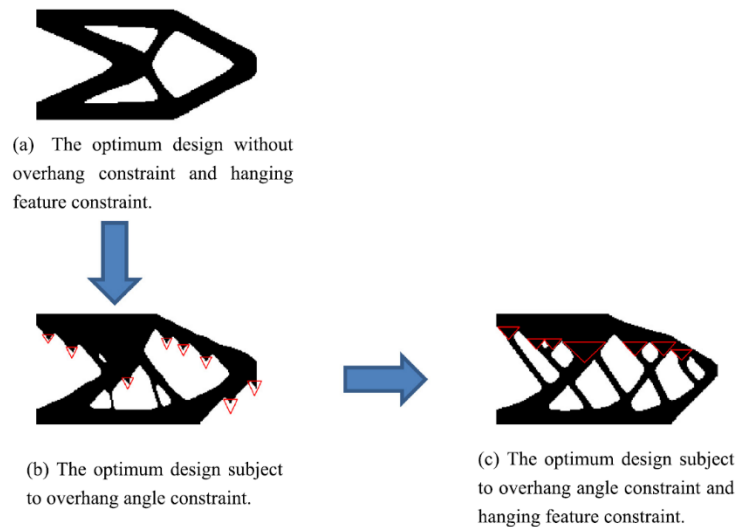
Figure 2.15: Optimum designs showing the difference in topologies of overhanging constraint alone against combined overhanging and hanging constraints [99].

Employing a continuous front propagation mechanism, Van de Ven et. al. [82],[101] made use of a "printable" density variable for overhang control. RAMP material interpolation was used in conjunction with the Method of Moving Asymptotes optimizer by Svanberg [55]. Figure 2.16 shows optimal designs with overhang constraints as obtained by Van de Ven et. al. [101] and Gaynor and Guest [76]

Figure 2.16: Optimal designs with 45˚overhang angles for a half and full MBB beam by [101] and [76].

Garaigordobil et.al. [98] and Zhao [102] formulated overhang constraints added to the material volume constraint in their topology optimization problem definition. In the former, after a contour detection is done, the constraint is computed as a ratio of the number of self-supported contours to the total number of acceptable and unacceptable contours. The work by Zhao formulated an overhang constraint by summing the density squares of unsupported elements. Using the Bi-directional Evolutionary Structural Optimization (BESO) approach, Minghao et.al. [103] developed a layer-wise overhang restriction constraint within the updating scheme. The framework using uniform cuboid voxels can achieve 45° overhang thresholds while arbitrary angle thresholds can be implemented by changing the aspect ratio of the voxels. Wang et.al. [100] formulated a consolidated objective function comprising of compliance and an overhang function and then attempting to simultaneously minimize both. In this case, instead of eliminating overhangs, their results included some unsupported features as should be expected in a minimization scheme.

2.4.2. Self-Supporting Constraint

AM technologies such as Selective Laser Melting (SLM) and Fused Deposition Modelling (FDM) need sacrificial structures for mechanical support and proper heat dissipation without which the part quality cannot be guaranteed. Support structures are therefore inevitable to support the base of the part but can be minimized or eliminated when printing features within the part. This constraint is very similar to an overhang and/or hanging constraint but slightly differs in the sense that a self-supporting constraint usually deals with the whole part while an overhang constraint deals with features or regions in a part. In general, the definitions of these constraints have been interchanged or taken as the same by several research efforts.

Guo et. al. [22] proposed two methods to ensure optimized topologies comply with certain self-supporting angles. The methods are known as Moving Morphable Components (MMC) and Moving Morphable Voids (MMV). The first method takes the inclination angle of features or components in the topology as the design variable. The second method introduces printable features (voids) such that their interfaces are represented by B-spline curves used in the problem formulation; thereafter, the problem is solved as a shape optimization problem rather than topology optimization. Langelaar [77] developed an AM filter for density-based topology optimization which has semblance as the typical layerwise AM process. In this way, any feature inclined at an unacceptable angle will be banned from the design space. Figure 2.17 shows Langelaar's AM filter for an optimized 2D half MBB beam built using different baseplate positions.

a) N case: C/C_{ref}=106%, M_{nd}=3.3%

b) E case: C/C_{ref}=102%, M_{nd}=1.6%

c) S case: C/C_{ref}=102%, M_{nd}=2.2%

d) W case: C/C_{ref}=99.9%, M_{nd}=1.1%

e) Reference case (unrestricted): $C=C_{ref}$, M_{nd}=2.2%
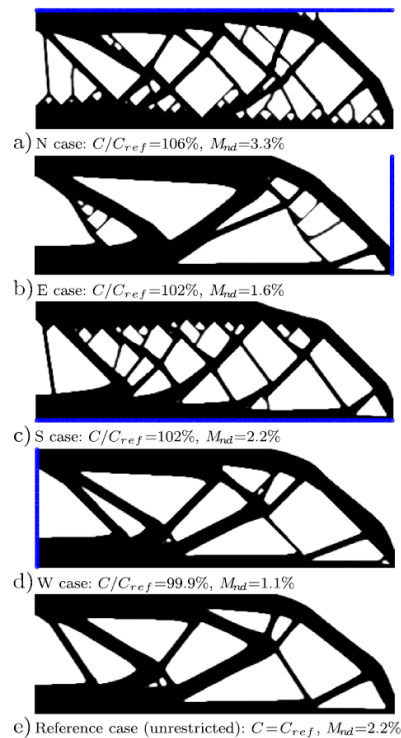
Figure 2.17: Topology optimized half MBB beam with AM filter and Heaviside projection with baseplate indicated in blue [77].

Another effort to factor a self-supporting constraint in topology optimization is seen in the work by Mezzadri et. al. [104] where they focused on both volume and compliance constraint-based topology optimization approaches for self-supporting support structures. To resolve the self-supporting problem, Zhang and Zhou [105] introduced polygon-featured holes as basic primitive designs whose movements, deformations, and intersections can control the outcome of the structural topology. They made use of a

finite cell method (FCM) which has the finite element method (FEM) incorporated in it. Other innovative works that capture self-supporting and overhang constraints can be seen in [106], [78], [107], [84].

There are several drawbacks to the constraint formulations discussed. Firstly, some of them are restricted to eliminating overhanging features at one angle threshold only e.g. Langelaar's overhang restrictive filter for 45°. Secondly, although most of them being integrated methods ensure structural optimality, they will usually contribute to increases in computation cost and inefficiency. This is caused by the several chains of gradient calculations that should be made due to the additional constraint or objective overhang functions. Furthermore, this will bring to question their capabilities to perform in complicated multiphysics and multiobjective topology optimization problems.

2.4.3. Void filling constraint

Powder-bed AM technologies build a part in a layerwise manner in such a way that unmelted powders fill holes and cavities within the part. Therefore, in most cases, it is paramount that these unmelted powders are removed during post-processing, so a usual design criterion is to ensure that there are channels through which these powders can be taken out. During topology optimization, there is the possibility of obtaining results with completely or partially enclosed cavities. Researches have been done to mitigate this problem by formulating void filling constraints within topology optimization. An innovative methodology proffered as a solution was formulated by Liu et. al. [90] in 2015 which they referred to as the Virtual Temperature Method (VTM). The first step was to establish the connectivity of the structure by classifying structures without voids as "simply-connected" and those with voids as "multiply-connected". Simply-connected structures should have holes or voids that have channels leading out of the structure while multiply-connected structures have completely closed voids. Once these definitions are implemented, the 'void' elements are assigned with a 'virtual' heat source while solid elements are assigned as thermally insulating materials. A heat conduction problem is then formulated and solved to obtain temperature values of all elements within the design domain. Thereafter, a constraint is set up within the optimization algorithm such that the maximum temperature in the domain during the process is enforced to be less than or equal to a threshold temperature set before the optimization's commencement. This will ensure that voids are avoided or minimized during topological formation. Figure 2.18 shows optimized topologies obtained with and without void elimination.
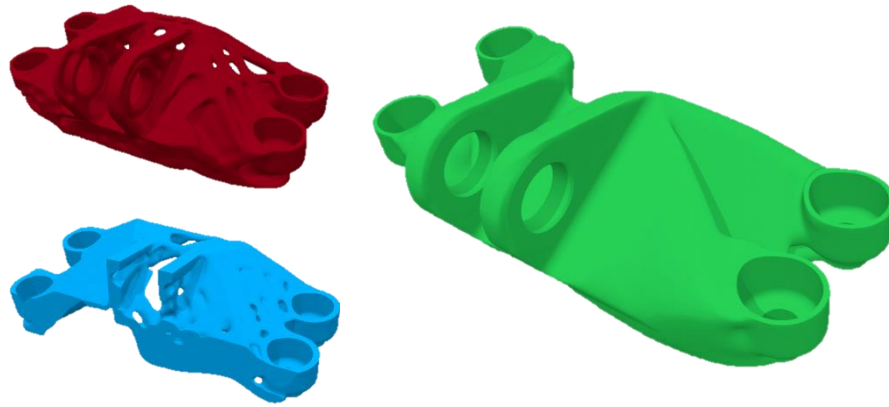
Figure 2.18: Optimized designs of an aerospace bracket. The two left designs are without the void filling constraint while this constraint is included in the optimized topology on the right.

2.4.4. Minimum feature thickness

Very thin features are undesirable in a design to be additively manufactured due to the minimum sizes allowable for different AM technologies. The minimum wall thickness is usually dictated by the melt-pool width in the case of Laser Powder Bed Fusion (LPBF) and nozzle diameter in the case of Fused Deposition Modelling (FDM). In most topology optimization algorithms, the minimum size feature is controlled by filtering methods with sensitivity and density filter being the most popular [48], [108], [109]. Osanov and Guest [110] addressed minimum feature size through the layer-wise nature of additive manufacturing process by a modified Heaviside Projection Method (HPM) which is common in achieving geometric constraints in topology optimization. The Heaviside Projection Method (HPM) is a popular filtering method for solving mesh-dependent and checkerboarding problems in topology optimization similar to sensitivity and density filtering. The modification of the HPM was in the search area of neighboring elements for filtering. The standard HPM uses a spherical search volume while the Osanov and Guest used a cylindrical volume to mimic the layer-by-layer AM process.

Minimization of thin features and support structures was carried out by Mhapsekar et. al. [84]. They implemented the density filter in SIMP for feature size control by using a cylindrical search volume as Osanov and Guest which is comparable to the layer-wise process of AM. Figure 2.19 and Figure 2.20 show the size feature control by Mhapsekar et. al.
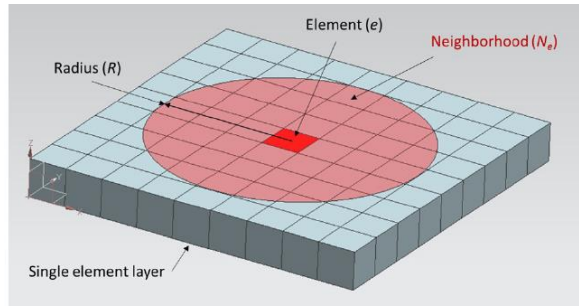
Figure 2.19: Single layer neighborhood of element [84].
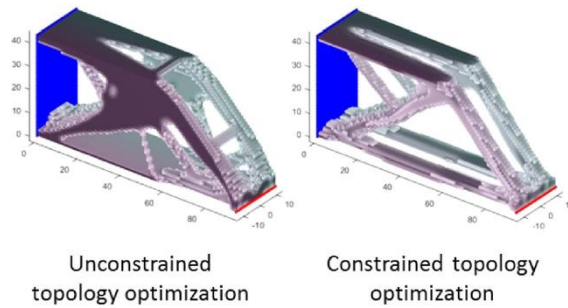
Figure 2.20: Unconstrained and constrained TopOpt cantilever topologies. It is observable that the right cantilever has a controlled size feature unlike that on the left [84].

2.4.5. Anisotropic material property considerations

In most additive manufacturing technologies, part anisotropy is prevalent especially in the build direction. In a study by Chiu et. al. [111], they discovered that when anisotropy is considered in topology optimization of parts to be additively manufactured, less material savings is achieved for a volume fraction minimization formulation as opposed to utilizing isotropic material properties. They concluded that anisotropy can significantly affect the topological optimality of parts and recommended using anisotropic material properties for AM-related topology optimization processes. Some works have considered topologically optimizing parts against anisotropy such as the strength-based topology optimization model developed by Mirzendehdel, Rankouhi, and Suresh [112] where they minimized a p-norm factor of safety function while limiting the designs to a compliance threshold. Liu and To [113] addressed both anisotropic material property considerations and self-supporting constraint by formulating a deposition path planning level set topology optimization algorithm. They considered material properties for both build and in-plane raster directions. The use of build orientation optimization to enhance the performance of parts to be additive manufactured was implemented by Ulu et.al [114].

In their work, they utilize the Euler angles of the parts as design variables and obtain the values that maximize the parts' minimum facture of safety.

2.5. Experimental validation studies for topology optimized parts

From the author's knowledge, no research work has investigated the effects of topology optimization/including manufacturability constraints on residual stress formation on the part surface or throughout the bulk material. This might be because many research efforts [115]–[117] suggest that residual stresses in LPBF are most impacted by temperature gradients and cooling rates/patterns. Many efforts, however, have studied the impact of topology optimization on structural performance. Zhu [118] developed an experimental testing method to investigate the correlation between the numerically obtained performance of topology optimized structures manufactured by stereolithography (SLA) and their practical values. Using SLA again, Li et.al [119] investigated the relationship between directional parameters and transverse isotropy of printed parts. They observed that the elastic or Young's Modulus varied by 6.6% while the strength varied by around 23.8% when they evaluated isotropic properties in the transverse direction. Clausen et.al [120] investigated the buckling performances of a topology optimized infill structure and an optimized solid structure based on compliance minimization. They discovered that a porous in-plane structure was as much as 5 times better than a solid structure while a porous out-of-plane structure was 3 times better. Other experimental validation and verification studies on topology optimized cellular-type structures can be seen in [121]–[123] and topology optimized parts for various applications can be seen in [124]–[127].

2.6. Some open-source frameworks for topology optimization

To date, Table 1 in [128] shows that a greater number of topology optimization codes handle 2D [129] [130] [54], [131]–[138] compared to 3D [130] [139]–[141] design problems and the reasons are not far-fetched: much less computational cost, ease of implementation especially considering new approaches, ease of understanding by beginners in this field, etc. As much as 3D cases are more practical and are getting more popular in implementation due to improvements in software and hardware, many real design problems can be simplified to 2D forms without losing significant accuracy. Unfortunately, a common attribute to many of the available open-source codes is the rigidity in defining initial free-form domains, loads, and support conditions. Additionally, users cannot easily translate the results obtained from optimization to manufacture-ready models. With the advancement of additive manufacturing technologies, it will be of immense benefit to have an open-source code that allows users to go almost

seamlessly from a structural problem to a printable model using topology optimization and without interfacing with too many software tools while saving computational cost. A few works have considered free-form designs, such as the PolyMesher developed by Talischi et.al. [133], which is a mesh generator for polygonal elements written in Matlab. They reported that polygonal meshes are immune to checkerboarding issues commonly associated with the use of lower-order triangular or rectangular meshes. Also, they described the good adaptability of these polygonal meshes to intricate domains. In 2013, a free form design modeler (FDDM) in conjunction with a topology variation modeler (TVM) was developed by Cai and Zhang [142]. They achieved this by using mathematical R-functions in the form of implicit Level Set Functions (LSFs). To interpret topological results, Chou and Lin [143] introduced the improved automated structural optimization system (IASOS) which they reported is an improvement on the automated structural optimization system (ASOS) by using a polygonal image-interpreting technique to replace the existing value-based method. Aage, Andreassen, and Lazarov [141] developed a fully parallel open-source framework suitable for high-resolution topology optimization capable of manufacture-ready designs. More recently in 2018, Gamache et.al. [144] introduced an image-based truss recognition system that was developed to interpret aircraft structures design via topology optimization.

Regardless of these innovative techniques to address the initialization and post-processing of structural design problems for topology optimization, in the author's best knowledge, there is still no freely available Matlab code that holistically covers free-form initialization, deployment of several topology optimization approaches, and post-processing for 2D topology optimization.

2.7. Summary

In this chapter, the design for additive manufacturing (DfAM) has been reviewed and topology optimization which is an important tool for structural design and optimization has been theoretically elaborated on. More focus was placed on topology optimization of structures under design-dependent loads because it falls under the scope of this work. Topology optimization tailored for additive manufacturing has also been reviewed by exploring the various efforts that have considered important AM constraints. Finally, a brief review of open-source frameworks for topology optimization was presented.

Based on this extensive review, several studies have investigated and developed frameworks for multiphysics and multiobjective topology optimization, however, they are usually limited to a pair of

design-independent and -dependent loads. To enhance topology optimization for DfAM by effectively designing parts that operate under complex load conditions, more load cases (especially involving several design-dependent loads) should be studied. Also, the development and availability of robust optimization-integrated AM constraints (e.g. overhang elimination) have been provided by several research efforts, notwithstanding, there is no assurance of the effectiveness of these schemes for topology optimization models considering design-dependent loads. Therefore, the development of a suitable scheme that introduces an AM constraint for part manufacturability with little to no effect on the multiphysics and multiobjective topology optimization model is recommended.

Chapter 3: Modeling Thermoelastic Stress and Centrifugal Loads for Topology Optimization considering Load Thresholding.

3.1 Introduction

This chapter will establish the thermal stress and centrifugal load equations of a rigid body under elevated temperature and angular rotation necessary to resolve the body's response for topology optimization. In Chapter 2, topology optimization has been very well established for pure mechanical loads such as point forces and restricted pressure. In literature, topology optimization for thermal/fluid effects based on maximizing cooling [145], minimizing heat conduction [146], [147], [32], or maximizing/minimizing pressure drop for fluid-flow problems [148], [149], [150] have been well studied. Rotor components close to the combustion chamber in gas or steam turbine engines operate under high thermal, rotational, and pressure conditions. These components are usually made of high-strength ductile superalloys with excellent fatigue [151] and creep properties [152]. They can also excellently retain their elasticity for over 400 MPa yield strength at significantly high temperatures [153]. Therefore, to topologically optimize these components for a single material, the consolidated compliance from thermal stress, pressure, and rotational loads can be minimized. The formulations are based on linear elastic material models since superalloys such as Hastelloy X are considered the component material and no plastic flow is induced under the load conditions. This chapter will focus on thermal stress and centrifugal loads while design-dependent pressure loads are left for Chapter 4.

3.2. Thermoelastic Stress Load (TSL)

Structures under thermal and mechanical loads (point forces or restrained pressure) will experience significant topological changes during optimization as opposed to being under mechanical loads only. The reason is that a body under elevated temperature deforms according to its thermal expansivity [154] in addition to its Young's Modulus [27]. The load experienced by a body or element resulting from an elevated temperature is referred to as thermal stress or thermoelastic stress load (TSL) [27]. As will be pointed out in later sections, the thermal stress load in an element is dependent on its amount of material within the volume occupied by the element. Therefore, as the topology of the entire structure is being updated, the magnitude and/or direction of this load on every element will change accordingly, the

reason they are referred to as design dependent. Figure 3.1 shows a structure with constant elevated temperature in (a) and steady temperature distribution in (b) with a mechanical load and a fixed boundary condition.
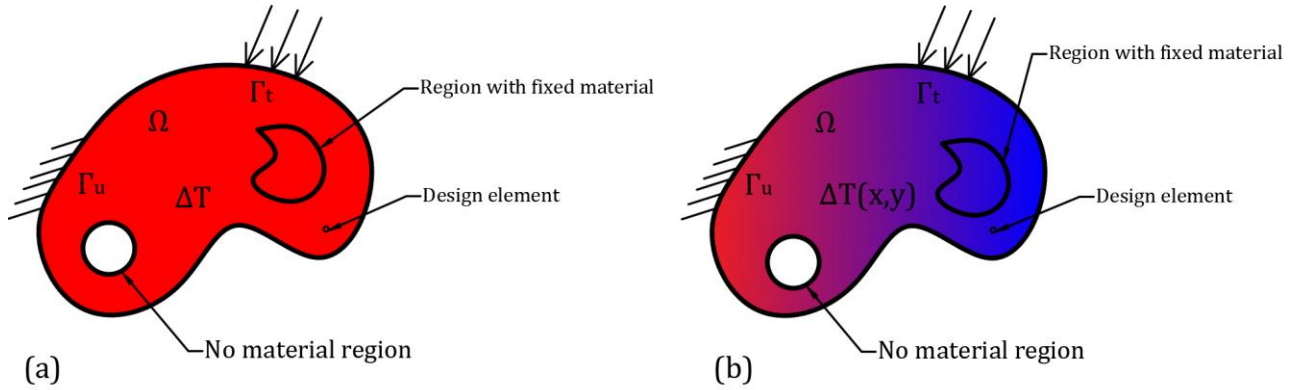
Figure 3.1: Thermo-mechanically loaded structures (a) with constant temperature change (b) with a temperature distribution

3.2.1 Thermal Stress Coefficient

In a thermo-elastic problem, the cell elastic strain energy of an element in a discretized material space will depend on its temperature change with ambiance, material's coefficient of thermal expansivity, and Young's Modulus. The cell's elastic strain energy can be defined as the potential mechanical energy in the elastic body [58]. For the rigid body in Figure 3.1, if we assume that the material properties are temperature independent, temperature distribution remains constant through any given period (steady-state), and no plastic strain, we can express the cell elastic strain energy Φ_e^m in terms of the cell's stress σ_e^m and strain ε_e^m as:

$$\Phi_e^m = \frac{1}{2}\int_\Omega \sigma_e^m \varepsilon_e^m d\Omega \tag{3.1}$$

For a solid element,

$$\Phi_e^m = \frac{1}{2}\iint_v \sigma_e^m \varepsilon_e^m dv$$

Recall that the total strain ε_e is a consolidation of the elastic strain from mechanical load ε_e^m and thermal load ε_e^{th}

33

$$\varepsilon_e = \varepsilon_e^m + \varepsilon_e^{th} \tag{3.2}$$

The total stress on the cell is

$$\sigma_e = D_e \varepsilon_e \tag{3.3}$$

Therefore, the stress from elasticity because of pure mechanical load can be obtained thus:

$$= \frac{1}{2} \iint_A (\varepsilon_e - \varepsilon_e^{th})^T D_e (\varepsilon_e - \varepsilon_e^{th}) h \, du \, dv$$

$$= \frac{1}{2} \iint_A (\varepsilon_e^T D_e \varepsilon_e - 2\varepsilon_e^T D_e \varepsilon_e^{th} + (\varepsilon_e^{th})^T D_e \varepsilon_e^{th}) h \, du \, dv$$

Thermal strain vector

$$\varepsilon_e^{th} = \alpha_e (T_e - T_{amb}) \phi^T \tag{3.4}$$

$$\Phi_e = \frac{1}{2} \iint_A (u_e^T B^T D_e B u_e - 2u_e^T B^T D_e \alpha_e \Delta T \phi^T + \alpha_e \Delta T^T D_e \alpha_e \Delta T \phi^T \phi) h \, du \, dv \tag{3.5}$$

The differential of strain energy w.r.t displacement should be zero for a steady heat problem, therefore

$$\frac{\partial \Phi_e}{\partial u_e} = \frac{1}{2} \iint_A (2B^T D_e B u_e - 2B^T D_e \alpha_e \Delta T \phi^T) h \, du \, dv = 0 \tag{3.6}$$

If elastic stress is a consequence of the thermal effects on the cell, the first term in 3.6 is the resultant load that is an effect of the thermal expansion from the second term, therefore, thermal load for an element with unit thickness can be expressed as

$$F_e^{th} = \iint_A B^T D_e \alpha_e \Delta T \phi^T \, du \, dv \tag{3.7}$$

Where

$$B_i = \begin{bmatrix} \dfrac{\partial N_i}{\partial u} & 0 \\ 0 & \dfrac{\partial N_i}{\partial v} \\ \dfrac{\partial N_i}{\partial v} & \dfrac{\partial N_i}{\partial u} \end{bmatrix} \tag{3.8}$$

for a plane stress problem,

$$D_0 = \frac{1}{1-\mu^2} \begin{bmatrix} 1 & \mu & 0 \\ \mu & 1 & 0 \\ 0 & 0 & \frac{1-\mu}{2} \end{bmatrix}$$

$$D_e = E_e D_0$$

$$\varepsilon_e^m = \varepsilon_e - \varepsilon_e^{th} \tag{3.9}$$

Where B and D_e are differential shape function matrix and material matrix for plane stress respectively, α is the coefficient of linear thermal expansivity, E_e is Young's Modulus, u_e is displacement vector of nodes of an element, μ is Poisson's ratio, ΔT is the change in temperature with ambiance, and $\phi = $ [1 1 0] is the thermal strain unit displacement vector for 2D problems. It should also be noted that steady-state thermal condition is assumed for this formulation, therefore, ΔT is independent of time.

D_e and α_e are material properties that both depend on the pseudo-density design variable, x_e. It should be noted that variables with subscript or superscript "e" indicate a property for an element in the discretized domain. The material matrix is expressed as:

$$D_e = E_e D_0 \tag{3.10}$$

Substituting equation 4.8 into 4.5 gives

$$F_e^{th} = \iint_A B^T E_e D_0 \alpha_e \Delta T \phi^T \, du \, dv$$

$$= E_e \alpha_e \Delta T \iint_A B^T D_0 \phi^T \, du \, dv \tag{3.11}$$

E_e and α_e can be combined into one variable called Thermal Stress Coefficient (TSC) [27] and denoted by β_e and can be expressed by the RAMP function, which has been highly recommended in literature for design-dependent loads [27], [155], in equation 4.10

$$\beta_e = E_e \alpha_e$$

$$= \frac{x_e}{1 + q_2(1 - x_e)} E_0 \alpha_0 \tag{3.12}$$

In 3.12, q_2 is the penalization factor of the RAMP scheme for TSC. q_1 is left for the penalization of the Young's Modulus property which will be presented in Chapter 5.

Therefore, thermal stress load F_e^{th} can be written as

35

$$F_e^{th} = \beta_e \Delta T \iint_A B^T D_0 \phi^T du dv \tag{3.13}$$

After integration,

$$F_e^{th} = \frac{\beta_e \Delta T}{2(1 - \mu)} [-1 \ -1 \ 1 \ -1 \ 1 \ 1 \ -1 \ 1]^T \tag{3.14}$$

3.2.2 Steady-State Heat Transfer

Structures under steady-state thermal distribution should have this distribution updated as topology changes. Also, if there are convective effects around surfaces, it should affect the temperature distribution in the design. For a steady-state heat problem, the thermal distribution can be updated on every iteration by calculating the heat transfer equation.

Fourier's equation for heat transfer is given as

$$\frac{\partial}{\partial x}\left(k\frac{\partial T}{\partial x}\right) + \frac{\partial}{\partial y}\left(k\frac{\partial T}{\partial y}\right) + \frac{\partial}{\partial z}\left(k\frac{\partial T}{\partial z}\right) + Q = \frac{\rho c \partial T}{\partial t} \tag{3.15}$$

In 3.15, x, y, z are spatial coordinates, ρ is the material density and c is the specific heat capacity. For every finite element, the temperature can be obtained as

$$T_e = [N_i]\{T_i\}_e \tag{3.16}$$

Where N_i and T_i are shape functions and nodal temperatures respectively. This equation can be differentiated to obtain the temperature gradient within the element given as

$$\begin{Bmatrix} \dfrac{\partial T}{\partial x} \\ \dfrac{\partial T}{\partial y} \\ \dfrac{\partial T}{\partial z} \end{Bmatrix} = \begin{bmatrix} \dfrac{\partial N_1}{\partial x} & \dfrac{\partial N_2}{\partial x} & \cdots & \dfrac{\partial N_i}{\partial x} \\ \dfrac{\partial N_1}{\partial y} & \dfrac{\partial N_2}{\partial y} & \cdots & \dfrac{\partial N_i}{\partial y} \\ \dfrac{\partial N_1}{\partial z} & \dfrac{\partial N_2}{\partial z} & \cdots & \dfrac{\partial N_i}{\partial z} \end{bmatrix} \tag{3.17}$$

3.17 can be rewritten as

$$\{T\}'_e = [B_i]\{T_i\}_e \tag{3.18}$$

The heat transfer equation in 3.14 can be rewritten by Galerkin method as follows [156]

$$\int_V \left(\frac{\partial q_x}{\partial x} + \frac{\partial q_y}{\partial y} + \frac{\partial q_z}{\partial z} - Q + \frac{\rho c \partial T}{\partial t}\right) N_i dV = 0 \tag{3.19}$$

36

The discretized finite element equations for heat transfer problems can be expressed in a general form as [156]

$$[C]\{\dot{T}\} + ([\tilde{K}_c] + [\tilde{K}_h] + [\tilde{K}_r])\{T\} = \{R_T\} + \{R_Q\} + \{R_q\} + \{R_h\} + \{R_r\} \tag{3.20}$$

Where $[C]$ is the matrix of material heat capacity, $[\tilde{K}_c]$ is the conductivity matrix, $[\tilde{K}_h]$ is the convective matrix, $[\tilde{K}_r]$ is the radiative matrix and $\{R_T\}$, $\{R_Q\}$, $\{R_q\}$, $\{R_h\}$, $\{R_r\}$ are heat loads by conduction, volume conduction, surface conduction, convection, and radiation respectively. k, h, Q, q_s are the thermal conductivity, convective heat transfer coefficient, heat energy, and surface heat flux respectively.

For steady and linear heat transfer, equation 3.19 becomes

$$([K_c] + [\tilde{K}_h])\{T\} = \{R_Q\} + \{R_q\} + \{R_h\} \tag{3.21}$$

The matrices are defined as

$$[\tilde{K}_c] = \int_V k[B]^T[B]dV$$

$$[\tilde{K}_h] = \int_S h[N]^T[N]dS$$

$$\{R_Q\} = \int_V Q[N]^T dV \tag{3.22}$$

$$\{R_q\} = \int_S q_s[N]^T dS$$

$$\{R_h\} = \int_S hT^e[N]^T dS$$

In 3.22 S and V denote surface and volume domains respectively.

3.3. Load considerations in rotating structures

Several components operate in dynamic states, a peculiar one being the operation of rotor components in a gas or steam turbine. In rotation, a structure comes under centrifugal loads that will exert a displacement response away from the center of rotation. The severity of this response will depend on the

structure's mass, rotational speed, and distance from the center of rotation. Also, the moment of inertia of a rotating structure contributes to the power consumed, therefore, minimization of its kinetic energy can be necessary for structural optimality depending on the position of the rotational axis [29]. The topology optimization model in the previous chapter essentially remains the same except for an additional objective - kinetic energy minimization.

If we assume a rigid body of mass m and density ρ_0 shown in Figure 3.2(a) is rotated by a shaft by Nrpm, the weighted multiobjective function can be written as
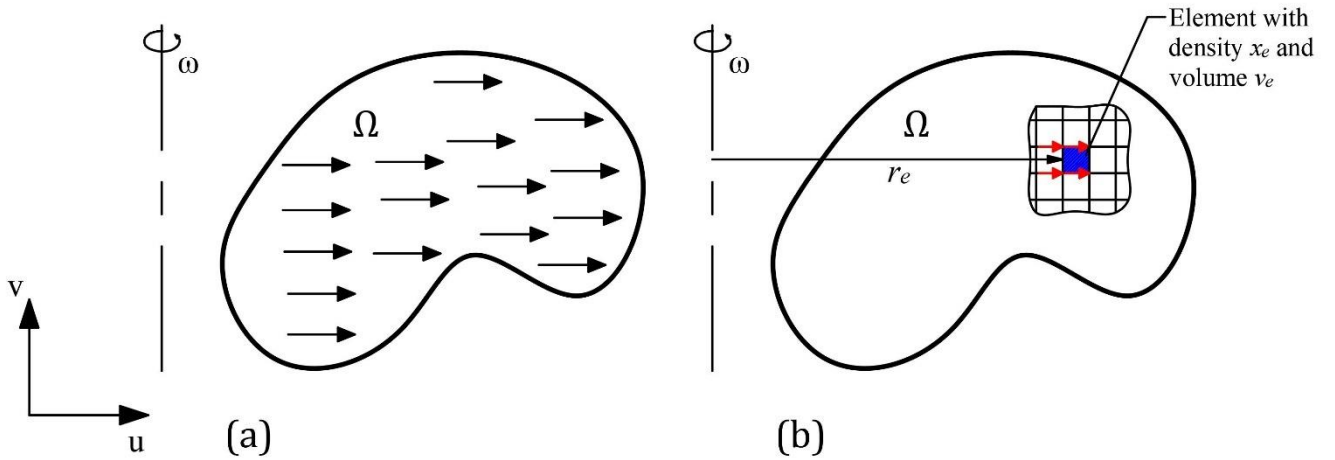
Figure 3.2: A rotating structure showing (a) the free body diagram (b) the nodal centrifugal forces (in red) on an element in a discretized region.

$$\min \text{ Obj. F} = w_1 C_c(x_e) + w_2 \Psi(x_e) \tag{3.23}$$

3.23 can be written as

$$\min \text{ Obj. F} = w_1 F_c U_c + w_2 \left(\frac{1}{2} I \omega^2\right) \tag{3.24}$$

Where $C_c(x_e)$ is the compliance function for centrifugal loads and $\Psi(x_e)$ is the kinetic energy function while F_c, U_c, I, and ω are the centrifugal force, displacement, moment of inertia, and rotational speed respectively of the structure.

Recall that

$$F_c = m\omega^2 r \tag{3.25}$$

In the finite element form, and considering the design variable x_e for optimization,

38

$$F_e^c = x_e \rho_0 \omega^2 r_e$$

$$F_e^c = x_e \rho_0 v_e \left(\frac{2\pi N}{60}\right)^2 r_e \tag{3.26}$$

The moment of inertial I of the rotating body around an axis at a distance r

$$I = mr^2$$

$$I_e = x_e \rho_0 r_e^2 \tag{3.27}$$

Inserting 3.26 and 3.27 into 3.24,

$$\min \text{ Obj.} F = w_1 \left\{ x_e \rho_0 v_e \left(\frac{2\pi N}{60}\right)^2 r_e \right\} U_c + w_2 \left\{ \frac{1}{2} x_e \rho_0 r_e^2 \left(\frac{2\pi N}{60}\right)^2 \right\} \tag{3.28}$$

To simplify the objective function for rotational loads to be used in topology optimization, the kinetic energy term is neglected because all the independent variables except U_c are present in both terms. 3.28 becomes

$$\min \text{ Obj.} F = \left\{ x_e \rho_0 v_e \left(\frac{2\pi N}{60}\right)^2 r_e \right\} U_c \tag{3.29}$$

The force definition in equation 3.26 can be further defined in finite element vector form for a homogenous bilinear square mesh as illustrated in Figure 3.4(b) by 3.30.

$$F_e^c = \frac{1}{4} x_e \rho_0 \left(\frac{2\pi N}{60}\right)^2 r_e [1\ 0\ 1\ 0\ 1\ 0\ 1\ 0] \tag{3.30}$$

Where f_u, f_v represent every nodal centrifugal force component in the u and v directions respectively.

3.4. A case study considering load thresholding

A case study is presented to compare thermoelastic stress and centrifugal loads. A cantilever structure with a temperature distribution as shown in Figure 3.3 is rotated about a vertical axis. Thermal boundary conditions of constant temperatures $400°C$ and $250°C$ are placed on two perimeter sections of the domain while other sections are assumed to be under adiabatic conditions. The cantilever rotates at $400\ RPM$. The material properties are assumed to be: linear thermal expansivity $\alpha = 3 \times 10^{-6}/K$, density $\rho_0 = 8000\ kg/m^3$, Young's Modulus $E_0 = 100\ GPa$, and Poisson's ratio $\mu = 0.3$. The domain

was discretized by 13,400 homogenous bilinear square elements with a length of 4 mm. Equations 3.14 and 3.30 were applied for thermoelastic stress load and centrifugal load respectively. The load fields and distributions are shown in Figure 3.4.
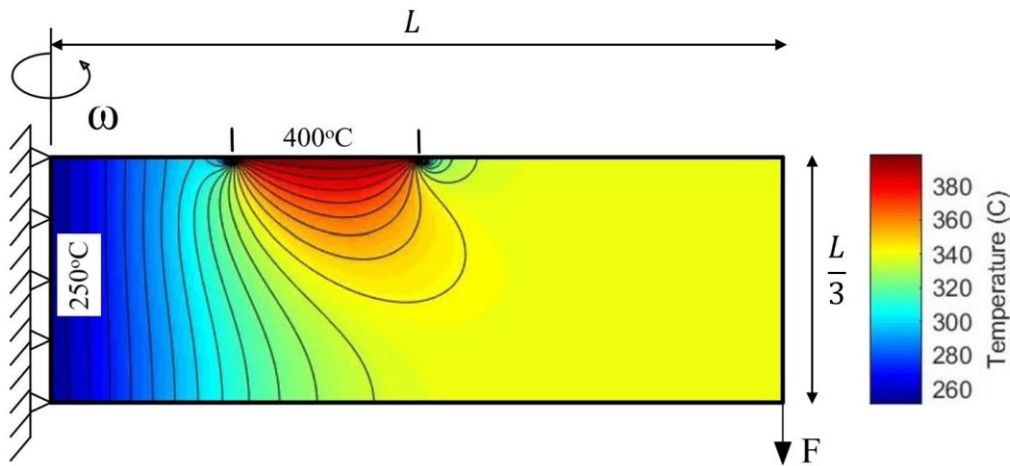
Figure 3.3: A rotating cantilever with a temperature distribution

The quiver arrows in Figure 3.4(a) show the gradient of the load field with larger arrows indicating larger gradients and the direction indicating the movement from smaller load areas to larger ones – essentially establishing the load path. As expected, centrifugal load paths are directed outwards from the center of rotation with a gradual load increase peaking at regions farthest away from the center of rotation. Thermoelastic stress load paths are expectedly more intricate with the gradients moving away from lower load to higher load regions. In Figure 3.4(b), the element load distributions are shown. Since homogenous mesh elements were used, an equal number of elements is observed in every load category for centrifugal loads. However, for TSLs, all the elements are acted upon by 60% and over of the maximum absolute load in the TSL vector. The inherent nonuniformity of the load gradients can have an impact on the topology optimization of structures under these loads, however, the most impact comes from the relatively close load contribution from every element in the optimization as experienced in the TSL vector. To simplify these load contributions for topology optimization, a threshold is introduced.
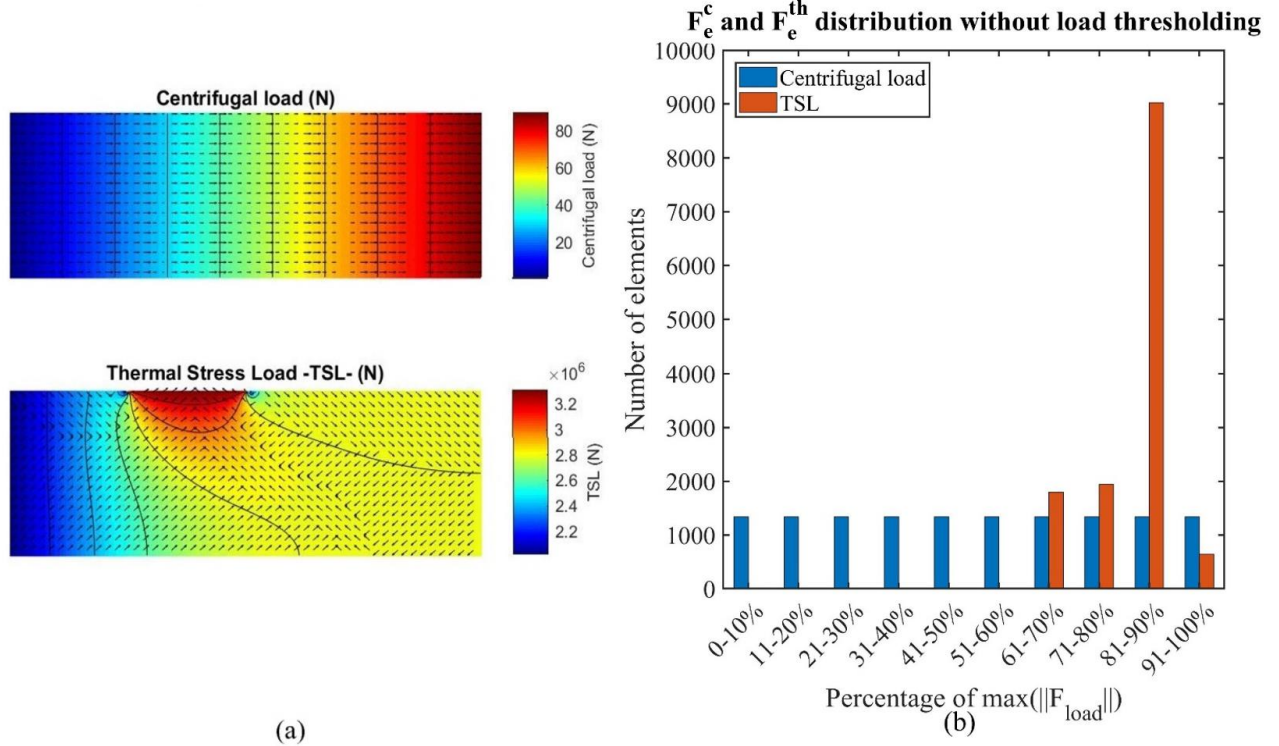
Figure 3.4: Centrifugal and thermoelastic stress (a) load fields (b) element load distribution.

Thresholding is common in topology optimization: as filters to obtain sharp or crisp boundaries in the resulting density field maps [83], [108], [109], [157], modeling geometric uncertainties [158], modeling AM overhang restrictive filters [76], etc. In this study, the smoothed Heaviside function expressed in the work by Wang et. al. [108] as opposed to the non-differentiable exact Heaviside function is utilized to place a threshold on the thermal stress and centrifugal load values as expressed in 3.31-3.33:

$$\hat{F}_{load} = H(F'_{load})F_{load} \tag{3.31}$$

$$H(F'_{load}) = \frac{\tanh(\beta\eta) + \tanh\big(\beta(F'_{load} - \eta)\big)}{\tanh(\beta\eta) + \tanh\big(\beta(1 - \eta)\big)} \tag{3.32}$$

$$F'_{load} = \frac{F_{load}}{\max(||F_{load}||)} \tag{3.33}$$

$H(F'_{load})$ is the smoothed Heaviside function where η is the threshold parameter which ranges from 0 to 1 and β is the smoothing parameter. The higher the smoothing parameter, the more exact the thresholding function i.e peaking threshold attains perfection at $\beta = \infty$. F'_{load} is a normalized load parameter obtained by dividing the load vector F_{load} by the maximum absolute load in the vector

41

$\max(||F_{load}||)$ as shown in 3.33. Figure 3.5 shows the Heaviside function for different smoothing parameters at $\eta = 0.5$.
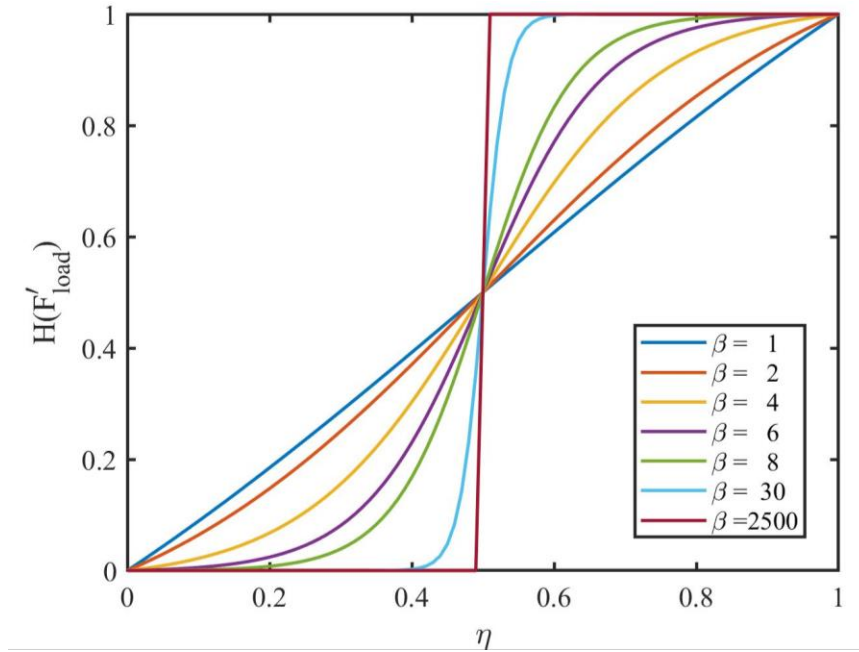
Figure 3.5: Smoothed Heaviside function for different smoothing parameters β.

3.31 and 3.32 are applied to the TSL and centrifugal load fields obtained in Figure 3.4 and the effects on the new load distributions are presented in Figure 3.6 to Figure 3.9. In these figures, it is observed that the thresholds ($\eta = 0.1, 0.4, 0.6, 0.8$) placed on centrifugal loads significantly affect the load distribution with over 50% of the loads on elements set to 0 when $\eta = 0.6, 0.8$. However, TSL field and distribution are not affected at all for $\eta = 0.1, 0.4$ in Figure 3.6 and Figure 3.7 while loads on a little over 500 elements are reduced when $\eta = 0.6$ in Figure 3.8. For $\eta = 0.8$ in Figure 3.9, loads on about 3000 elements (about 22% of the total number) are set to 0 for TSL distribution. On the one hand, load thresholding affects centrifugal loads considerably and if used in topology optimization, a significant inaccuracy in load representation is expected. Moreover, centrifugal loads exhibit directional uniformity ensuring fewer numerical instabilities during optimization
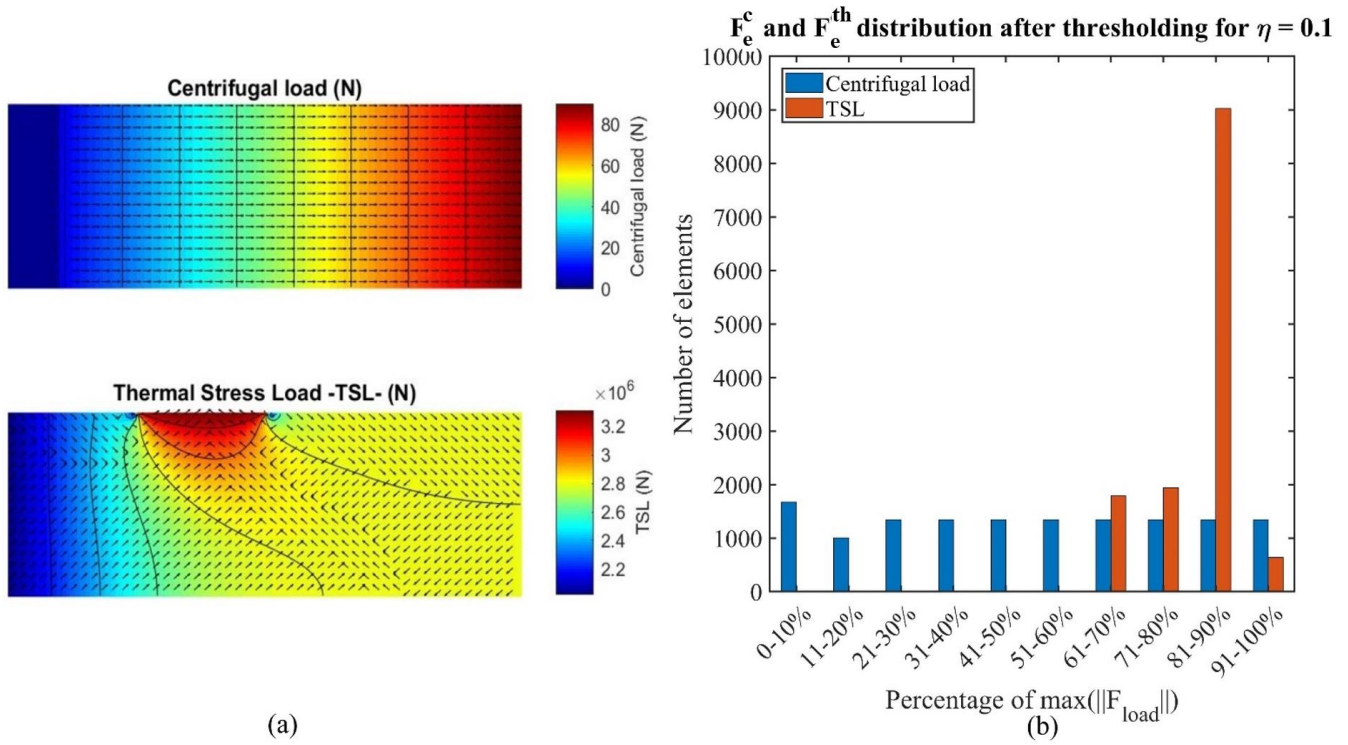
Figure 3.6: Centrifugal and thermoelastic stress load (a) fields (b) distributions for η=0.1
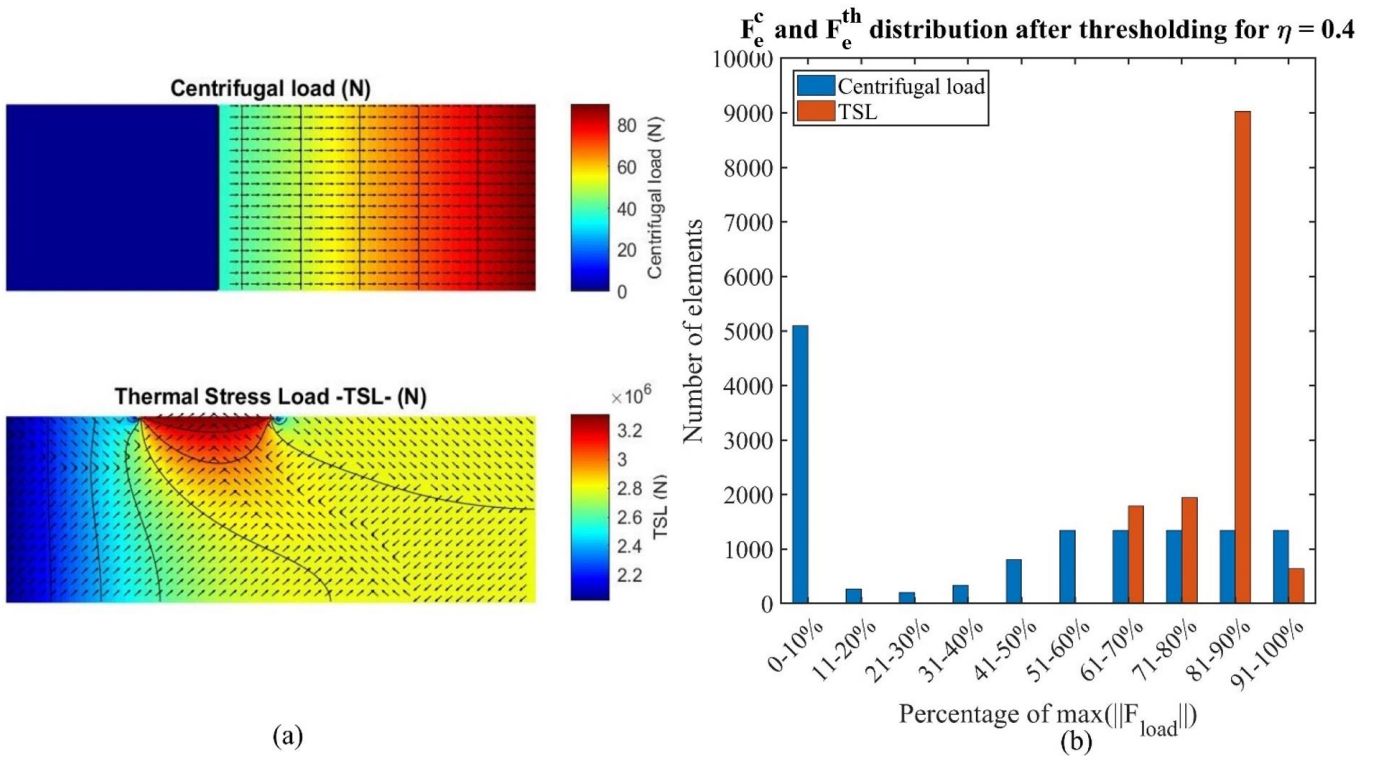
Figure 3.7: Centrifugal and thermoelastic stress load (a) fields (b) distributions for η=0.4
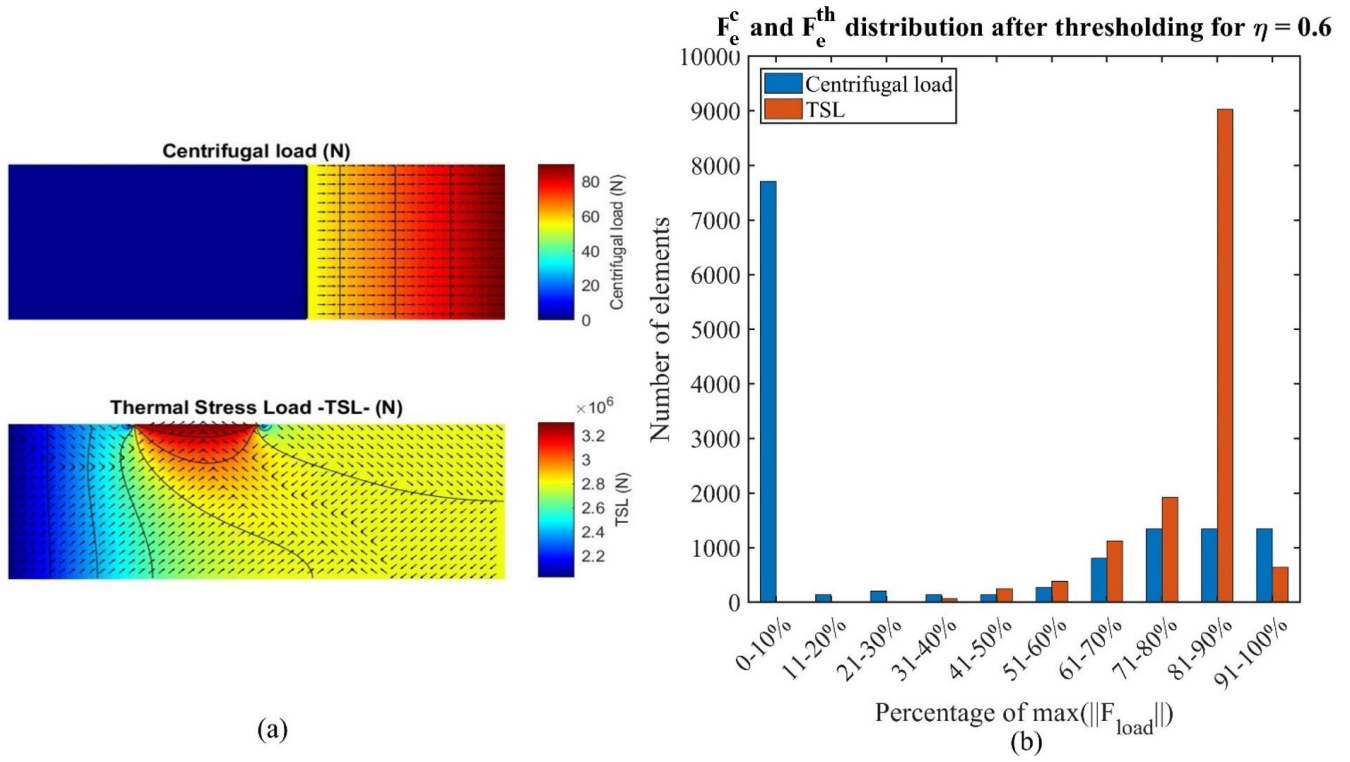
Figure 3.8: Centrifugal and thermoelastic stress load (a) fields (b) distributions for η=0.6
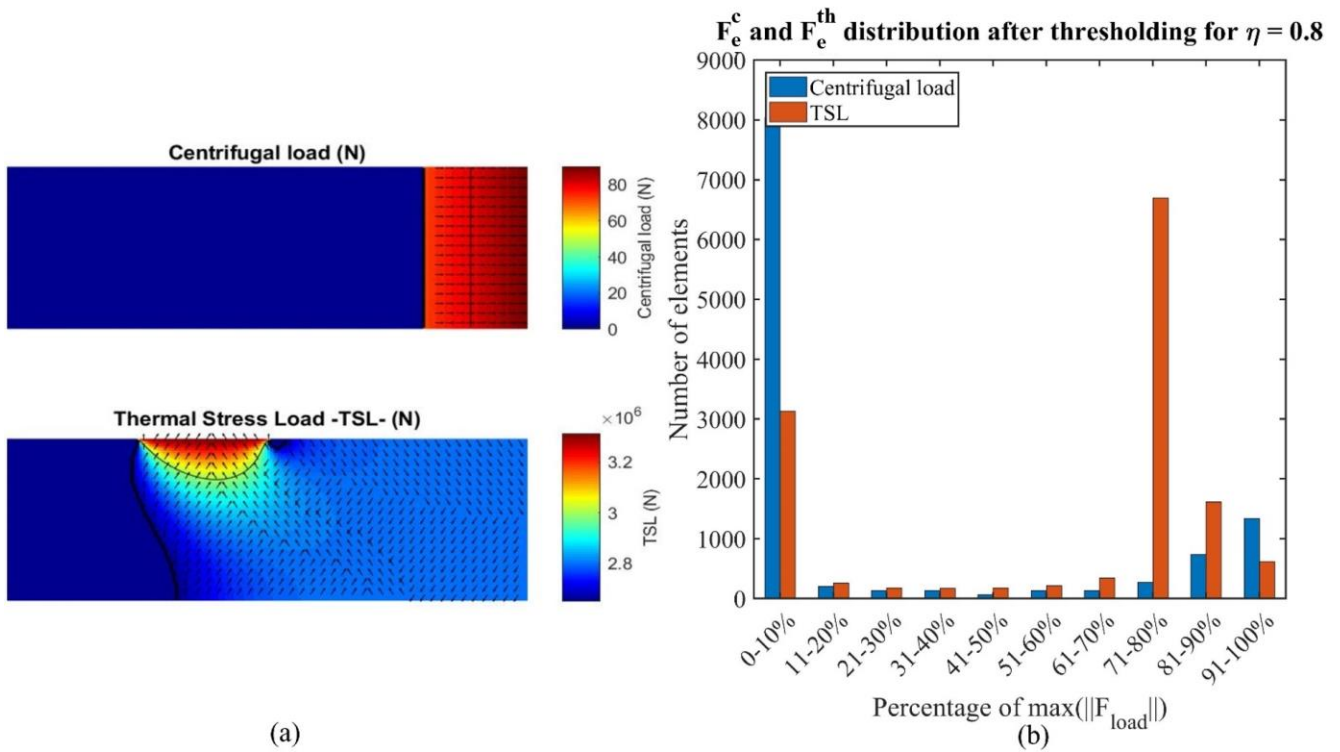
Figure 3.9: Centrifugal and thermoelastic stress load (a) fields (b) distributions for η=0.8

Conclusively, there is less need for thresholding centrifugal loads in topology optimization. On the other hand, for TSL, some distortion in the field and distribution is only found when $\eta = 0.8$, however, the field map is very similar to the initial map before thresholding whereas the load on around 3000 elements is set to 0. As will be observed in Chapter 5, thresholding the TSL field is quite beneficial to ensure the optimizer can update the pseudo-density design variables based on less random sensitivity information thereby reducing the chance of numerical instabilities in later iterations of the optimization.

3.3 Summary

In this chapter, the modeling of thermoelastic stress and centrifugal loads for topology optimization has been elaborately presented. The thermoelastic stress load (TSL) on an element in the discretized model is derived from its strain energy noting that the thermal strain resulting from an elevated temperature will cause thermal or thermoelastic stress load on the element. Centrifugal loads are much easier to derive from Newton's Second Law. The fields and distribution from both loads were analyzed with the use of the Heaviside function as a thresholding strategy. It was observed that centrifugal loads might not require thresholding for two reasons: first, thresholding generally simplifies the load model leading to a less accurate displacement response of the structure to the load, second, there is directional uniformity in the centrifugal load field ensuring less numerical instabilities during optimization with or without thresholding. Whereas, TSLs across elements are closely related in magnitude with about 97% of all elements having load values between 60% and 90% of the maximum elemental load. Also, there is high directional nonuniformity that can induce significant numerical challenges during optimization. Although there is bound to be some loss in accuracy for TSLs when thresholding is used, achieving a stable optimization process outweighs this downside.

Chapter 4: Topology Optimization of Structures under Design-Dependent Pressure Loads by a Boundary Identification and Load Evolution (BILE) Model

4.1.   Introduction

Topology Optimization of structures under pressure loads can be formulated either as design-independent or design-dependent subject to the nature of the design problem. For design-dependent pressure loads, as the optimization carries on, these loads might change in direction only or in both magnitude and direction depending on the methodology devised to update the changing pressure. If they change in magnitude, there will be a load sensitivity term in the sensitivity function that has to be calculated for and it is usually non-trivial. A significant challenge in topology optimization for design-dependent pressure load is identifying the change in the topological boundaries. In this chapter, the Boundary Identification - Load Evolution (BILE) model is proposed and it is set up by obtaining boundary and loading nodes located on the nodes of boundary elements throughout the optimization process. This two-step process of boundary identification and load movement or evolution involves firstly, a volume fraction threshold, which increases on every iteration for boundary identification. Secondly, a parameter is introduced that defines the number of iterations for load evolution between two boundary identification steps, which can also control the speed of optimization.

4.2.   Problem formulation using the SIMP model

The mathematical basis of conventional topology optimization is robust and well understood. If we consider a structural element in Figure 4.1(a), which comprises material and non-material domains, we assume the entire domain is chosen such that it accommodates given loads and boundary conditions. When the structure is optimized for design-independent or restricted pressure loads, there is a change in the topology but the magnitude and direction of the pressure load remain the same as observed in Figure 4.1(b). However, when acted upon by design-dependent pressure loads, the resulting topology as well as the pressure surface, magnitude, and direction change also in Figure 4.1(c). In this structure, we have fixed degrees of freedom Γ_u (can be applied to point, surface or body), loads on surfaces Γ_t, and body forces F_b. This chosen domain, usually called a ground structure, can be optimized based on minimizing the system's internal energy. The minimum internal or strain energy problem can be formulated from

the principle of virtual work which introduces an arbitrary virtual displacement v for an elastic structure with a fixed boundary $\mathbf{\Gamma_u}$, [53]:

$$\int_\Omega \epsilon^T(v)\big(D\epsilon(u)\big)d\Omega = \int_\Omega F_b^T v d\Omega + \int_{\Gamma_t} P^T v d\Gamma \tag{4.1}$$
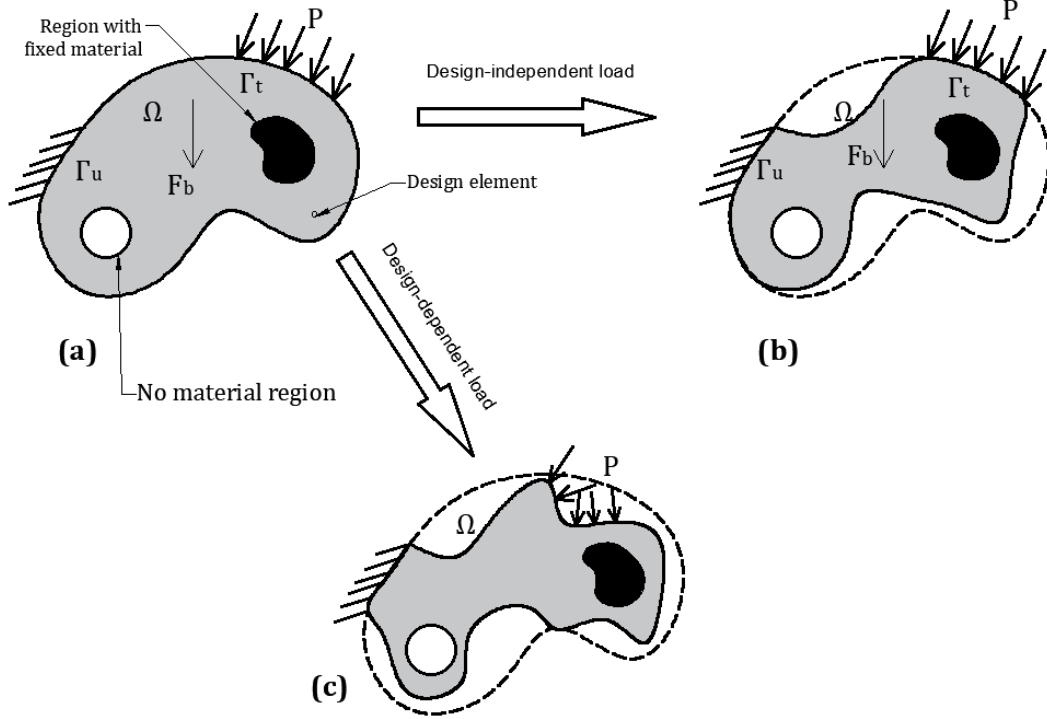
Figure 4.1: A structural element showing (a) Its original geometrical state with load and boundary conditions, (b) change in the state due to design-independent load (c) change in the state due to design-dependent load (dotted boundary in (b) and (c) show the original state in (a))

The left-hand side of 4.1 is the strain energy of the system in the elastic domain which is a combination of work done by forces F_b, applied on Ω and surface traction forces P on Γ_t; D is the material matrix while ϵ is the total strain in the elastic region. It should be noted that u and v are spatial variables as opposed to velocity fields which is common in structural optimization. By using notations from functional analysis and energy bilinear form for internal work and load linear form for external work,

$$a(u, v) = l(v), \quad \forall v \in V \tag{4.2}$$

where

$$a(u, v) = \int_\Omega \epsilon^T(v)\big(D\epsilon(u)\big)d\Omega \tag{4.3}$$

and

$$l(v) = \int_\Omega F_b^T v \, d\Omega + \int_{\Gamma_t} P^T v \, d\Gamma \tag{4.4}$$

Topology optimization based on obtaining the stiffest structural layout means the minimization of compliance or strain energy. It aims at ensuring the structural layout gives the least response possible to external loads and surface traction forces. Therefore, the structural problem by minimizing compliance $l(\mathbf{u})$ can be formulated thus:

$$
\begin{aligned}
&\text{Minimize} && l(\mathbf{u}) \\
&\text{subject to} && a(\boldsymbol{u}, \boldsymbol{v}) = l(\boldsymbol{v}), \quad \forall \boldsymbol{v} \in \mathbf{V} \\
&\text{and} && design\ constraints
\end{aligned} \tag{4.5}
$$

4.5 is subjected to the comparison of internal work, $a(\boldsymbol{u}, \boldsymbol{v})$ and external work, $l(\boldsymbol{v})$ on the system. This can be translated to the finite element equation

$$K(x)U(x) = F \tag{4.6}$$

where K and U are the stiffness matrix and global displacement vector; respectively, due to the external load vector F. With compliance $C \equiv l(\mathbf{u}) = F^T U$ and volume constraint, the optimization problem in 4.5 transforms to:

$$\min\ C = F^T U = U^T K U = \sum_{e=1}^{n} E_e(x_e) u^T k_0 u$$

$$\text{subject to:} K(x)U(x) = F$$

$$\frac{\sum_{e=1}^{n} V(x_e)}{f V_0} \leq 1 \tag{4.7}$$

$$\text{where } 0 < x_{min} \leq x_e \leq 1 \text{ and } 0 \leq E_e \leq E_0$$

4.7 applies the classical SIMP interpolation function because a minimal limit greater than 0 is set on the density design variable to avoid singularities in the stiffness matrix. In the modified SIMP function [54], this limit is placed on the material property (Young's Modulus) and the problem statement in 4.7 becomes:

$$\min C = F^T U = U^T K U = \sum_{e=1}^{n} E_e(x_e) u^T k_0 u$$

$$\text{subject to: } K(x)U(x) = F$$

$$\frac{\sum_{e=1}^{n} V(x_e)}{fV_0} \leq 1 \tag{4.8}$$

$$0 \leq x_e \leq 1$$

$$0 < E_{min} \leq E_e \leq E_0$$

In this case, 0 density design values are permitted without risking singularities in the stiffness matrix. The Young's modulus function becomes

$$E_e(x_e) = E_{min} + x_e^p (E_0 - E_{min}) \tag{4.9}$$

For structures under pressure loads, the problem formulation follows the same procedure as discussed but extended to uniformly distributed load P, on a line, in a 2D domain, or on a surface in a 3D domain. As illustrated in Figure 4.1(b), the design-independent pressure's magnitude, direction, and location on the structure remain the same throughout the optimization process. However, for an unconstrained or design-dependent pressure load in Figure 4.1(c), there will be the movement of pressure nodes, depending on the evolving topology at every iteration which might also involve changes in pressure magnitudes. The challenge, therefore, is two folds: tracking the design's evolving topological boundary and applying the pressure load appropriately on every iteration of the optimization. Although there have been several studies done to resolve these challenges [67], [159] [72], [160], this study proposes a simplistic model that is easy to apply and computationally efficient.

4.3.   The BILE model

Essentially, when a solid design is acted upon by a fluid medium, every surface of the solid in contact with the fluid will be acted upon by fluid pressure and if the design's geometry is updated, all newly formed surfaces in contact with the fluid will take up the same pressure as illustrated in Figure 4.2(a) and Figure 4.2(b). Initially, in a density-based finite element topology optimization method, the pressure-loading surface is strictly defined by the design domain, but as the density of the finite elements is updated, some boundary elements end up with either intermediate or zero density values. This destroys the integrity of the original surface and a new surface geometry has to be determined. Therefore, the

foremost challenge is to establish a threshold function that selects boundary nodes within a discretized model from elements with intermediate density values.

(a)　　　　　　　　　　　　　　　　　　(b)
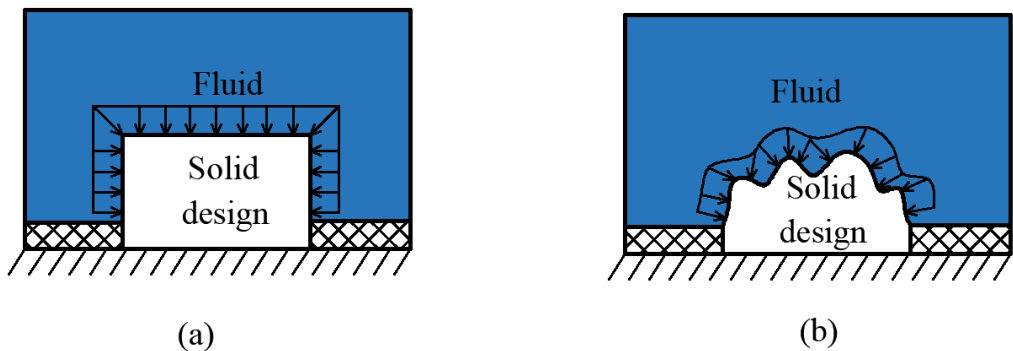
Figure 4.2: Fluid pressure changes to topological surface variations

From these carefully selected boundary nodes, loading nodes are derived and act as points for equivalent forces [159] which will evolve as the optimization progresses. Although [159] utilized a pseudo-equal potential curve to identify loading surfaces, in the BILE model, a simple boundary identification is done by selecting nodes that have neighboring elements with a mean density value below a predefined threshold. Loading nodes are then drawn from the boundary nodes within an orthogonal view from original pressure surfaces. Finally, the direction of pressure loads which should be normal to the loading surface on every node is achieved by computing the gradient of two nearest but opposite nodes for every node of interest. The simple BILE model is elaborately discussed in subsequent sub-sections.

4.3.1. Identification of topological boundary

The first step for this model is to define the boundary nodes of the design on every iteration. In Figure 4.3, we observe that at the beginning of optimization, a uniform density value is applied to all elements and the boundary of this design is defined by all the nodes (in red) on the four sides of the domain. As the optimization progresses to an nth iteration, a new topology is formed and its boundary is defined by new nodes based on a threshold density value. The mean density value, $\bar{x}_{n,i}$ of all neighboring elements $x_{n,i}$ about a node n, shown in Figure 4.4, is used to compare with the threshold density value f_{th}.
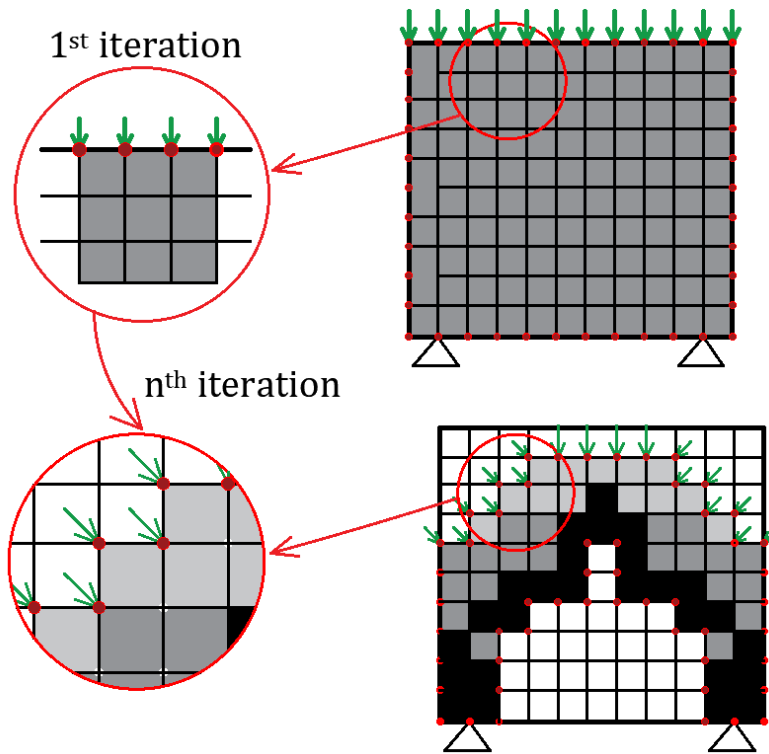
Figure 4.3: Topological boundary and load evolution for design-dependent pressure loads
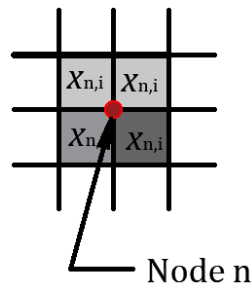
Figure 4.4: Elements $x_{n,i}$ surrounding a node n.

The threshold density value typically increases and is different on every iteration because as the optimization matures the topological boundaries become more defined and boundary elements adopt larger design density values. In Figure 4.5, the mean density of boundary elements throughout the optimization is shown. In the first 20 iterations for all three plots, the mean density oscillates around 0.2 but steadily increases thereafter. To apply a threshold to the density of boundary elements, the dotted plot is modeled by an appropriate function. An exponential function in 4.10, as opposed to a linear one, is utilized to step up this value after every iteration because the rate at which boundary elements become more defined rapidly increases at later stages in optimization:

$$f_{th} = f\exp^{(\frac{it}{\mu}-1)} \qquad (4.10)$$
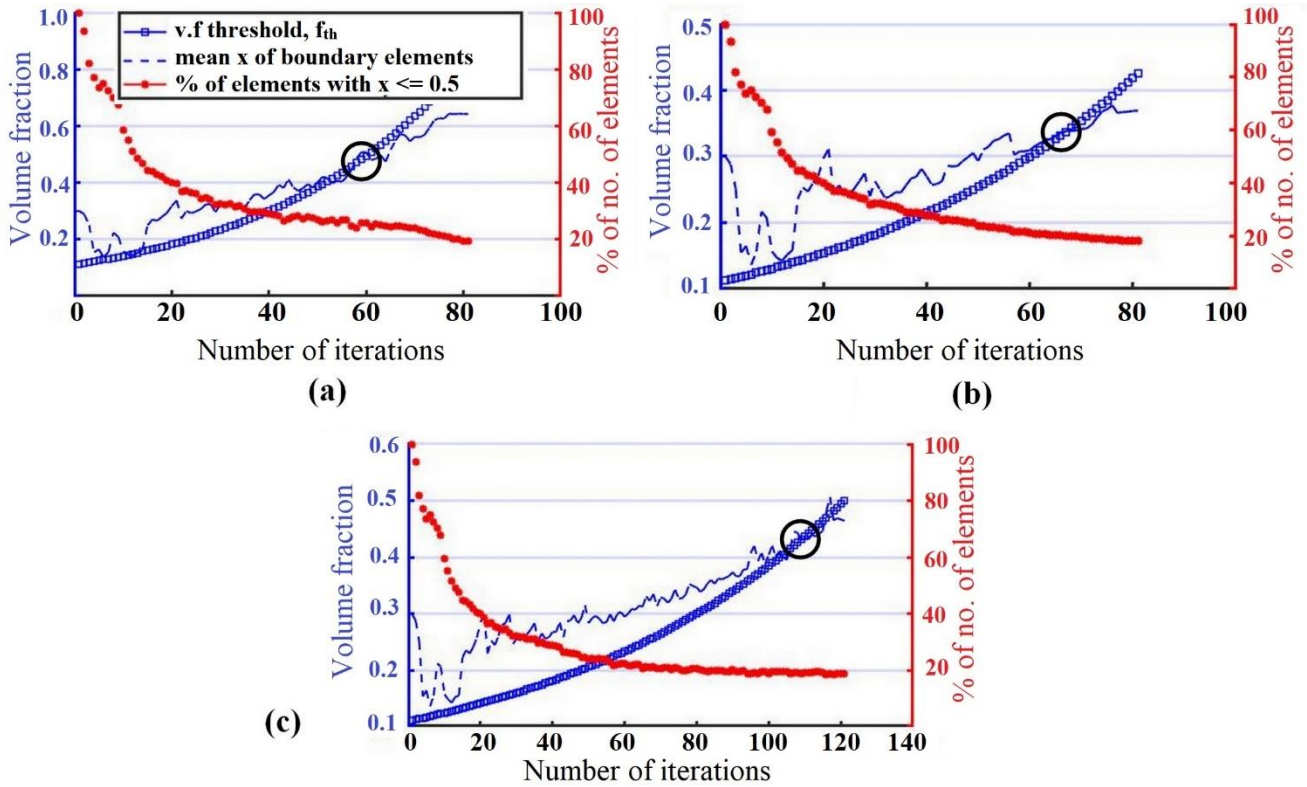
Figure 4.5: Volume fraction threshold, the mean density of boundary elements and percentage number of low and intermediate-density elements (0.5 and below) at (a) μ = 40, (b) μ=60 and (c) μ=80.

In 4.10, f_{th} is the volume fraction threshold at every iteration, it is the iteration number, μ is a factor that controls the threshold's rate of increase, while f is the volume fraction constraint in the problem definition. After several numerical investigations, μ can be given a value of 50 – 150 for most problems but assigned a value greater than 150 for optimizations that are anticipated to be much slower. In any problem, f_{th} is capped at 0.8. Figure 4.5 shows for a numerical solution how the exponential function defines a unique value of volume fraction threshold which is usually less than the average density value of boundary elements. Towards the end of optimization, both values converge (indicated by a circle) because the boundary elements are more defined and have density values approaching 1 (solid). For $\mu = 40$ in Figure 4.5(a), f_{th} quickly converges to the mean density of boundary elements at around the 50th iteration, but as μ is increased to 60 in Figure 4.5(b) and 80 in Figure 4.5(c), f_{th} is kept lower than the mean density of boundary elements for a longer period (65th and 110th iterations respectively). Therefore, higher values of μ should be used for potentially slower optimization problems. The figure also shows

that there is a significant drop in the percentage of elements with a density value of 0.5 and less during the early stages of optimization (0 to 20th iteration) which steadily drops as the optimization matures.

During the early stages of optimization, the number of nodes with a mean density of surrounding elements less than the threshold is expectedly high from discussions in the previous paragraph, therefore to reduce this number, surrounding adjacent nodes as shown in Figure 4.6 are investigated and used as a basis for choosing a boundary node.
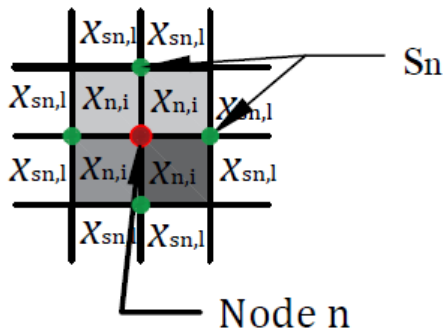
Figure 4.6: Surrounding adjacent nodes S_n to node n.

Every surrounding node S_n to node n also has surrounding density elements $x_{sn,l}$. $x_{n,i}$ is a vector of density elements surrounding node n for i ranging from 1 to 4 for 2D quadrilateral elements and 1 to 12 for 3D hexahedral elements while $x_{sn,l}$ is the corresponding vector of density elements surrounding node Sn for l from 1 to 4. For every node n, there are four Sn nodes in the 2D domain and six in the 3D domain. Boundary nodes in a 2D domain can be chosen by the selection criteria:

$$bn = \begin{cases} \text{Node } n & \langle \forall (\bar{x}_{sn,l} < f_{th}) \in [1,2] \rangle \, \| \, \langle \{ \forall (x_{n,i} > 0) = 2 \} \wedge (\bar{x}_{n,i} > f_{th}) \rangle \\ 0 & \text{any other case} \end{cases} \quad (4.11)$$

In 4.11, bn is a vector of nodes that define the boundary at every iteration. As previously mentioned, the initial iterations in optimization are characterized by high numbers of intermediate or grey elements, therefore even with the seemingly narrow band created by the selection criteria in 4.11, bn will still consist of many nodes that do not smoothly define the boundary. To obtain a set of nodes that closely define the boundary on every iteration, an outer node selection is made from the collection of boundary nodes as illustrated in Figure 4.7.
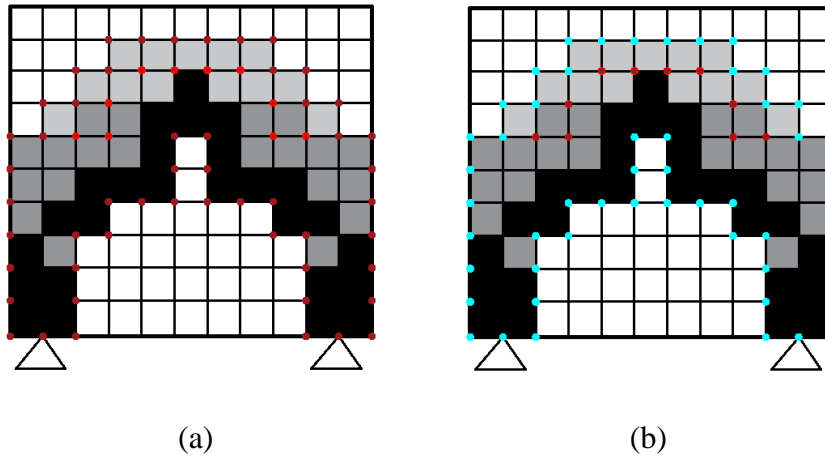
Figure 4.7: The nth iteration of an optimization showing (a) all the boundary nodes, bn in red by the selection criteria in equation 3.2 and (b) final boundary nodes, in cyan, emanating from a selection of outer nodes from (a)

4.3.2. Pressure load application and evolution

Loading nodes are selected from the generated boundary nodes to form the loading surface. These loading nodes are the basis on which equivalent forces are applied to the design. In this study, simple assumptions are employed to identify loading nodes. A loading node, Ln, is equal to a boundary node if:

    i.   The node is a translational distance away from any node on the initial load surface of the design problem (in the direction of any mesh grid,).

    ii.   There is no other boundary node between the node being investigated and the initial load surface.

The selection of loading nodes is illustrated in Figure 4.8
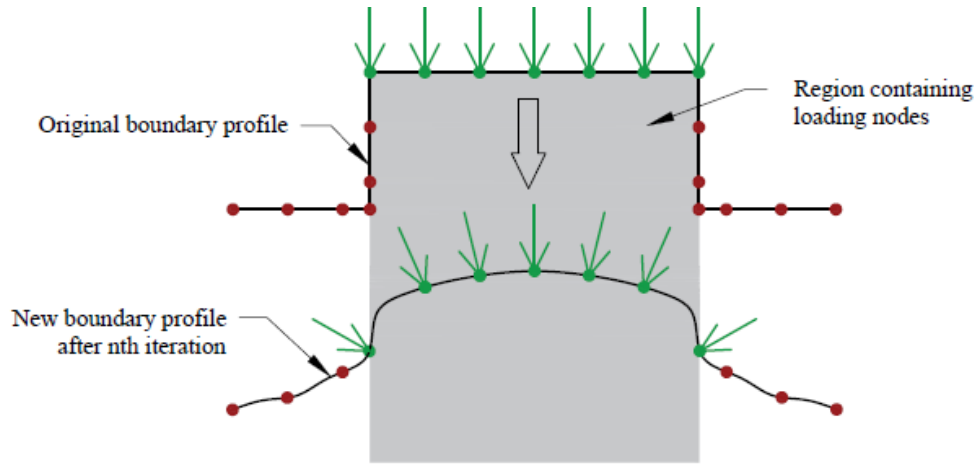
Figure 4.8: Loading node selection from boundary nodes (boundary nodes in red, loading nodes in green).

When the loading nodes are known, the angle at which each equivalent force acts on its respective node has to be determined. For a node under investigation, this angle is calculated counter-clockwise from the normal of a line joining two closest loading nodes to the positive vertical direction as shown in Figure 4.9(a). This angle is given as:

$$\Delta\theta_j = \left| \tan^{-1}\left(\frac{\Delta v_j}{\Delta u_j}\right) \right|$$

$$\theta_j = \begin{cases} \Delta\theta_j & +\Delta u_j, +\Delta v_j \\ \pi - \Delta\theta_j & +\Delta u_j, -\Delta v_j \\ \pi + \Delta\theta_j & -\Delta u_j, -\Delta v_j \\ 2\pi - \Delta\theta_j & -\Delta u_j, +\Delta v_j \end{cases}, \quad j = 1,2,3 \dots n \qquad (4.12)$$

In 4.12, j is the number of a loading node in $\overrightarrow{Ln}$ of length N. From these calculated angles, the equivalent forces can be expressed as:

$$F_j = \frac{PA}{N}\{\cos(\theta_j)\, u + \sin(\theta_j)\, v\} \qquad (4.13)$$

P is the pressure magnitude, A is the area of the surface under pressure tantamount to the length of a line or curve segment for 2D problems, N is the length of loading node vector Ln which will be presented in subsequent paragraphs, while u and v are Cartesian spatial coordinates for horizontal and vertical directions respectively. In the BILE model, since equivalent forces that represent pressure loads are located on the outer nodes of boundary elements, the norm of each nodal force is approximated to being

equal across all nodes and in every iteration. To further elaborate on the aforementioned, if we assume the finite elements in Figure 4.3 are squares of length l, and n is the number of nodes on the loading surface with a pressure P (force/length in the 2D case), consequently,

- in the 1$^{\text{st}}$ iteration, the norm of each equivalent force is given as $\frac{P \times 11l}{n} = \frac{P \times 11l}{12} = 0.92Pl$

- in the n$^{\text{th}}$ iteration, the norm of each equivalent force is given as $\frac{P \times 17l}{n} = \frac{P \times 17l}{18} = 0.94Pl$

As observed, there will exist very little change in the norm/magnitude of every equivalent force from one iteration to the next. The finer the mesh, the less this change. The only dissimilarity in the equivalent nodal forces is their horizontal and vertical force components which depend on the angle the forces are subtended at. However, this angle does not depend on the density of the elements rather on the location/orientation of the two closest loading nodes to the node under investigation.

This method of approximating the equivalent force directions and angles is illustrated in Figure 4.9.
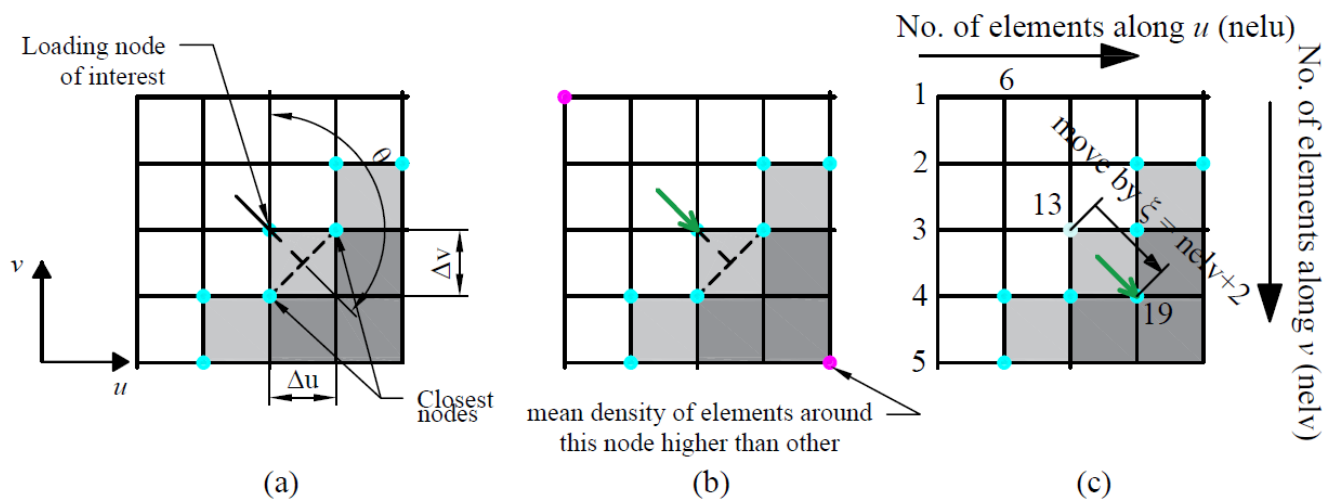
Figure 4.9: (a) Generating equivalent force angles for a loading node (b) determining the force direction at this node (c) load movement by ξ

Once the force angle is established, the direction and movement of this load from the node to the next is determined. To obtain the force direction, the mean densities of surrounding elements two nodes away from the node of interest on opposite sides and along the axis of the force (shown in magenta in Figure 4.9(b)), are investigated and compared with each other. Whichever opposite node has a mean density of surrounding elements higher than the other dictates the direction of the force at the loading node of

56

interest, this is shown in Figure 4.9(b). The movement of loading nodes are determined by an updating scheme in 4.14:

$$Ln_{j,k+1} = \begin{cases} Ln_{j,k} + \xi & \bar{x}_{j,i}^{k+1} < f_{move\_thresh} \\ Ln_{j,k} & \bar{x}_{j,i}^{k+1} \geq f_{move\_thresh} \end{cases} \qquad (4.14)$$

$\overrightarrow{Ln}$ is a vector of loading nodes, k is the optimization iteration number, ξ is a load evolution parameter that corresponds to the movement of a loading node from its present location to the closest node in the force direction at that node. For an iso-parametric four-node square element, this parameter is typically the movement to any of the remaining three nodes in the finite element related to the node under investigation. In this model, a key assumption/approximation is that in every load evolution iteration, a loading node is only allowed to move to another node in the same finite element (e.g. for a four-node isoparametric square element, a loading node will only move to any of the other three nodes which are either a horizontal, vertical or diagonal distance away). In Figure 4.9(c), a diagonal movement is utilized due to the orientation of the equivalent force and density of surrounding elements. f_{move_thresh} is a density threshold that controls load movement and can be given a value between 0.8 and 1 from numerical investigations.

In this model, the load evolution is carried out an integer-multiple-number of times boundary identification is done. This model is developed in Matlab with its foundation on the 88-line code recommended by Andreassen et al. [54]. A workflow of the BILE model for topology optimization of structures under design-dependent pressure loads is shown in Figure 4.10.
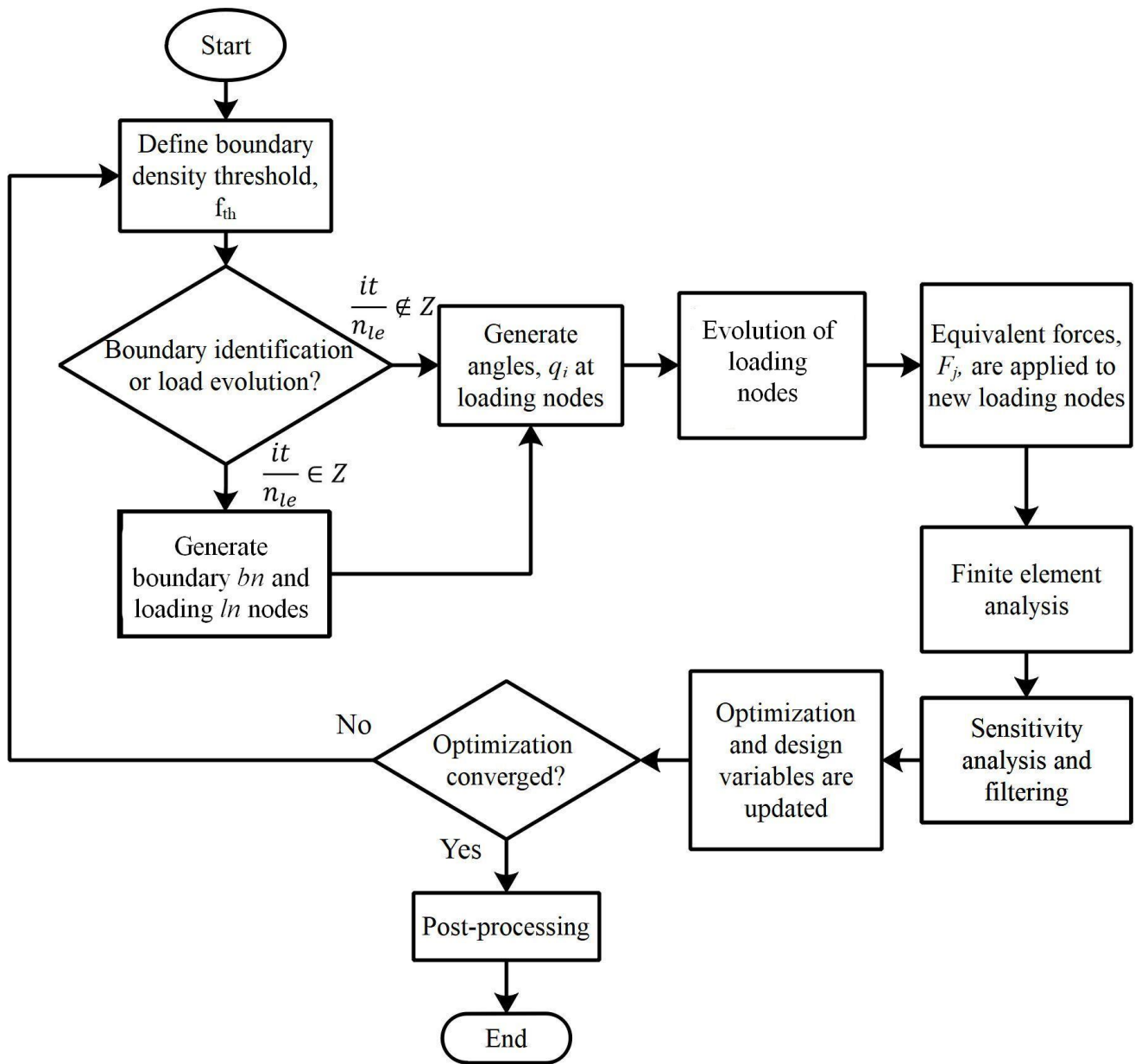
Figure 4.10: Workflow of the BILE model for topology optimization of structures under design-dependent pressure loads (Z is a set of positive integers).

In Figure 4.10, n_{le} is the number of iterations between two boundary identification steps, while Z is the integer number space. In other words, if boundary identification is to be done once in three iterations, n_{le} should be 3. In the first iteration, $it = 0$, boundary identification must be carried out, and in subsequent iterations the ratio $\frac{it}{n_{le}}$ determines if boundary identification is done or not. After several numerical investigations using the BILE model, it is recommended that n_{le} be given a higher value (4 to 7) in the infant stages of optimization and decreased (to 2 or 3), when the optimization stabilizes. This study

solves the non-linear topology optimization problem using the Optimality Criteria Method for all examples presented and Method of Moving Asymptotes (MMA) [55] in the last example.

4.4. Sensitivity analysis and Filtering

Sensitivity analysis is a very important step in gradient-based topology optimization methods. It is simply obtaining the first derivatives of the objective and constraint functions with-respect-to the design variable. The adjoint method elaborately discussed in [161] is used for sensitivity analysis. This method has previously been applied to control systems and is now adapted to multidisciplinary optimization problems [162]. The objective function, compliance is redefined as an augmented function of the density design variable, x with an introduction of a Lagrange multiplier:

$$C^* = C(U, x) - \lambda^T(KU - F) \tag{4.15}$$

From the definition of the compliance function in the problem statement in Equation 2.8, Equation 4.1 can become

$$C^* = U^T KU - \lambda^T(KU - F) \tag{4.16}$$

The first derivative of 4.16 becomes

$$\frac{\partial C^*}{\partial x} = \frac{\partial U^T}{\partial x}KU + U^T K\frac{\partial U}{\partial x} + U^T\frac{\partial K}{\partial x}U - \lambda^T(\frac{\partial K}{\partial x}U + K\frac{\partial U}{\partial x} - \frac{\partial F}{\partial x}) \tag{4.17}$$

The first two terms on the RHS of 4.17 can be arranged to have

$$\frac{\partial C^*}{\partial x} = 2U^T K\frac{\partial U}{\partial x} + U^T\frac{\partial K}{\partial x}U - \lambda^T(\frac{\partial K}{\partial x}U + K\frac{\partial U}{\partial x} - \frac{\partial F}{\partial x}) \tag{4.18}$$

The Lagrange multiplier, λ is an arbitrary variable that can adopt any value. For a rigid body in equilibrium, $KU - F = 0$, therefore a value of $2U$ is assigned to this variable to eliminate the derivative of U. 4.18 then becomes

$$\frac{\partial C^*}{\partial x} = -U^T\frac{\partial K}{\partial x}U + 2U^T\frac{\partial F}{\partial x} \tag{4.19}$$

The first term on the RHS of 4.19 is trivial therefore focus is frequently placed on the second term. The sensitivity of the "load" term is usually calculated by finite difference schemes [69], which can be tedious and involve several function calls that increase computational cost. In this model, which is an element-based search [67] for nodes that define loading surfaces, the pressure load converted to

equivalent forces acts directly on loading nodes with every equivalent force approximately maintaining the same magnitude on every iteration. As discussed in section 3b, between iterations, there will be insignificant changes in the magnitude of every equivalent force since the length of the load line and the number of loading nodes increase or decrease simultaneously. The finer the mesh, the much less this change. Therefore, the magnitude of every equivalent nodal force is kept constant throughout the optimization. However, the equivalent force is allowed to change direction depending on its corresponding loading angle which is a function of the layout of neighboring nodes that have been selected only from four nodal square mesh elements. Therefore, the force magnitude is not dependent on the density of boundary elements. Also, since the number of elements that host loading nodes is usually small compared to the total number of mesh elements, the partial derivative $\frac{\partial F}{\partial x}$ can be set to zero. Therefore, the sensitivity of compliance for every element becomes

$$\frac{\partial c_e}{\partial x_i} = -u_e^T \frac{\partial K}{\partial x_i} u_e = -p x_i^{p-1}(E_0 - E_{min})u_e^T k_0 u_e \qquad (4.20)$$

Assuming each element has a unit volume for a constant mesh size space- and time-wise,

$$\frac{\partial v_e}{\partial x_e} = 1 \qquad (4.21)$$

The formation of checker-boarding features is a usual occurrence due to binary values density variables are forced to take. To resolve this problem and obtain realistic solutions, filtering becomes important. Several filtering methods exist amongst, which sensitivity, density, and Heaviside function filtering are most popular. A sensitivity filter is utilized and is expressed as [54]:

$$\frac{\partial \hat{c}_e}{\partial x_e} = \frac{1}{max(\gamma, x_e) \sum_{i \in N_e} H_{ei}} \sum_{i \in N_e} H_{ei} x_i \frac{\partial c_e}{\partial x_i} \qquad (4.22)$$

where N_e is the set of neighboring elements i which have center-to-center distance $d(e, i)$ to element e less than set filter radius r_{min}. To avoid divisions by zero in the fraction in 4.22, γ is assigned a small value as 10^{-3}. H_{ei} is a weight factor expressed as:

$$H_{ei} = \max(0, r_{min} - d(e, i)) \qquad (4.23)$$

4.5.   Numerical Examples

In this section, some examples are presented to explain and show the validity of the BILE model. For all examples, the design domain is discretized by 5,000 to 13,000 four nodal square plane stress elements, with the number depending on the type of problem as some get increasingly difficult to converge with an increase in mesh elements. For all examples, the pressure magnitude is set at 1 and material properties are $E_0 = 1$, $E_{min} = 1 \times 10^{-9}$, $v = 0.3$. The filter radius is set to 2.5 times the finite element length. Optimality Criteria Method (OCM) was used as an optimizer for all problems. The Method of Moving Asymptotes (MMA) was used only in the first and last examples for computational comparisons with OCM. For all examples, convergence was set at a density error limit of 0.015 and the number of iterations capped at 300. An Intel Core i7 CPU processor with a speed of 3.6 GHz and RAM size of 16.0 Gigabyte was used. The choice of values for threshold volume fractions f_{th} and number of iterations between successive boundary identification steps, n_{le} are discussed in the first example.

4.5.1. Unidirectional externally loaded structures

The BILE model is used to study how a design-dependent unidirectional pressure load can influence the resulting topology of an optimized structure. The design domain shown in Figure 4.11 is a rectangle of length L and width $\frac{L}{2}$. The pressure load is located at the top edge with two fixed points $0.1L$ away from the two bottom vertices and 7200 (120 × 60) square mesh elements were used, this problem was solved by the optimality criteria method. This representative example has also been studied by several other authors [67], [65], [159], and the resulting topology is arch-like. Figure 4.12 shows the history of volume fraction threshold f_{th} which defines the topological boundary on every iteration. There is a steady increase in this value from around 0.1 to 0.35 because the topological boundary becomes more distinct as optimization progresses. In the same figure, the number of iterations for load evolution between successive boundary identifications n_{le} is shown and is kept at 7 for the first 63 iterations. It reduces to 4 thereafter while ending at a value of 3 in the 84th iteration. It should be noted that when n_{le} is a value of 7, there are 7 iterations, which strictly perform load evolution (meaning a change in location of the equivalent force) in between two successive boundary identification iterations. This number can be varied depending on how topologies mature for specific problems but overall, it is recommended that it should drop once optimization approaches convergence. Three major regimes of the optimization history at the 4th, 63rd, and 84th iterations have been highlighted by dotted lines and respective topological figures. Initially in optimization when a majority of the elements are "grey", f_{th} is low, compliance C is

high while overall volume fraction remains the same. As the optimization matures, f_{th} is allowed to increase exponentially, while C rapidly drops till it reaches a steady-state with some numerical instability just before the 60th iteration. This history for these variables is similar for all examples using the BILE model. Although the optimization was allowed to run above 100 iterations, it converges at the 81st iteration which took approximately 56 seconds using the OCM. The optimization was also carried out using the MMA and this resulted in a total time of 108 and 73 seconds for volume fractions 0.35 and 0.4 respectively. When a finer mesh is applied, it is recommended that the maximum number of iterations and n_{le} placed on the optimization be increased likewise.
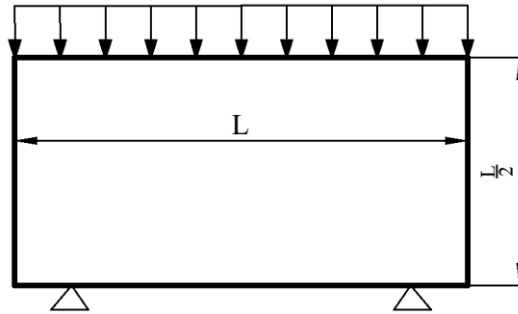
Figure 4.11: Domain and boundary conditions for a structure under uni-directional pressure load.
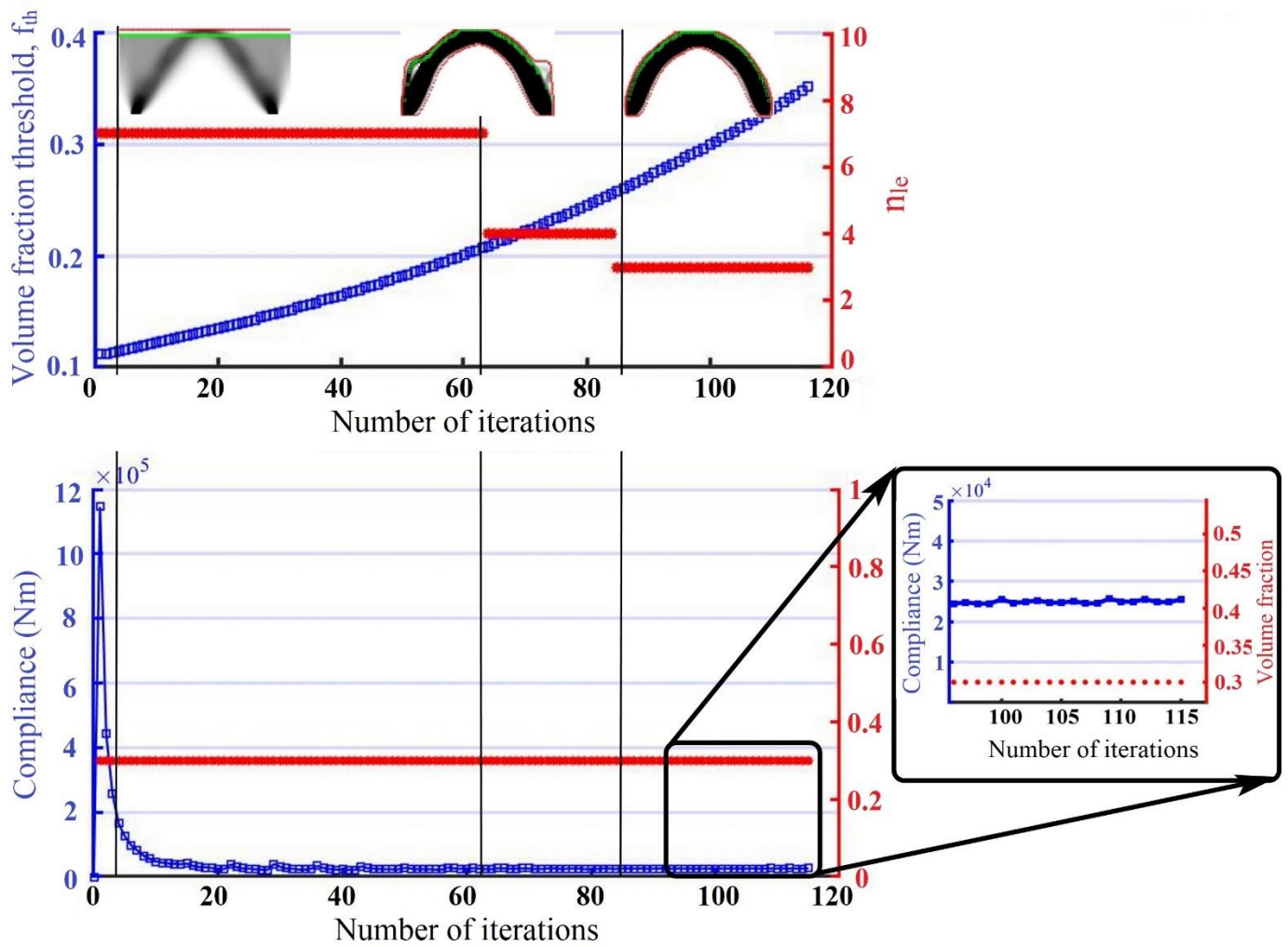
Figure 4.12: Histories of f_{th}, n_{le}, C and f.
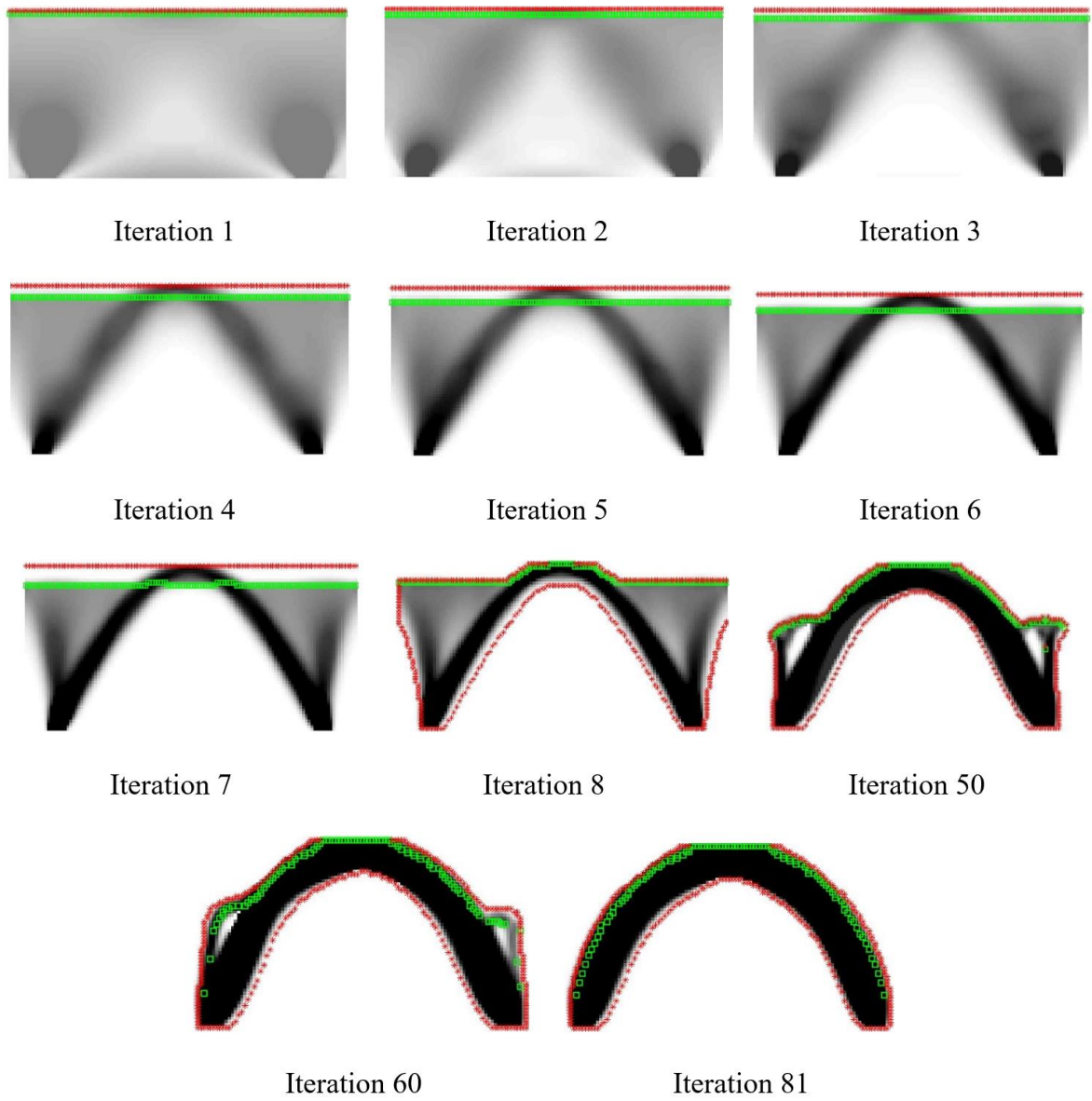
Figure 4.13: Several iterations of the optimization in example 1 showing boundary nodes and loading nodes in red and green respectively.
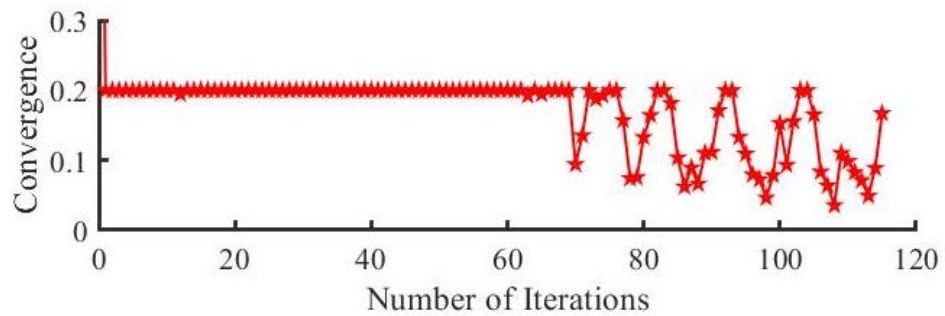
Figure 4.14: Convergence history for the optimized unidirectionally loaded structure

In Figure 4.13, we observe that the load nodes evolve by ξ from the 1st to 8th iteration for every iteration movement. At the 8th iteration, though, a fresh boundary identification was done from where new boundary nodes are determined and loading nodes extracted from them. Therefore boundary identification is carried out every iteration after n_{le} iterations. The convergence history is shown in Figure 4.14.

4.5.2. Multi-directional externally loaded structures

For a multi-directional external load problem, the same design domain in example 1 is used but additional pressure loads are placed on the left and right-hand sides shown in Figure 4.15, all other design and optimization parameters are left the same. We observe a similar arch-like structure as in example1 but in a more curved form. Optimization convergence was reached in approximately 44 seconds for 60 iterations. This problem has also been solved by several researchers [72], [65] and the resulting topologies are similar.

(a)   (b)

(c)   (d)
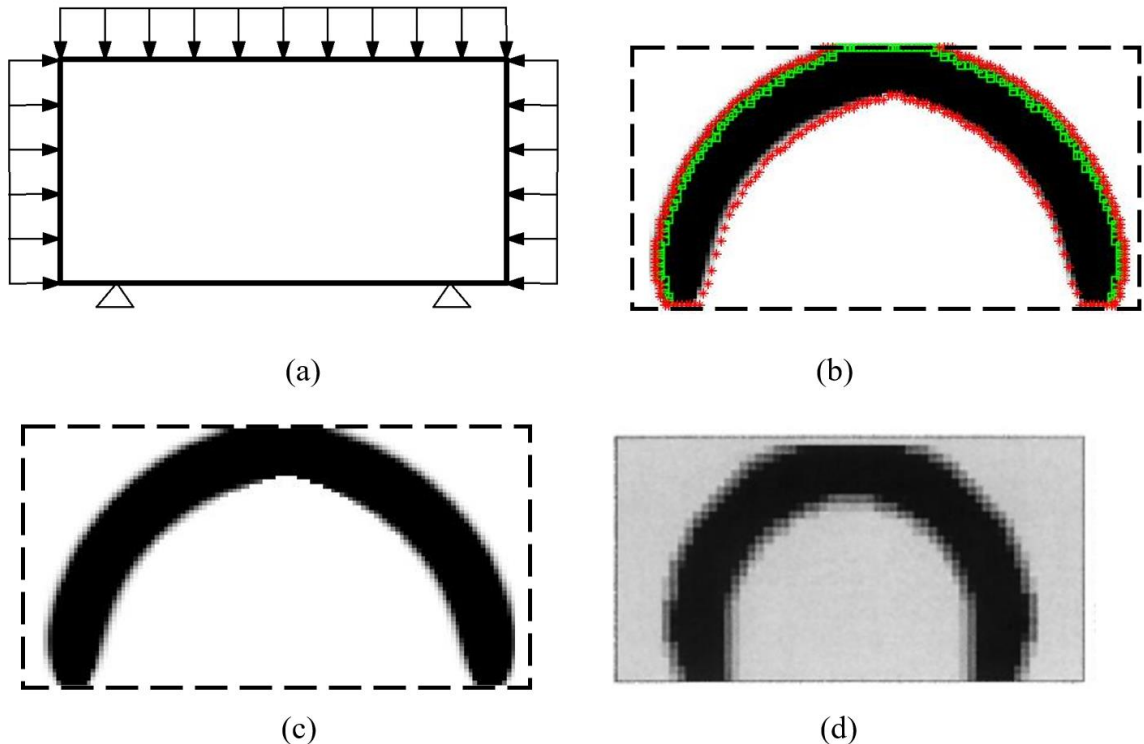
Figure 4.15: Structure under multi-directional pressure load (a) Design domain and boundary conditions (b) Optimized structure showing the boundary and loading nodes (c) Optimized structure (d) optimized result by Chen and Kikuchi [67].

Apart from the more curved form the resulting topology takes, there are more loading nodes identified at the bottom external sides of the topology which is influenced by the extra side pressures absent in the example in 4.5.1.

4.5.3. Solid and hollow structures submerged in fluid

Although several factors should be considered when designing submerged pressure vessels, we will use the BILE model to optimize strength/stiffness. One of the many applications of submerged pressure vessels is underwater structures, which will have a water pressure head acting all on every external surface. In this example, two different structural forms shown in Figure 4.16 are considered. They are completely solid structures that have similar design domains but are defined by different boundary conditions.
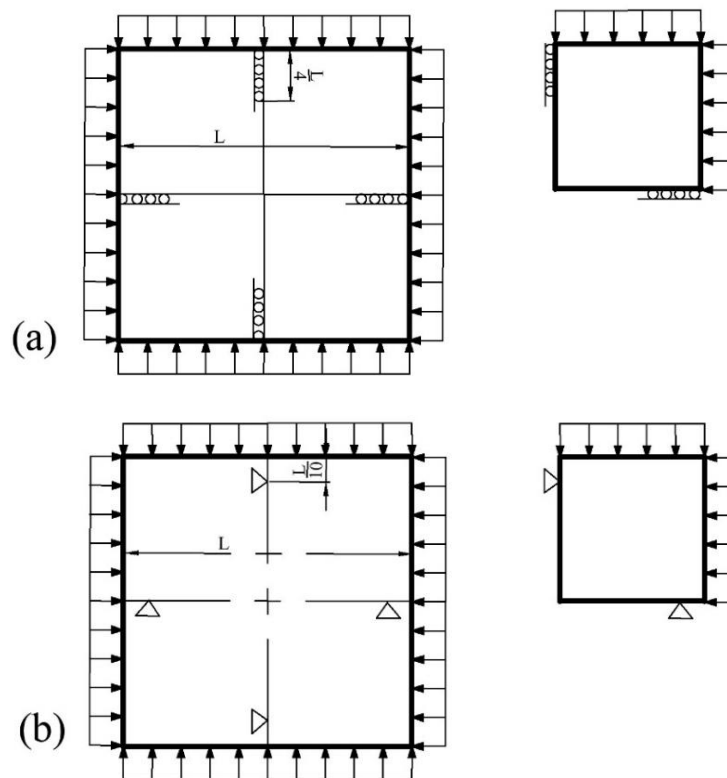
Figure 4.16: Design domain and boundary conditions for solid submerged structures with a quarter design on the right for implementation. (a) roller supports (b) completely fixed supports.

For Figure 4.16(a) and Figure 4.16(b), the design domain is a square with constant pressure acting all over the external surface; Figure 4.16(a) is supported by rollers to restrict freedom in one axis at the support locations while Figure 4.16(b) has its support locations completely fixed. The optimization is

constrained to a volume fraction of 10% and 25% in the first and second designs respectively. For the first design (Figure 4.16(a)), the same value for n_{le} was used as in previous examples (4.5.1 and 4.5.2) but reduced earlier in optimization. A smaller initial n_{le} was utilized for the second design (Figure 4.16(b)) because of the position of the supports as the loads will have less travel distance compared to Figure 4.16(a). It is important that n_{le} is carefully selected and reduced during optimization depending on the problem being solved. The evolution of the first design is shown in Figure 4.17 while the histories of n_{le}, f_{th} and full optimized solid is shown in Figure 4.18. From the iterations shown in Figure 4.17, a gradual and steady progression to the final topology is observed and it is the reason why a higher number of load evolution iterations was reserved for the early stages in the optimization only i.e n_{le} is 7 only for the first 40 iterations shown in Figure 4.18. Also, the number of mesh elements can influence n_{le} where a smaller mesh size should mean the use of a higher initial n_{le}. The total time for optimization was approximately 60 seconds for 70 iterations.

(a) Iteration 1   (b) Iteration 8   (c) Iteration 36

(d) Iteration 50   (e) Iteration 70
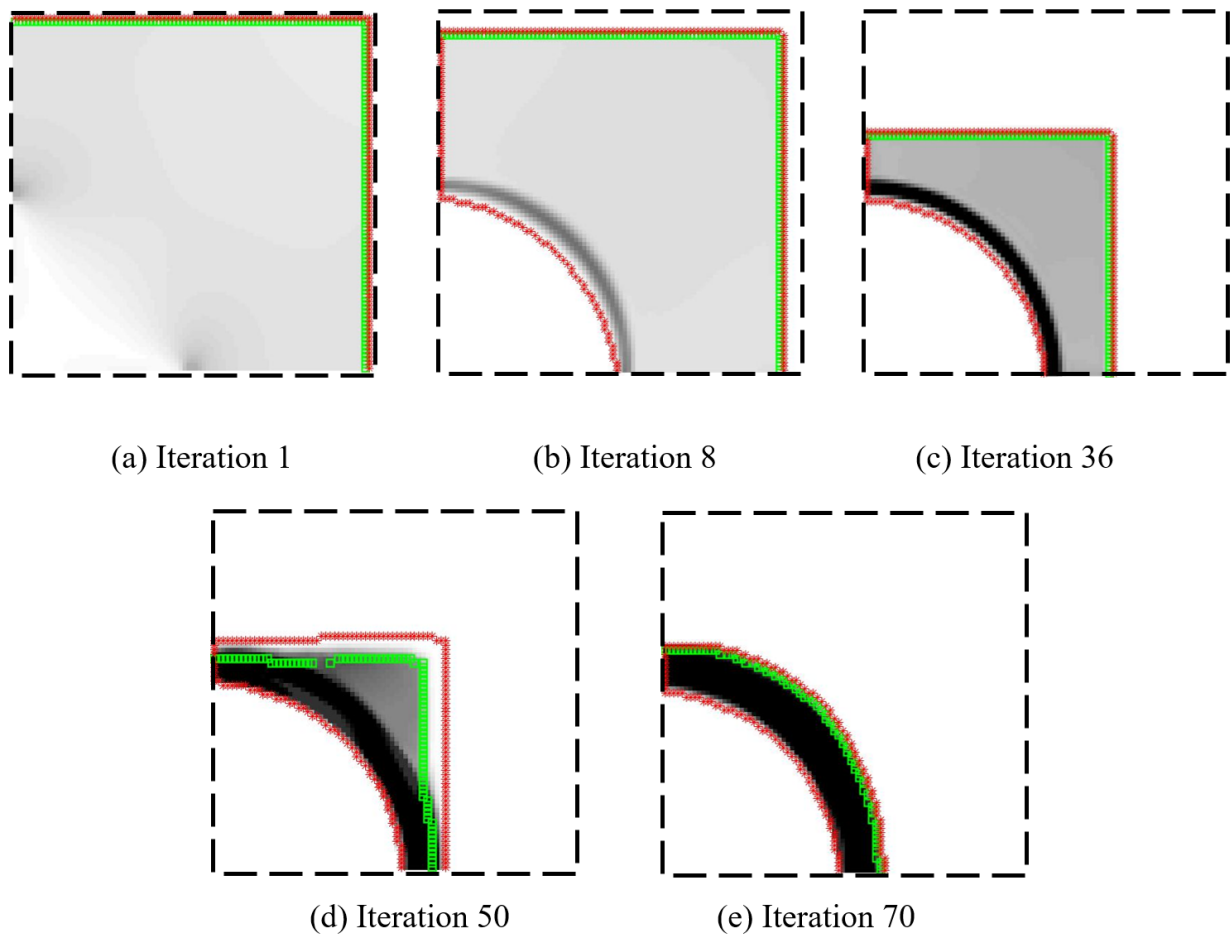
Figure 4.17: Optimization history for the design problem in Figure 4.16(a) of a submerged structure.

(a)

(b)
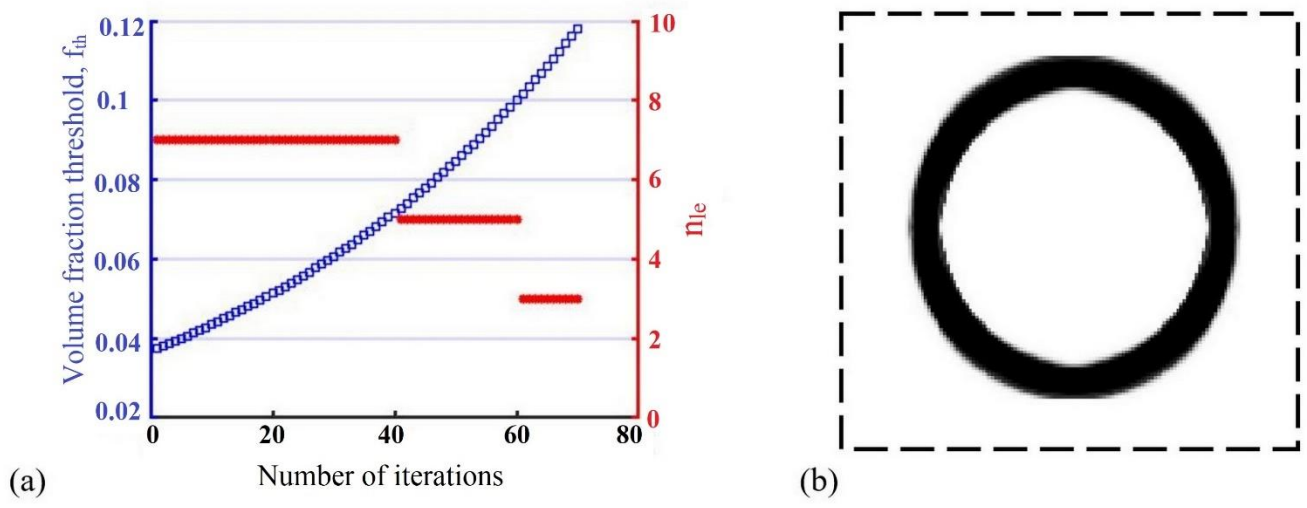
Figure 4.18: (a) Optimization history for n_{le} and f_{th} , (b) Final topology for Figure 16a.

The optimization of the second design presented in Figure 4.16(b) is shown in Figure 4.19. The resulting topology shows the heavy influence of change in boundary conditions on a design. In this example also, it is observed that two values of n_{le} are maintained throughout the optimization: 3 is assigned in the first 45 iterations and 2 is assigned after that. Unlike the first design, the pressure load has less travel distance throughout the optimization because the fixed supports are close to the domain edges. These design problems have also been studied by [159], [69], and [67], and they show closely matching topologies to the results obtained by the BILE model.

(a)

(b)
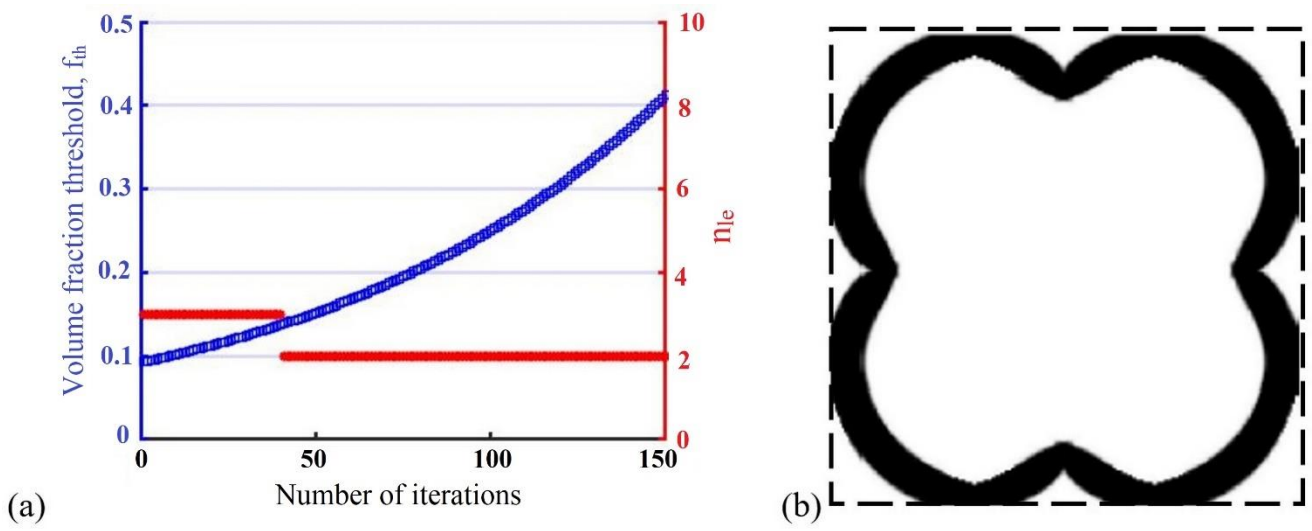
Figure 4.19: (a) Optimization history for n_le and f_th, (b) Final topology for Figure 4.16b

The final sets of designs for this example are hollow rectangular structures shown in Figure 4.19. the first design problem, Figure 4.20(a) is self-supported and the second design, Figure 4.20(c) has extra external supports fixed at some points on the edges of the inner surface.
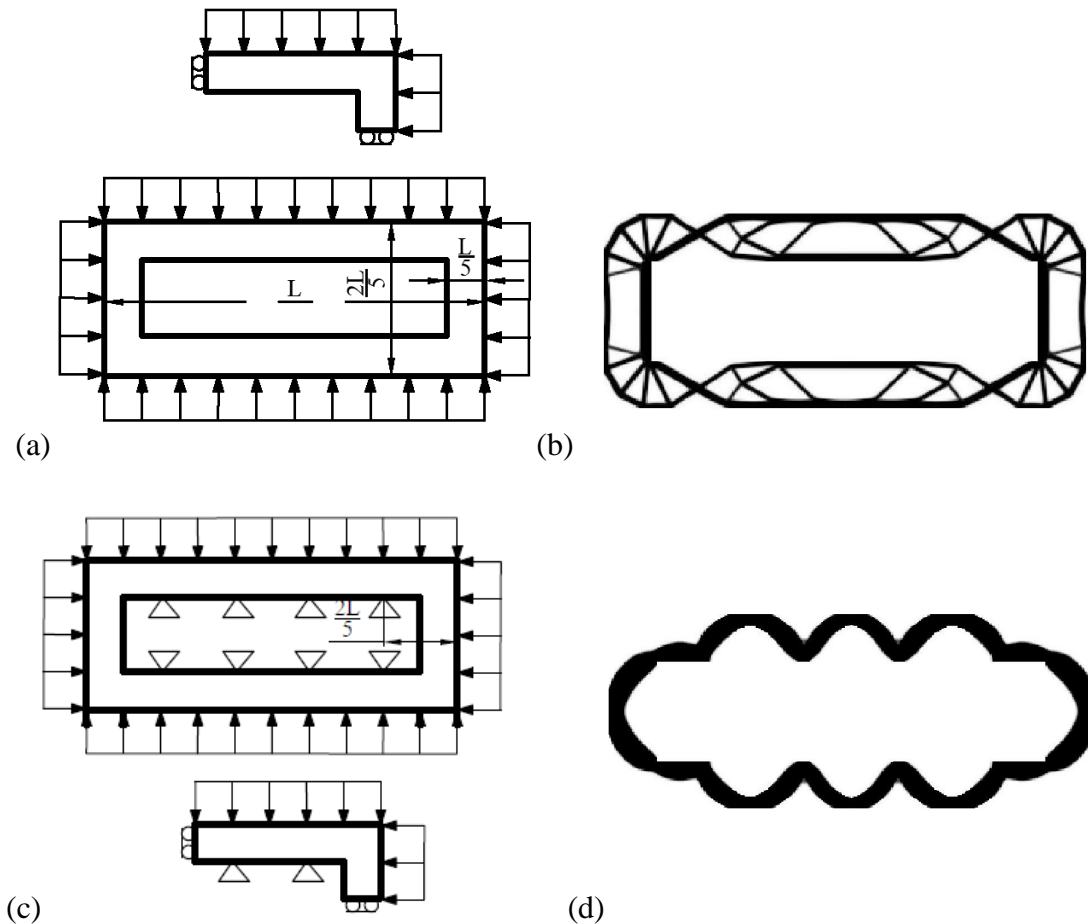
Figure 4.20: Topology optimization of submerged hollow structures (a) (c) Design problem definitions (b) (d) Optimized solutions

The result of optimization for the first structure (Figure 4.20(b)) shows a weak point close to either the left or right side and it is reasonable why this design will not be adopted in actual design implementation. The compliance of this optimized design is $57.8C$ Nm, where C is a value from actual material properties. To improve this design, extra supports can be introduced within the first design resulting in Figure 4.20(c), this has been previously recommended by Liang et.al. [160]. The optimized result in Figure 4.20(d) shows no distinct weak point and we can conclude it is an improved design from (a) because it has significantly lower compliance of C Nm, approximately 60 times less. This design probem has also been studied by [163] and [67].

4.5.4. Internally loaded structures

This penultimate example shows how the BILE model solves the topology optimization of internally loaded structures. The design problem consists of the same domain as the first two examples in this section but pressure load acts on the bottom edge shown in Figure 4.21.
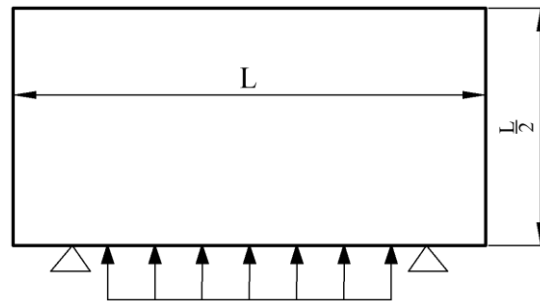
Figure 4.21: Design domain and boundary conditions

This example finds application in several underwater pressure structures such as the Liquid and Gas Storage tank in the upstream exploration and production stages in the oil and gas industry [67]. Since the progression of optimization towards convergence was anticipated to be steeper compared to the examples in the last previous section, n_{le} values used in the examples in 4.5.1 and 4.5.2 were adopted here. This problem slightly differs from previous numerical problems because the number of intermediate elements with volume fraction 0.5 and below drops more rapidly comparatively. In Figure 4.22 it is observed that these elements (density 0.5 and below) constitute only 30% of the total number of elements at the 20th iteration as opposed to 40% in the numerical example presented in Figure 4.5. Likewise, we observe the mean density of boundary elements to be higher than 0.4 before the 5th iteration compared to Figure 4.5 which does not exceed 0.3. This is likely a result of the fixed boundary conditions being placed adjacent and on the same loading surface as the pressure load. Consequently, the optimization might result in extra structures formed within the arch (similarly presented in [65]) when a 'move' threshold f_{move_thresh} as in previous examples is used. Therefore a higher move threshold (between 0.9 and 1) is recommended. The final topologies for volume fraction 0.1, 0.2 and 0.3 are shown in Figure 4.23.
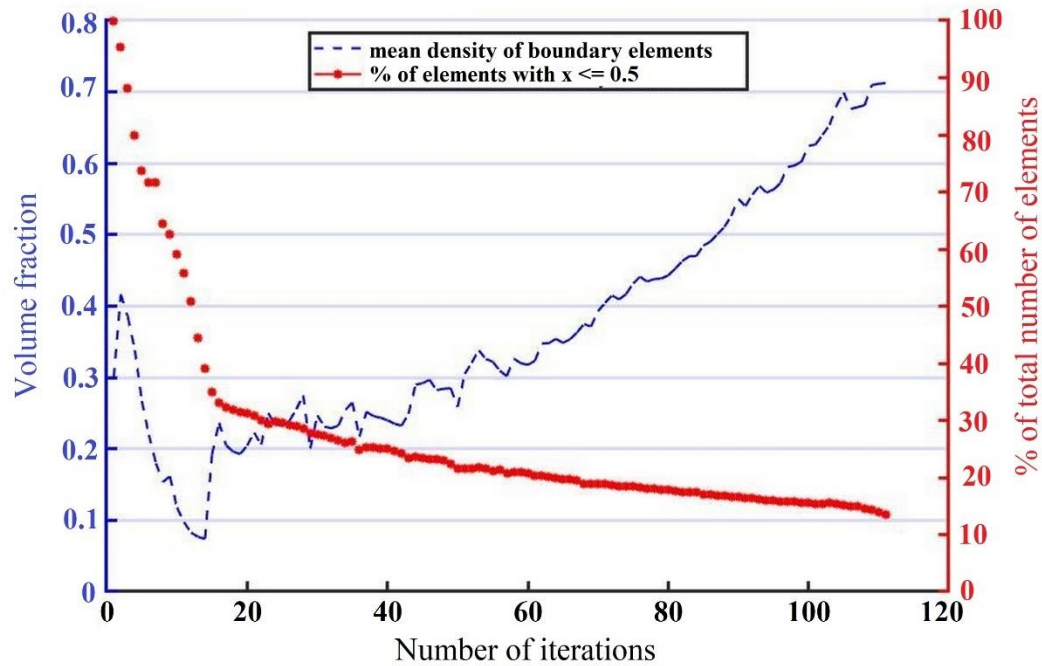
Figure 4.22: Mean density of boundary elements and percentage of elements with a volume fraction of 0.5 and below for optimization of an internally loaded structure.

| (b) | (b) | (c) |
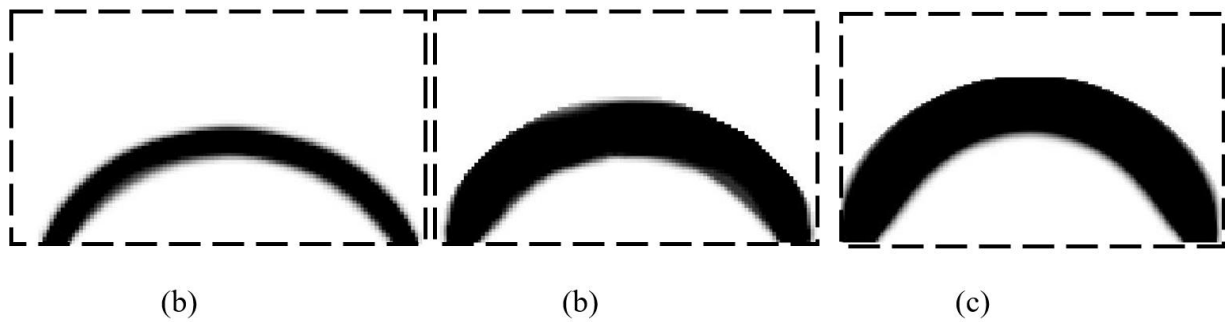
Figure 4.23: Topology optimized structures for volume fraction of (a) 0.1 (b) 0.2 and (c) 0.3

4.5.5. The Piston problem

The final example is the popular piston problem defined in Figure 4.24. The domain is fixed at the center of the bottom edge signifying the piston's contact with the connecting rod while it is supported in the horizontal direction on the left and right edges signifying the combustion chamber's cylindrical walls; the pressure load acts on the top edge. Results of the topology optimized structure using OCM and MMA closely match with slight differences in some "internal" features shown in Figure 4.25. As anticipated,

71

OCM gives slightly lower compliance of C Nm compared to MMA which gives $1.15C$ Nm. Generally, designs by several authors such as Lee and Martins [73], Li et.al. [67], Wang et. al [164], Bruggi and Cinquini [165], and Sigmund and Clausen [166] have similar strut-like features that stem from the center of the bottom edge.
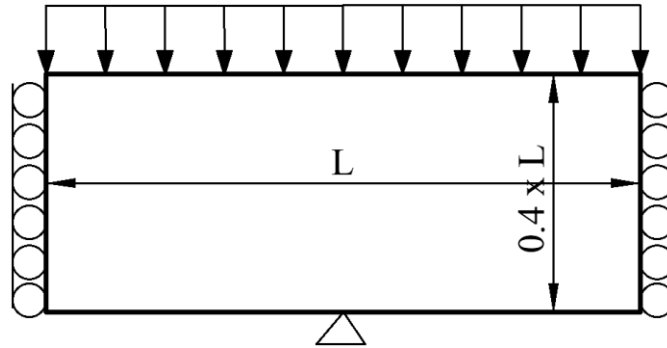
Figure 4.24: Design domain and boundary conditions of the piston problem.

| (a) | (b) |
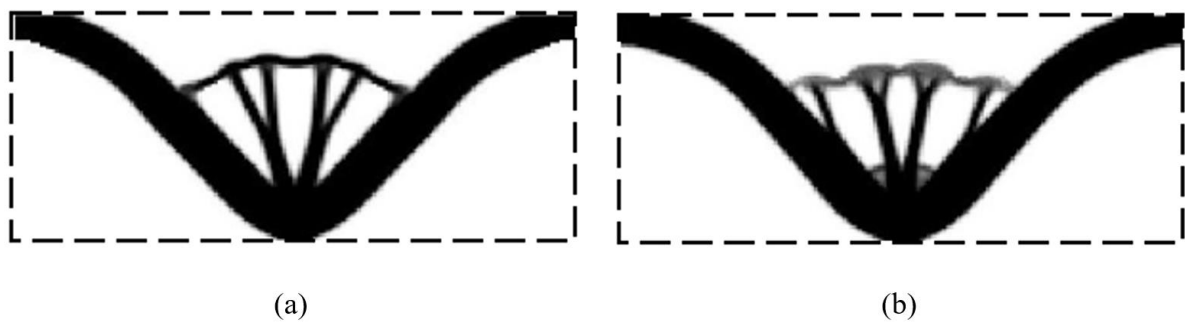
Figure 4.25: Optimized solutions of the piston problem for a volume fraction of 0.3 (a) OCM (b) MMA

4.6.   Summary

In this study, a new, simple but realistic BILE model was proposed to deal with topology optimization of design-dependent pressure loads. Using the modified SIMP model, OCM, and MMA as optimizers, the BILE model effectively tracks evolving topological boundaries while introducing a load evolution or movement and can be summarised as:

1) A unique value of a threshold volume fraction is defined on every iteration by an exponential function. Boundary nodes are then extracted from boundary elements based on this threshold.
2) Loading nodes are obtained from these boundary nodes with influence from the original loading pattern of the design.

3) Equivalent force angles are calculated for every loading node and the pressure load is substituted by equivalent forces, which have the same magnitude across all loading nodes and in every iteration.

Some advantages of this model are:

1) From point 3 above, there are insignificant differential changes of the equivalent forces with-respect-to the density design variable causing load sensitivity to be zero, thereby eliminating tedious computations.

2) Reduced computational cost is a consequence of 1; most results were obtained under 80 seconds and 100 iterations for problems discretized by 5,000 to 13,000 four-nodal square elements.

3) Boundary identification and load evolution schemes are very easy to implement.

This model is also easily adaptable to 3D cases, as the major extension will involve considering an additional loading angle (ϕ) such that the equivalent nodal force becomes a function of the nodal force magnitude $\left(\frac{PA}{n}\right), \theta$ and ϕ; this can also be written as $F_j = f(\frac{PA}{n}, \theta, \phi)$. A challenging aspect of this model is the selection of optimized values of volume fraction threshold and n_{le}. These variables can be smartly determined from experience and an understanding of the design problem, nonetheless, this work can be further developed by systematically selecting the aforementioned controlling parameters depending on the design problem. In general, this model is a promising tool for topology optimization of structures under design-dependent loads and further work will be done to enhance the workflow and develop 3D case studies.

Chapter 5: Weighted Multi-Objective Topology Optimization by Sensitivity Scaling

5.1. Introduction

In this chapter, the weighted strategy for multiobjective topology optimization for design-independent loads is first presented to explain the significance of Pareto optimal sets and weight selection in multiobjective optimization (MOO) problems. Next, the multiobjective topology optimization problem formulation and sensitivity analysis of a mix of design-independent load (point force load) and design-dependent loads (centrifugal and TSL from Chapter 3) are studied. Using the Optimality Criteria Method (OCM), a sensitivity scale factor is introduced in the consolidated sensitivity equation to always ensure the sensitivity of load contributions that cause more numerical instability in the optimization are comparable to those that result in better stability. A series of design solutions are obtained using different weight factors and the topological density images, histories of the scale factors, sensitivity, and objective functions are analyzed. Finally, a practical design case is optimized while comparing the results with the capabilities of HyperWorks, a commercial structural optimization software.

5.2. Weighted Multiobjective Topology Optimization for Design-Independent force loads

A general multiobjective optimization (MOO) problem is given as [167]:

$$\min_{x} f(x) = [f_1(x), f_2(x), f_3(x), \ldots \ldots \ldots, f_k(x)]^T \tag{5.1}$$

$$\text{subject to: } g_j(x) \leq 0; j = 1,2,3, \ldots \ldots \ldots m$$

in 5.1, $f(x)$ is a vector of objective functions, $f_k(x)$ is an objective function in $f(x)$ with k defining the number of functions. $g_j(x)$ is a series of constraint functions with j ranging from 1 to m; this also limits the feasible design domain. x is a vector of design variables with a finite number length in the real integer space.

For MOO problems, there can be several optimums, therefore, the Pareto optimal set is used to define a set of solutions. For a solution to be considered a point in the set, it is impossible to improve one objective by moving from that point without a decline in another objective. To achieve the Pareto optimal set in

MOO problems, the use of the weighted sum of objectives is very popular and well established for years [28], [167]–[173].

Multiobjective topology optimization is a common type of MOO and taking a simple cantilever problem with two load cases as shown in Figure 5.1, the Pareto optimal set is obtained by varying the weights of the objective contributions (compliance in this case) from 0 to 1 with the sum of all weights amounting to 1. First, the problem statement is written in 5.2 as a p-norm function to minimize the maximum of all objective functions [168], [174]:

Figure 5.1: Simple cantilever design problem with two load cases.

$$\min_{x_e} C = \left(\sum_{i=1}^{k} (w_i C_i)^Q \right)^{\frac{1}{Q}} \tag{5.2}$$

For the special case where $Q = 1$, 5.2 becomes a linear weighted sum given as

$$\min_{x_e} C = \sum_{i=1}^{k} w_i C_i \tag{5.3}$$

The problem statement for two load cases can be represented as:

$$\min_{x_e} C = w_1 C_1 + w_2 C_2 = w_1 F_1^T U_1 + w_2 F_2^T U_2 = w_1 \sum_{e=1}^{n} E_e u_{1,e}^T k_0 u_{1,e} + w_2 \sum_{e=1}^{n} E_e u_{2,e}^T k_0 u_{2,e}$$

$$\text{subject to: } KU_1 = F_1$$

$$KU_2 = F_2$$

$$\frac{\sum_{e=1}^{n} V_e}{f V_0} \leq 1 \tag{5.4}$$

$$w_1 + w_2 = 1$$

$$0 \leq x_e \leq 1$$

$$0 < E_{min} \leq E_e \leq E_0$$

For this problem, the modified SIMP material interpolation function is utilized as given in 5.5:

$$E_e(x_e) = x_e^p (E_0 - E_{min}) + E_{min} \tag{5.5}$$

Where p is the penalty on the pseudo-density design variables.

The sensitivity of the compliance function similar to 4.20 in Chapter 4 is given as:

$$\frac{\partial C}{\partial x} = -\left\{ w_1 \left(U_1^T \frac{\partial K}{\partial x} U_1 \right) + w_2 \left(U_2^T \frac{\partial K}{\partial x} U_2 \right) \right\} \tag{5.6}$$
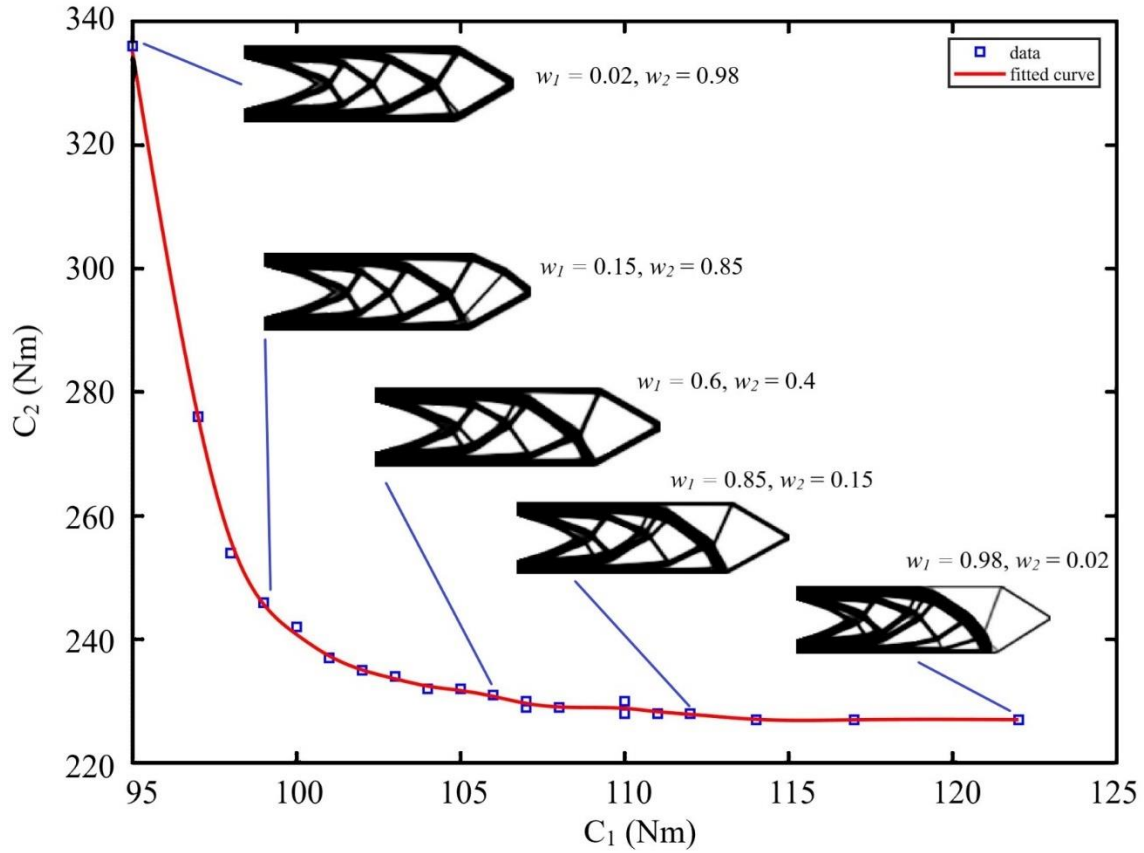
Figure 5.2: Plot of the Pareto optimal set for the cantilever problem in Figure 5.1.

In Figure 5.2, it is observed that the weights of the load case determine the structural layout of the optimized topology. The weights also depict the gradient [167] of the consolidated compliance function such that

$$\nabla_{C_i} C = \begin{Bmatrix} \dfrac{\partial C}{\partial C_1} \\ \dfrac{\partial C}{\partial C_2} \end{Bmatrix} = \begin{Bmatrix} w_1 \\ w_2 \end{Bmatrix} \tag{5.7}$$

Recall that an infinite number of Pareto optimal sets can be obtained on the right of the curve in Figure 5.2, therefore, to obtain the overall minimum Pareto optimal set for C, and noting that C is a function of x, the grad in 5.7 can be written as:

$$\frac{\partial C}{\partial x} = \frac{\partial C}{\partial C_1} \frac{\partial C_1}{\partial x} + \frac{\partial C}{\partial C_2} \frac{\partial C_2}{\partial x} \tag{5.8}$$

From 5.7, 5.8 can be written as:

$$\frac{\partial C}{\partial x} = w_1 \frac{\partial C_1}{\partial x} + w_2 \frac{\partial C_2}{\partial x} \tag{5.9}$$

By setting $\dfrac{\partial C}{\partial x} = 0$, we obtain

$$\frac{w_2}{w_1} = -\frac{\dfrac{\partial C_1}{\partial x}}{\dfrac{\partial C_2}{\partial x}} \tag{5.10}$$

$$\frac{w_2}{w_1} = \left\| \frac{\dfrac{\partial C_1}{\partial x}}{\dfrac{\partial C_2}{\partial x}} \right\| \tag{5.11}$$

From 5.9, the minimum Pareto optimal set can be obtained by selecting weight factors of the objective functions that are a ratio of their respective sensitivity functions. For design-dependent loads, these analogies are quite different. After all, the sensitivity functions become more intricate because the loads depend on the design variables. This contributes to numerical instabilities that make the optimization a lot more difficult to converge. However, the ratio of the sensitivities as demonstrated in 5.9 can be applied in a sort of 'sensitivity scaling' scheme to enhance the stability of the optimization for design-dependent loads; this is presented in the following sections.

5.3 Weighted Multiobjective Topology Optimization for Design-Independent and Design-Dependent Loads

In this section, the cantilever problem in Figure 3.2 of Chapter 3 is studied here. However, a point force is added at the bottom right vertex of the cantilever as illustrated in Figure 5.3. A similar rotating cantilever problem is tackled in [29], however, without temperature distribution. This problem is resolved by minimizing the structure's compliance, however, because compliance values (in turn sensitivity values) from the various load contributions might be dissimilar in magnitude, they are usually normalized. Two normalization strategies are popular in literature: one is dividing the compliance functions by an initial or reference value as seen in [175]–[177], the other is by utilizing a min-max scaling as observed in [168], [170], [172], [178], [179]. In this work, the second normalization is used while streamlining it to the use of max scaling as done in [170]. From 5.2, the problem statement becomes:
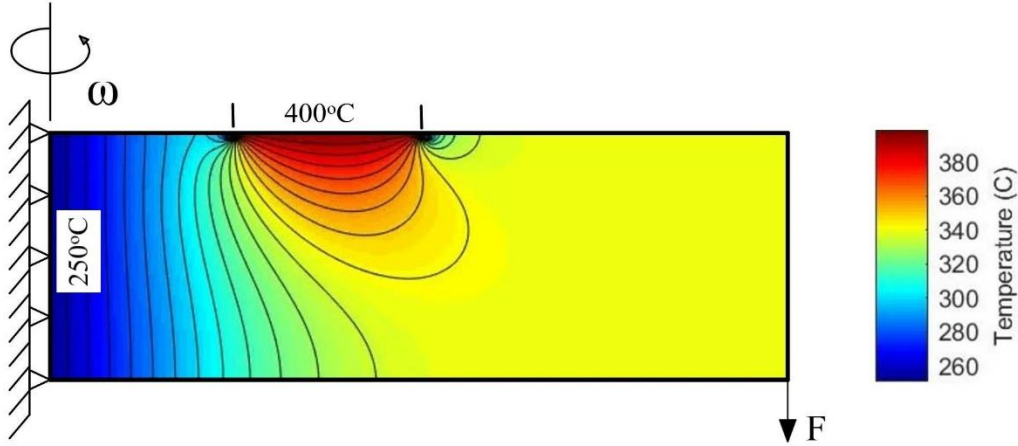
Figure 5.3: A cantilever problem with a temperature distribution, point force, and rotated about an axis by an angular velocity.

$$
\min_{x_e} \hat{C} = \left\{ w_{th}^Q (\hat{C}_{th})^Q + w_c^Q (\hat{C}_c)^Q + w_f^Q (\hat{C}_f)^Q \right\}^{\frac{1}{Q}}
$$

$$
= \left\{ w_{th}^Q \left(\sum_{e=1}^n \frac{c_e^{th}}{c_{e,max}^{th}} \right)^Q + w_c^Q \left(\sum_{e=1}^n \frac{c_e^c}{c_{e,max}^c} \right)^Q + w_f^Q \left(\sum_{e=1}^n \frac{c_e^f}{c_{e,max}^f} \right)^Q \right\}^{\frac{1}{Q}}
$$

subject to: $KU_{th} = F_{th}$

78

$$KU_c = F_c$$

$$KU_f = F_f$$

$$(\widetilde{K}_c)T = R_T$$

$$\frac{\sum_{e=1}^{n} V_e}{fV_0} \leq 1 \tag{5.12}$$

$$0 \leq x_e \leq 1$$

$$0 < E_{min} \leq E_e \leq E_0$$

Material function based on RAMP is used:

$$E_e = \frac{x_e}{1 + q_1(1 - x_e)} E_0 \tag{5.13}$$

$$\beta_e = \frac{x_e}{1 + q_2(1 - x_e)} E_0 \alpha_0$$

Where $C, \check{C}_{th}, \check{C}_c, \check{C}_f$ are the consolidated/global normalized compliance function, normalized compliance from TSL, normalized compliance from centrifugal loads, and normalized compliance from a point force respectively. $(c_e^{th}, c_{e,max}^{th})$, $(c_e^c, c_{e,max}^c)$, and $(c_e^f, c_{e,max}^f)$, are the elemental compliance values and maximum elemental compliance values for TSL, centrifugal loads, and point force respectively. (F_{th}, U_{th}), (F_c, U_c), (F_f, U_f) are the load and displacement vectors for thermoelastic stress, centrifugal, and point force respectively.

In literature $Q = 1$, and $Q = 2$ are very popular [168] where the former transforms the consolidated compliance function to a linear weighted sum of the individual compliance functions and the latter upwards is a min-max optimization approximation. In this work, $Q = 1$ is used, therefore, the consolidated compliance function in 5.12 is given as:

$$\min_{x_e} \hat{C} = w_{th}\hat{C}_{th} + w_c\hat{C}_c + w_f\hat{C}_f$$

$$= w_{th} \sum_{e=1}^{n} \frac{c_e^{th}}{c_{e,max}^{th}} + w_c \sum_{e=1}^{n} \frac{c_e^c}{c_{e,max}^c} + w_f \sum_{e=1}^{n} \frac{c_e^f}{c_{e,max}^f} \tag{5.14}$$

5.2.1. Sensitivity Analysis, Sensitivity Scaling, and Filtering

Sensitivity analysis is simply obtaining the derivative of the objective and constraint functions with-respect-to the pseudo-density design variable. The derivative of the compliance function is well described in 4.15 to 4.19 in Chapter 4 using the adjunct method. First, the derivative of the left-hand side of 5.14 will become

$$\frac{\partial \check{C}}{\partial x} = w_{th} \frac{\partial \check{C}_{th}}{\partial x} + w_c \frac{\partial \check{C}_c}{\partial x} + w_f \frac{\partial \check{C}_f}{\partial x} \tag{5.15}$$

Therefore, 4.19 is presented here for the derivative of each load case:

$$\frac{\partial c_e^{th}}{\partial x_e} = -(u_e^{th})^T \frac{\partial k_e}{\partial x_e} u_e^{th} + 2(u_e^{th})^T \frac{\partial F_e^{th}}{\partial x_e} \tag{5.16}$$

$$\frac{\partial c_e^{c}}{\partial x_e} = -(u_e^{c})^T \frac{\partial k_e}{\partial x_e} u_e^{c} + 2(u_e^{c})^T \frac{\partial F_e^{th}}{\partial x_e} \tag{5.17}$$

$$\frac{\partial c_e^{f}}{\partial x_e} = -\left(u_e^{f}\right)^T \frac{\partial k_e}{\partial x_e} u_e^{f} + 2\left(u_e^{f}\right)^T \frac{\partial F_e^{f}}{\partial x_e} \tag{5.18}$$

Since $F_{f,e}$ in 5.18 is design-independent, its derivative with x_e is 0, therefore, 5.18 becomes

$$\frac{\partial c_e^{f}}{\partial x_e} = -\left(u_e^{f}\right)^T \frac{\partial k_e}{\partial x_e} u_e^{f} \tag{5.19}$$

In this work, the Optimality Criteria Method (OCM) [129], [130] as elaborated in Chapter 2 is used as an optimizer. Although this optimizer is identified as less robust than other convex approximation methods such as MMA and GCMMA [180], IPOPT [181], MDQA [182], GCMMA-GBMMA [183], it is a very stable optimizer with much less parameter tuning, unlike the others. Also, optimizers such as OCM and MMA are only capable of resolving monotonic structural optimization problems [27]. A topology optimization problem is referred to as monotonic if the sign of the sensitivity function stays the same for all elements in the domain and throughout the optimization process. The sensitivity function in 5.19 obtained for point force compliance is monotonic as the sign never changes, however, those for TSL and centrifugal loads, 5.16 and 5.17, are not because of the load sensitivity term they possess.

Strictly speaking, OCM and MMA are ordinarily not capable of handling these complicated multiobjective topology optimization formulations, however, a sensitivity scaling scheme is presented in this work to ensure the overall sensitivity term stays monotonic or *near* monotonic. This is done by

scaling the "unstable" sensitivity terms such that the stable term drives the overall or consolidated sensitivity term. To achieve this, some scale factors are introduced to individual sensitivity functions. The individual scaled sensitivities become:

$$\frac{\partial \hat{C}_{th}}{\partial x} = \Upsilon_{th} \frac{\partial \check{C}_{th}}{\partial x} \tag{5.21}$$

$$\frac{\partial \hat{C}_c}{\partial x} = \Upsilon_c \frac{\partial \check{C}_c}{\partial x} \tag{5.22}$$

$$\frac{\partial \hat{C}_f}{\partial x} = \Upsilon_f \frac{\partial \check{C}_f}{\partial x} \tag{5.23}$$

5.21 to 5.23 can be inserted into 5.15 to obtain the overall scaled sensitivity function:

$$\frac{\partial \hat{C}}{\partial x} = w_{th}\left(\frac{\partial \hat{C}_{th}}{\partial x}\right) + w_c\left(\frac{\partial \hat{C}_c}{\partial x}\right) + w_f\left(\frac{\partial \hat{C}_f}{\partial x}\right)$$

$$= w_{th}\left(\Upsilon_{th}\frac{\partial \check{C}_{th}}{\partial x}\right) + w_c\left(\Upsilon_c\frac{\partial \check{C}_c}{\partial x}\right) + w_f\left(\Upsilon_f\frac{\partial \check{C}_f}{\partial x}\right) \tag{5.24}$$

In 5.24, $\Upsilon_{th}, \Upsilon_c, \Upsilon_f$ are scale factors for the sensitivities from TSL, centrifugal load, and point force respectively. They are defined thus:

$$\Upsilon_{th} = \frac{\max\left(\left\|\frac{\partial \check{C}_{th}}{\partial x_e}\right\|\right)}{\max\left(\left\|\frac{\partial \check{C}_f}{\partial x_e}\right\|\right)} \tag{5.25}$$

$$\Upsilon_c = \frac{\max\left(\left\|\frac{\partial \check{C}_c}{\partial x_e}\right\|\right)}{\max\left(\left\|\frac{\partial \check{C}_f}{\partial x_e}\right\|\right)} \tag{5.26}$$

$$\Upsilon_f = \frac{\max\left(\left\|\frac{\partial \check{C}_f}{\partial x_e}\right\|\right)}{\max\left(\left\|\frac{\partial \check{C}_f}{\partial x_e}\right\|\right)} = 1 \tag{5.27}$$

Moving forward, the sensitivity before scaling can be rewritten as

$$\frac{\partial \check{c}_e}{\partial x_e} = \frac{w_{th}}{c_{e,max}^{th}} \left(\frac{\partial c_e^{th}}{\partial x_e} \right) + \frac{w_c}{c_{e,max}^c} \left(\frac{\partial c_e^c}{\partial x_e} \right) + \frac{w_f}{c_{e,max}^f} \left(\frac{\partial c_e^f}{\partial x_e} \right) \tag{5.28}$$

$$\frac{\partial \check{c}_e}{\partial x_e}$$

$$= \frac{w_{th}}{c_{e,max}^{th}} \left(-(u_e^{th})^T \frac{\partial k_e}{\partial x_e} u_e^{th} + 2(u_e^{th})^T \frac{\partial F_e^{th}}{\partial x_e} \right) + \frac{w_c}{c_{e,max}^c} \left(-(u_e^c)^T \frac{\partial k_e}{\partial x_e} u_e^c + 2(u_e^c)^T \frac{\partial F_e^{th}}{\partial x_e} \right)$$

$$+ \frac{w_f}{c_{e,max}^f} \left(-(u_e^f)^T \frac{\partial k_e}{\partial x_e} u_e^f \right) \tag{5.29}$$

Finally, the scaled sensitivity is given as:

$$\frac{\partial \hat{c}_e}{\partial x_e}$$

$$= \frac{w_{th}}{c_{e,max}^{th}} Y_{th} \left(-(u_e^{th})^T \frac{\partial k_e}{\partial x_e} u_e^{th} + 2(u_e^{th})^T \frac{\partial F_e^{th}}{\partial x_e} \right) + \frac{w_c}{c_{e,max}^c} Y_c \left(-(u_e^c)^T \frac{\partial k_e}{\partial x_e} u_e^c + 2(u_e^c)^T \frac{\partial F_e^{th}}{\partial x_e} \right)$$

$$+ \frac{w_f}{c_{e,max}^f} Y_f \left(-(u_e^f)^T \frac{\partial k_e}{\partial x_e} u_e^f \right) \tag{5.30}$$

The derivatives of the design-dependent loads with-respect-to the pseudo-density design variable x_e are given as:

$$\frac{\partial F_e^{th}}{\partial x_e} = \frac{\partial \beta_e}{\partial x_e} \frac{\Delta T}{2(1-\mu)} [-1 \; -1 \; 1 \; -1 \; 1 \; 1 \; -1 \; 1]^T \tag{5.31}$$

where

$$\frac{\partial \beta_e}{\partial x_e} = \frac{1 + q_2}{\left(1 + q_2(1 - x_e) \right)^2} E_0 \alpha_0 \tag{5.32}$$

$$\frac{\partial F_e^c}{\partial x_e} = \rho_0 \left(\frac{2\pi N}{60} \right)^2 r_e \tag{5.33}$$

Assuming each element has a unit volume for a constant mesh size space- and time-wise,

$$\frac{\partial v_e}{\partial x_e} = 1 \tag{5.34}$$

A sensitivity filter is utilized as in Chapter 4 and is expressed as [54]:

$$\frac{\partial \check{c}_e}{\partial x_e} = \frac{1}{max(\gamma, x_e) \sum_{i \in N_e} H_{ei}} \sum_{i \in N_e} H_{ei} \, x_i \frac{\partial \check{c}_e}{\partial x_i} \tag{5.35}$$

where N_e is the set of neighboring elements i which have center-to-center distance $d(e, i)$ to element e less than set filter radius r_{min}. To avoid divisions by zero in the fraction in 5.33, γ is assigned a small value as 10^{-3}. H_{ei} is a weight factor expressed as:

$$H_{ei} = max(0, r_{min} - d(e, i)) \tag{5.36}$$

A flowchart showing the major steps in the multiphysics and multiobjective topology optimization model is shown in Figure 5.4.
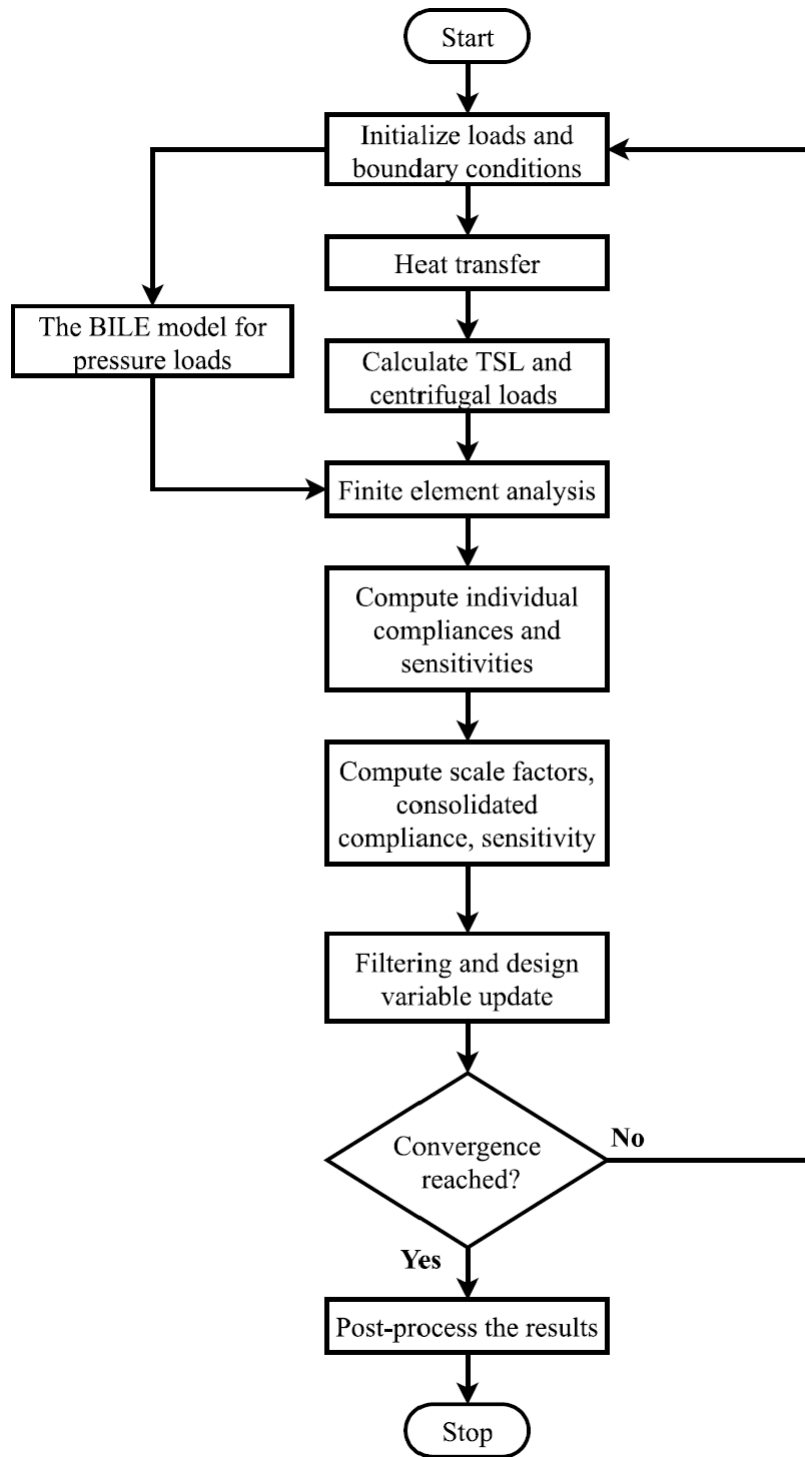
Figure 5.4: Workflow of the multiphysics and multiobjective topology optimization model

5.2.2. Numerical Results

5.2.2.1. Effects of TSL thresholding on numerical stability

In this section, the effects of thresholding TSL as concluded in Chapter 3 are presented. Three values – $0, 0.5, 0.8$ – of the threshold parameter η are used and the optimization each time is run for 30 iterations as the targeted number of minimum iterations for this case. The weighted factors for this problem were assigned as $w_{th} = 0.5, w_c = 0, w_f = 0.5$. In Figure 5.5, when $\eta = 0$, there is no threshold placed on the TSL vector, therefore, all the nodal TSLs in the finite element mesh contribute to the displacement response for thermoelastic compliance and in turn the compliance sensitivity. As pointed out in Chapter 3, the magnitude of every elemental TSL load is at least 60% of the maximum. As a result, the sensitivities of all the elements in the optimization domain become closely matched creating no distinct load path for a structural layout to be established thereby inducing instabilities in the optimality criteria. This further creates erroneously large sensitivity magnitudes after some iterations until the optimization produces indefinite numerical values. This is seen in Figure 5.5 for $\eta = 0$ where the optimization fails after the 5th iteration. For $\eta = 0.5$, the optimization up until the 25th iteration and similar issues as described previously arise. Finally, for $\eta = 0.8$, the optimization lasts till the 30th iteration and beyond. As opposed to the previous cases, setting a higher threshold ensures that there is a more defined load path in thermoelastic compliance sensitivity. Although a higher threshold can quite underestimate the TSL in some iterations (3rd and 5th in Figure 5.5), this occurs in a few iterations in the early stages of the optimization.
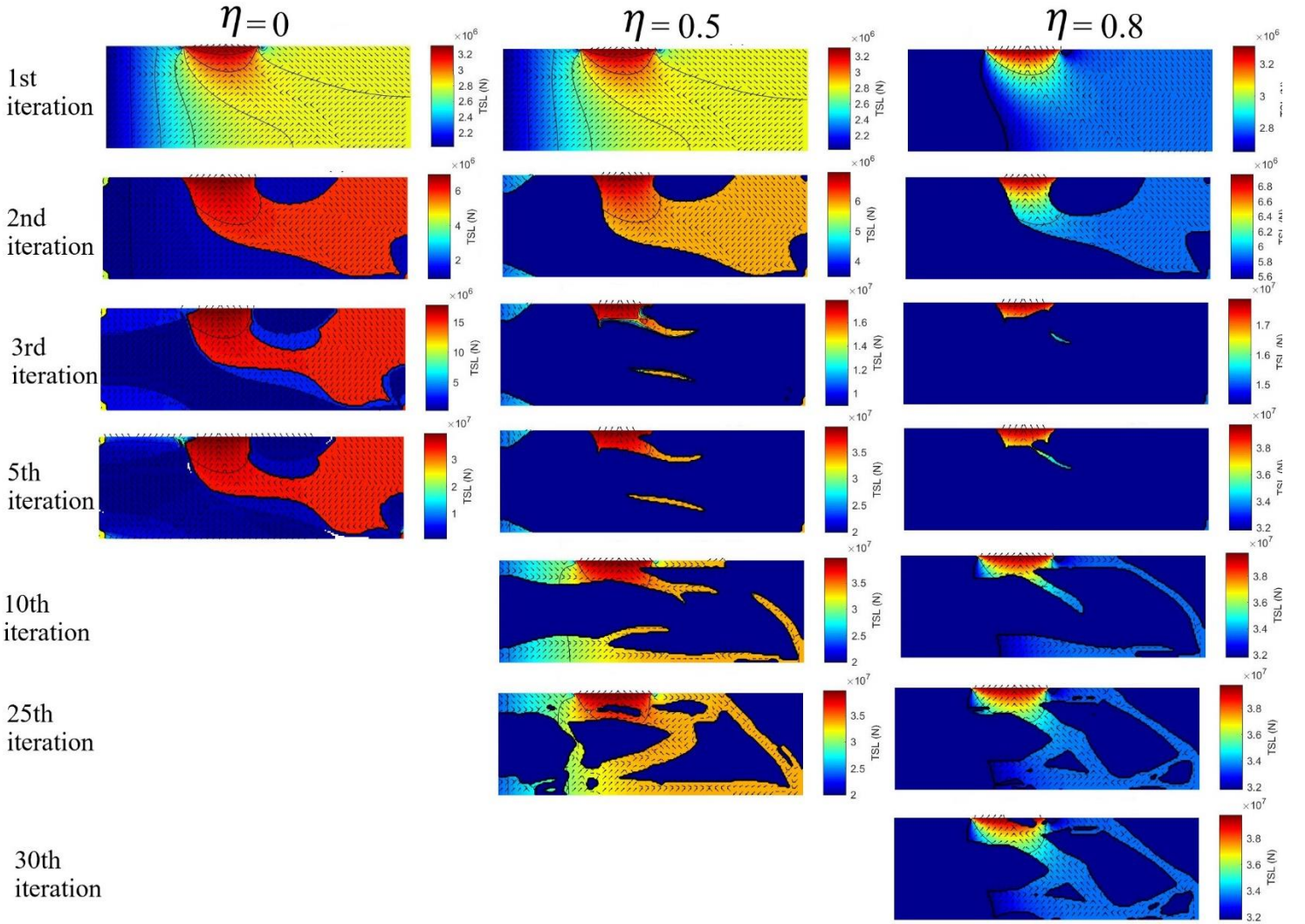
Figure 5.5: TSL field for η=0, 0.5, and 0.8 for the rotating cantilever problem in Figure 5.3.

5.2.2.2. Bi-objective topology optimization for a pair of design-dependent and -independent loads.

The results of topology optimization for a pair of objectives for the rotating cantilever are presented in this section for $\eta = 0.8$ on TSL only. Additionally, the scale factors for sensitivity contributions from TSL and centrifugal loads are further scaled down to a factor of 10^{-1}. This is to ensure that the full range of the weight factors $0 < w_i < 1$ is studied with minimal numerical instability. In the first half of this study, the pair of TSL and point force is considered, therefore the weight factor for centrifugal loads is set to 0 ($w_c = 0$). The consolidated compliance function (RHS of 5.14) becomes:

$$\min_{x_e} \hat{C} = w_{th}\hat{C}_{th} + w_f\hat{C}_f \tag{5.37}$$

While the sensitivity function becomes:

86

$$\frac{\partial \hat{C}}{\partial x} = w_{th}\left(Y_{th}\frac{\partial \check{C}_{th}}{\partial x}\right) + w_f\left(Y_f\frac{\partial \check{C}_f}{\partial x}\right) \tag{5.38}$$

First, the most stable result is presented in Figure 5.6 and it comes from optimizing the cantilever subjected to a point force only. Since the sensitivities from other load cases are scaled to that of the point force, the results in Figure 5.6 are taken as the reference for the bi-objective and tri-objective cases. For all problems under this section, 13400 bilinear square elements are used in the discretized domain while the convergence limit is set at 10^{-3} for the design variable or a maximum of 80 iterations.
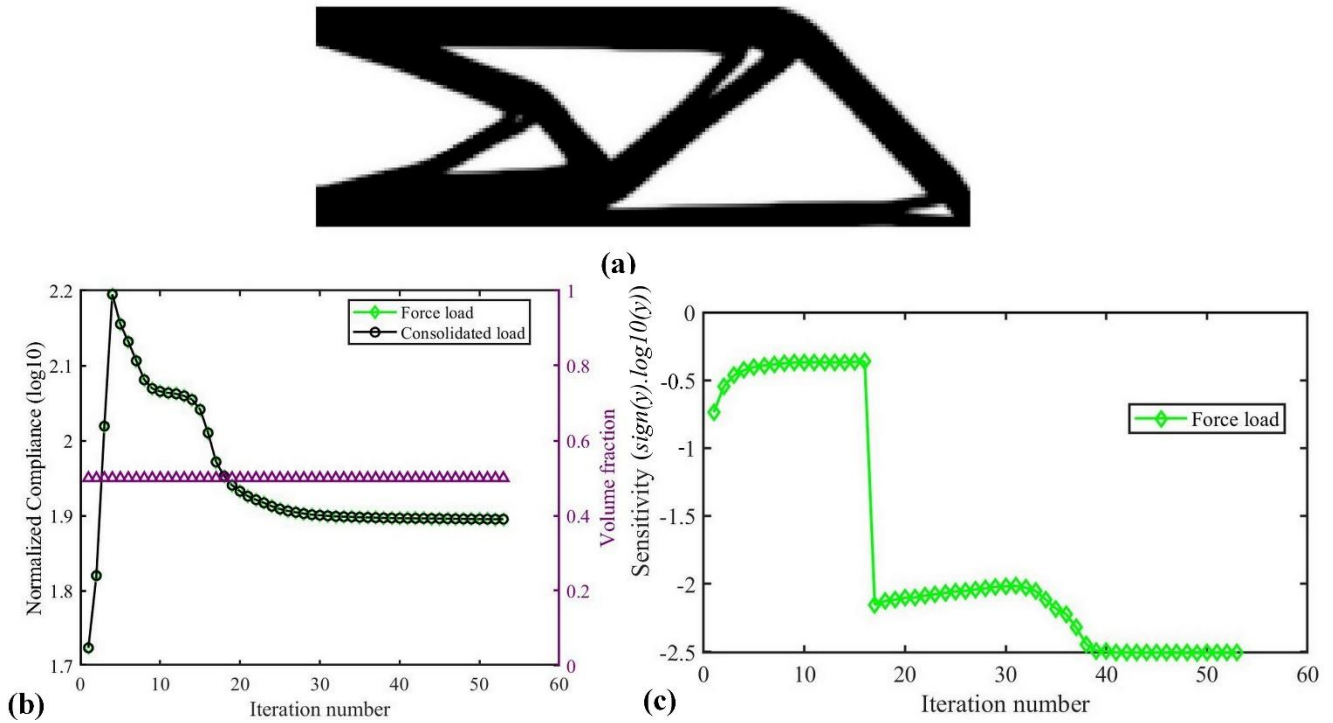
Figure 5.6: (a) Topology (b) normalized compliance history and (c) sensitivity history for the cantilever problem for $w_f = 1$.

In Figure 5.6, the normalized compliance history shows that the objective is minimized and convergence is attained just after 50 iterations. It should be noted that the scale on the y-axis of the plots is computed as:

$$\text{sign}(y).\log_{10}(y) \tag{5.39}$$

The sensitivity presented all through this chapter is the sum of the sensitivities of all elements for either a load case or a consolidated objective. A deep dive is observed in the sensitivity shown in Figure 5.6(c), this happens at a point in the optimization where there is a shift in the distribution of the design variable

from more uniform intermediate values (~0.5) to values closer to 0 or 1. There now exists a significant number of elements that are close to but not equal to 0. Since the RAMP interpolation function is used, elements with very low-density values (close to but not 0) keep a significant portion of their sensitivities while those close to or up to 1 have an increase in their sensitivities thereby causing a sharp increase in the overall sensitivity.
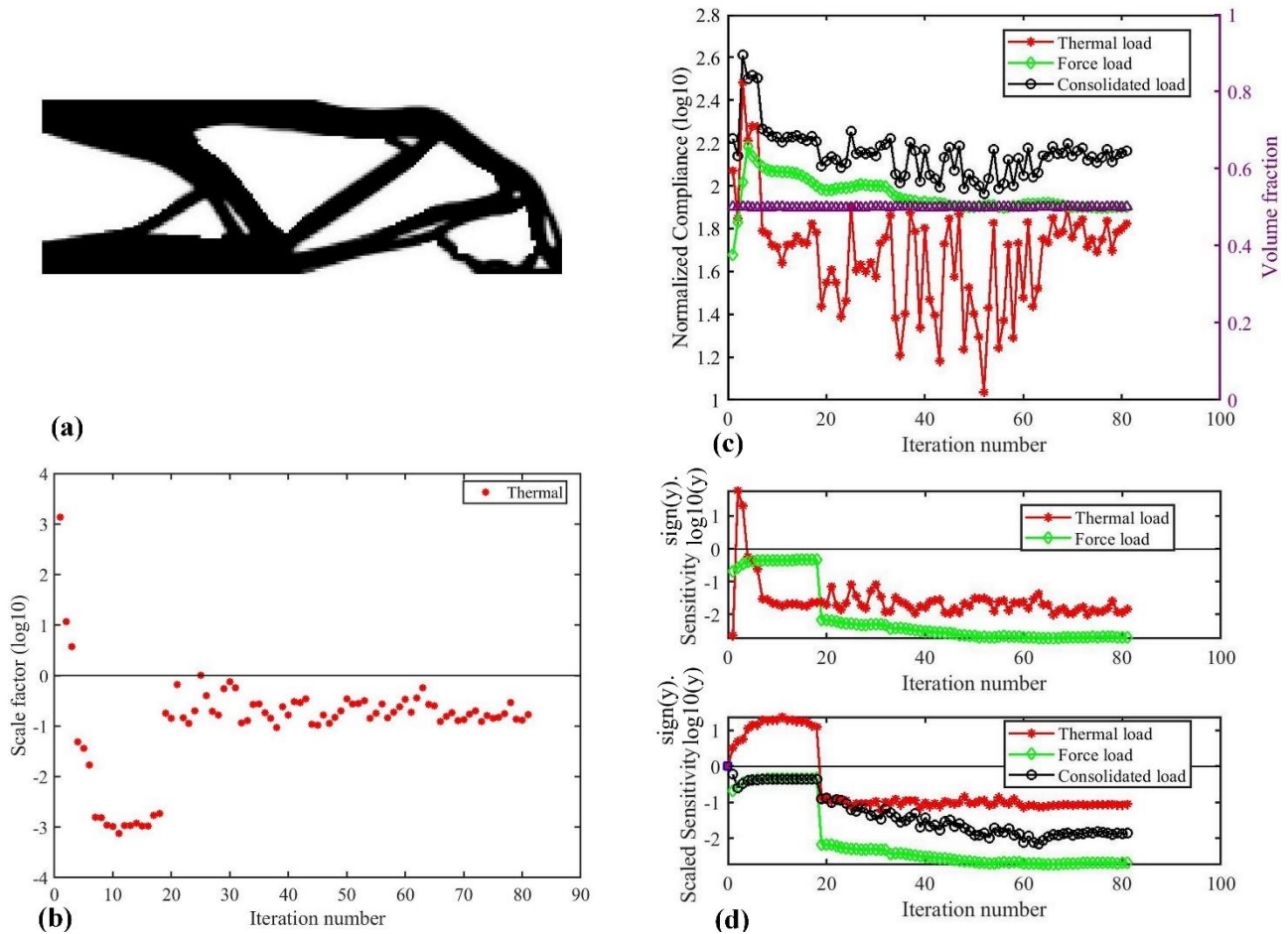
Figure 5.7: (a) Topology, (b) scale factor history, (b) normalized compliance history, and (c) sensitivity history for the cantilever problem for $w_{th} = 0.1$ and $w_f = 0.9$.
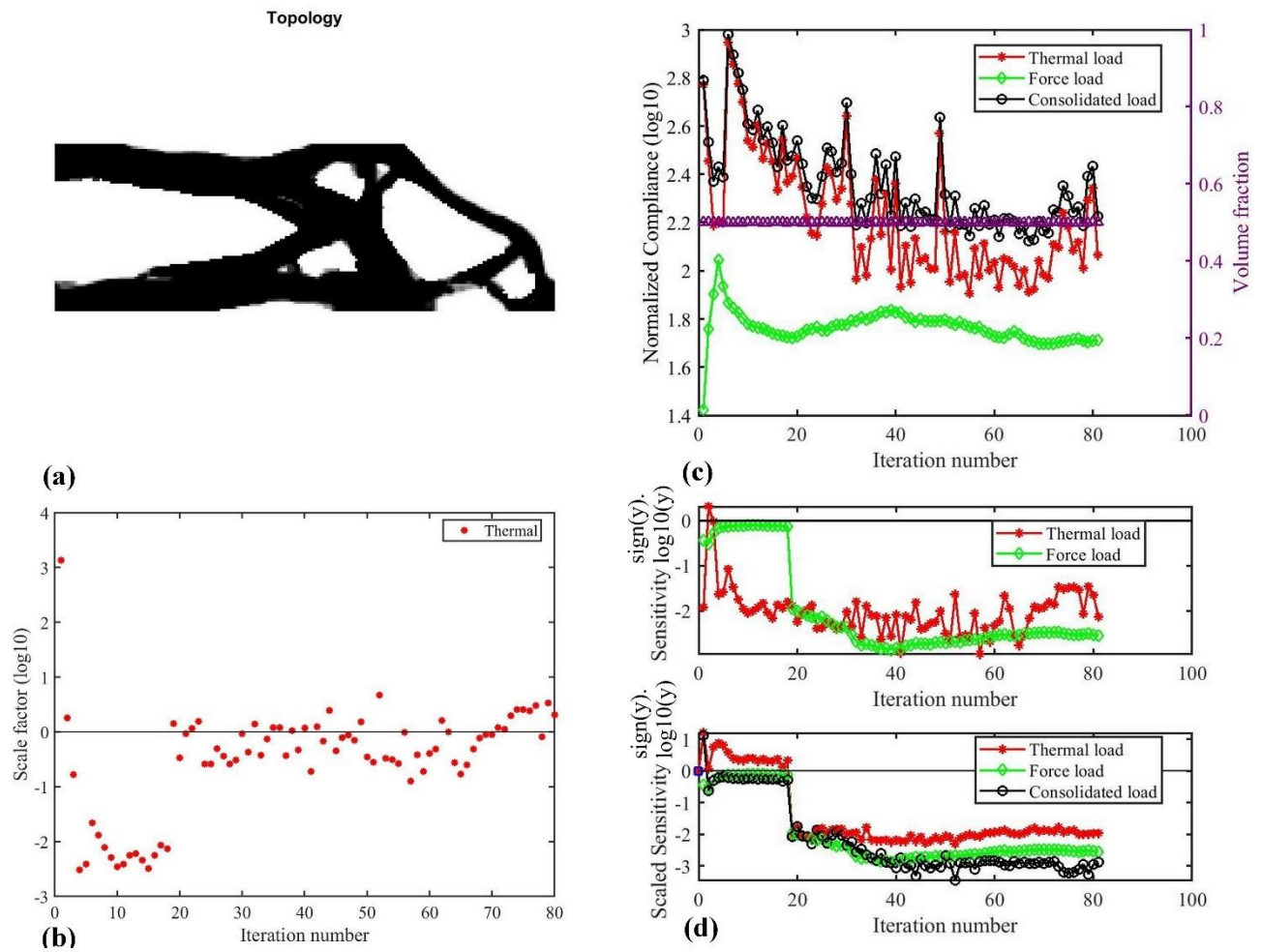
Figure 5. 8: (a) Topology, (b) scale factor history, (b) normalized compliance history, and (c) sensitivity history for the cantilever problem for $w_{th} = 0.5$ and $w_f = 0.5$.
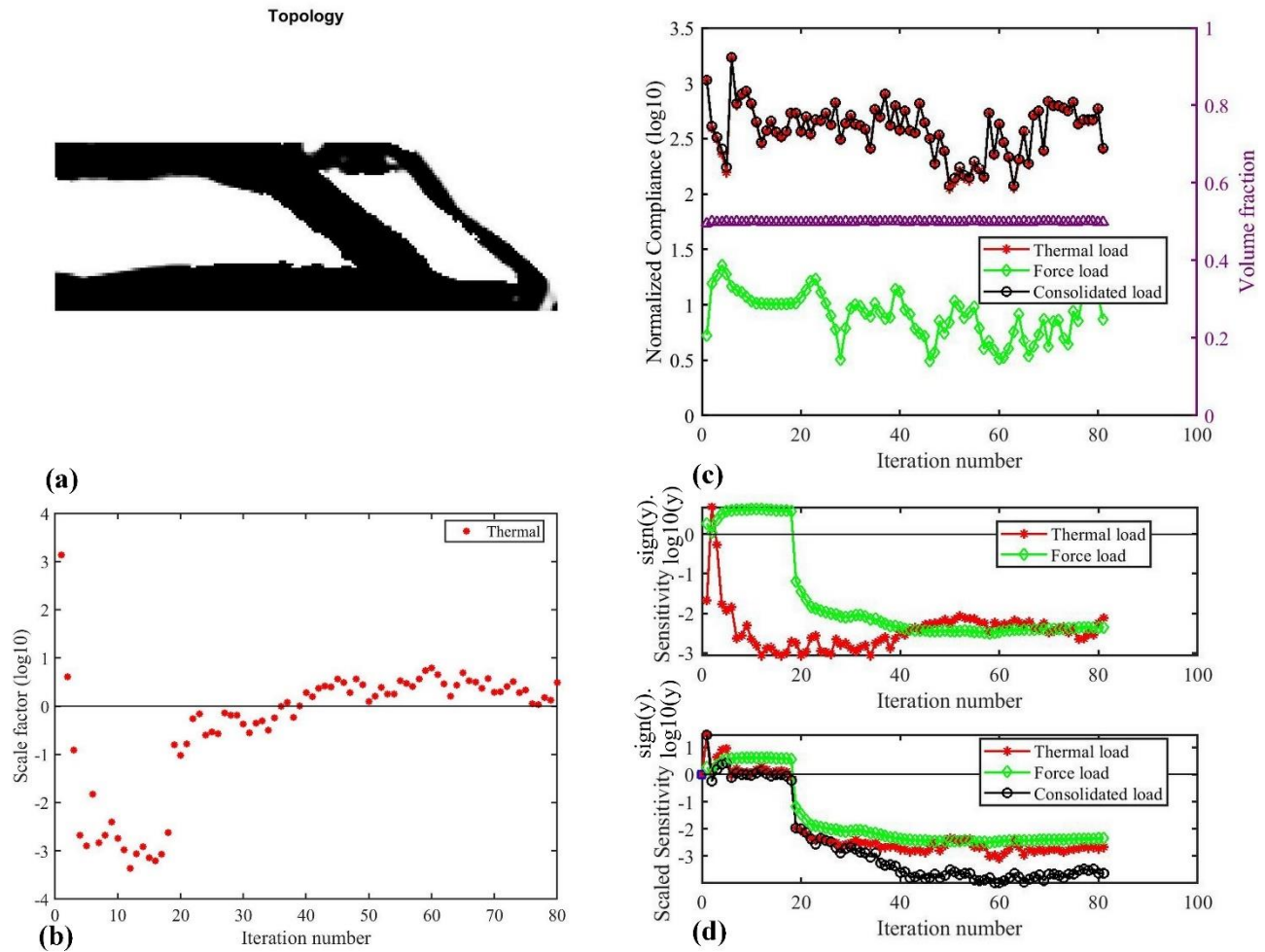
Figure 5.9: (a) Topology, (b) scale factor history, (b) normalized compliance history, and (c) sensitivity history for the cantilever problem for $w_{th} = 0.9$ and $w_f = 0.1$.

In Figure 5.7 to Figure 5.9, it is observed that very low scale factors ($0 < \Upsilon_{th} \ll 1$) are initially (first 20 iterations) required to balance up the sensitivity of the TSL load case with that of the point force because TSLs cause a greater sensitivity due to the load vector randomness. However, after around 20 iterations, the sensitivity stabilizes and Υ_{th} maintains values closer to 1. The sensitivity histories from TSL are also initially complicated but become more in-line with that of the point force after some iterations. There is, therefore, no complication in the consolidated sensitivity history and this is important for the optimization to arrive at a structurally meaningful layout. Lastly, as w_{th} is increased relative to w_f compliance minimization becomes poorer. Therefore, the less the values w_{th} assume, the better the objective minimization.

Next, the pair of centrifugal loads and a point force is presented. 5.37 and 5.38 becomes:

$$\min_{x_e} \hat{C} = w_c \hat{C}_c + w_f \hat{C}_f \tag{5.37}$$

While the sensitivity function becomes:

$$\frac{\partial \hat{C}}{\partial x} = w_c \left(\Upsilon_c \frac{\partial \check{C}_c}{\partial x} \right) + w_f \left(\Upsilon_f \frac{\partial \check{C}_f}{\partial x} \right) \tag{5.38}$$
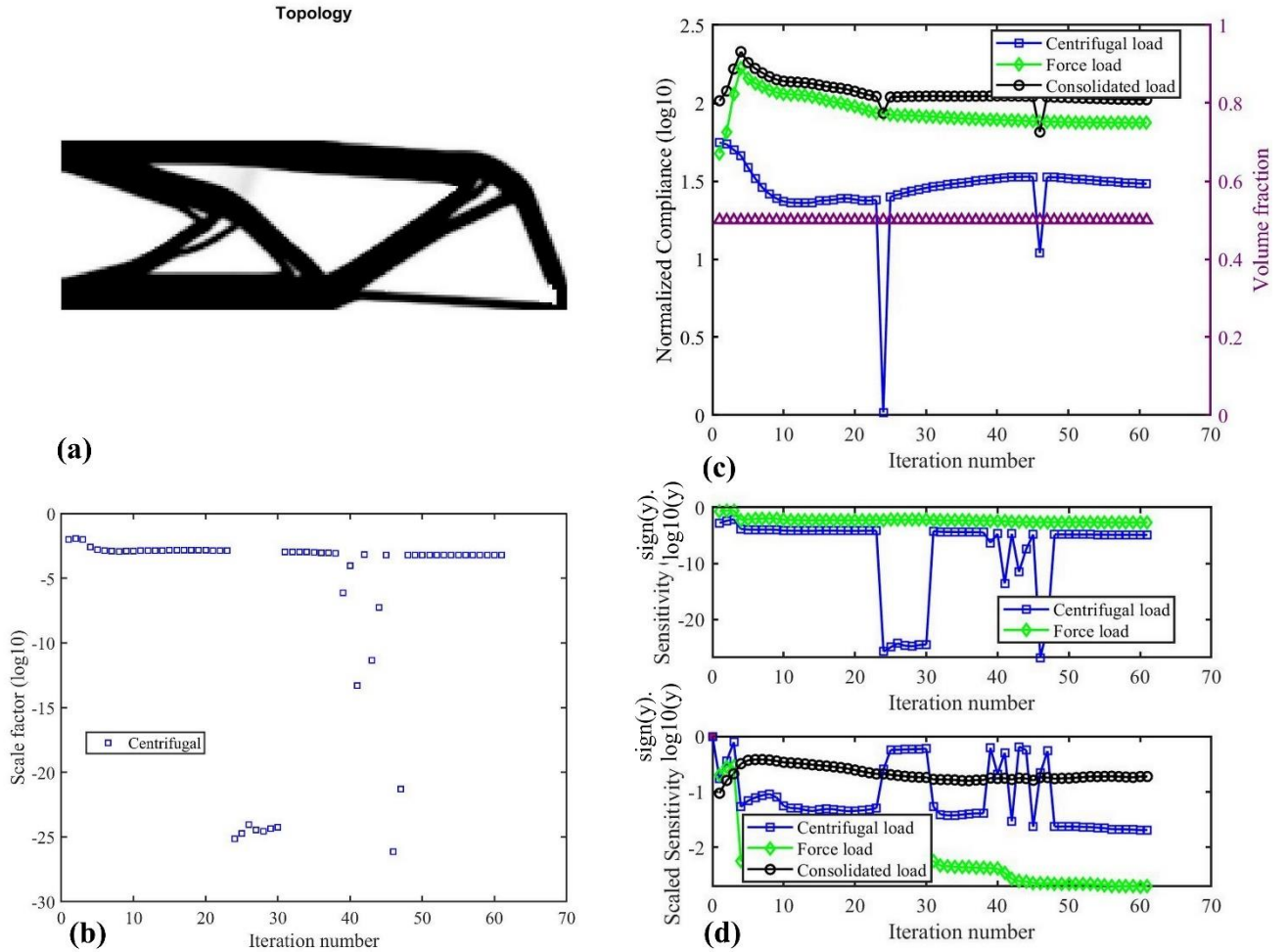
Figure 5.10: (a) Topology, (b) scale factor history, (b) normalized compliance history, and (c) sensitivity history for the cantilever problem for $w_c = 0.1$ and $w_f = 0.9$.
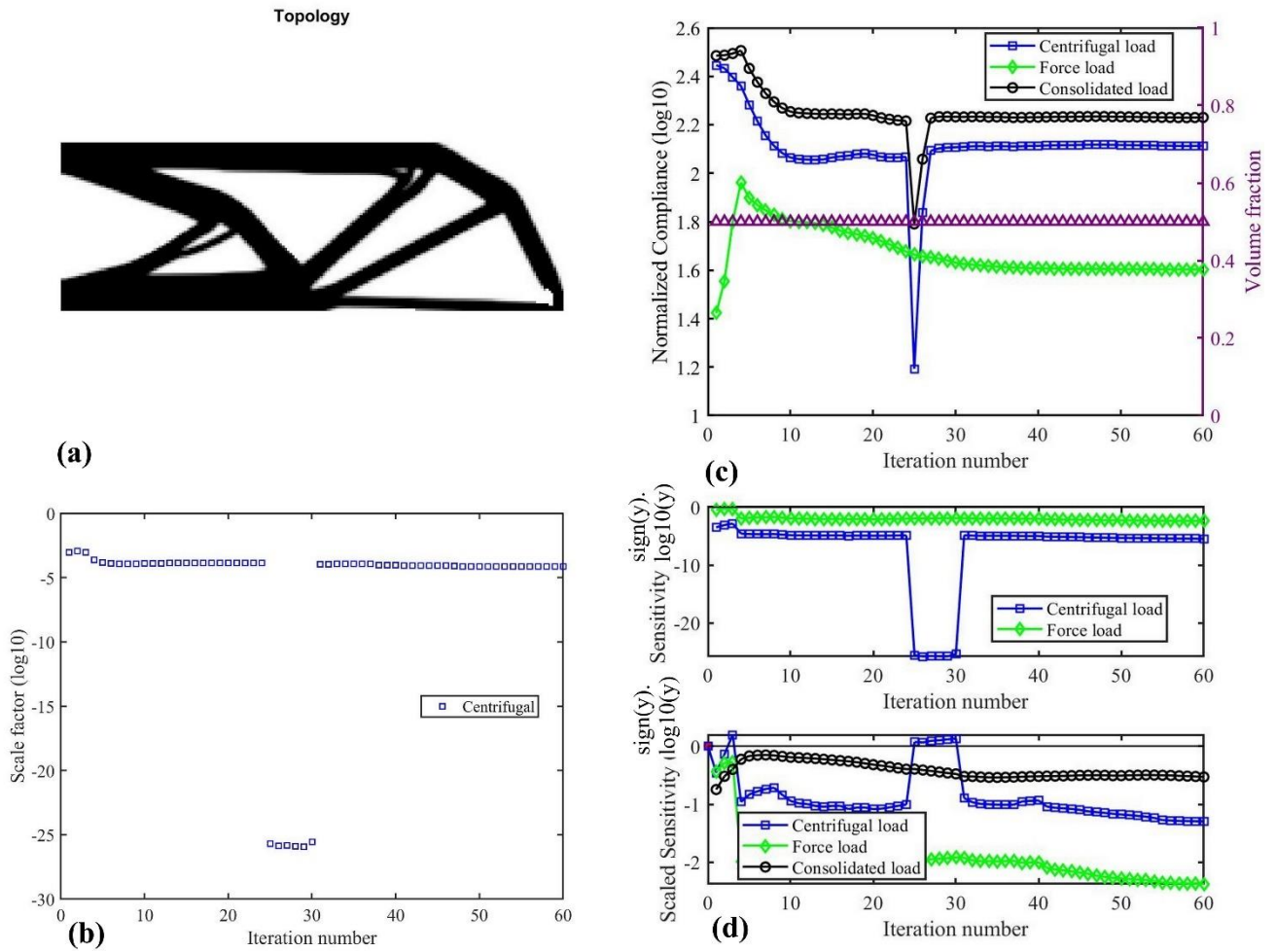
Figure 5.11: (a) Topology, (b) scale factor history, (b) normalized compliance history, and (c) sensitivity history for the cantilever problem for $w_c = 0.5$ and $w_f = 0.5$.

Topology

(a)

(b)

(c)

(d)
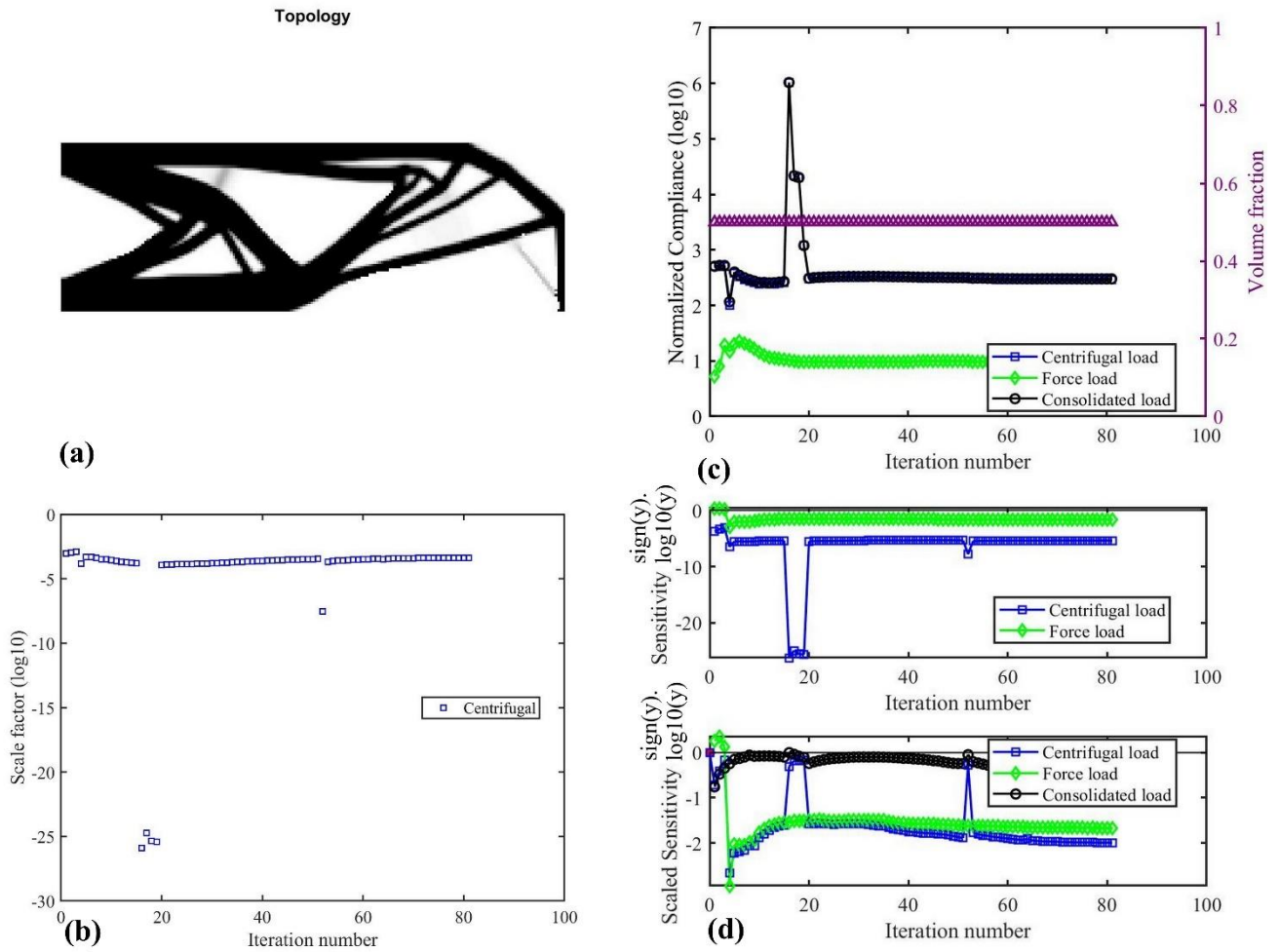
Figure 5.12: (a) Topology, (b) scale factor history, (b) normalized compliance history, and (c) sensitivity history for the cantilever problem for $w_c = 0.9$ and $w_f = 0.1$.
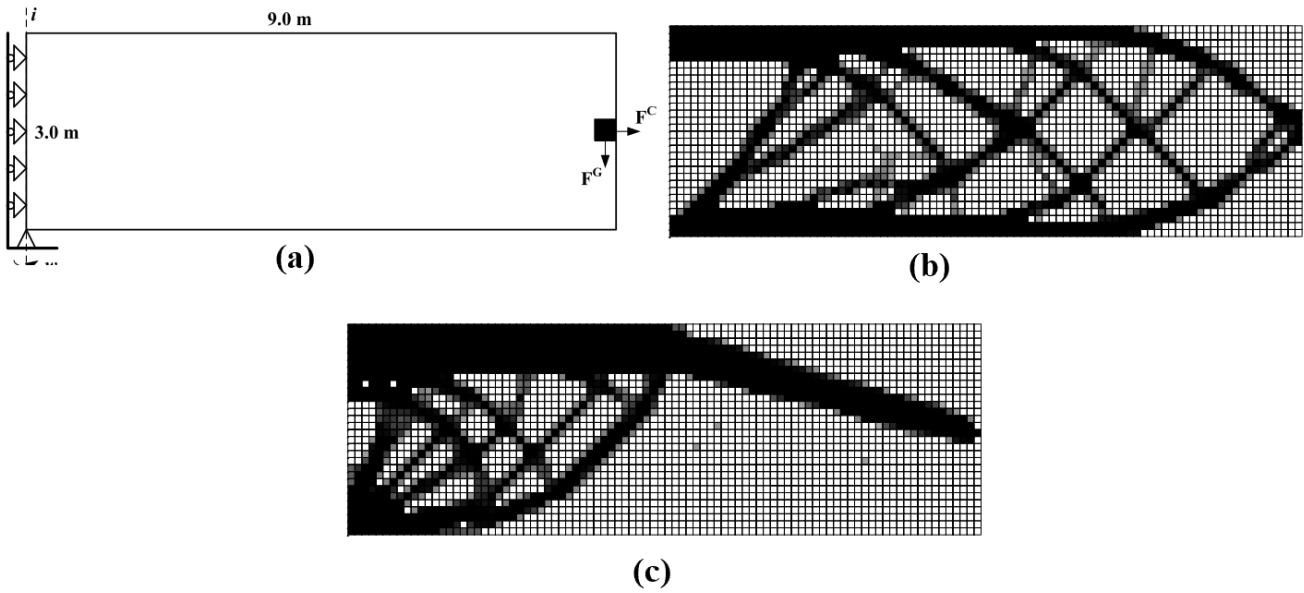
Figure 5.13: Topology optimization of a rotating cantilever structure by Zheng and Gea [29] shown in (a) considering (b) gravitational force from the non-structural mass depicted in (a) – can be referred to as a point force, and (c) gravitational and centrifugal forces from both structural and non-structural masses.

From Figure 5.10 to Figure 5.12, it is observed that the scale factor history is less complicated for centrifugal loads compared to TSLs. It generally means that centrifugal loads contribute to better numerical stability compared to TSLs and this reflects in the distinction of the topological results. For the compliance and sensitivity histories, the general trends as observed for TSLs apply here also, however, these histories are much less complicated for centrifugal loads. It is also important to note that during some periods in the optimization when centrifugal sensitivities become very high possibly due to '*floating*' intermediate elements, the scaling ensures that they remain comparable to the force sensitivities. Interestingly, there is a good correlation between the results obtained at higher w_c values in this study and those obtained by Zheng and Gea [29] back in 2006 as shown in Figure 5.13. It is a general conclusion that when centrifugal loads are considered for a rotating structure, more mass is deposited close to the axis of rotation.

Finally, for this section, the full weight factor variation is presented in Figure 5.14 by plotting the normalized consolidated compliance function against the weight factor ratios $\frac{w_{th}}{w_f}$ and $\frac{w_c}{w_f}$:
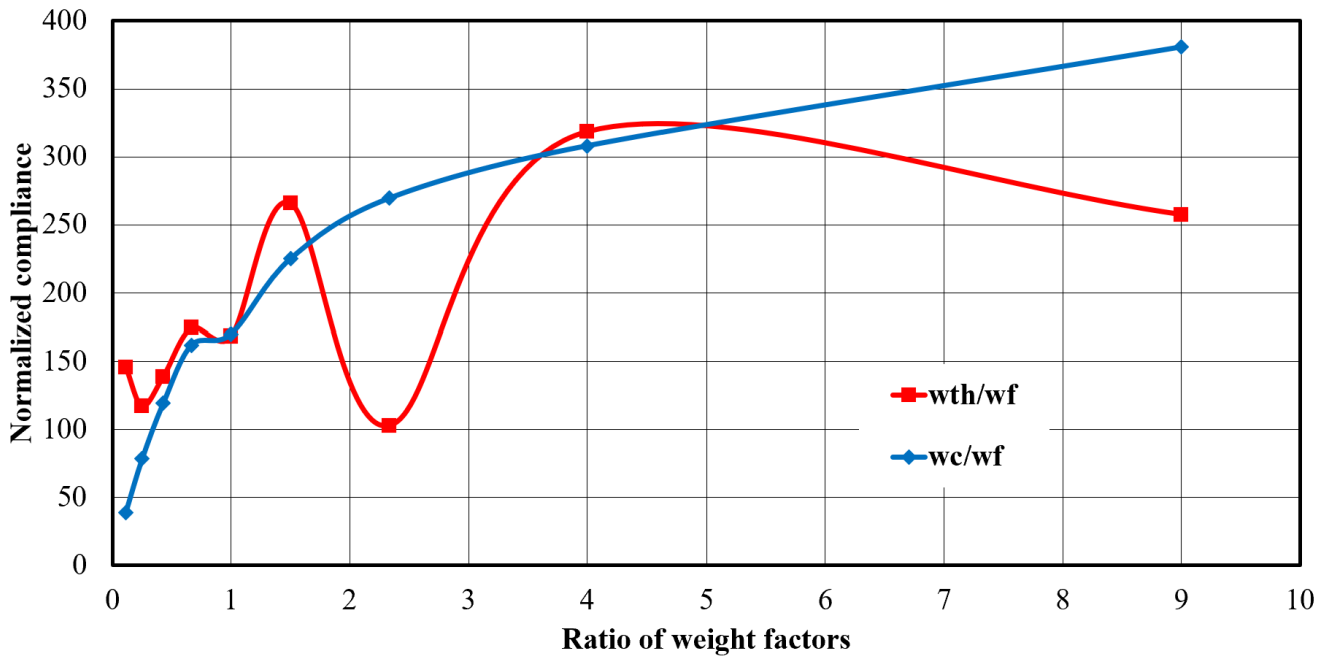
Figure 5.14: Effects of weight factor ratio on the normalized compliance for two pairs of loads

In Figure 5.14, the normalized compliance against $\frac{w_{th}}{w_f}$ can be described as a sinusoidal increase, therefore, fairly less predictable. However, a gradual increase is observed in the normalized compliance values as $\frac{w_c}{w_f}$ increases. This also further establishes the loads' contributions to optimization stability as observed in previous figures.

5.2.2.3. Tri-objective topology optimization for two design-dependent loads and one design-independent load.

Finally, the results of topology optimization for all loads on the rotating cantilever are presented in this section for $\eta = 0.8$ on TSL only. As in the previous section, the scale factors for sensitivity contributions from TSL and centrifugal loads are further scaled down to a factor of 10^{-1}. However, the maximum iteration number is reduced to 40 as further iterations caused more numerical instability with little topological changes. Three topological, scale, compliance, and sensitivity results each for low-, medium-, and high-value weight factors for TSL and centrifugal loads are presented.
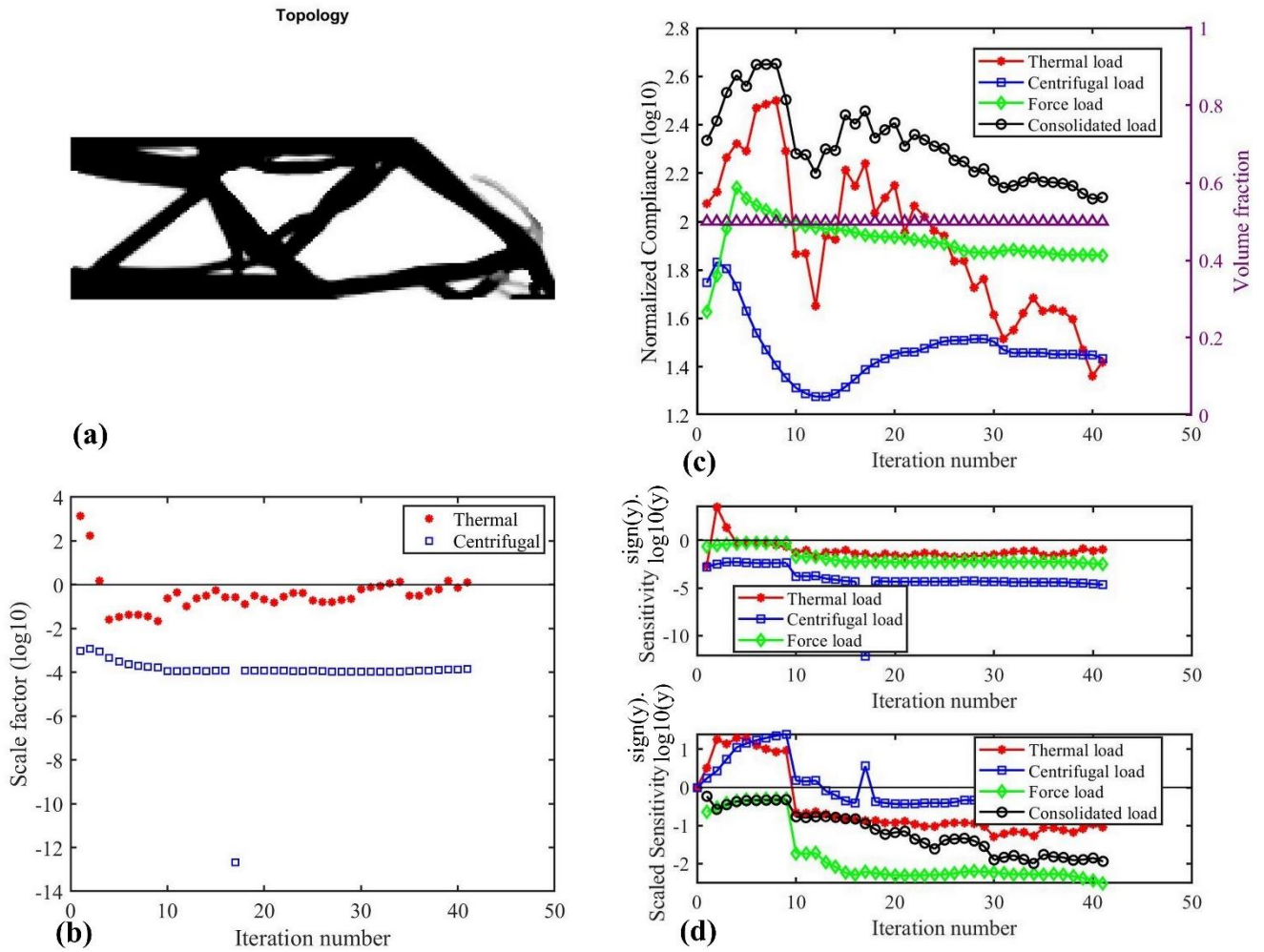
Figure 5.15: (a) Topology, (b) scale factor history, (b) normalized compliance history, and (c) sensitivity history for the cantilever problem for $w_{th} = 0.1, w_c = 0.1$ and $w_f = 0.8$.
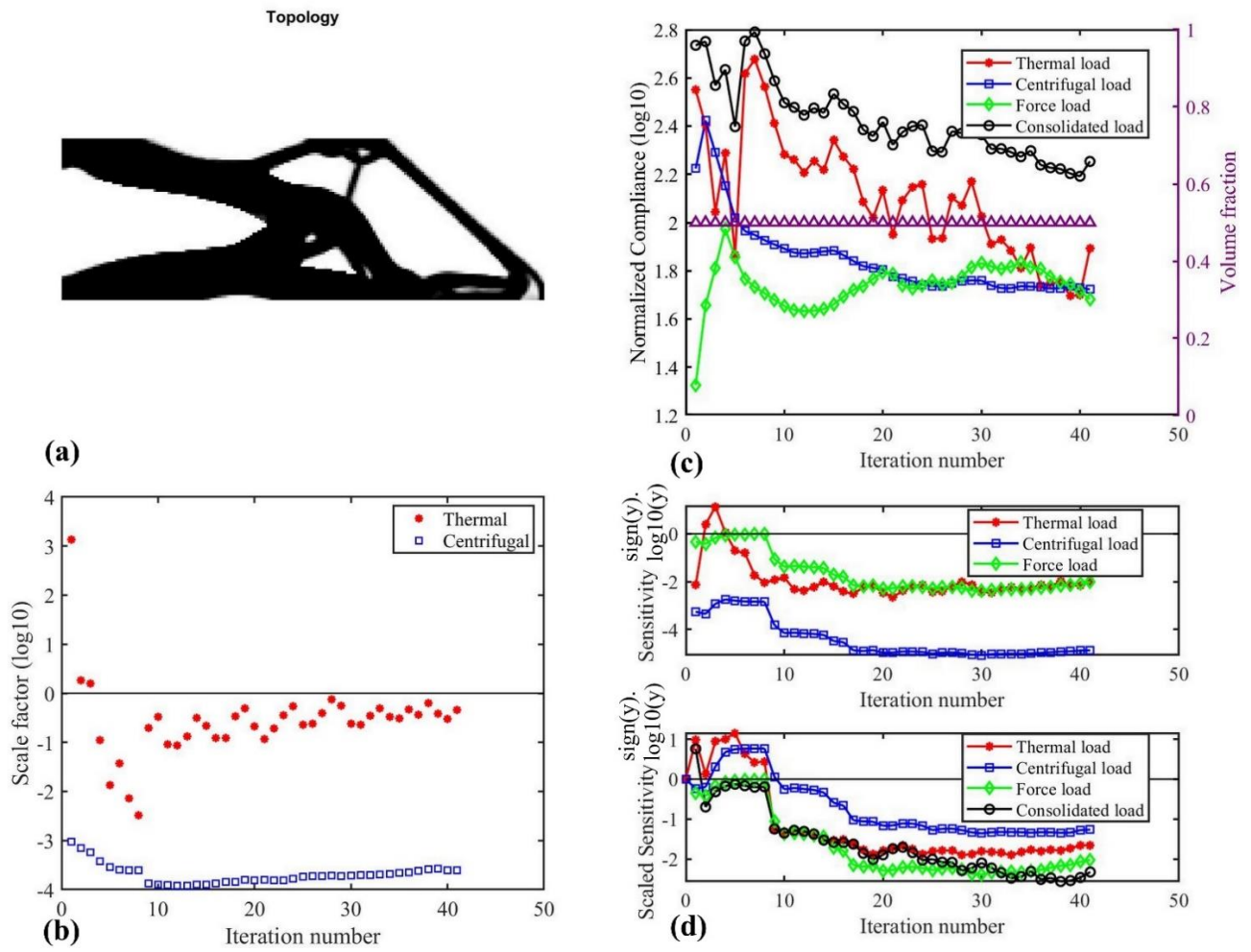
Figure 5.16: (a) Topology, (b) scale factor history, (b) normalized compliance history, and (c) sensitivity history for the cantilever problem for $w_{th} = 0.3, w_c = 0.3$ and $w_f = 0.4$.
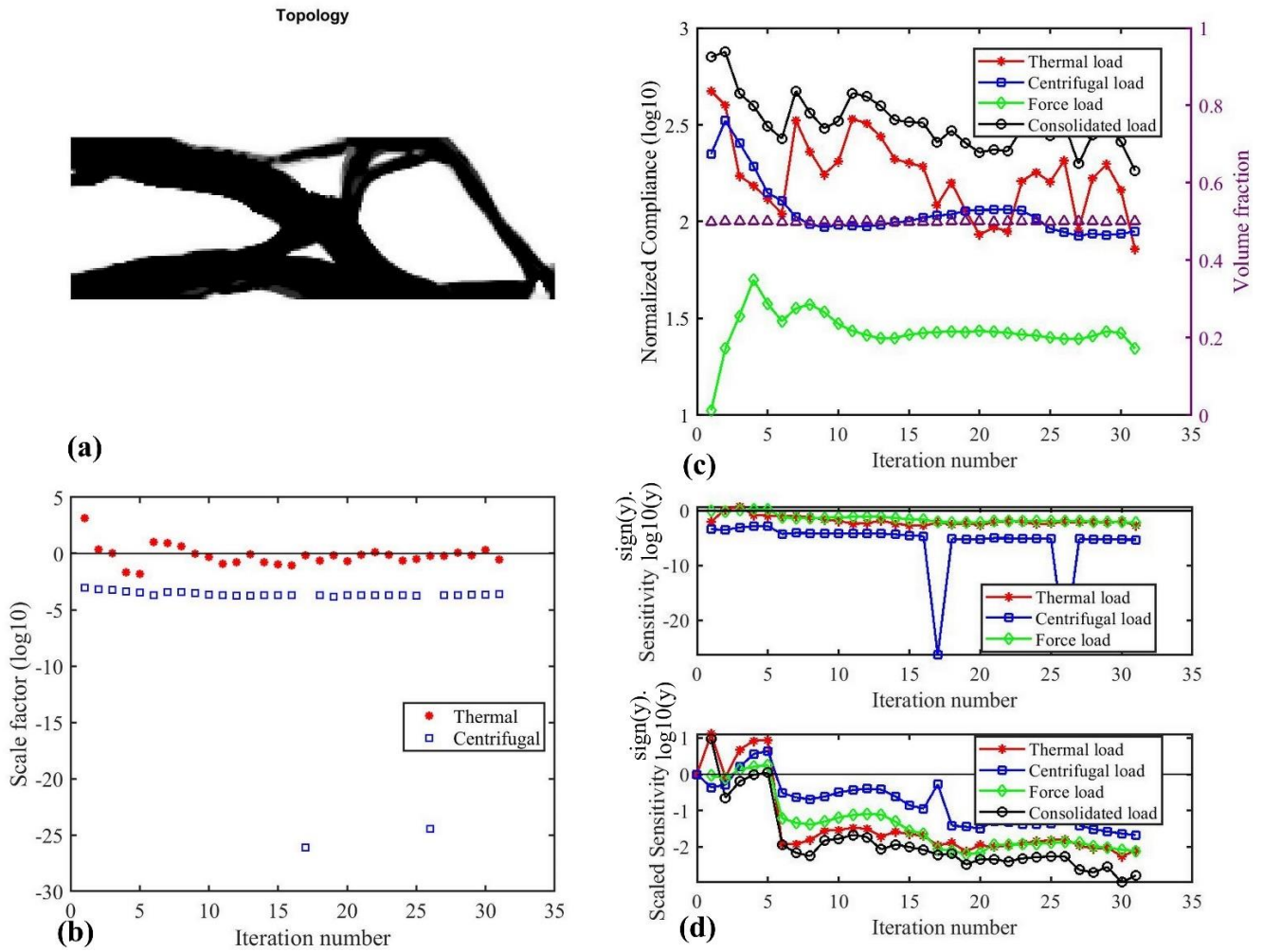
Figure 5.17: (a) Topology, (b) scale factor history, (b) normalized compliance history, and (c) sensitivity history for the cantilever problem for $w_{th} = 0.4, w_c = 0.4$ and $w_f = 0.2$.

For the optimization of all three loads shown in Figure 5.15 to Figure 5.17, compliance minimization is best at low weight factors of design-dependent loads; also, the final normalized compliance slightly increases as their weight factors increase. This minimization considering all three loads using the regular OCM optimizer will be impossible without scaling the sensitivity contributions of design-dependent loads. As observed in previous sections, the scale factors for TSLs are relatively closer to 1 while those for centrifugal loads are in the range of $0 < \Upsilon_c < \Upsilon_{th} < 1$. This implies that the centrifugal sensitivities are higher in magnitude than TSL sensitivities as observed in Figure 5.15(d), Figure 5.16(d), and Figure 5.17(d). As a result of sensitivity scaling, the force sensitivities are kept the lowest throughout the optimization ensuring numerical stability and a definite structural layout.

Finally, for this section, the full weight factor variation is presented in Figure 5.18 by plotting the normalized consolidated compliance function against the weight factor ratios $\frac{w_{th}}{w_f}$ and $\frac{w_c}{w_f}$ for all loads considered in this study.
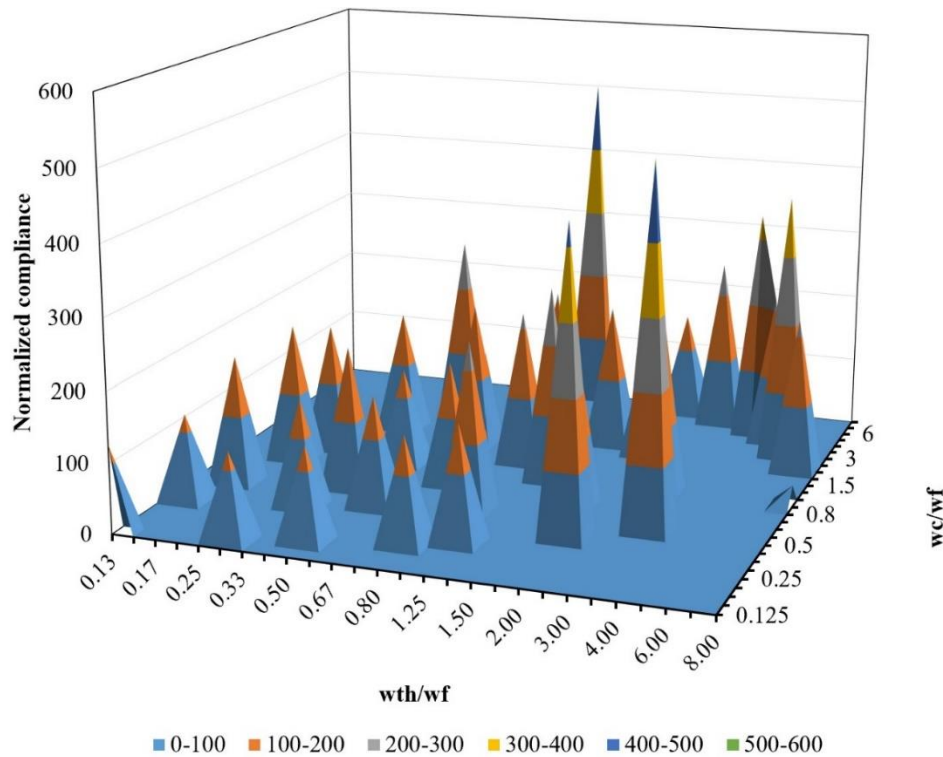
Figure 5.18: Effects of weight factor ratio on the normalized compliance for all three loads combined

In Figure 5.18, lower weight factors for TSL and centrifugal loads give considerably lower normalized compliances as their height maps are lower. However, there are some higher combinations of weight factor ratios that can give relatively low compliance values. This might be a result of the sinusoidal trend for $\frac{w_{th}}{w_f}$ when considering TSLs and point force only as observed in Figure 5.14.

5.2.2.4. Tri-objective topology optimization for TSLs, centrifugal loads, and design-dependent pressure loads.

To apply the developed methodology to a practical design scenario, the labyrinth seal mounted in the balancing drum of a steam turbine is studied. This is a suitable example because the loads on the seal are a high-temperature distribution, boundary fluid pressure, and a high rotational speed. Cangioli et.al. [184] studied a thermo-elastic bulk flow model on labyrinth seals and they outlined a list of practical values for these loads, therefore, they will be adopted here also. Figure 5.19 shows the location of the seal on the steam turbine shaft and a model of a labyrinth seal in (a). The figure also shows the free body diagram of a cross-section of the seal in (b) which will be used for topology optimization. Some material properties assumed for this study are density $\rho_0 = 8220 \ kg/m^3$, linear thermal expansivity $\alpha_0 = 1.6 \times 10^{-5}/K$, and Young's Modulus $E_0 = 190 \ GPa$. The design specification consists of a '*teeth-like*' feature at the top of the domain that must be present in the final topologies. Therefore, this feature is left preserved throughout the optimization process. As in the previous example, it is assumed that no plastic flow is induced as a result of the applied loads, therefore, the FEA is carried out under linear elastic conditions. For this problem, 8960 elements were used, the volume fraction target is 0.4, and a RAMP penalization factor of 40 was used. The consolidated normalized compliance in 5.24 and sensitivity function in 5.30 remain the same with subscript p (for pressure) replacing f.

s

(a)   **(b)**
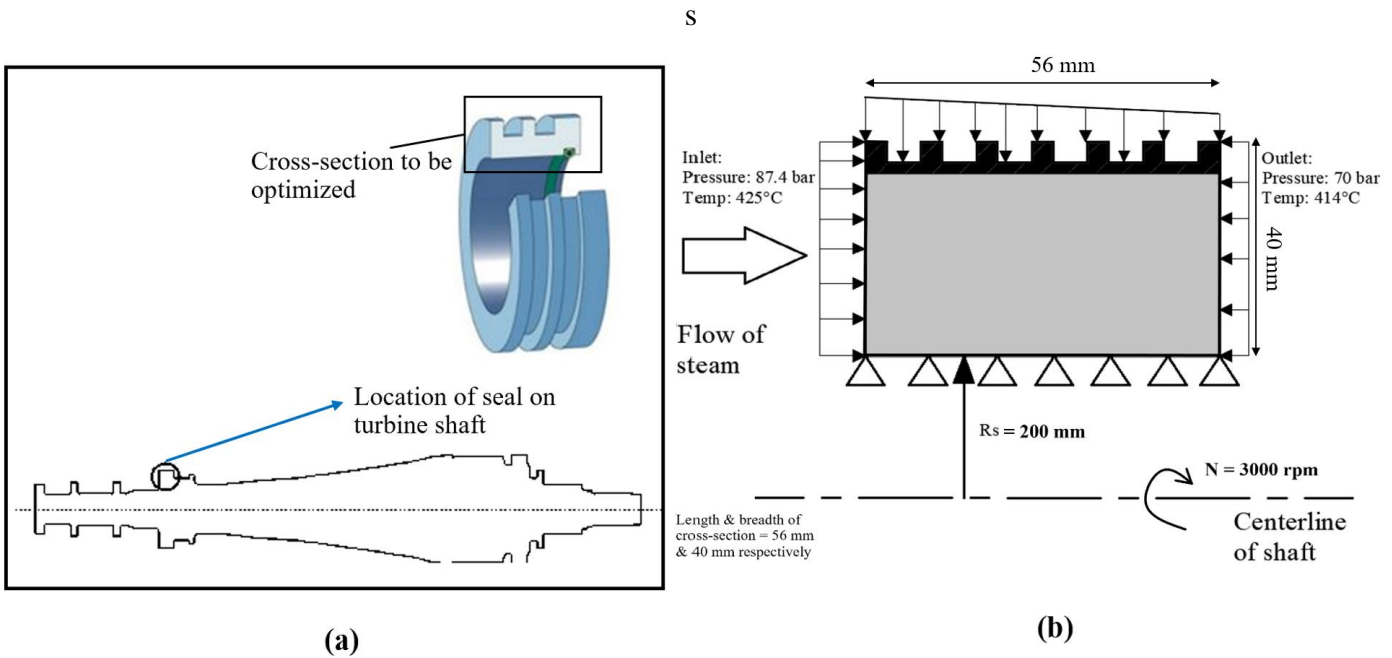
Figure 5.19: (a) The location of a labyrinth seal on a turbine shaft [169] and a model seal [170], (b) free-body diagram of a cross-section of the seal showing the loads and boundary conditions.

100

First, steady-state thermal analysis is carried out on the seal, and the distribution is seen in Figure 5.20.
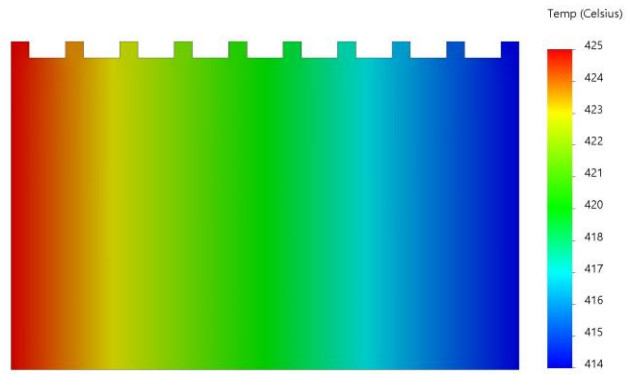
Figure 5.20: Temperature distribution of labyrinth seal
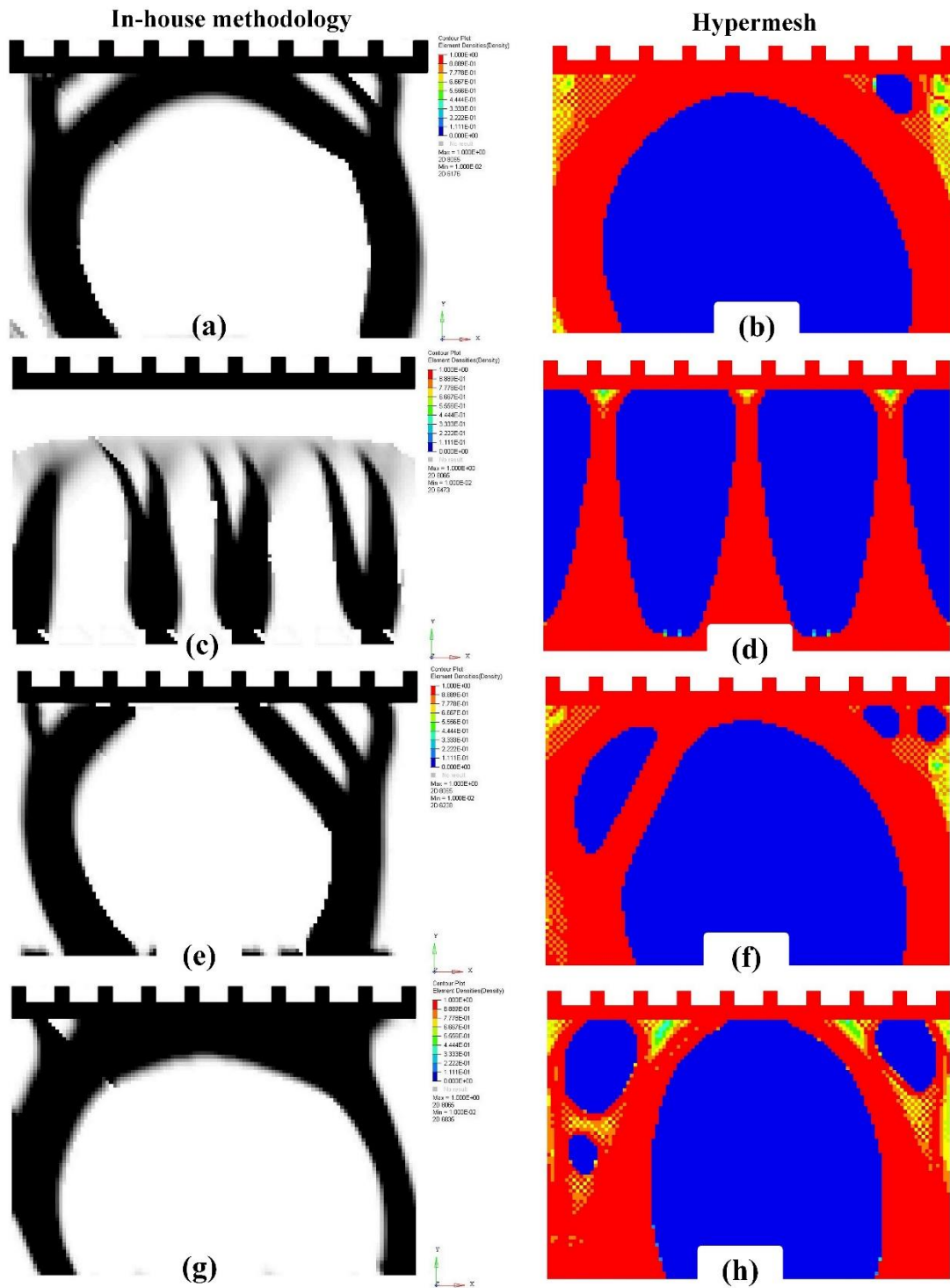
Figure 5.21: Resulting topologies for TSL, centrifugal, and pressure loads for (a) in-house, $w_{th} = 0, w_c = 0, w_p = 1$, (b) Hypermesh $w_{th} = 0, w_c = 0, w_p = 1$, (c) in-house, $w_{th} = 0, w_c = 0.9, w_p = 0.1$, (d) Hypermesh $w_{th} = 0, w_c = 1, w_p = 0$, (e) in-house $w_{th} = 0, w_c = 0.1, w_p = 0.9$, (f) Hypermesh $w_{th} = 0, w_c = 10, w_p = 1$, (g) in-house $w_{th} = 0.15, w_c = 0.2, w_p = 0.65$, (h) Hypermesh, $w_{th} = 1, w_c = 25000, w_p = 110$.

In Figure 5.21, the topological results are obtained from the in-house developed methodology and a commercial FEA/structural optimization software – Hypermesh by Hyperworks®. For the in-house methodology, black is solid and white is void while for Hypermesh, red is solid, and blue is void. Although there are many key similarities between both methodologies, there are very important differences also. A major difference is the fluid pressure effect on the final structure. As presented in Chapter 4 and several works of literature [71], [75], [185]–[188], design-dependent pressure loads leave arch-like features or structures on the external surfaces they act on. Although this is observed in the results from the in-house development methodology, they are absent from the results obtained by Hypermesh. Due to this fact, several intermediate elements are sticking to the left and right edges of the initial domain which might cause difficulties when attempting to interpret the results for further studies/use. For almost pure centrifugal loads in In Figure 5.21(c) ($w_{th} = 0, w_c = 0.9, w_p = 0.1$), there is a disconnection between the bottom and top features; this is possible because there is no structural boundary condition on the top features (the teeth) and since the weight factor for centrifugal loads is much higher than others, more material is deposited closer to the axis of rotation thereby cutting off the preserved teeth.

Finally, very large weight factors such as $w_c = 25000$ in Figure 5.21(h) are used in Hypermesh to balance out the sensitivity and compliance values for numerical stability. This is unnecessary in the in-house methodology because of sensitivity scaling. Conclusively, there are several differences between the in-house methodology and Hypermesh; first, the scaled sensitivity approach is absent in Hypermesh, secondly, they use the SIMP function as opposed to the RAMP which is widely recommended for design-dependent loads, thirdly, they utilize design-independent pressure loads. Additionally, differences in the optimizers used can cause disparities in the final compliances and consequently the topologies.

5.3.   Summary

A multiobjective topology optimization methodology has been elaborated for either a mix of design-independent and design-dependent loads or only design-dependent loads. First, a Pareto front was implemented on a simple cantilever problem with 2 load cases to show the essence of weight factors in multiobjective topology optimization. Next, the developed methodology was presented. In addition to thresholding loads with high magnitudes and irregular nodal load directions as elaborated in Chapter 3, sensitivity scaling is introduced to ensure the sensitivities from loads that lead to numerical instabilities in the optimizer are comparable to those that are more stable. This ensures that weight factors are kept between 0 and 1. To show the effectiveness of the proposed methodology, two design cases were studied. The first case study was a rotating cantilever subjected to an elevated temperature distribution and a point force. An extensive study was carried out on a pair of design-dependent and design-independent loads, as well as all three loads combined. The second case study was on a labyrinth seal in a steam turbine. The design problem was topologically optimized by the in-house methodology and Hypemesh. Finally, comparisons were made with results from Hypermesh. Results between both methodologies showed a good basic correlation while significant topological differences were observed in the effect of pressure loads. For both case studies, adopting lower weight factors (typically below 0.5) for TSLs and centrifugal loads contributed to less numerical instabilities while resulting in lower compliance values and more distinct/practical structural topologies.

Chapter 6: A Post-Topology Optimization Process for Overhang Feature Elimination in Additive Manufacturing.

6.1.   Introduction

This chapter is focused on developing a new, fast, and efficient post-topology optimization process for overhang feature elimination in additive manufacturing. As overhanging features directly impact down-skin surface roughness and overall printability; they are strong justifications for gaining arguably the most attention of all structural-based manufacturing constraints from researchers. In this new post-topology optimization method, every stage of transforming theoretically optimal structures to manufacture-enabled structures from the identification of unsupported features to the introduction of support-free trusses is done within the density voxel field of the optimized topology. Also, to eliminate the increase in material volume which naturally characterizes post-topology optimization methods, a volume correction stage is included and is optional depending on the user's preferences. Another key importance of post-topology optimization methods is their independence from optimizers, interpolations functions, and other 'tuning' parameters that may affect the optimization process. The overhang elimination process will be presented for 2D cases in this article and will be extended to 3D cases in the future.

6.2   Description of methodology

This study is primarily predicated on the use of Laser Powder-Bed Fusion (LPBF) AM as the manufacturing technology but can be extended to Fused Deposition Modelling (FDM). LPBF, as shown in Figure 2.2, uses metal powder in a bed as feedstock which a laser selectively scans layer by layer (likened to a micro-welding process [189]) till the part is completely printed [190], [191]. One of the foremost design rules for this technology is introducing sacrificial supports for overhanging features with inclination angles less than 40° to the build plate for print success [192] and also for limiting poor surface roughness on the down-skin [193], [194]. Leary et. al. [195] identified three distinct zones for overhanging features in FDM: Robust zone, $\phi \geq 40°$ with features having no identifiable defect, Compromised zone, $30° \leq \phi < 40°$, with features having identifiable defects and Failed zone, $\phi < 30°$ with features that are completely not self-supporting. In many cases, the minimum overhanging feature

angle applied during pre-processing for LPBF and FDM printing can range between 35° and 50°. In the current methodology, support trusses inclined at a specified minimum angle are introduced into the optimized topology in unsupported areas. This process is explained in the following sub-sections:

6.2.1 Detecting overhanging features

The process of detecting overhanging features is done in two major steps: first, identifying the boundary of the topologically optimized design using mesh nodes, and second, extracting nodes from boundary nodes that define overhanging or unsupported features according to an imposed self-supporting angle threshold. The density-based gradient topology optimization method is adopted in this study and homogenous, uniform four-noded quads are the element type.

6.2.1.1 Boundary Identification

The topological boundary is defined by boundary nodes that are selected by comparing the mean density of elements around a mesh node with a threshold value. As observed in Figure 6.1, node n is surrounded by elements with density $x_{n,i}$; the mean density value, $\bar{x}_{n,i}$ is used to compare with a threshold density value f_{th}. If $\bar{x}_{n,i}$ is lower than f_{th}, node n is selected as a boundary node. f_{th} in this study is 0.1 and it can be tightened or relaxed depending on the contrast of the topological boundary. Furthermore, for optimal designs that might have a significant number of intermediate density elements $(0 < x < 1)$, elements $x_{sn,l}$ associated with nodes Sn surrounding node n are also used in the selection of boundary nodes. $x_{n,i}$ is a vector of density elements surrounding node n for i ranging from 1 to 4 for 2D quadrilateral elements and 1 to 12 for 3D hexahedral elements while $x_{sn,l}$ is the corresponding vector of density elements surrounding node Sn for l from 1 to 4. For every node n, there are four Sn nodes in the 2D domain and six in the 3D domain. Boundary nodes in a 2D domain can be chosen by the selection criteria:

$$ bn = \begin{cases} \text{Node } n & \langle \forall (\bar{x}_{sn,l} < f_{th}) \in [1,2] \rangle \parallel \langle \{ \forall (x_{n,i} > 0) = 2 \} \wedge (\bar{x}_{n,i} > f_{th}) \rangle \\ 0 & \text{any other case} \end{cases} \quad (6.1) $$
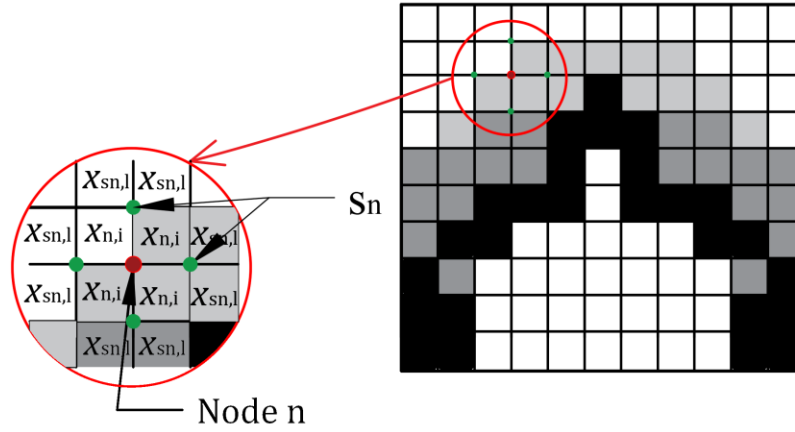
Figure 6.1: Identifying a boundary node and its surrounding nodes in a topological boundary

6.2.1.2 Identifying unsupported features

The angles subtended by the tangents to the topological boundary at every boundary node obtained in 2.1.1 are computed. Using an optimized half MBB beam, these tangent angles defined in (6.2) are graphically described in Figure 6.2.

$$\theta_{bn} = \tan^{-1}\left(\frac{v_2 - v_1}{u_2 - u_1}\right) \qquad (6.2)$$
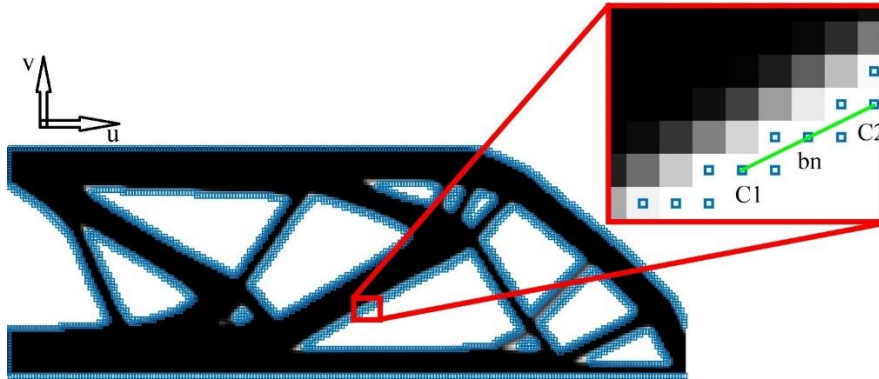
Figure 6.2: Boundary nodes (blue squares) of an optimized design with an enlarged portion showing coordinates C1 (u_1, v_1) and C2 (u_2, v_2) of the line tangent at a node bn.

In (2), for a boundary node bn, C1 (u_1, v_1) is the cartesian coordinate of the closest node (apart from those that are one element away from bn along $\vec{u}$) on the left of bn; the same analogy follows for C2. Equation (2) is calculated for all boundary nodes and each angle is compared with the overhang angle threshold. To select nodes that define overhanging edges or surfaces, the selection criteria are applied:

107

$$ovn = \begin{cases} \text{Node } bn & \{(\theta_{bn} < \theta_{thresh}) \wedge (\bar{x}_{bn+\xi,i} < 0.1f_{th})\} \\ 0 & \text{any other case} \end{cases} \tag{6.3}$$

In (3), ovn is a set of nodes that define overhanging edges, θ_{thresh} is the feature inclination angle limit or overhanging angle threshold while ξ is a small movement from a node in ovn to another mesh node vertically downwards. The parameter ξ which is elaborately described in [185] is in this study assigned as two nodes away from the ovn node under investigation in the downward vertical direction. Overhanging features in the optimized topology in Figure 6.2 can be observed in Figure 6.3 for a 45° angle threshold. To maintain a definite edge in the overhanging regions, a continuous connection of the overhanging nodes is made as observed in the enlarged portion of Figure 6.3. We recall that the overhang nodes, ovn are drawn from boundary nodes bn which are located at the element vertices or mesh grid of the design domain. Moving forward, these nodes are repositioned to element centers for convenience. An overhang node is moved from its mesh point to the center of the element located at the top right side of the mesh point.
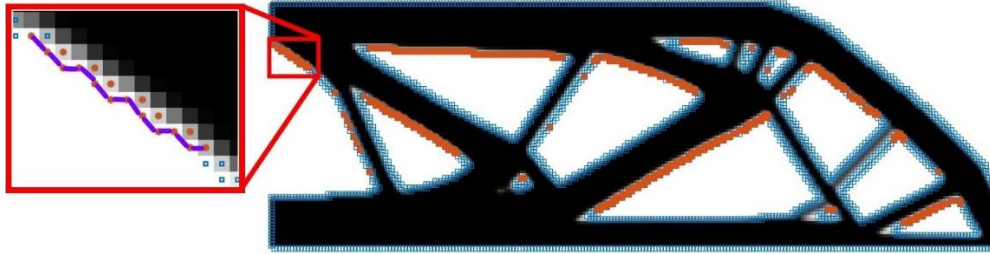
Figure 6.3: Nodes in orange showing overhanging edges for the optimized topology in Figure 6.2. the enlarged region shows an edge connection made in purple

Once unsupported features are identified, the next step of adding self-supported trusses is initiated.

6.2.2 Introducing support-free trusses

To introduce support-free trusses into an optimized topology, geometrical forms of topology optimized designs against overhang elimination in literature are first analyzed. Most of these studies in literature have results with geometrically similar internal features [101], [196], [76], [197], [198], [98]. Results from three studies [76], [197], and [196] are shown in Figure 6.4.
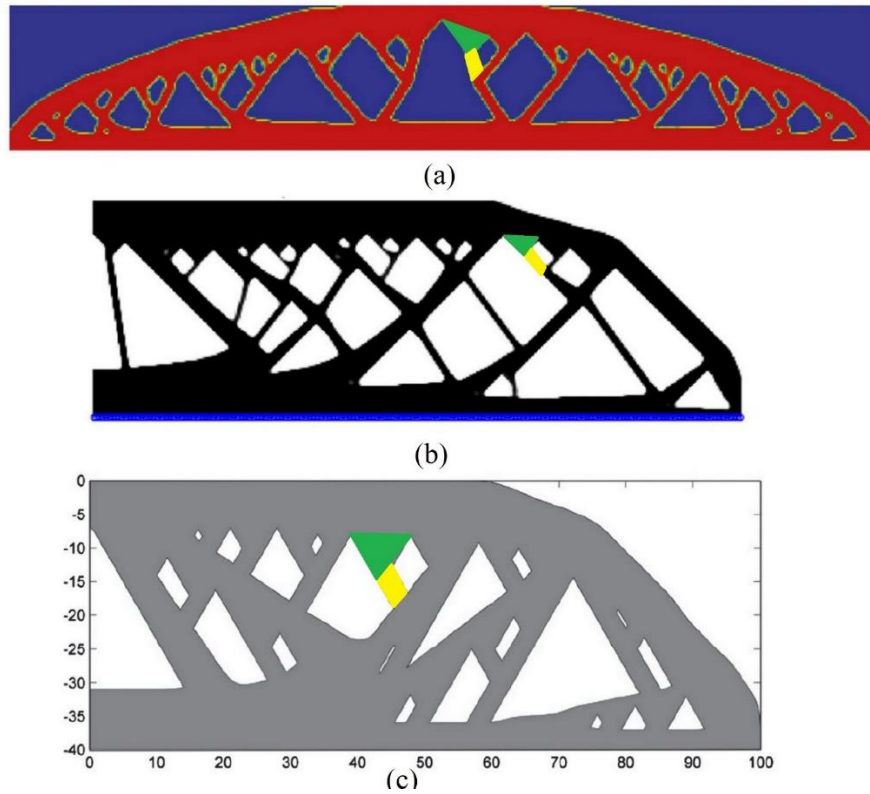
Figure 6.4: Optimized topologies considering overhang elimination from studies by (a) Gaynor and Guest [13], (b) Langelaar[14], (c) Leary [16]. Similar geometrical internal structures are highlighted in green and yellow

The geometrical similarities in Figure 6.4 can be observed in the internal features which consistently have two parts: the highlighted green portion which will be designated as a 'root' and a yellow portion designated as a 'stem'. A combination of the root and stem will represent a self-supported truss member to be introduced in an unsupported optimal topology for overhang elimination. Therefore, the focus will be drawn on designing this root and stem for every truss member.

i.   Designing the root: In the enlarged portion in Figure 6.3, the nodes that form the edge connection are used to define the new truss's root and these nodes are shown in Figure 6.5(a) again. The base length of the root is determined by two nodes which are a distance χ nodes apart, in Figure 6.5(a), χ is 5 nodes. Invariably, a longer χ translates to a larger truss root while a shorter χ to a smaller truss root. The angle of inclination of a line joined by these two nodes is calculated and will be designated as θ_χ. If the overhang angle threshold is θ_{thresh}, as shown in Figure 6.5(b), projections of $\theta_{thresh} - \theta_\chi$ and $\theta_{thresh} + \theta_\chi$ are made on the design elements from the two nodes. The elements in the intersection (Figure 6.5(c)) of these projections form

109

the truss root in Figure 6.5(d) and are assigned as solids with a density value of 1. All elements that form the root of the self-supported truss are shown in green in Figure 6.5.

ii.   Designing the stem: First, the lowest element in the root is identified, then all other elements inclined at approximately θ_{thresh} downwards from this element are identified and assigned as solids (Figure 6.5(e,f)). The direction of projection from the lowest element is made the same as that of the overhang nodes for the first support-free truss on the overhanging feature. As observed in Figure 6.5(g), this direction is changed for the next truss stem but the same angle θ_{thresh} is maintained.
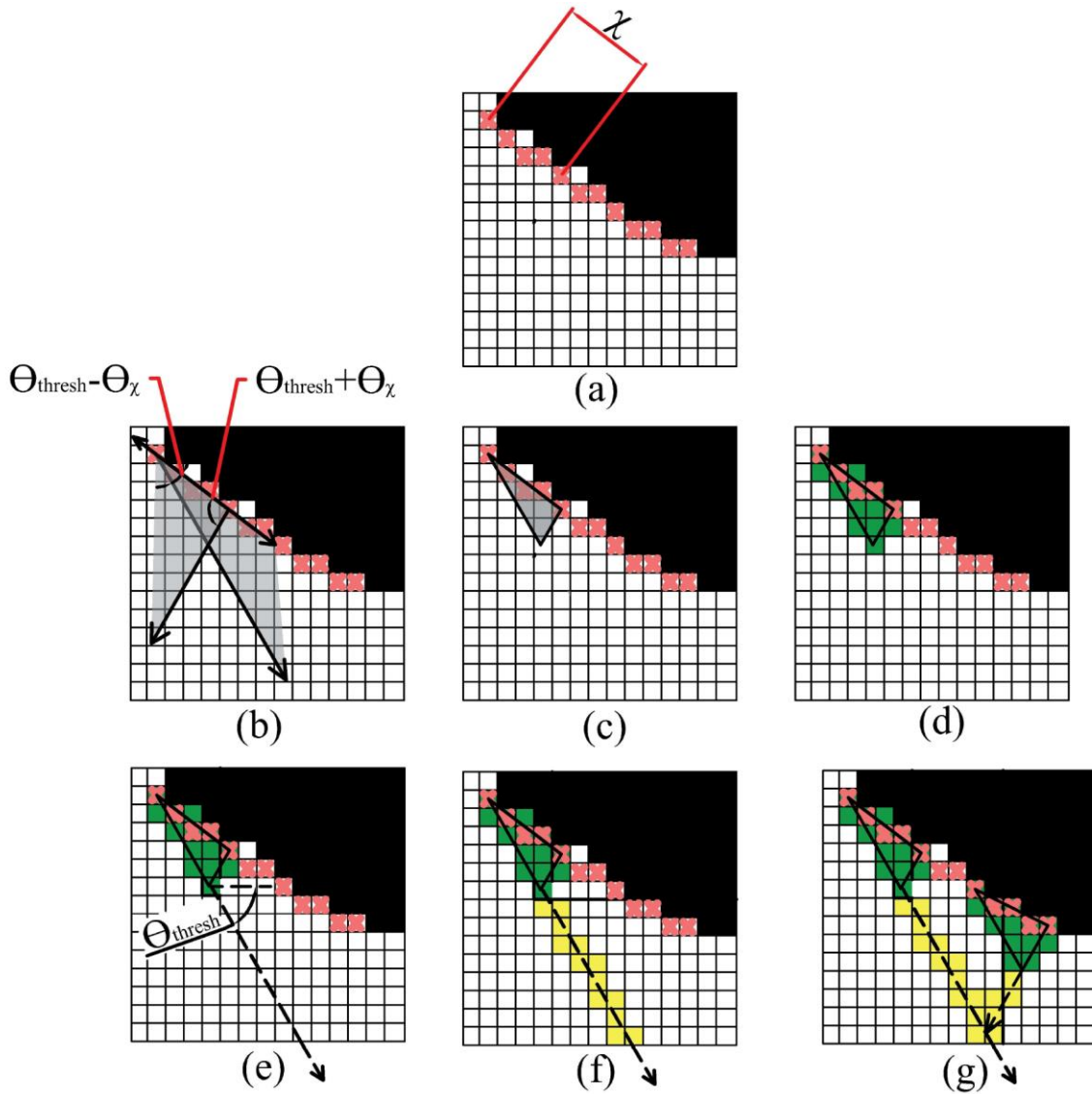
Figure 6.5: Stages in modeling support-free trusses for an overhanging feature. (a-d) modeling the root (e,f) modeling the stem (g) introducing a second truss

110

From the aforementioned steps, we can expect a 'checkerboard' density distribution of the additional support-free trusses as shown in Figure 6.5(g), therefore further fine-tuning is carried out to obtain smoother boundaries. The densities of elements that define the support-free trusses are filtered in (6.4) and thresholded by a Heaviside function in (5).

$$\tilde{x}_{st} = \frac{\sum_{j \in N_{st}} H_{st,j} x_j}{\sum_{j \in N_{st}} H_{st,j}} \tag{6.4}$$

$$\hat{x}_{st} = 1 - e^{-\beta \tilde{x}_{st}} + \tilde{x}_{st} e^{-\beta} \tag{6.5}$$

While st denotes the additional support-free elements in (4) and (5), $\tilde{x}_{st}$ and $\hat{x}_{st}$ are the filtered and physical densities respectively of st elements, N_{st} is a set of neighboring elements whose center-to-center distance, $\Delta(st, j)$ to a support-free element is less than a specified filter radius, r_{min}. β is a regularization parameter that determines the thresholding severity of the Heaviside projection. $H_{st,j}$ is a weight factor for support-free elements expressed as

$$H_{st,j} = \max(0, r_{min} - \Delta(st, j)) \tag{6.6}$$

Figure 6.6 highlights the implementation of the proposed methodology which commences with obtaining an optimized topology for a particular design case in (a), then a boundary identification is done according to Equation (6.1) in (b). Thereafter, overhanging features are determined by identifying overhanging nodes from boundary nodes according to Equation (3) in (c), then support-free trusses are added underneath overhanging features following the procedure in Section 2.1.3 in (d), finally, a density filter and Heaviside projection are applied to the introduced support-free trusses in (e).
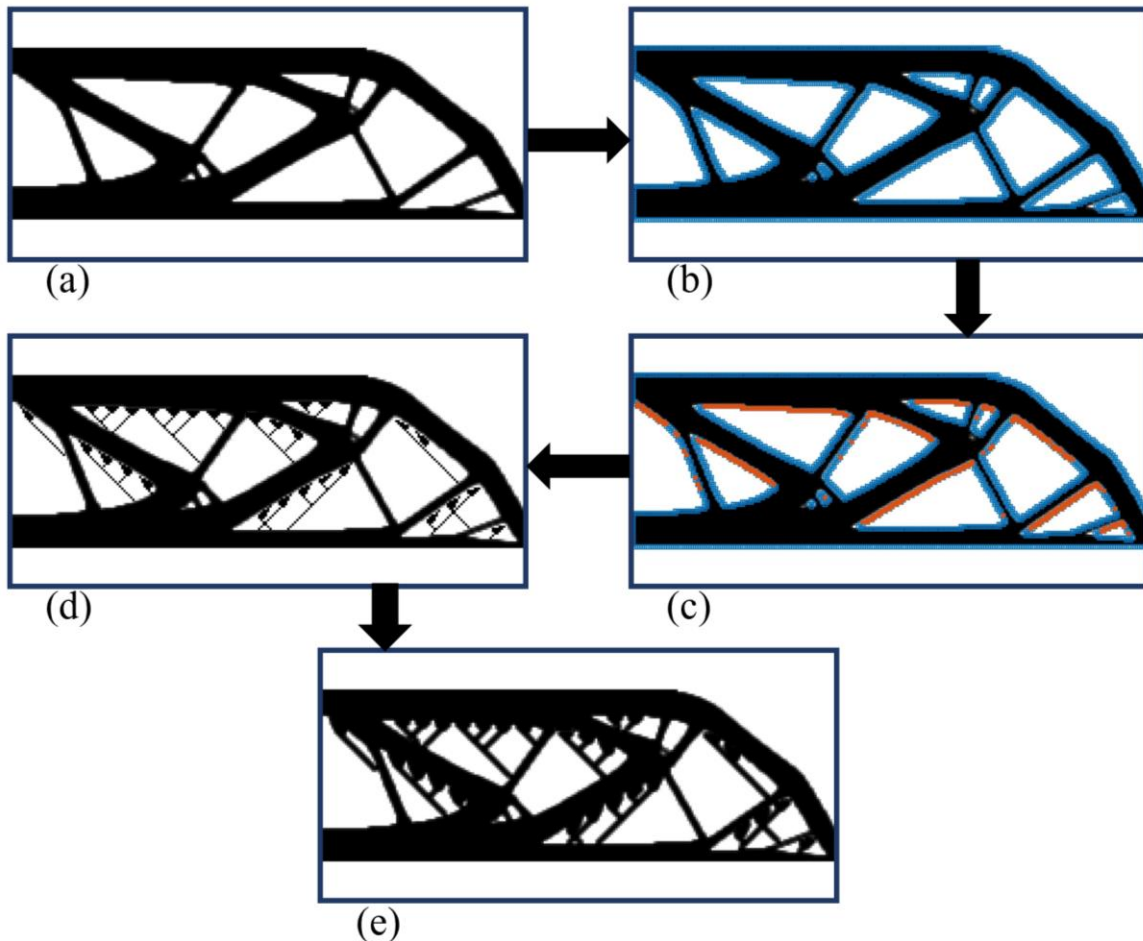
Figure 6.6: The post-process methodology showing the major stages (a) An optimized topology (b) boundary identification of optimized topology (c) identification of overhang features subtended less than 45° to the build plate (build plate is assumed to be just below the horizontal bottom surface of the structure)(d) inclusion of support-free trusses to identified overhanging features (e) applying the density filter and Heaviside projection to support-free trusses.

6.3   Numerical studies

To investigate the feasibility of the proposed methodology, a couple of design problems are topologically optimized with and without overhang elimination while examining some aspects of the post-T.O. process. First, overhang elimination considering volume correction is studied, second, the effects of feature size limitation and angle threshold on compliance and volume fraction of the resultant support-free structure are investigated. Finally, the proposed methodology's independence from material interpolation schemes and optimizers is studied while comparing the computational costs of key stages of the methodology with and without volume correction.

112

In this study, the Method of Moving Asymptotes (MMA) [199] and Optimality Criteria Method (OCM) are utilized as optimizers while Simple Isotropic Material with Penalization (SIMP) and Rational Approximation of Material Properties (RAMP) as material interpolation methods. The core strength of the proposed methodology, being a post-T.O. process, is its adaptability to any and every class of T.O. using uniform quad elements in a discretized domain.

6.3.1 Overhang elimination with volume correction

A consequence of adding support-free trusses to overhanging features is an increase in the desired volume fraction. In Figure 6.6, there is a 7% increase in volume fraction from (a) to (e). This volume increase potentially becomes larger when the truss thickness and/or angle are increased. For example, the increase in volume fraction in Figure 6.6 rises from 7% to 10% when the filter radius is increased from $4a$ to $5a$: a is half the length of a finite square element. Also, Leary et. al. [196] realized an over 30% increase in volume fraction for 60° support-free trusses. Therefore it is necessary to correct this volume fraction for designs subject to strict material requirements. To achieve this, a volume correction according to (7) is proposed and computed after the step in Figure 6.6(e)

$$f_{new} = f - \gamma(f_{old} - f) \tag{6.7}$$

f is the required volume fraction, f_{old} is the volume fraction after support-free trusses have been added, f_{new} is the new computed volume fraction for the forthcoming step and γ is a correction factor that typically ranges from 1 to 1.5 after several numerical investigations.

A second topology optimization process is done using the newly obtained f_{new} which gives a topology with a volume less than that of the original topology. Thereafter, steps (b) to (e) in Figure 6.5 are carried out to end up with a topology having a volume fraction closely matching the required value.

Table 6.1: Overhang elimination with and without volume correction for an optimized topology at different orientations. The red lines show the location of the build plate on the design.

Without volume correction	With volume correction
Without overhang elimination: $C_0 = 0.208 \, Nm, f_0 = 0.5$	
$C = 0.96C_0, f = 1.11f_0$	$C = 1.19C_0, f = f_0$
$C = 0.95C_0, f = 1.22f_0$	$C = 1.21C_0, f = 1.03f_0$
$C = 0.99C_0, f = 1.07f_0$	$C = 1.07C_0, f = f_0$

$C = 0.98C_0, f = 1.09f_0$ $C = 1.08C_0, f = f_0$
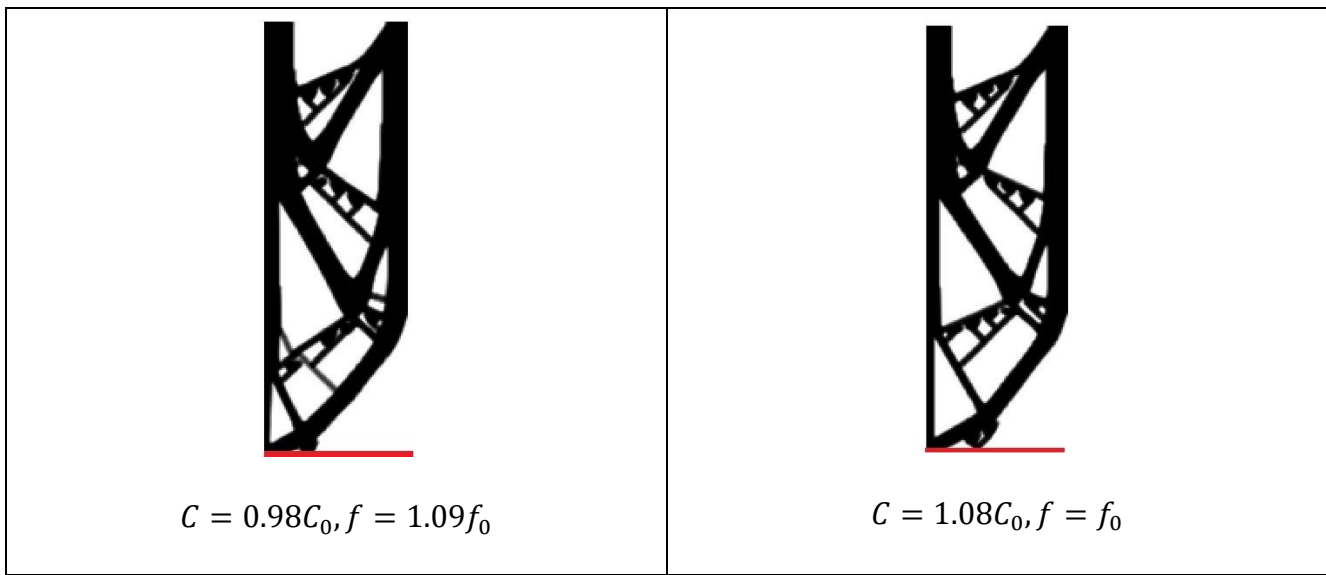
In Table 6.1, comparisons are made between overhang-restricted topologies with and without volume correction. We observe up to 22% increase without volume correction and after correction is done, the original volume fraction is maintained although slight changes may be obtained such as the 3% increase in the second orientation. A fallout from volume correction is an increase in compliance; this is expected because in attempting to correct the volume, a lower volume fraction is used in the second topology optimization process resulting in a higher compliance history compared to the first T.O. process as observed in Figure 6.7. Another observation from Table 6.1 is that part orientation greatly affects the volume of support-free trusses needed for overhang elimination and final compliance value. In Figure 6.7, although the compliance after the 1st T.O. process without volume correction is the lowest in all scenarios, there is a significant jump in the volume fraction. However, the volume fraction after the 2nd T.O. process with volume correction is right at the originally specified value while the compliance is at an intermediate value between the 1st and 2nd T.O. processes. Summarily, going for volume correction or not is dependent on which requirement between strength and volume is more stringent for the designer.
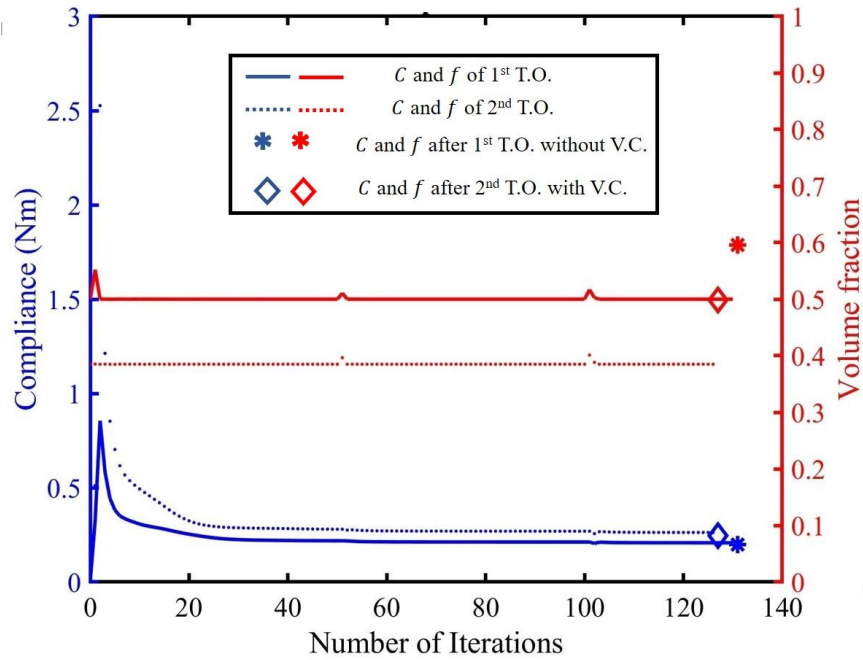
Figure 6.7: Compliance, C, and volume fraction, f history of topology optimization stages, and overhang elimination with and without volume correction. T.O. and V.C. mean topology optimization and volume correction respectively and the required volume fraction is 0.5

The basic workflow of this methodology is shown in the schematic diagram in Figure 6.8
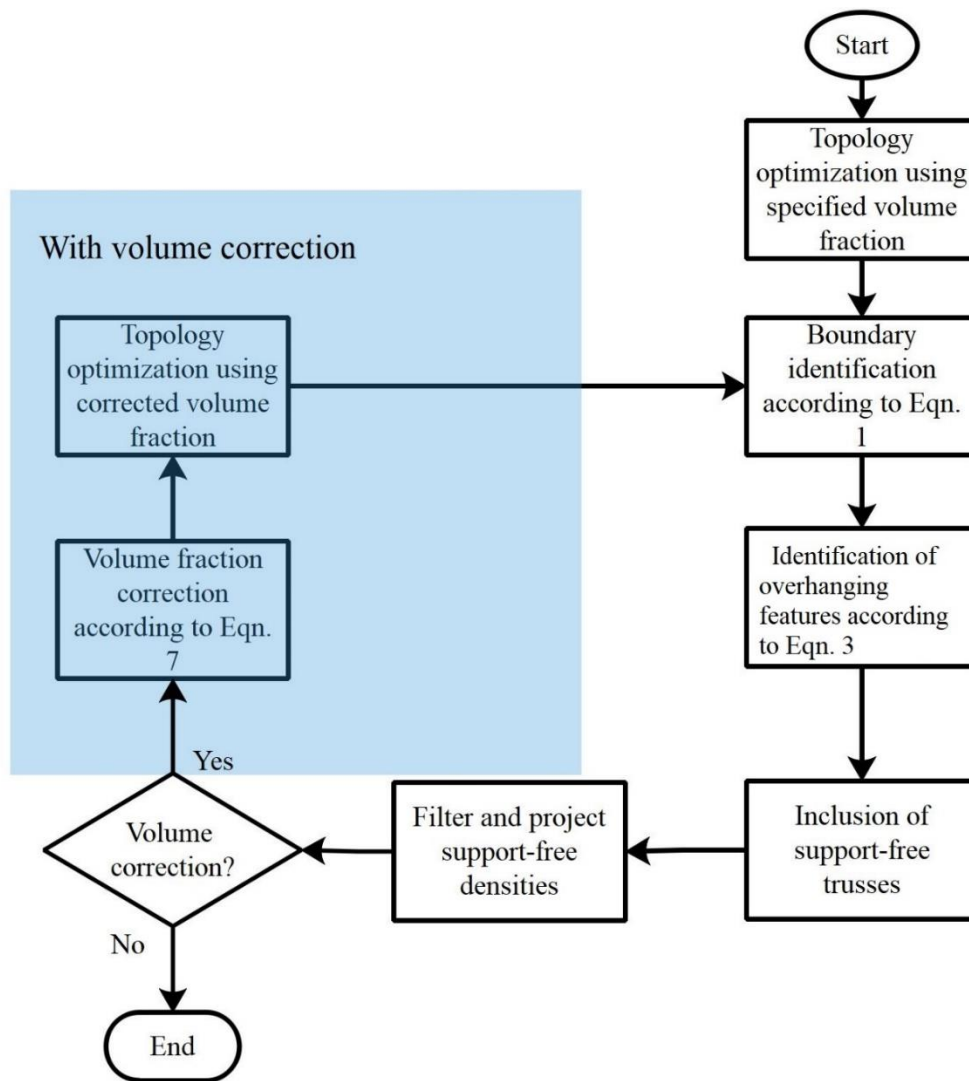
Figure 6.8: Workflow of post-topology optimization overhang elimination scheme

6.3.2 Effects of minimum feature thickness and angle threshold

In structural design for AM using T.O., controlling the minimum feature size is important because of manufacturability restrictions on the AM technology. Theoretically, the minimum feature size for LPBF can be as low as the laser's beam diameter but in practice, it should be a multiple of the diameter. In the case of FDM, in theory, minimum feature thickness can assume the size of the nozzle but in practice, an integer multiple is recommended [200]. Minimum values of 0.3 mm and 1 mm have been recommended for LPBF and FDM respectively [192], [200]. Likewise, the printability of overhanging features is dependent on the angle of inclination and AM technology. In literature, several research efforts ([76], [192], [201], [200]) have identified between 40° to 50° as the range of minimum angle threshold to successfully print overhanging features without support structures in LPBF and FDM. Notwithstanding,

this angle threshold can be varied depending on the feature thickness. Typically, smaller feature thicknesses can allow a relatively small feature to be printed at much lower angles ($< 30°$)[76] Nonetheless, this might increase the surface roughness of downfacing surfaces. It is, therefore, necessary to ensure feature thickness and angle of inclination are flexible parameters for a robust overhang elimination procedure. In this methodology, r_{min} and θ_{thresh} are the controlling parameters; Figure 6.9(a-b) shows different values of these parameters and how they influence compliance and corrected volume fraction.
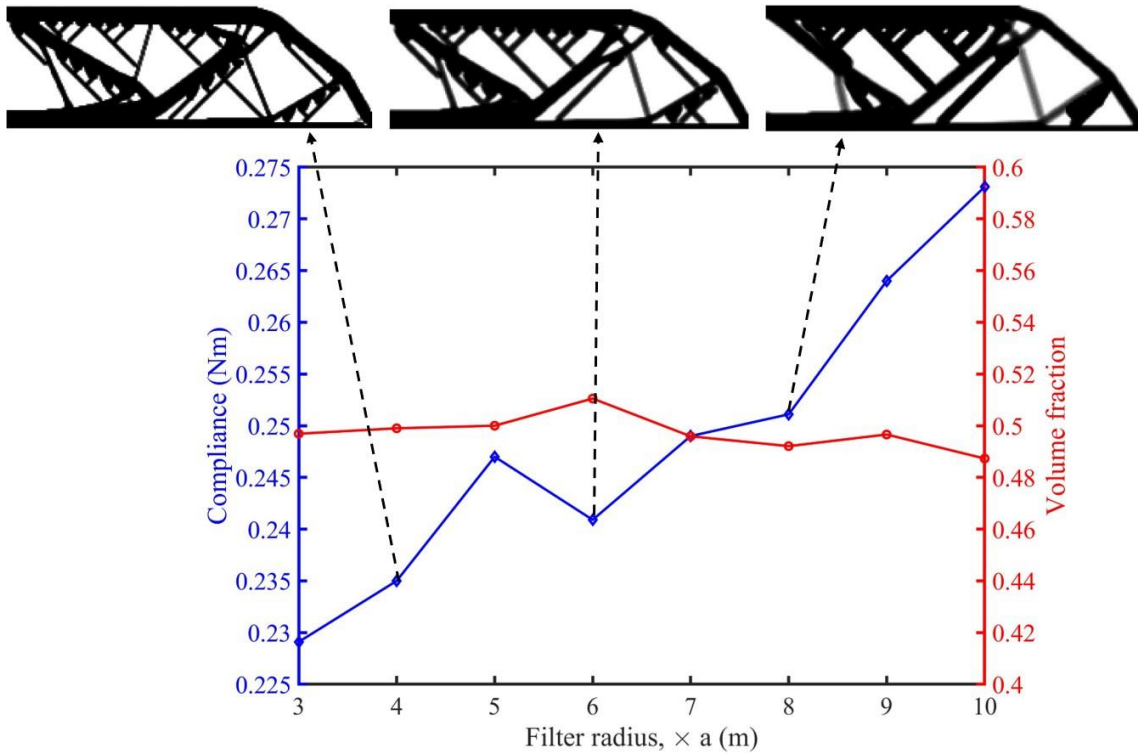
(a)
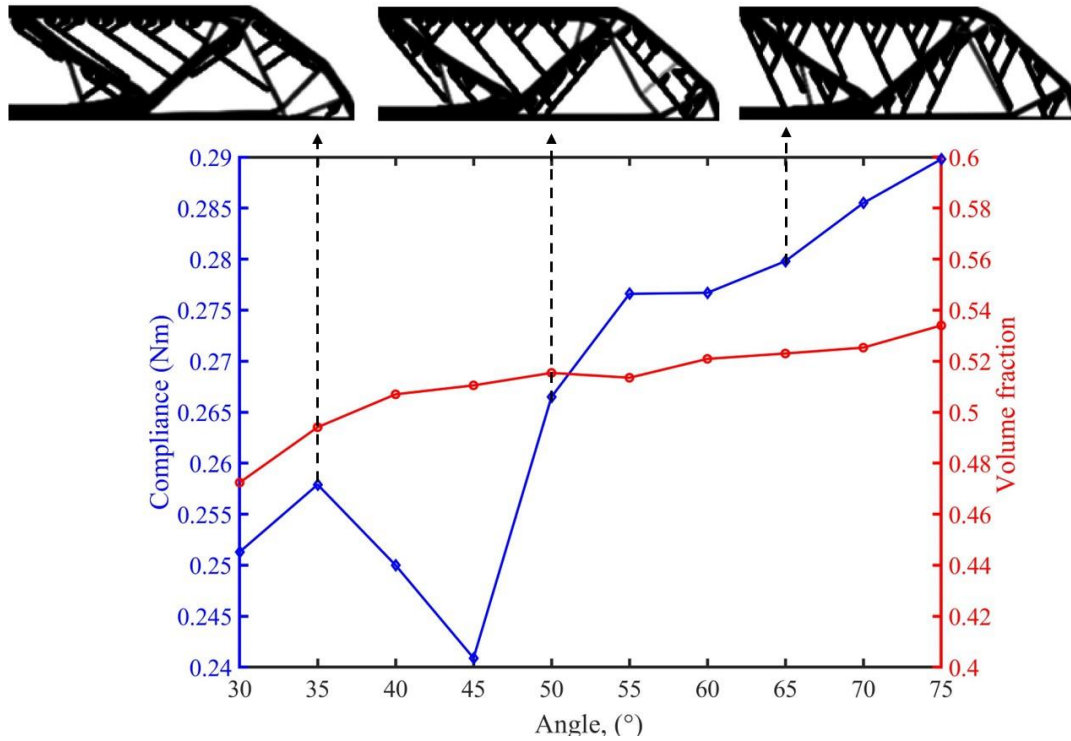
(b)

Figure 6.9: Effect of (a) filter radius and (b) overhanging angle threshold on compliance and volume fraction for γ=1.2. The filter radius is an integer multiple of half the finite element length, a.

We immediately observe that an increase in feature thickness and overhang angle threshold in Figure 6.9(a-b) translates to an increase in compliance. There is an approximately 19% increase in compliance in both cases from left to right because as feature thickness or angle increases, there is more material relatively assigned to the additional 'inefficient' trusses. This trend is not seen in volume fraction because it is a corrected parameter. However, there is a small increase in the volume fraction in Figure 6.9(b) but this can be adjusted by increasing the correction factor γ slightly.

6.3.3 Material interpolation methods and optimizers

An important characteristic of a post-process overhang elimination method is its independence from material interpolation schemes and optimizer types. Several studies have shown that the RAMP interpolation scheme compared to SIMP has proven to be more effective in handling thermo-mechanical and other design-dependent topology optimization problems [59], [56], [155], [202]. Also, optimizers for non-linear structural optimization vary in specific functionalities such as attempting to obtain global solutions and solving non-monotonic problems prevalent in thermo-mechanical topology optimization. When optimizing for these complicated scenarios, the computational cost is increased, and convergence

can become more difficult to attain. Therefore, rather than complicate already intricate topology optimization models with an integrated overhang elimination scheme, a post-process method becomes crucial. Using a different and more complicated hook design problem in Figure 6.10, the post-process method is used to show its independence from optimizers and material interpolation methods.
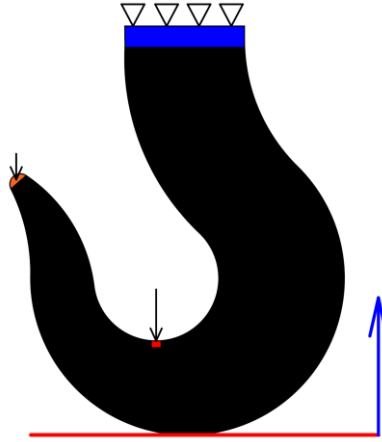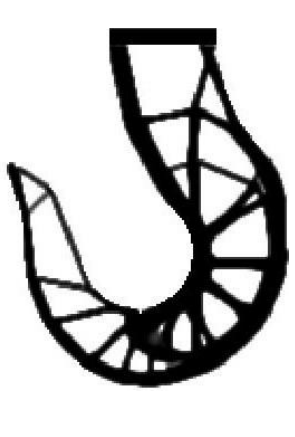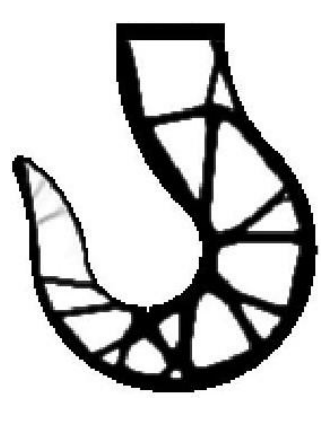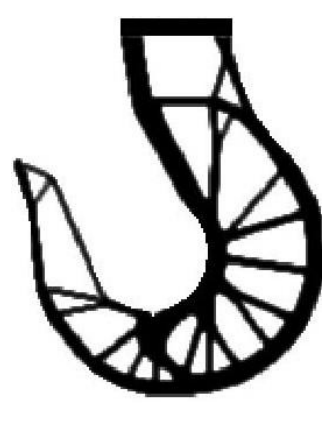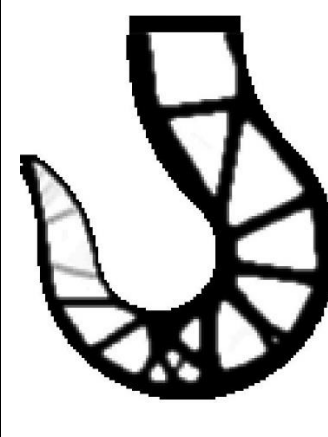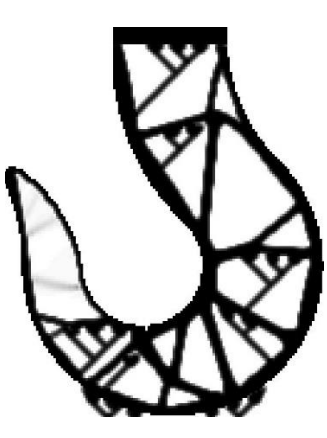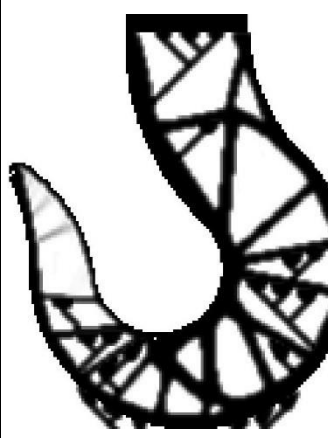
Figure 6.10: A hook design problem. Forces are shown in the black arrows, the build plate is shown in red, and the build direction in blue

Table 6.2: Optimized topologies with and without overhang elimination for optimizers (OCM and MMA) and material interpolation functions (SIMP and RAMP)

	OCM		MMA	
	SIMP	RAMP	SIMP	RAMP
Without overhang elimination				
With overhang elimination				

The resulting topologies without overhang elimination in Table 6.2 are all similar with SIMP having slightly more finer features, furthermore, overhang elimination is applied seamlessly irrespective of the interpolation method and optimizer type. We observe small overhang regions in the corrected models shown in red in Table 6.2 that are acceptable as long as their lengths are within the allowable horizontal overhang length of the AM technology. Additionally, Liu and Yu [203] in an experimental study discovered that small-sized horizontal overhangs printed fine and are, therefore, allowable in a design. Van de Ven [82] also suggested that in practical settings, eliminating overhangs might not be necessary except in impenetrable regions. However, the length of small overhang regions can be further reduced

by decreasing χ which will ensure more strut roots are formed within the overhanging feature. Some rough edges can be observed in the figures in Table 6.2. The rough edges can be avoided by increasing the resolution of the optimization or eliminated by using a mesh-based tool (such as MeshLab [204]) to smoothen the part.

The computing time can show the efficiency of the proposed methodology and will be discussed. Using 14,630 four-node square elements on an intel core i7, 16 Gb RAM, the time duration of different stages in this methodology was recorded for the problem in Figure 6.11. As anticipated, in Table 6.3 and Figure 6.11, out of an average total duration of 354 seconds, the two T.O. stages (stages 1 and 4) took up an average combined duration of about 340 seconds or over 90% in Figure 6.12(a). Each boundary identification and overhang elimination stage (stages 2 and 3) took a little over 11 seconds or 3% and 1 second or 0.3% respectively. These stages (2 and 3) take a combined 3.3% of the computational cost and are therefore comparatively much less expensive than other stages. Also in Figure 6.11, irrespective of the interpolation method or optimizer, the performance of the boundary identification and overhang elimination stages remain fairly constant and they take significantly less time compared to both topology optimization stages. Reasonably, we expect an increase in these time values using more design elements but their performances are detached from the T.O. process being a major contribution of this methodology. Furthermore, executing this methodology without volume correction cuts the total time duration by half and reduces stages 2 and 3 to a combined value of 8% in Figure 6.12(b). Additionally, optimizing the implementation of stages 2 and 3, e.g. eliminating iterative sub-routines, reducing stored arrays, and applying parallel computing methods, will greatly further reduce their computational cost contributions.

Table 6.3: Duration of stages in the post-T.O. process overhang elimination method with volume correction for a sample problem, two material interpolation methods, and optimizers.

	OCM – secs (%)		MMA – secs (%)	
	SIMP	RAMP	SIMP	RAMP
Stage 1: Initial T.O.	158 (47)	181 (46)	144 (38)	150 (45)
Stage 2: Boundary ID	11.6 (3.4)	11.6 (3)	12.3 (3.3)	11.2 (3.3)
Stage 3: Overhang Elimination	1.9 (0.56)	1.54 (0.39)	2.08 (0.55)	1.2 (0.36)
Stage 4: Final T.O.	149 (44)	183 (47)	195 (52)	162 (48)
Stage 5: Repeat 2 and 3	16 (4.7)	14.3 (3.6)	20.9 (5.6)	12.6(3.7)
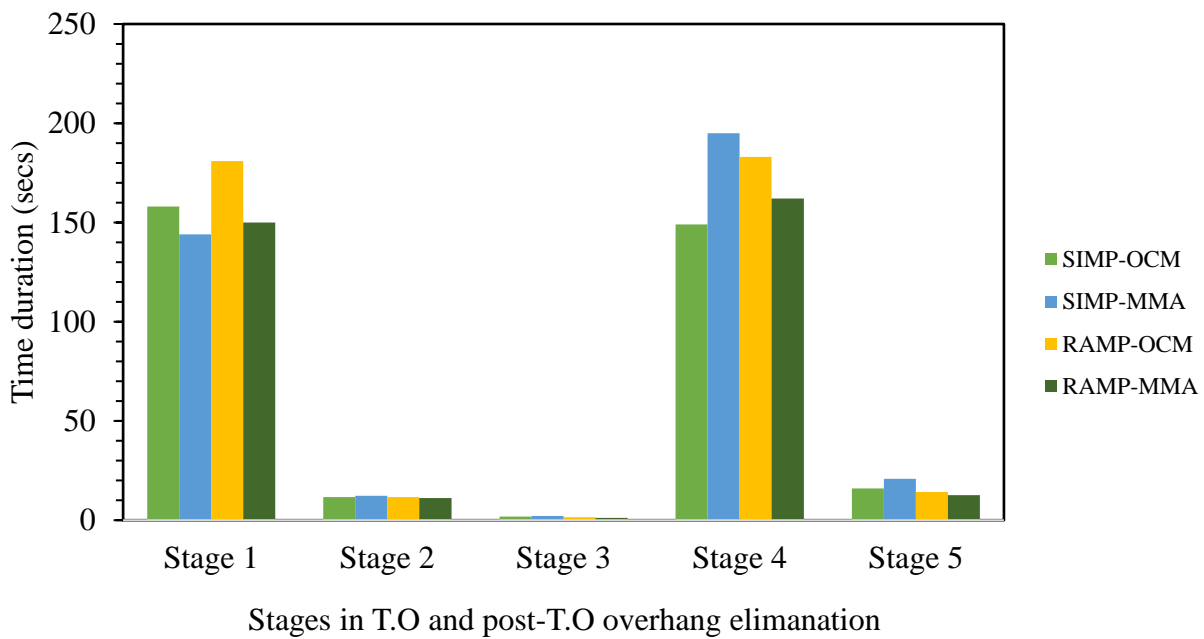
Figure 6.11: Time duration of stages in T.O. and post-T.O overhang elimination with volume correction
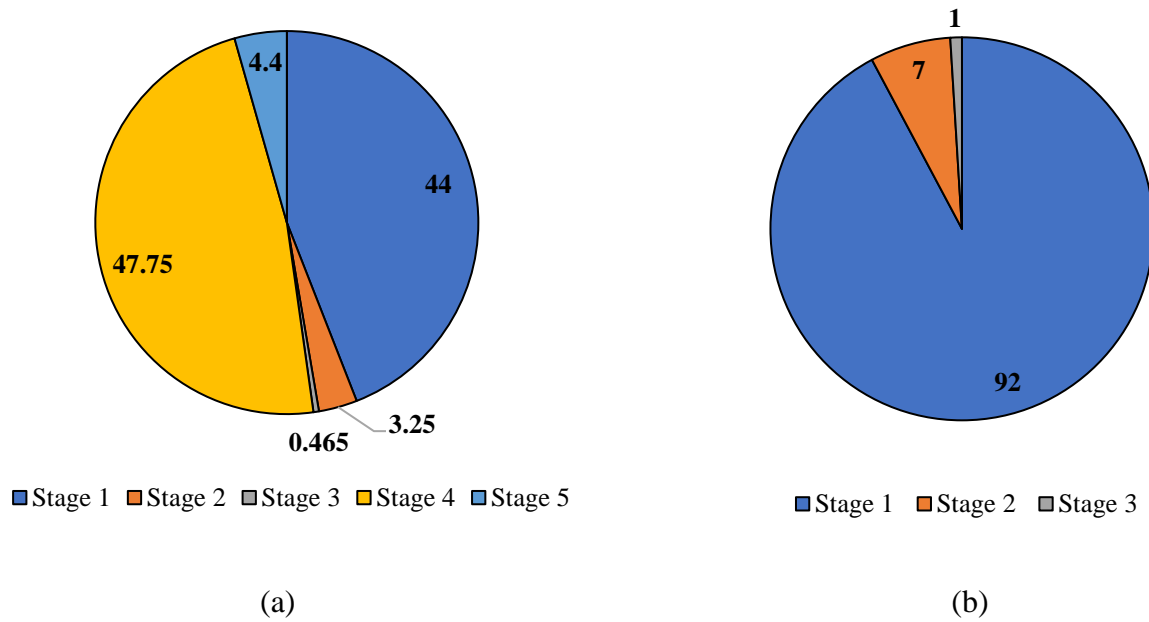
Figure 6.12: Percentage time duration of the stages in proposed methodology (a) with volume correction and (b) without volume correction

6.4 Manufacturability

To further assess the practical viability of this methodology, the half MBB beam and hook design samples in previous sections are printed via LPBF and FDM. The half MBB beam is printed in two orientations: the flat base on the build platform as shown in Figure 6.13(b) and the flip side is shown in Figure 6.14(c). The hook design is only printed the right way up as shown in Figure 6.13(d) and (e). Some LPBF and FDM process parameters used are shown in Table 6.4 and Table 6.5 respectively. In both AM processes, the overhang angle was taken as 45°. The optimized half MBB structure in Figure 6.13(a) is without overhang elimination, therefore, internal support structures were added. In addition to the increased build time and volume, these structures can offer difficulties during removal and increase the part surface roughness as observed in the figure. However, when the proposed overhang elimination model is applied in two orientations, Figure 6.13(b) and (c), we have well-printed structures with observably better down-surface qualities even with very short horizontal overhangs. The same scenarios are seen for the hook design in Figure 6.13(d) and (e).

Table 6.4: LPBF process parameters used for manufacturability studies

Parameter	Type/value
Machine	EOS M290
Material	Hastelloy X
Power	190 W
Speed	1000 m/s
Layer thickness	$40\mu m$
Scanning strategy	Stripe
Beam offset	$40\mu m$
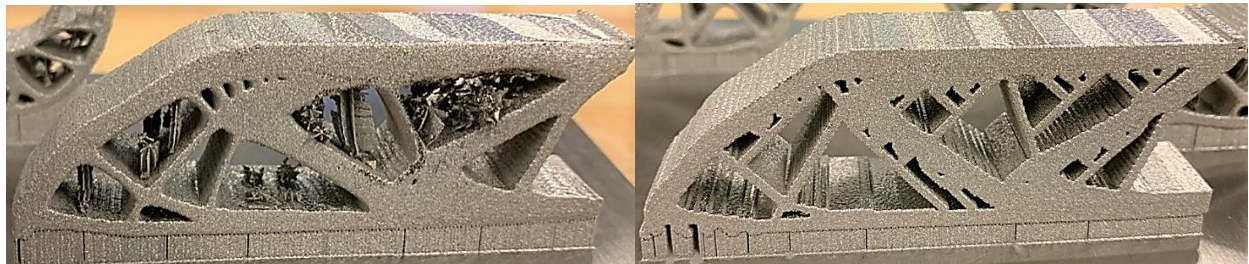
(a)

(b)

(c)

<div align="center">(d)   (e)</div>

Figure 6.13: LPBF manufacturability tests showing an optimized half MBB beam (a) without overhang elimination (b) with overhang elimination (c) with overhang elimination in a flipped orientation (d) an optimized hook without overhang elimination (e) an optimized hook without overhang elimination (e) an optimized hook with overhang elimination.

The same parts were printed using FDM and an overhang angle threshold of 45°. In the parts with internal support structures (Figure 6.14(a) and (d)), even though downfacing surface quality might not be excessively adversely affected, the difficulty in support removal is noticed. Also in comparison to the optimized parts with overhang elimination in Figure 6.14(b), (c), and (e), the optimized parts without overhang elimination exhibit poorer part print possibly due to the presence of extra support material and its interference with the extruder nozzle. Also, the optimized parts with overhang elimination consumed less material and time because of the absence of internal support structures.

Table 6.5: FDM process parameters used

Parameter	Type/value
Machine	Anycubic Mega i3
Material	Polylactic acid (PLA)
G_Code generator	Cura SteamEngine 4.6.1
Layer thickness	$200\mu m$
Infill density	20%
Support infill rate	25%
Bed temperature	$70°C$
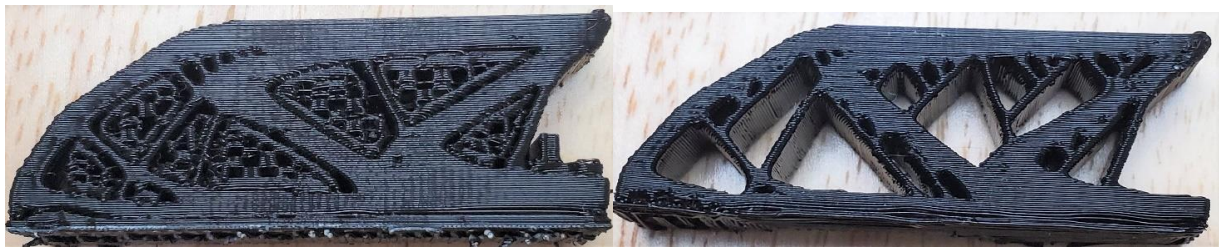
(a)

(b)
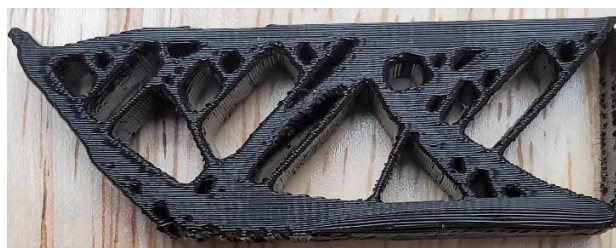
(c)

<div align="center">(d)   (e)</div>

Figure 6.14: FDM manufacturability tests showing an optimized half MBB beam (a) without overhang elimination (b) with overhang elimination (c) with overhang elimination in a flipped orientation (d) an optimized hook without overhang elimination (e) an optimized hook with overhang elimination.

6.5 Summary

In this study, a novel and alternative post-topology optimization method for dealing with the overhanging feature problem in many AM technologies such as LPBF and FDM has been presented. First, topology optimization is carried out on the design problem, secondly, boundary identification [185] and overhang detection as outlined in section 6.2 are done. Thirdly and finally, additional structural elements subject to a specified feature thickness and angle are introduced to support previously detected unsupported features. This addition can result in as much as a 22% increase in the volume fraction and a 4% decrease in compliance. For strict design volume adherence, a volume fraction (f) correction can be introduced to obtain a new and lower f which will be used in the final topology optimization, boundary identification and, overhang elimination stages. Several key reasons why this methodology is attractive are:

i.   Although the proposed method is post topology optimization, there is a seamless workflow from topology optimization because the type and number of design elements, density variables, feature size limit, and other controlling parameters are inputs. There is, therefore, no data conversion or transformation needed and consequently, both tools (topology optimization and overhang elimination) can be deployed easily as one.

ii.   There is complete independence from several aspects of the topology optimization method used such as interpolation methods, optimizer types, parameter tuning, and others. Due to the nature of many integrated overhang elimination methods, they may either perform poorer or breakdown completely when major changes are introduced in the topology optimization scheme [197], [76], [102], [98], [100].

iii.   This methodology allows for ample design expression regarding the geometrical properties of the additional support-free struts. In other words, the user or designer can dictate strict strut requirements such as thickness, orientation or angle, space between strut roots, and size of strut root (which in turn influences the number of struts added).

iv.   A direct consequence of post-topology optimization overhang elimination schemes is an increased final volume of the design. This is addressed by a volume correction step in this proposed methodology.

v.   The feasibility of the proposed methodology in practice was investigated by printing test samples via LPBF and FDM.

Notwithstanding the several aforementioned benefits, there are a few challenges and limitations this methodology offers. In 3D design problems which will be more valuable, designing the struts' roots will not be as straightforward as presented here; the base of each strut, prismatically shaped, will be defined by χ_1 and χ_2 along the axes perpendicular to the build direction. Also, the direction of strut inclination will become a little trickier and might require some optimization. The major limitation of this methodology is the shape of the finite element used. Currently, homogenous square (in 2D cases) or hex (which will be the case for 3D problems) elements are utilized. Although this is a popular type of element used in most topology optimization algorithms, the proposed methodology must be tweaked to accommodate other shapes. Moving forward, 3D extensions of the proposed methodology will be implemented and presented in the future.

Chapter 7: Experimental Validation of Topology Optimized Metal Parts Considering Overhang Feature and Size Control.

7.1   Introduction

Beyond manufacturability, to validate the post-topology optimization strategy for overhang elimination elaborated in Chapter 6, residual stress and bending test experiments are carried out on a sample problem. Leary et.al. [196] theoretically investigated the temperature distribution of self-supporting structures during AM process build. They discovered that these structures help to reduce the heat transfer resistance during the print thereby alleviating peak and average temperatures. Since the major contribution to residual stress in parts produced by metal AM is high-temperature gradients and rapid cooling [117], it, therefore, becomes important to investigate the influence of these self-supporting structures on the residual stress of the as-built part. First, in this Chapter, a preliminary X-Ray Diffraction (XRD) study is carried out to find a correlation or not between self-supporting features in a topologically optimized structure and the surface type 1 residual stress values [205] for AM Hastelloy X parts. Secondly, a robust 3-point bending test is done to observe the influence of these structures on their load-displacement responses and compare results with numerically obtained compliance values.

7.2   The Messerschmitt-Bolkow-Blohm (MBB) beam problem

Besides the cantilever problem, the MBB beam is a widely adopted case study for most topology optimization algorithms or models [76], [81], [98], [106], [120], [206] for both numerical and experimental studies. It is adopted here to analyze residual stress and load-displacement responses of the as-built AM structure. The beam is first topologically optimized by the SIMP method [50], [207], [208] based on compliance minimization for a volume fraction of 0.5. Thereafter, the post-topology optimization algorithm is carried out on the density map to eliminate unsupported or overhanging features. In this study, three categories of optimized beams are studied: those without overhang elimination (WOE), different minimum feature sizes (na – where n is an integer multiple of half the finite element size - a - used in the optimization), and different overhang angle thresholds (θ). The MBB beam problem is shown in Figure 7.1, in (a), the problem with load and support locations is presented while (b) shows an input image file of half the domain used in *ibipp.m* for the optimization. *ibipp.m* is

an open-source program that has been developed to initialize free-form design domains for topology optimization and generate STL files for printing – this will be presented in Chapter 8.

(a)

(b)
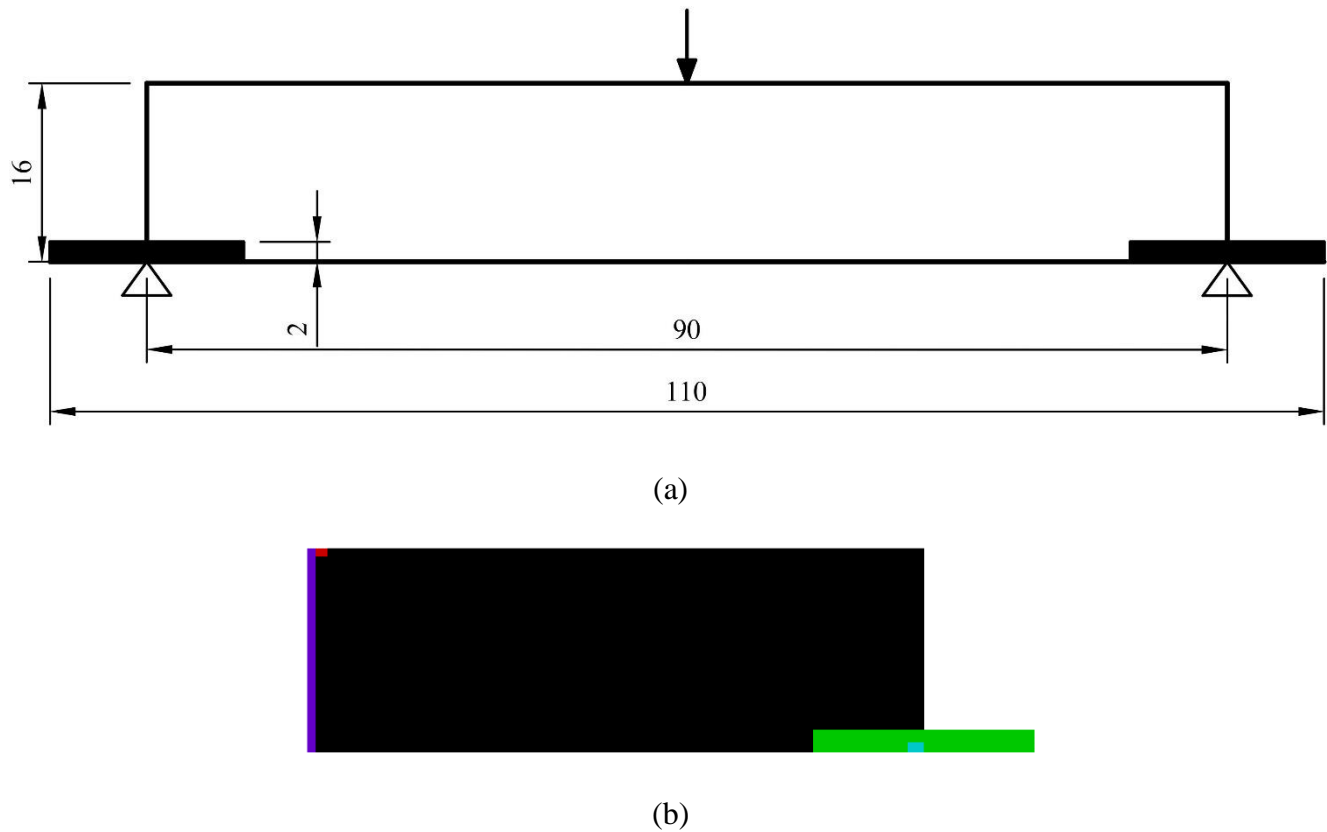
Figure 7.1: (a) The MBB problem showing the load and support locations and domain dimensions (b) the half MBB initial design domain used for optimization in *ibipp.m*.

In Figure 7.1, a preserved region (shown in black in (a) and green in (b)) around the supports is added to improve stability during the bending tests. The problem is discretized using 270×77 (20790) bilinear homogenous square elements with a finite element length of $2a = 0.4\ mm$. The Optimality Criteria Method [129] was used as the gradient optimizer and 0.01 or 0.1 after 250 iterations were set as the convergence criteria. Altogether, 12 optimized designs were generated: two designs without overhang elimination, of minimum feature radii - $5a$ and $7a$ conveniently named $5a$-WOE and $7a$-WOE respectively, 10 designs having overhang angle thresholds at $45°, 50°, 55°, 60°,$ and $65°$ with minimum feature radii of $5a$ and $7a$ respectively. In subsequent sections, the minimum feature size should be interpreted as the minimum feature radius. Figure 7.2 shows the different optimized designs in 2D and 3D:
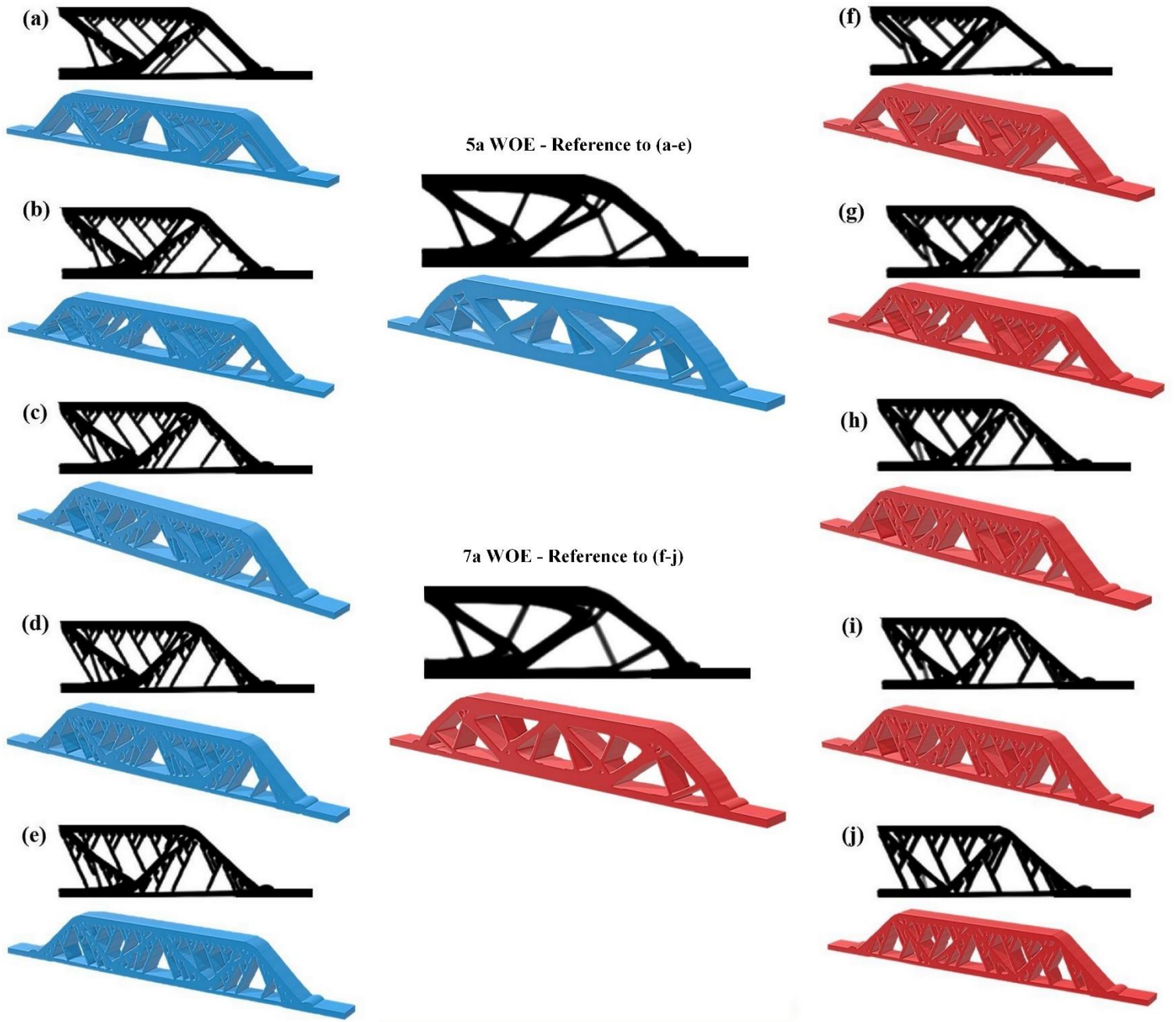
Figure 7.2: Optimized designs showing the reference designs without overhang elimination (WOE) for minimum size $5a$ and $7a$ (middle figures), (a-e) $5a$ and (f-j) $7a$ with angles $45°, 50°, 55°, 60°,$ and $65°$ respectively.

7.3　Experimental Procedures

7.3.1　Sample Production

An EOS M290 LPBF machine equipped with a Ytterbium fiber was used to produce the tensile and topologically optimized samples. The printing was done under an argon environment and the build plate temperature was $80°C$. The Hastelloy x powders were gas-atomized and they were supplied by EOS GmbH. Other process parameters are shown in Table 7.1. Three repetitions of the optimized beam samples as shown in Figure 7.2 were printed also, with their build orientations as they are shown in the figure. Tensile samples oriented at $0°, 45°,$ and $90°$ to the plane of the substrate or build platform as shown in Figure 7.3 were printed with three, three, and five repetitions respectively for mechanical testing. The dimensions of the tensile samples can be seen in [151], [209]. The optimized samples tested for residual stresses were left on the substrate for measurement to prevent any stress relief. After residual stress tests were done, all samples were cut using electrical discharge machining (EDM). The printed samples are shown in Figure 7.4.

Table 7.1: LPBF process parameters used for residual stress and bending tests

Parameter	Type/value
Power	215 W
Speed	1150 m/s
Layer thickness	$40\mu m$
Scanning strategy	Stripe with 67° rotation
Hatching distance	90 μm
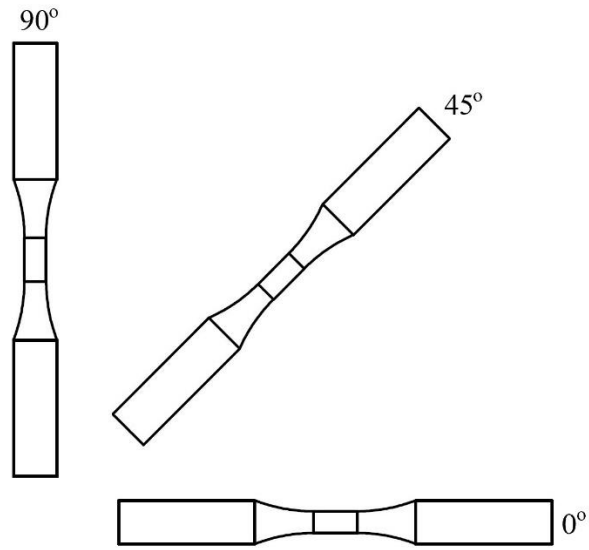
Figure 7.3: Tensile samples in different orientations
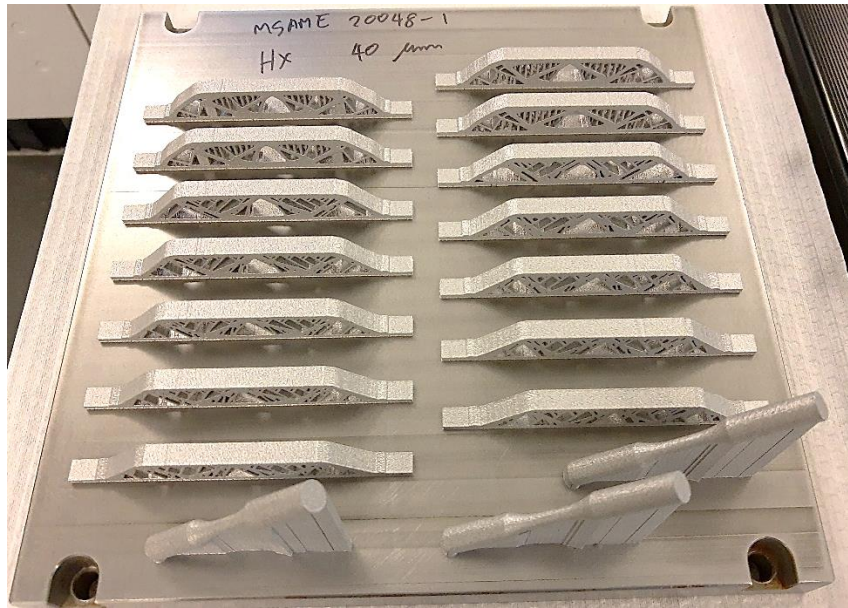
Figure 7.4: Printed tensile and optimized beam samples

7.3.2 Residual Stress Measurements

Preliminary residual stress measurements were done by X-Ray Diffraction (XRD) using a PULSTEC® μ-X360s Portable X-ray Residual Stress Analyzer. Two repeats of all optimized samples were analyzed by x-ray spot sizes or collimator sizes of $1\ mm$ and $2\ mm$ each. The target material was set to Ni-alloy with a diffraction plane of $\{3,1,1\}$ while the x-ray incident angle was 30°. The direction of the measured residual stress σ_x is shown in Figure 7.5.

(a)

(b)
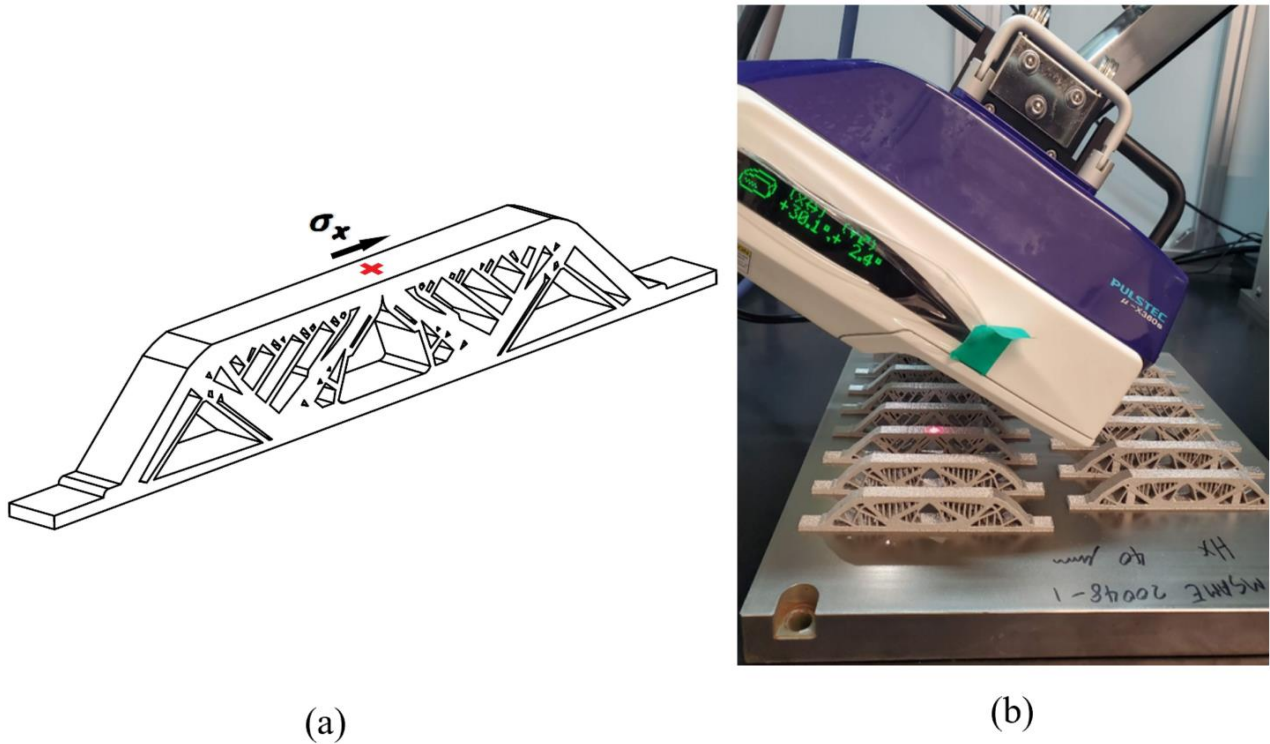
Figure 7.5: (a) The measured location, shown in the red 'x', and direction of the residual stress value, (b) the PULSTEC X-Ray residual stress analyzer

7.3.3 Mechanical Testing

Room temperature quasi-static tensile tests were done using the Instron® 8874 servo-hydraulic machine in the displacement control mode at a crosshead speed of 0.45 mm/min following ASTM E8 standard [210]. The load capacity of the testing machine was $\pm 25kN$ and an Instron® 2630-120 extensometer with a gauge length and travel of $8\ mm$ and $\pm 4\ mm$ respectively was used. Thereafter, 3-point bending tests were carried out on the sample size using a crosshead speed of 1.5 mm/min. All tensile and bending samples were carried out under the same experimental conditions. The tensile and bending test setups are shown in Figure 7.6.

<center>(a)   (b)</center>

<center>Figure 7.6: (a) Tensile and (b) bending test setups.</center>

7.4. Results and Discussion

7.4.1. Residual stress

Parameters such as scanning pattern, dwell time, and other process-related variables that have significant effects on the thermal history of a printed part are most likely to cause residual stresses [117]. The residual stress plots at the top-surface center of all optimized Hastelloy-X MBB beam samples are shown in Figure 7.7. Given the comparatively high standard deviations, it is observed that there is no significant effect of the overhang angle threshold and minimum feature size on the surface residual stress. The overlapping error bars for WOE, 45° and 50° show that the residual stress values for both feature sizes are indistinguishable within the standard deviation limits. Also, for the optimized cases without overhang elimination, there is no considerable residual stress difference with those that were optimized for manufacturability. A major reason could be that there are few structural differences between all samples (even with samples without overhang elimination as they were printed with support structures), especially during the build. This will cause their thermal histories to be closely related therefore leaving little to no difference on the surface residual stress values. In literature, studies have shown that the scan length and direction of the process hugely influence the residual stress formation and magnitudes [116], [117], [211]. Also, there have been suggestions to focus on finding the relationships between process

<center>136</center>

parameters and their associated residual stress distributions [212], and to validate commercial software packages on AM process simulation with experimental residual stress results [211]. Although Leary et.al. [196] noticed thermal history improvements when structures are optimized with manufacturability considerations, this may not have significant impacts on the residual stress distribution which in fact, is the most critical phenomenon considering thermal histories. However, since this study was limited to Hastelloy X as material and a few minimum feature sizes, an extended study using a few more materials and feature sizes is recommended.
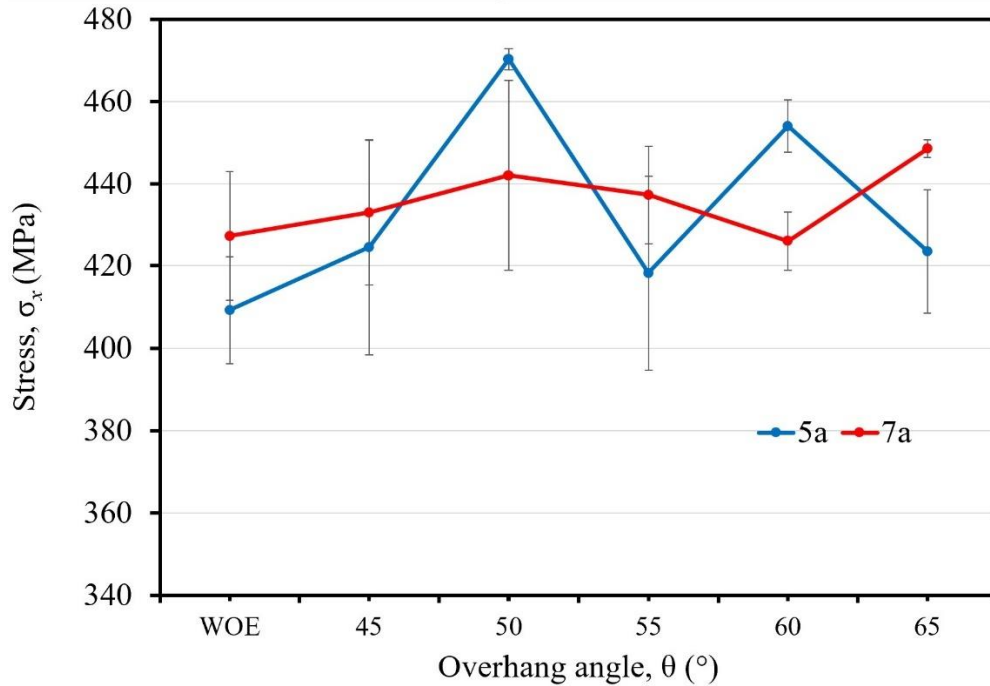
Figure 7.7: Effect of overhang angle threshold and minimum feature size on residual stress formation.

7.4.2. Quasi-Static Response

The engineering stress-strain curve and yield stress plots of the tensile samples printed in three orientations are shown in Figure 7.8. In Figure 7.8 (a), the vertical sample experiences more ductility than other orientations although the yield stress is the lowest in Figure 7.8(b). Similar trends for the reduction in mechanical strength as the build orientation moves towards 90° can be seen in [119] [213]. However, since Hastelloy is a very ductile material [151], [209] very high elongation is observed at lower yield strengths. The Young's Modulus is highest at 90° with a value of 158 MPa and while this is in the range of reported additively manufactured Hastelloy X parts [151], [209] at 153 ± 5.5 GPa, the Young's Modulus for 0° and 45° fell a little short at 141 and 136 MPa respectively. The same trend of Young's Modulus can also be noticed in [118] although the samples reported were printed using DSM

Somos 14120 and Stereolithography (SLA). In this study, the yield stress drops slightly with an increase in the build orientation angle; the mean yield stress value is at 455 MPa. The slight reduction in the yield stress (rather than increase) with an increase in the orientation angle can be attributed to a small noisiness/nonlinearity in the engineering stress-strain results. The mean of the Young's Modulus and yield stress were taken and used in an FEA simulation and the computation of the final compliance of the optimized beam structures.

(a)   (b)
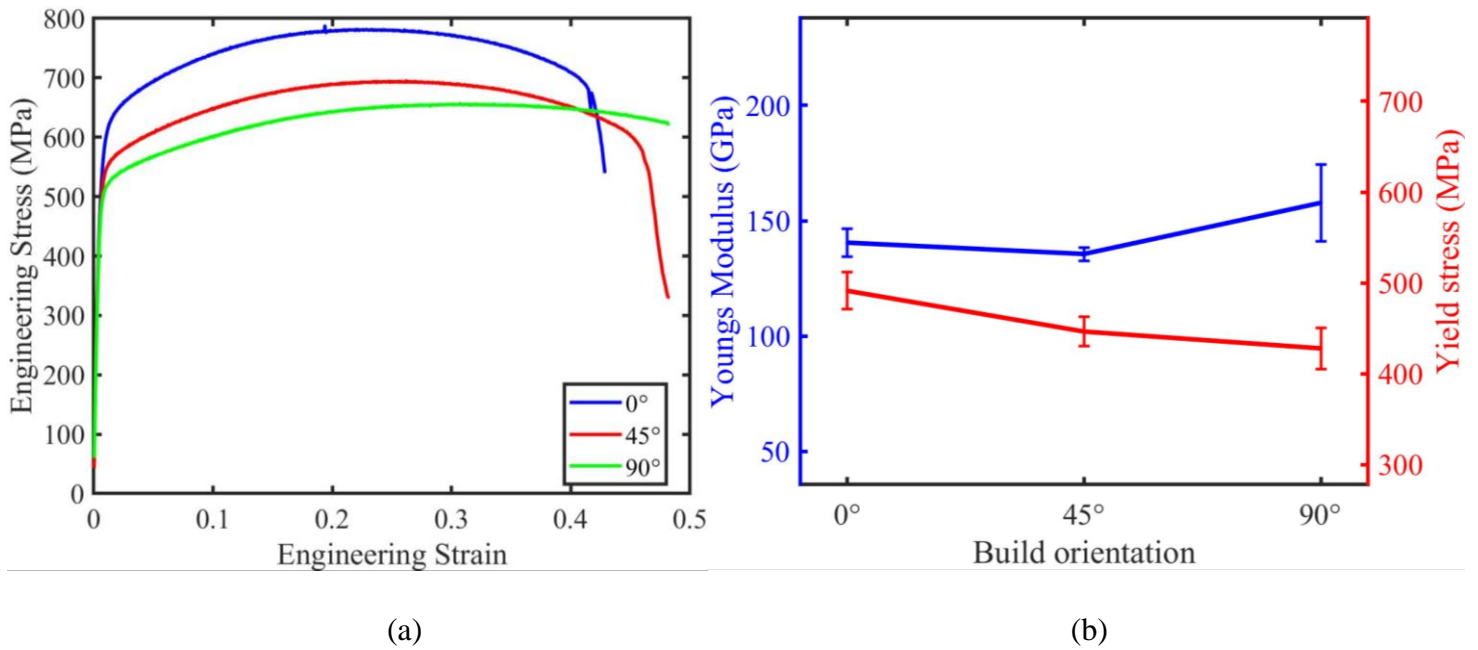
Figure 7.8: Quasi-static tensile responses for Hastelloy X (a) Engineering stress-strain curves (b) Yield stress and Young's Modulus plots.
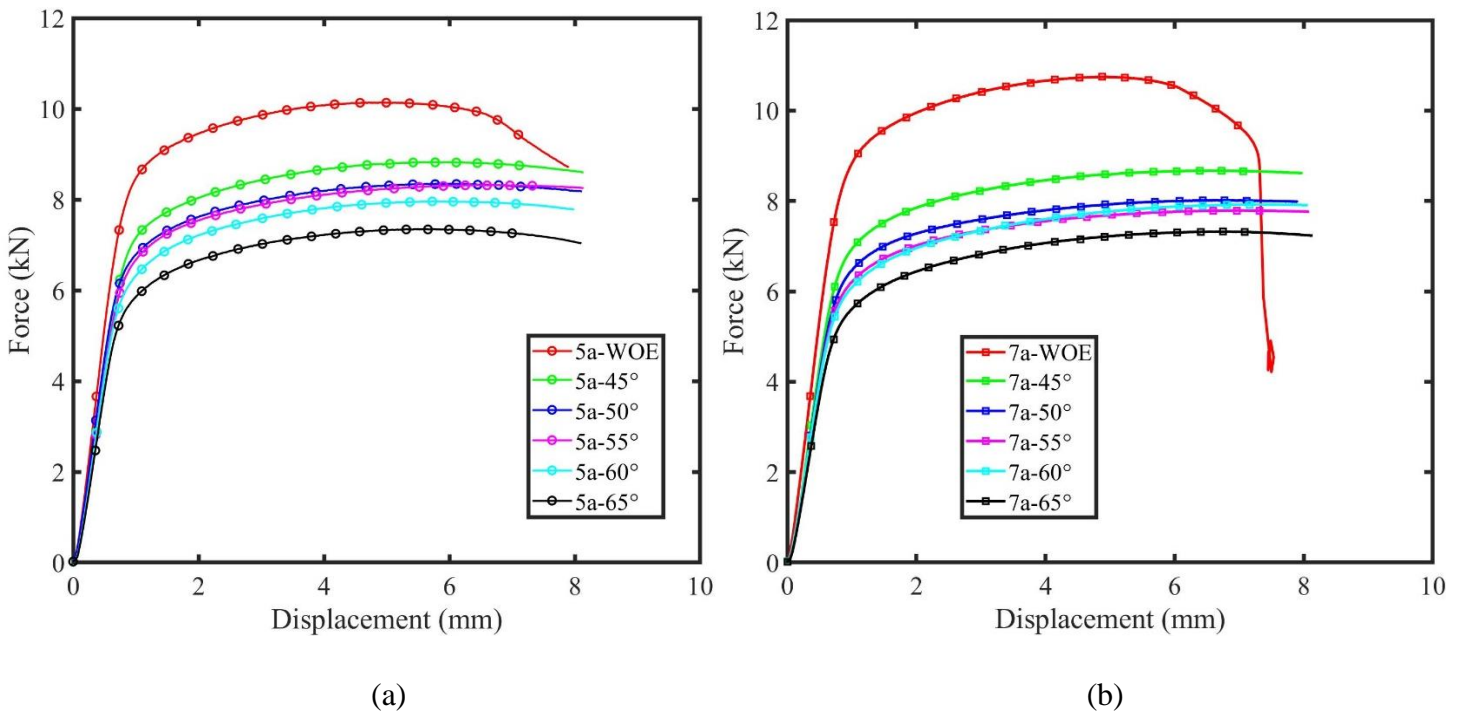
Figure 7.9: Load-displacement plots for the optimized MBB beams with a minimum feature size of (a) $5a$ (b) $7a$

The load-displacement plots of the optimized beams for minimum feature sizes $5a$ and $7a$ are shown in Figure 7.9. For the optimized beams without overhang elimination (WOE) the load-displacement plots are quite similar and this is not far-fetched from their similar structural topology seen in Figure 7.2 with only insignificant feature differences. These WOE beams can overcome more work compared to the optimized beams with overhang elimination. Since no manufacturability constraint (overhang elimination) was placed on them, their structural optimality is higher than those optimized under the constraint, consequently performing better functionally. For each minimum feature size, the higher the overhang angle threshold, the less work is overcome. Also, it is observed that at a particular angle threshold, a move from $5a$ to $7a$ slightly decreases the performance of the beam samples. It is expected that this decline in performance will exacerbate with a further increase in the minimum feature size. Therefore, while considering manufacturability, limiting the overhang angle threshold and minimum feature size to a minimum is recommended. Therefore, for relatively simple topologies, build orientation optimization may be considered only to obtain functionally optimal parts while eliminating overhanging regions. However, when dealing with significantly complex parts, introducing support-free trusses might be more beneficial to avoid difficulties in printability and support removal since build orientation optimization only might not be very helpful to eliminate overhanging regions.

7.4.3. Numerical and Experimental Comparisons

Finally, the maximum forces in the load-displacement results obtained in the previous section will be compared with the compliance values obtained after optimization. Additionally, an FEA simulation is carried out to observe the similarities between numerical and experimental deformations of the optimized beams. Figure 7.10 shows the influence of the overhang angle threshold and minimum feature size on numerically obtained compliance values and the maximum force from the load-displacement response. An increase in compliance invariably results in a decrease in the maximum load possible for the structure. A similar trend for different topologies is seen in [118]. From Figure 7.10, when the manufacturability of a structure is considered by thresholding the overhanging feature angle and minimum feature size, there is more than a 40% increase in the compliance and a 30% decrease in the maximum load carried by the structure for $65°$ angle threshold and $7a$ minimum size. Between angle and feature size thresholds, from this study, the overhang angle threshold appears to influence the compliance and performance more, however, it should be noted that the marginal difference between successive angles and feature sizes is $5°$ and $4a$ respectively. *The feature size is the diameter of the linear density filter which is twice the filter radius ($2 \times r_{min}$), therefore $5a$ and $7a$ represent diameters of $10a$ and $14a$ respectively.* The maximum change resulting from a change in the minimum feature size is between $5a$ $55°$ and $7a$ $55°$ beams with a 9% increase in compliance from 2700 Nm to 2950 Nm. Although there is also a maximum increase of 9% between successive angle thresholds from $60°$ to $65°$, there is an 18% increase in the compliance when moving from a structure without overhang elimination (WOE) to one with a $45°$ angle threshold. This is understandably so because the minimum feature size is an integral specification in topology optimization to obtain mesh-independent results and prevent the formation of checkerboarding features [108], [109], [129], [208], [214].
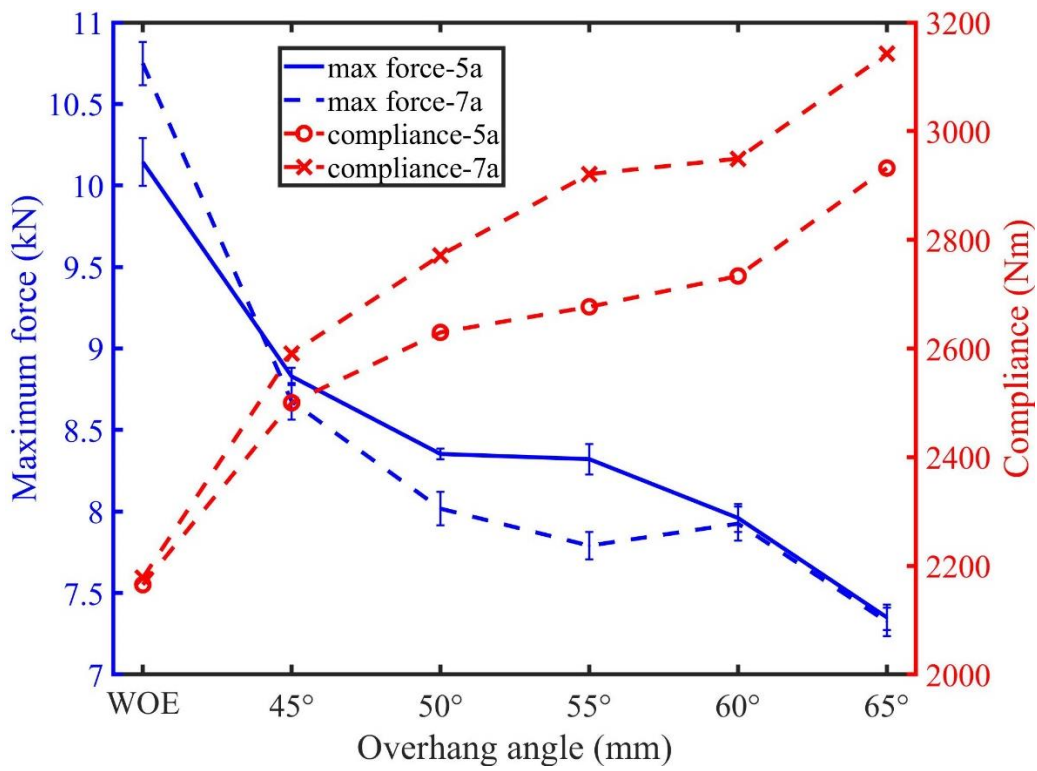
Figure 7.10: Influence of overhang angle threshold and minimum feature size on numerically obtained compliance values and the maximum force from the load-displacement response.
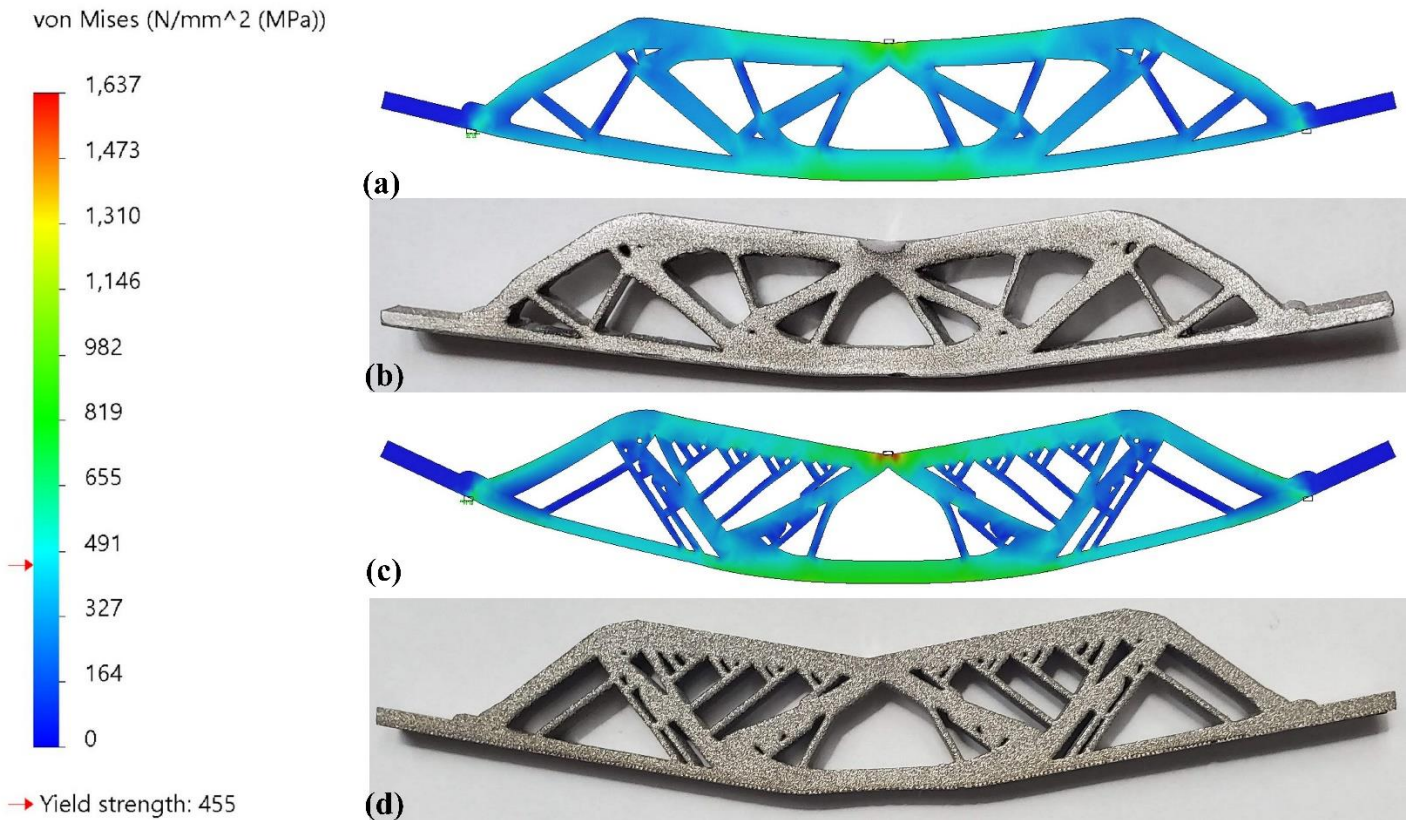
Figure 7.11: Deformed optimized MBB beam for (a) $7a$ WOE – simulation (b) $7a$ WOE – experiment (c) $5a$ $45°$ – simulation (d) $5a$ $45°$ – experiment

In Figure 7.11, the deformed beams representing $7a$ WOE and $5a$ $45°$ from simulation and experiment are shown. The simulation was carried out in Solidworks®'s static analysis and the material properties investigated in the experimental study were used. A maximum force of 8750 N was applied at the middle of the beam (where the load for the bending test was located). The matching deformation profile in both cases is noticed and areas of high-stress concentration at the top and bottom features are consistent with the deformed locations in the tested beams. The $5a$ $45°$ beam experiences comparatively higher stresses and deformation further substantiating the effects of manufacturing constraints in a design.

7.5. Summary

In this chapter, an experimental study on the effects of manufacturing constraints – overhang angle threshold and minimum feature size – on residual stress formation and performance of as-built Hastelloy X samples has been done. 12 optimized MBB beams having structural variations from manufacturing constraints were studied. Without considering build orientation optimization, the study has shown that:

a. Preliminary results point to the fact that these structural variations have little influence on the surface residual stress values for Hastelloy X parts. Irrespective of the minimum feature size or overhang angle threshold, the surface residual stresses remain relatively constant.

b. Manufacturing constraints have significant effects on the performance of a structure. The less the number of constraints and the lower their magnitudes, the better their performance.

c. The overhang angle threshold was observed to adversely affect structural performance more than the minimum feature size.

Chapter 8: IBIPP for Topology Optimization: An Educational and Research Tool.

8.1.   Introduction

This work presents an open-source image-based initialization and post-processing (IBIPP) code for 2D topology optimization. Over the years, there have been several impressive research and educational open-source codes for topology optimization. They have made teaching, learning, and research in this field relatively easy, especially for those new to it. From the classic 99-line, SIMP density-based code by Sigmund [129] to much newer codes such as the new generation 99-line code [130], an ANSYS APDL code using the BESO method [215], elaborations on the use of sequential integer programming [216], using a geometry projection method [217], etc, the research and academic communities have been served with a plethora of open-source topology optimization codes. However, there are still several advancements that can be made to either enhance the flexibility and ease of use or seamlessly integrate several packages into one or enable practical results for manufacturing. To easily and seamlessly initialize arbitrary domains, loads, and boundary conditions, deploy several topology optimization approaches, and obtain manufacture-ready models, IbIPP has been developed, and technical details of its framework are elaborated in the following sections.

8.2   Interpretation of Digital Images

A digital image is a discrete representation of data in spatial (location) and intensity (color) properties [218]. Several image data types can be defined depending on the intensity or color. Four common data types are binary, grayscale, RGB (Red, Green, and Blue) or true-color, and floating-point [218]. Binary images have one-pixel intensity data with an integer value of either 0 or 1, and grayscale images have one intensity data with integers between 0 and 255, RGB images have three intensity data with each integer from 0 to 255. In contrast, floating-point images store intensity data as floating points rather than integers. In this work, RGB intensity is used as it allows for a clear distinction between features in the image and relatively easy processing.

To initialize 2D design problems for topology optimization approaches discussed in the previous section, an image that accurately depicts features of the problem such as loads, boundary conditions, preserved and non-design regions can be developed and processed as an input. Using basic image vectorization and processing techniques, colors assigned to the features of the design problem can be analyzed, and

variables necessary for initialization extracted thereafter. A digital image comprises several pixels and is analogous to a discretized domain made up of finite elements. In Figure 8.1(a), the image defined by a function $f(x, y, z)$ has $m \times n$ number of pixels [219] with each pixel having an intensity of $c_{x,y}$. For a true-color representation, the image function can be expressed in (8.1).

$$f(x, y, z) = \begin{bmatrix} f(0,0,c_{0,0}) & f(0,1,c_{0,1}) & \cdots & f(0,n-1,c_{0,n-1}) \\ f(1,0,c_{1,0}) & f(1,1,c_{1,1}) & \cdots & f(1,n-1,c_{1,n-1}) \\ \vdots & \vdots & \cdots & \vdots \\ f(m-1,0,c_{m-1,0}) & f(m-1,1,c_{m-1,1}) & \cdots & f(m-1,n-1,c_{m-1,n-1}) \end{bmatrix} \tag{8.1}$$

where x and y indicate the pixel location while c indicates the intensity, for an RGB image, c is a vector of size 3 and the overall data size is $m \times n \times 3$. If this image is assumed to be the domain of a design problem, as shown in Figure 8.1(b), every element in the domain will represent a pixel area Ω. Therefore, (8.1) can be interpreted as (8.2-8.4), and the size of i and j are dependent on the level of image discretization. A new matrix consisting of finite elements can be derived from the image as:

$$g(i, j, :) = f[\alpha_{i,j}, \beta_{i,j}, :] \tag{8.2}$$

where $g(i, j, :)$ contains submatrices of f where $\alpha_{i,j}$ and $\beta_{i,j}$ are the row and column indices respectively in f for a pixel area $\Omega_{i,j}$ as observed in Figure 8.1(b). the domain function $g(i, j, k)$ can be written as

$$g(i, j, k) = \begin{bmatrix} g(1,1,d_{1,1}) & g(1,2,d_{1,2}) & \cdots & g(1,nelx,d_{1,nelx}) \\ g(2,1,d_{2,1}) & g(2,2,d_{2,2}) & \cdots & g(2,nelx,d_{2,nelx}) \\ \vdots & \vdots & \cdots & \vdots \\ g(nely,1,d_{nely,1}) & g(nely,2,d_{nely,2}) & \cdots & g(nely,nelx,d_{nely,nelx}) \end{bmatrix} \tag{8.3}$$

(8.3) can be rewritten as

$$g(i, j, k) = \begin{bmatrix} d_{1,1} & d_{1,2} & \cdots & d_{1,nelx} \\ d_{2,1} & d_{2,2} & \cdots & d_{2,nelx} \\ \vdots & \vdots & \cdots & \vdots \\ d_{nely,1} & d_{nely,2} & \cdots & d_{nely,nelx} \end{bmatrix} \tag{8.4}$$

where $d_{i,j}$ is obtained as

$$d_{i,j} = \frac{1}{np_{i,j}} \sum_{\Omega_{i,j}} c_{x,y} \qquad (x, y) \in \Omega_{i,j} \tag{8.5}$$

where $np_{i,j}$ is the number of pixels in element (i, j) within an area $\Omega_{i,j}$.
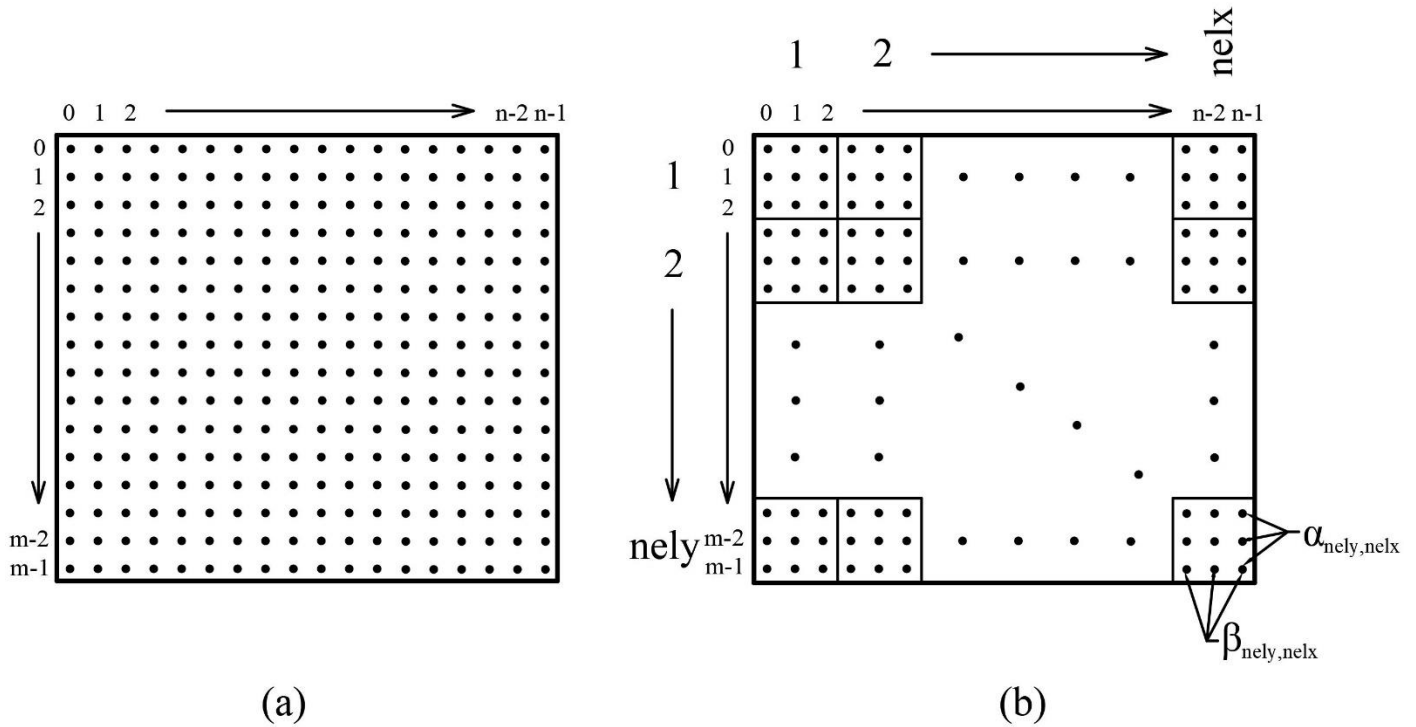
Figure 8.1: Coordinate representation of an image in (a) by common image processing packages, (b) an analogous representation of finite elements.

In (8.3), $nely$ and $nelx$ are the numbers of elements in the y and x directions respectively in a uniformly segmented image while $d_{i,j}$ is the mean color intensity of the area signified by i,j. The reader is referred to [218], [219], and [220] for more details on this subject and related information.

8.3   MATLAB Implementation

IbIPP is a platform developed for 2D topology optimization which covers arbitrary design domain initialization, easy deployment of several open-source Matlab codes, and generating 3D-printable models. Using color codes, the design problem is represented as an image format, and several subroutines are applied to transform the data into useful inputs for topology optimization. Apart from homogenous square finite elements with unit length used for meshing, parameters are customizable. The program is initialized by entering the following code in the Matlab command prompt:

```
ibipp(domain,nelx,volfrac,...)
```

where `domain` is the name of the image file in string format (Portable Network Graphics - png is recommended), `volfrac` is the volume fraction constraint placed on the problem while "`...`" indicates that the user can declare several other parameters through optional and name-value inputs. In

146

`ibipp.m` which is the main file, the major sections are default parameters' declaration, input parser for required, optional, and name-value inputs, declaration of optimization parameters, declaration of parameters for load and boundary conditions, declaration of post-process parameters, domain initialization, resolution of load, boundary conditions, preserved and non-design domains, topology optimization, and post-processing. The critical aspects of the code are the sub-routines written for domain initialization, resolution of loads, boundary conditions, preserved and non-design domains, and post-processing. These will be discussed in detail in the following subsections from 8.3.1 to 8.3.5.

8.3.1 Domain interpretation (`imageprocessor.m`)

Before `ibipp.m` is run, the image representing the design problem must be prepared according to some set requirements. Any software or tool that allows a user to draw 2D sketches and specify RGB values for coloration can be used. The user is encouraged to use tools that enable sketching, and color application without permitting rendering capabilities such as 'lighting' or 'environmental' settings. There are 8 unique features identifiable by the program: design and non-design elements, nodes of point loads and pressure, fixed nodes in x only, in y only, and x and y, preserved elements. The design domain is categorized into these features depending on the color intensities. The features are assigned some color codes, as shown in Table 8.1.

Table 8.1: Design features and their color code representation

Design feature	Color code	Element value $f(i,j)$
Designable domain	$R \cap G \cap B < 200$	1
Non-designable domain	$R \cap G \cap B > 200$	0
Point load	$200 \leq R^* \leq 255, G = 0, B = 0$	$20 + \dfrac{R - 200}{5}$
Pressure	$200 \leq R \leq 230, 100 \leq G^* \leq 150, B = 0$	$30 + \dfrac{G - 100}{5}$
Preserved region	$R = 0, 200 \leq G \leq 255, B = 0$	4
Fixed region	$R = 0, G = 0, 200 \leq B \leq 255$	51
Region fixed along x	$100 \leq R \leq 150, G = 0, 200 \leq B \leq 255$	52
Region fixed along y	$R = 0, 200 \leq G \leq 255, 200 \leq B \leq 255$	53

*Note: **ibipp** interprets any element with a color code outside the outlined rules as 0 or white*

[*] must be a multiple of 5 to allow several load cases; also, R and G must start at 200 and 100, respectively.

To enable multiple loads, the values of R and G for point loads and pressure in Table 8.1 must be a multiple of 5 and must start from $R = 200$ for a point load and $G = 100$ for a pressure load. This helps to preserve the order and method of associating load cases with their corresponding magnitudes. How the load nodes are subsequently extracted and the magnitudes applied are explained in section 3.3. In Figure 8.2, a half-MBB and another slightly more complicated design problem illustrate how images are generated for design problems. It is observed that for the load and boundary conditions in Figure 8.2(a,f), the regions in the design domain directly affected are depicted by the appropriate color codes according to Table 8.1. The size of these regions is dependent on the resolution intended for the optimization. The finer the resolution, the less the area these colored load and boundary regions should cover in Figure 8.2(b,g). It is noteworthy that the choice of $nelx$ by the user should be carefully selected. In Figure 8.2 (c,h to e,j), using a coarse resolution can lead to a wrong interpretation of the digital image, while a finer resolution ensures all features are well replicated. Notwithstanding, to strike a balance between correct image interpretation and computational cost resulting from applying finer resolutions, a rule of thumb for choosing an appropriate $nelx$ should be a minimum of twice the ratio of the smaller bounding box dimension and the least dimension of the smallest feature. The disjoint observed in some boundaries between features is a result of boundary elements that have color codes that are a mean of two different features. This might result in a color code that does not match any rule in Table 8.1 and those elements are therefore assigned a value of 0 (white) as pointed out in the sentence at the bottom of Table 8.1. The image interpretation is carried out by the subroutine

```
[dom,nely] = imageprocessor(domain,nelx)
```

In lines 2 to 11 in this subroutine, the image is read, discretized, and RGB values extracted. The element values are applied from lines 12 to 25 according to Table 8.1 and as illustrated in Figure 8.3. The outputs of `imageprocessor.m` are `dom` and `nely,` which are the matrix $f(i,j)$ and number of elements along the y-axis.

Some points noteworthy when preparing an image file: the user is encouraged to use the minimum values of RGB ranges provided in Table 8.1 except for white (255, 255, 255), a colored region should not be bounded by a line of another color (e.g. a green region should not be bounded by a black line). Finally, the user is encouraged to go through the examples provided to have a better understanding of how to prepare an image for a design problem.
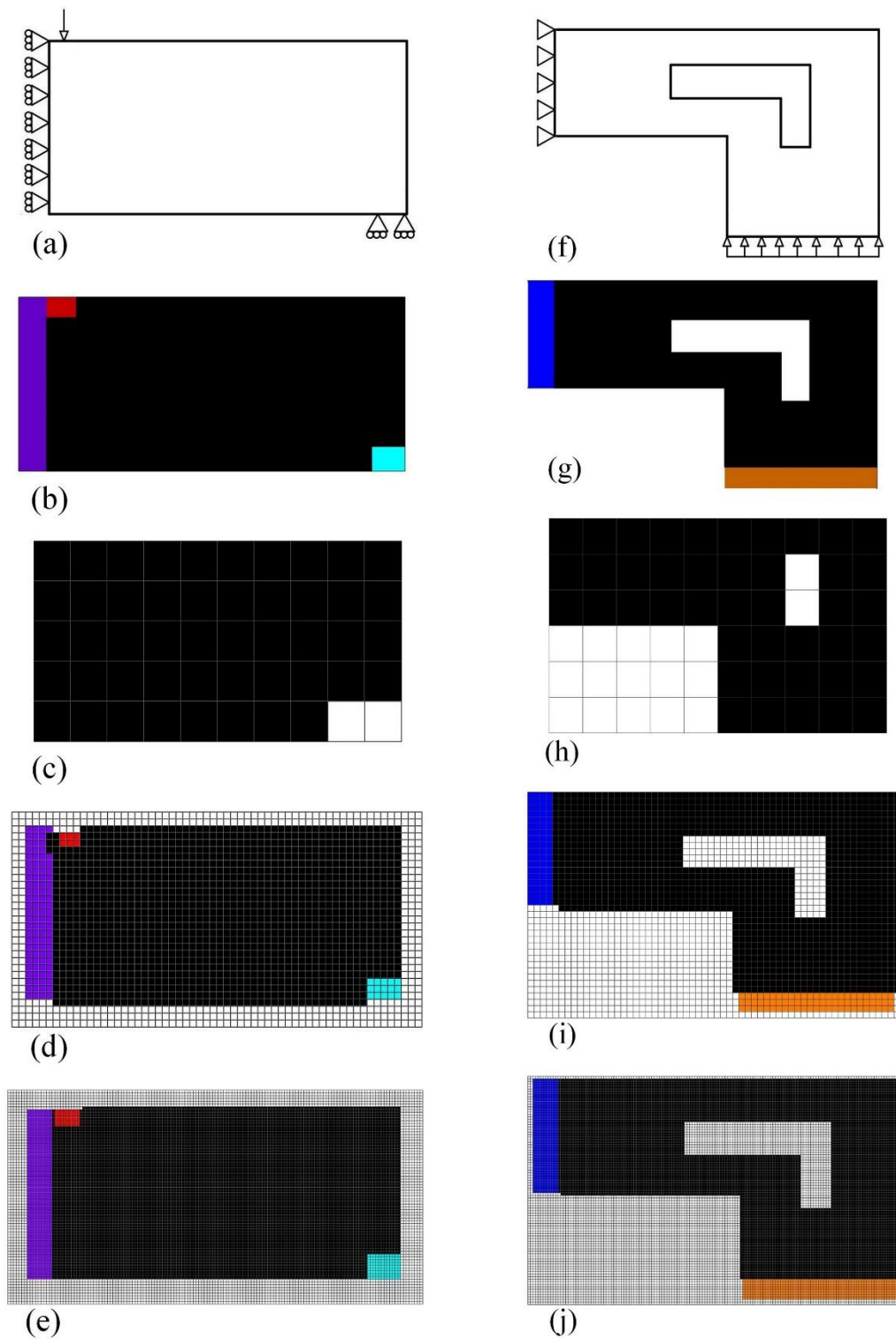
Figure 8.2: Effect of element size on image interpretation by ibipp.m. This shows (a,f) the design problems to be optimized, (b,g) input image representative of the design problems, and domain discretization by (c,h) 10×5(6) (d,i) 60×31(36), and (e,j) 150×77(90) mesh elements.

149

$$f(i,j) = \begin{bmatrix} 51 & 1 & 1 & 1 & 1 & 1 & 20 \\ 51 & 1 & 1 & 1 & 1 & 1 & 1 \\ 51 & 1 & 0 & 0 & 0 & 1 & 1 \\ 51 & 1 & 0 & 0 & 0 & 1 & 21 \\ 51 & 1 & 1 & 1 & 1 & 1 & 1 \\ 51 & 1 & 1 & 1 & 1 & 1 & 1 \end{bmatrix}$$
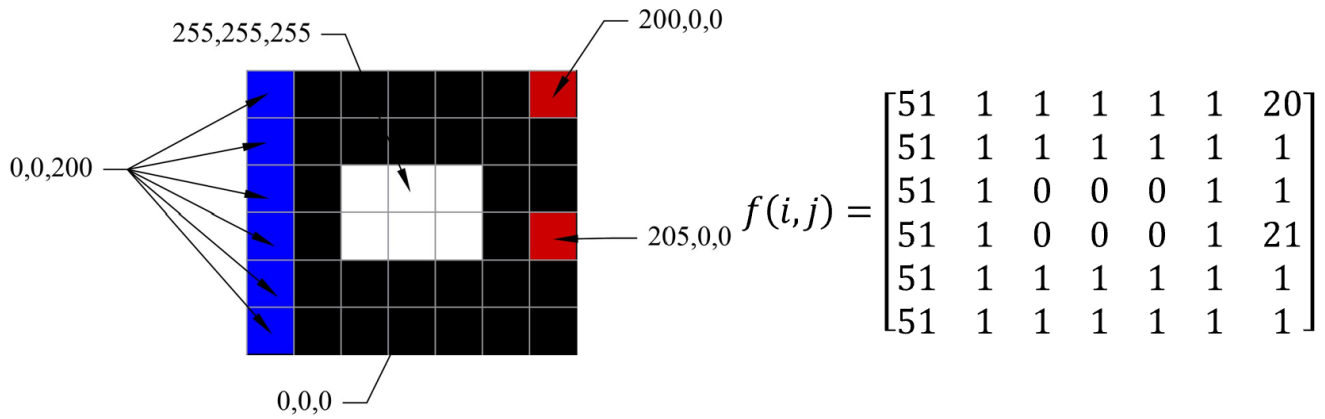
Figure 8.3: Image interpretation by the color codes and corresponding element values as outlined in Table 1

8.3.2 Resolution of loads, supports, Non-design, and Preserved domains (`loadandsupport.m`)

After interpreting the digital image into a matrix with element numbers representative of design features, the transformation of this matrix to useful nodal or elemental quantities must be carried out. This is done in the 59th line in `ibipp.m` where the subroutine `loadandsupport.m` is initiated. The subroutine is called by the following function command

```
[F,fixeddofs,NonD,MusD,volfrac,edofMat1] = loadandsupport(nelx,...
        nely,Fmag,Fang,Pmag,dom,pre_support,pre_load,volfrac)
```

In addition to `nelx`, `nely`, `dom`, and `volfrac`, other inputs to this function are `Fmag` which is a vector of force magnitudes depicted as F in Figure 8.4, `Fang` which is the corresponding vector of force angles depicted as ϕ in Figure 8.4, `Pmag` which is a vector of pressure magnitudes, `pre_support` which is an option to preserve elements carrying fixed nodes, and `pre_load` which is an option to preserve elements that define the load nodes. In this subroutine, lines 5 to 9 declare the connectivity matrices of the domain's nodal numbers and degrees of freedom which are used to extract load and support nodes.

8.3.2.1 Unidirectional Forces

Lines 12 to 30 extract the force nodes and apply the corresponding force magnitudes to form several load cases as many as the different element numbers representing forces. The user is allowed a maximum

150

of 11 force loads on a design domain from Table 8.1. Each force that represents a load case is stored in a unique column in the force matrix (the reader is referred to [54] and [129] for a robust explanation on implementing load cases in topology optimization), therefore, the size of the force matrix is determined by the total degrees of freedom (row dimension) and the number of forces (column dimension). As observed in the enlarged portion of Figure 8.4(a), the force node is located at the approximate center of the force elements and this should be considered when preparing the image representative of the design problem.
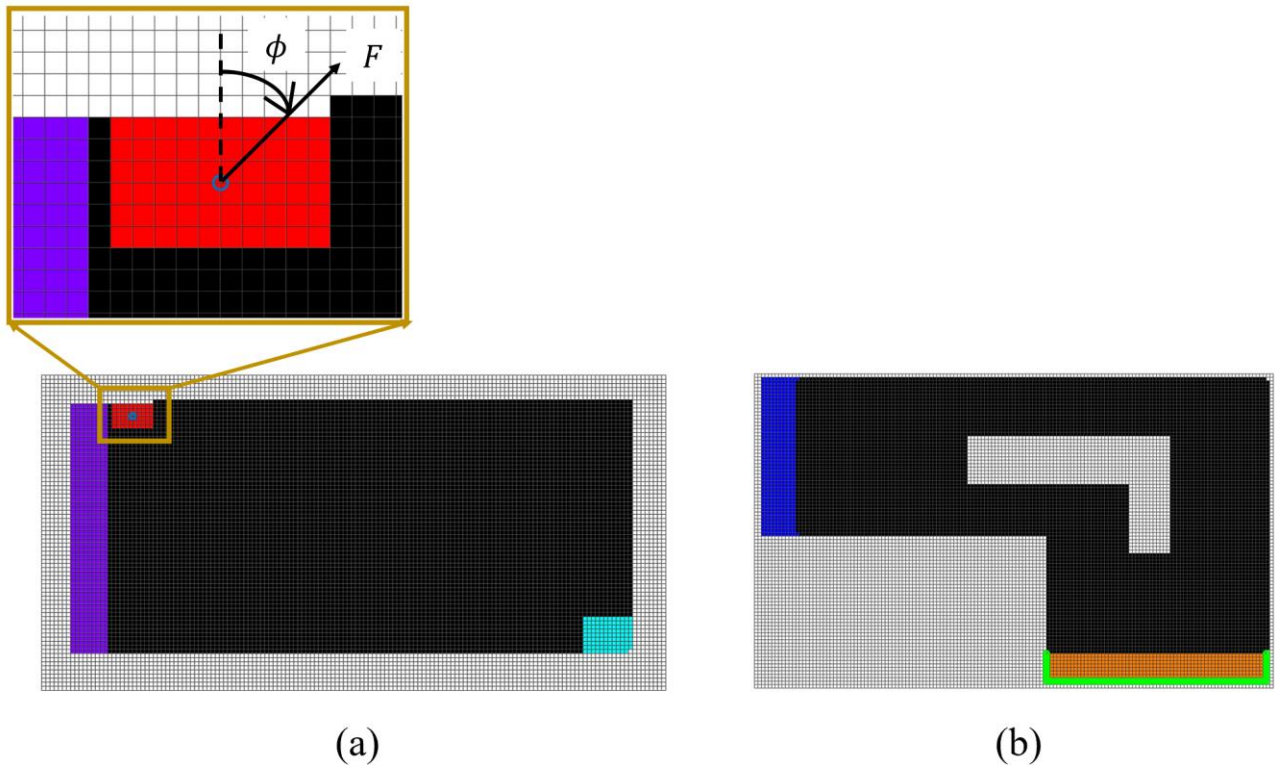
Figure 8.4: Extracting (a) a force node (in blue) and (b) pressure nodes (in green) from corresponding force (shown in red) and pressure (shown in orange) elements.

8.3.2.2 Pressure

Lines 33 to 78 implement pressure loads by first extracting boundary nodes using the subroutine `boundcurve.m` (in Line 37); this will be discussed further in the next sub-section. Pressure nodes and their corresponding angles are obtained by `boundcurve.m`. This is important because pressure loads are applied as equivalent nodal forces at the boundary of the design domain where the 'pressure elements' are situated. In Figure 8.4(b), the orange elements are 'pressure' elements, and the green outline depicts the pressure nodes at the boundary of design and non-design domains. The magnitude of

151

the equivalent forces captured in line 43 is computed as the pressure magnitude divided by the number of pressure nodes. The equivalent forces are then resolved to their rectangular coordinates from line 44 to 79 using the pressure magnitudes and angles. Like force loads, the program allows 11 different pressure loads according to the rule in Table 8.1 with each pressure load computed as a load case in the load matrix. For a design with a combination of unidirectional forces and pressures, the force and pressure load matrices are concatenated to form the global force matrix as computed in line 80.

8.3.2.3 Defining supports

Three major support types are feasible in this program: fixed, pinned, and roller supports. For a fixed support type, the degrees of freedom (DOFs) of all the nodes in the fixed region (depicted in blue) are constrained as shown in Figure 8.4(b). Like the fixed support is the pinned support with the difference in the area covered by the pinned support. Whereas the fixed support typically covers a larger area, a pinned support should cover a relatively small area. For roller supports, the support area also covers a small area but only one DOF of each node is fixed. The cyan-colored region in Figure 8.4(a) depicts a roller support type with DOF along the y-axis fixed. This area in the figure is relatively large for descriptive reasons and should be typically smaller for practical purposes. Lines 86 to 90 compute fully fixed DOFs while 91 to 96 and 97 to 102 compute fixed x- and y-DOFs respectively.

8.3.2.4 Preserved and Non-design domains

In IbIPP, three design features can be held as solids throughout the optimization: preserved, support, and load-carrying elements. Depending on the requirements of the user, multiple features can be preserved by making appropriate selections of the inputs 'preserveLoad' and 'preserveSupport' according to Table A in the Appendix. For features intended for preservation by design, there is no special selection as they should be represented in green in the input image file according to Table 8.1. Finally, regions that must be void throughout the optimization process are termed non-design features and carry an element value of 0 in the matrix $f(i, j)$. The implementation of preserved and non-design domains is carried out in Lines 106-137.

8.3.3 Boundary Identification (`boundcurve.m`)

In 8.3.2.2, a pressure load is implemented as a series of equivalent nodal forces acting normal to the pressure surface which is a curve in 2D. Consequently, in Line 37 in `loadandsupport.m,` the

`boundcurve.m` is initiated to obtain boundary nodes (Lines 3-11) and their corresponding angles (Lines 12-32) normal to the pressure curve.
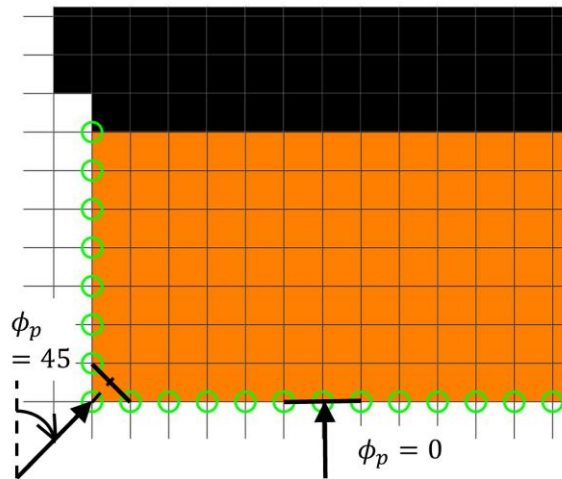
Figure 8.5: An enlarged portion of the pressure region in Figure 8.4(b) showing how pressure angles are computed.

For a node to be considered a boundary node, the mean of its surrounding elements must be between 0 and 1. In Figure 8.5, an enlarged portion of Figure 8.4 is shown to illustrate how pressure angles are computed; ϕ_p represents the angle of the equivalent force at a pressure node. For a node under consideration, the angle is obtained by connecting a line between its two nearest nodes and taking the angle from the positive vertical line to the normal to this line. Invariably, the angles possible are 0°, 45°, and 90°. A more elaborate strategy in identifying less distinctive topological boundaries can be seen in [185].

The last line in `loadandsupport.m` computes a new volume fraction to capture the effect of non-design regions during optimization.

8.3.4 Adjusting Topology Optimization codes for IbIPP

Three finite element-based topology optimization approaches have been adopted for IbIPP introduced in 8.1. For each approach, one open-source code is adopted: top88.m by Andreassen et.al [54] for SIMP/RAMP density-based method, esoL.m by Xia et.al. [221] for BESO, and levelset88.m by Otomori et.al [135] for the level-set method using a reaction-diffusion equation. Although there are newer and more efficient codes by several other authors, these were chosen because of their adaptability with IbIPP and relative popularity. To integrate the codes into IbIPP, some lines must either be deleted or modified. These modifications are as follows:

In top88.m, the material properties are slightly modified, with the user having the ability to choose the Young's Modulus and Poisson's ratio values; the default values are set to 1 and 0.3, respectively. The lines that define the loads and supports are deleted while the column size of the preallocated displacement matrix is made equal to that of the force matrix. Line 47 is changed to accommodate the Heaviside projection in conjunction with the existing density and sensitivity filters. Line 54 is changed to include the stiffness matrix setup for the RAMP interpolation scheme when the sensitivity function after projecting the physical densities is added after Line 67. In Line 66, columns are activated for the displacement and force matrices. The objective and sensitivity calculations from Lines 58 to 60 are also modified to include an option for the RAMP interpolation scheme. After Line 77, the updated physical density through the Heaviside Projection is included. An important update is enforcing the values of preserved and non-design elements to 1 for solids and 0 for voids, respectively, after updating the physical densities. In calculating the new volume fraction in Line 85, the sum of the physical densities is divided by the difference between the total number of elements and the number of non-design elements. Finally, the continuation scheme for the regularization of β is added after Line 87 using an if-else statement.

Most of the changes made in esoL.m are similar to those in top88.m. These changes can be seen in the following sections: material properties, define loads and supports, print results and plot densities, optimality criteria update of design variables.

Finally, in levelset88.m, the changes are also similar to those made in previous codes. The following sections have been modified: Parameter definition, Load and boundary settings, FE-analysis, calculate sensitivities, print results, and update level set function.

8.3.5 Post-processing (`datatostl.m`)

Several practical design problems can either be formulated or approximated as 2D problems. With this post-processing function, users can obtain manufacture-ready models, especially for 3D printing technologies. With IbIPP, a user can initialize arbitrary design domains, run topology optimization using any of the three major approaches with ample parameter control, and generate printable STL models almost seamlessly; all processes are carried out in Matlab while utilizing a regular desktop computational power. Two modeling types are possible in IbIPP: extrusion and revolution, also, symmetry can be applied. To initiate the subroutine `datatostl.m`, the name-value input 'modelName' and a corresponding filename ending with .stl in strings must be included as a function input. The subroutine is run when the following function call is made:

`datatostl(nelx,nely,xPhys,tx,form,ht,lr,theta,symm)`

`tx` is the STL filename which must end with .stl and be in string format, `form` is the modeling type, `ht` is a factor for extrusion-based modeling and it defines the extrusion length when it is multiplied by the minimum 2D dimension as illustrated in Figure 8.6(a), `lr` is a factor for revolution-based modeling that defines the distance of the optimized topology from the axis center. This distance is obtained when `lr` is multiplied by $nelx$. The axis of revolution is always parallel to the left side of the optimized 2D model as shown in Figure 8.6(b) and `theta` is the revolution angle. Finally, for symmetric design cases, `symm` allows the user to generate the mirror model of the optimized topology. Symmetric modeling and the mirror axis are specified when `symm` adopts a string input of left, bottom, right, or top as shown in Figure 8.6(c).
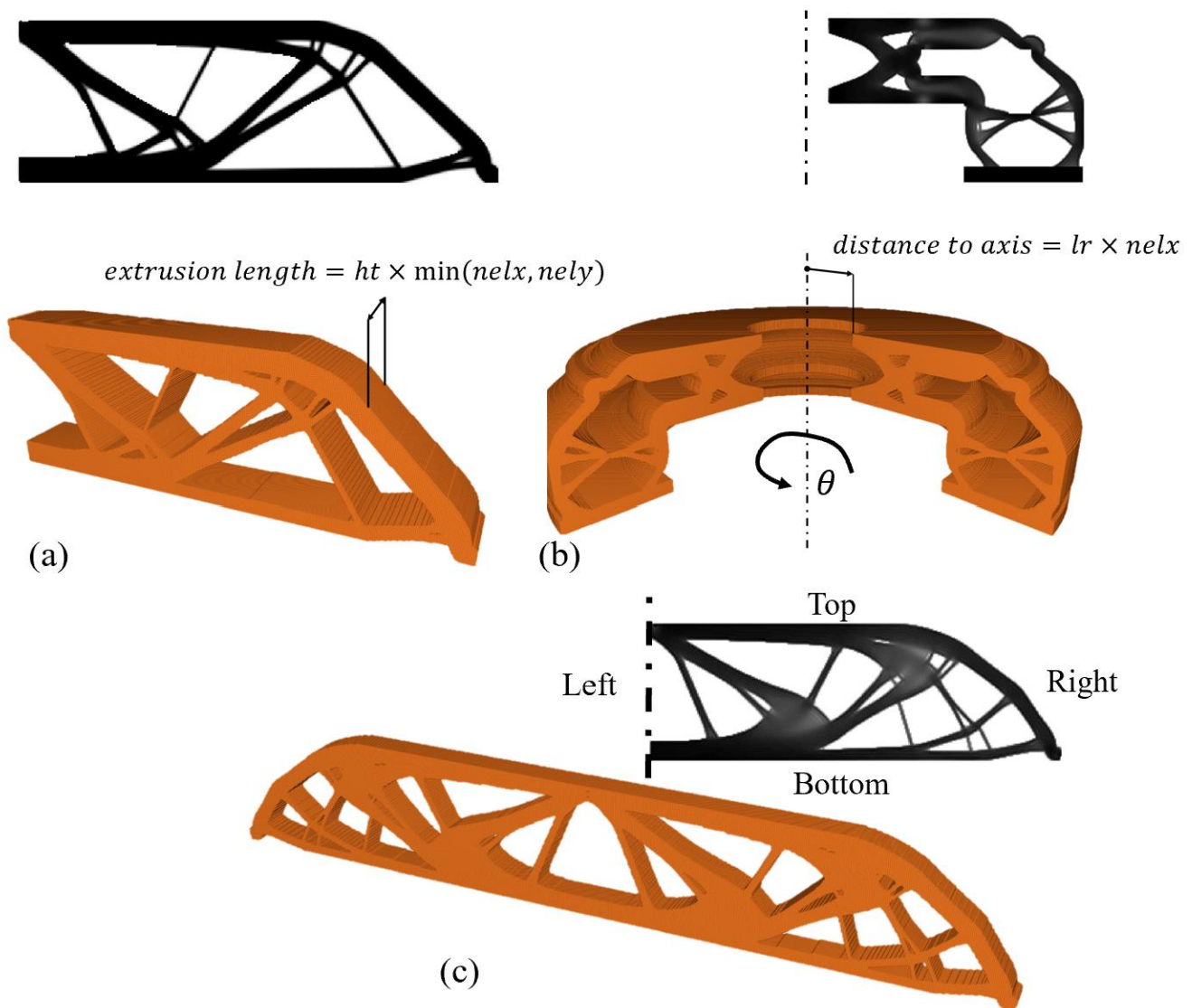
Figure 8.6: Modeling options available in IbIPP. (a) Extrusion (b) Revolution (c) Symmetry

In Line 2 in datatostl.m, a threshold of 0.5 is placed on every element of the pseudo-density matrix such that any value below is approximated to 0 or void. Lines 4 to 21 obtain the mirror form of the pseudo-density matrix only when symm has a value. Lines 23 to 35 generate a 3D matrix of the optimized topology depending on the modeling type. While simple instructions in Lines 26 to 28 handle extrusion, a subroutine revolve2D.m developed by Treeby and Cox in their k-wave Matlab Toolbox [222] was utilized to revolve a 2D matrix into 3D in Line 34. The subroutine was modified with the addition of Lines 60 to 75 in revolve2D.m to accommodate any angle of revolution. Finally, the 3D matrix is transformed into an STL file in Line 36 by the subroutine stlwrite.m developed by Sven [223].

8.4　Numerical Results

Examples are presented to elaborate on how IbIPP can be applied to different topology optimization problems. Although IbIPP is constrained to the use of homogenous 4-nodal equal bilinear quadrilateral elements, other setup and optimization parameters are easily customizable. As pointed out in section 3.4, all examples are based on the topology optimization approaches namely: SIMP density-based method implemented in top88.m by Andreassen et.al [54], BESO in esoL.m by Xia et.al. [221], and level-set method using a reaction-diffusion equation in levelset88.m by Otomori et.al [135]. To apply changes in the optimization algorithms, the reader is referred to the aforementioned articles for more details. Details of all input parameters possible in IbIPP are outlined in table A in the Appendix.

8.4.1　Example 1

Two simple problems are presented; the first is the half-MBB/MBB problem in Figure 8.7(a), which is one of the benchmark designs for topology optimization in literature over the years [109], [224], [225], [130], the other is a Hammerhead pier supporting four grid lines [224] in Figure 8.7(d). For the half-MBB, the input image in Figure 8.7(b) has the red region with color code 200,0,0 that represents the force location, the cyan region with color code 0,200,200 that represents support elements fixed in the $y-axis$ only and the purple region with color code 100,0,200 that represents support elements fixed in the $x-axis$ only. For the Hammerhead pier in Figure 8.7(d), there are four forces with regions that have color codes $(200,0,0), (205,0,0), (210,0,0), (215,0,0)$ from left to right and fixed support region with color code 0,0,200. In IbIPP, fixed DOFs are obtained from support elements while the force location is situated at the center of the load region. As observed in Figure 8.7(b,e), to better represent the design problems, the load and support regions are made as small as possible to reduce the number of elements in these regions consequently pin-pointing the force location and reducing the number of fixed DOFs. However, recall that the smaller the load and support regions the higher the resolution required for optimization, so the user should strike a balance between model accuracy and computational cost. The optimized topologies in Figure 8.7(c,f) are obtained by entering the following commands:

```
ibipp('half_mbb.png',500,0.4)
```
→ Half-MBB

```
ibipp('hammerhead.png',350,0.5,[1,1,1,1],[180,180,180,180],'preserve
    Load',1,'optimization','levelset','tau',1e-4)
```
→ Hammerhead pier
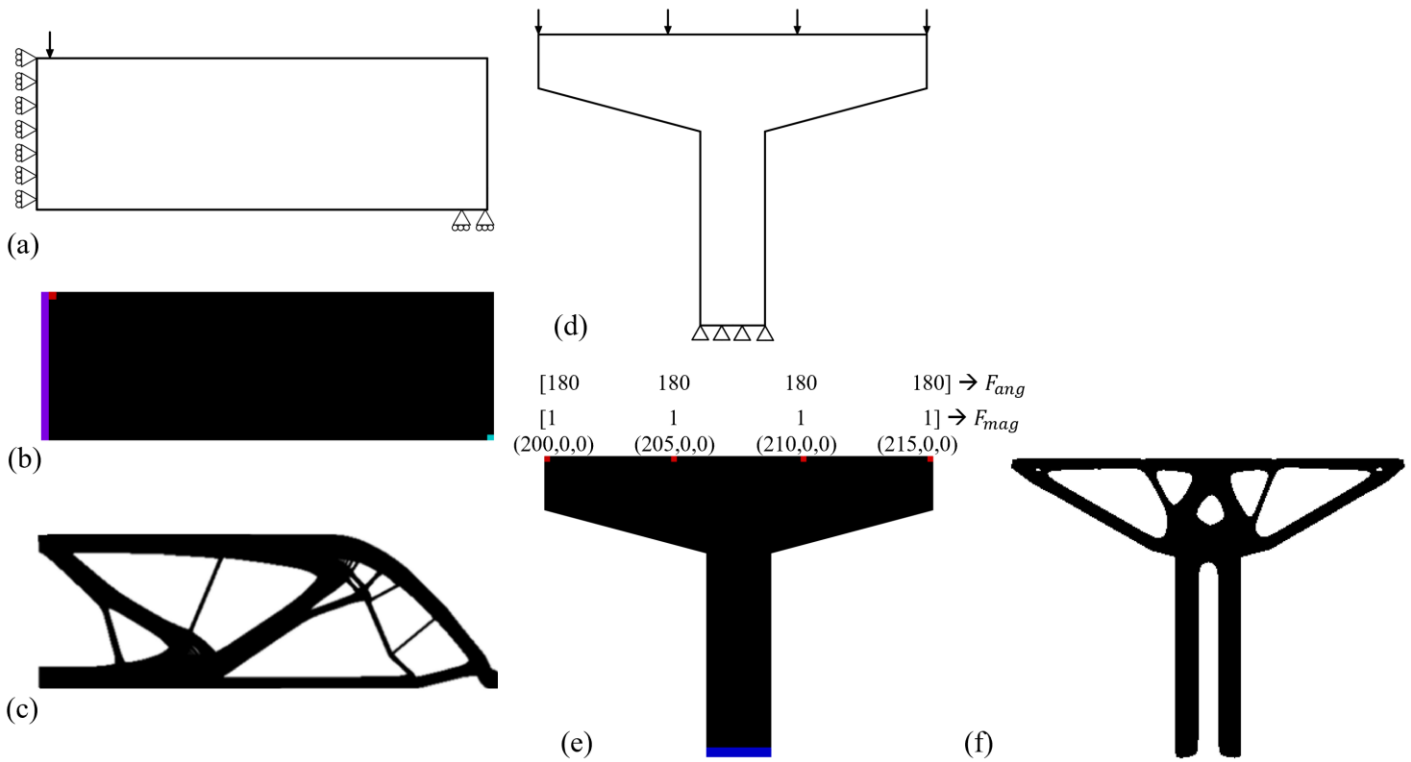
Figure 8.7: Topology optimization of (a) a half-MBB and (d) a hammerhead pier with the digital image inputs for IbIPP shown in (b) and (e), and the optimized structures in (c) and (f) respectively.

With only three input arguments for the half-MBB problem, IbIPP invokes several default values shown in Table A in the Appendix. Thus, a user can run an optimization using three arguments so long a single force is the load requirement. For multiple load cases, as seen in the Hammerhead pier, the force magnitudes and angles should be in vector form in the input argument while ensuring that the right vector element corresponds to the right load case as shown in Figure 8.7(e).

8.4.2 Example 2

The design problems showcased in this example show how preserved regions can be represented in the input image. To preserve some thickness of the bosses in the 2-point loading mechanical part in Figure 8.8(a) and the bracket in Figure 8.8(d) [142], the green preserved regions are included beside the red load regions. Therefore, in addition to 'preserveLoad', 'preserveSupport' is included as an input argument as shown in the function declarations below:

```
ibipp('2point.png',550,0.5,[2,2],[0,0],'preserveSupport',1,'preserve
        Load',1,'filterRadius',2)→ 2-point loading mechanical part
```

```
ibipp('bracket.png',500,0.4,1,90,'preserveSupport',1,'preserveLoad',
    1,'filterRadius',2,'optimization','BESO','ER',0.15)→ bracket
```

At the boundary between force and preserved regions, there exists an element-sized interface that is neither a force nor a preserved region but a design domain (which may remain or be removed after optimization). This is so because this interface is a mean of both regions ($mean([200,0,0], [0,200,0]) = [100,100,0]$) and therefore falls within the designable domain according to Table 8.1. The significance of this interface is greatly reduced when a high resolution is used for optimization. The optimized topologies are observed in Figure 8.8(c,f) and a close examination of Figure 8.8(c) will reveal that the elements within this interface have lower density values compared to neighboring elements. However, if the topology is extruded or revolved, more often than not, there will be no opening since a threshold of 0.5 for a solid element is placed on the density matrix in `datatostl.m`.
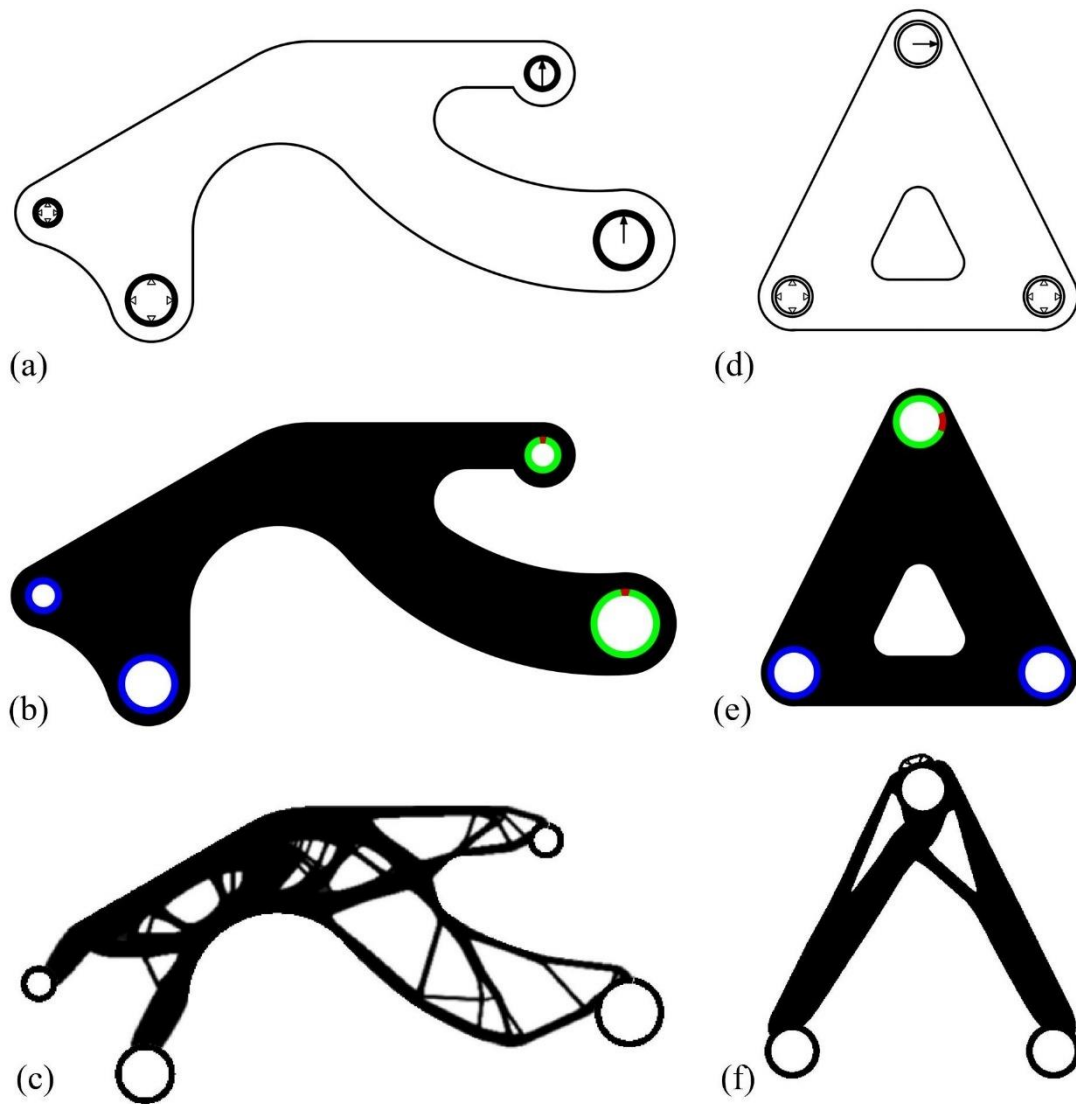
Figure 8.8: Topology optimization of a 2-point loading mechanical part (a-c) and a bracket (d-f). (a,d) show the design domains, (b,e) show the image input for IbIPP, and (c,f) show the optimized topologies

8.4.3 Example 3

In this penultimate example, a proximal femur model in Figure 8.9(a) is optimized. Two pressure loads are located at two top surfaces while the bottom surface is given a fixed condition. In the image representation, it is observed that the load and fixed regions are almost invisible except enlarged in Figure 8.9(b). This is due to the thin outer layer was preserved at the top of the bone, and consequently, and a fine resolution was used for optimization. As was pointed out in Example 1 for force loads, every pressure load region with a different magnitude is assigned a unique color code starting with $G = 100$

in steps of 5. The image in Figure 8.9(b) has two pressure load cases having color codes 200,100,0 and 200,105,0 from left to right. As is common for the optimization of structures under pressure loads, there are some grey regions or elements with intermediate density values in the optimized topology in Figure 8.9(c). In this example, the RAMP density-based approach was utilized for optimization, and to reduce intermediate elements formed, especially in later stages of the optimization, a gradual increase from a low to high penalization factor can be utilized. Using a high penalty value throughout the optimization is feasible but will likely cause numerical instabilities as the number of iterations increases. The problem was solved by the function declaration:

```
ibipp('bone.png',400,0.5,'pressure',[1,2],'filter',3,'filterRadius',
              1.5,'preserveLoad',2,'densityType','RAMP')
```
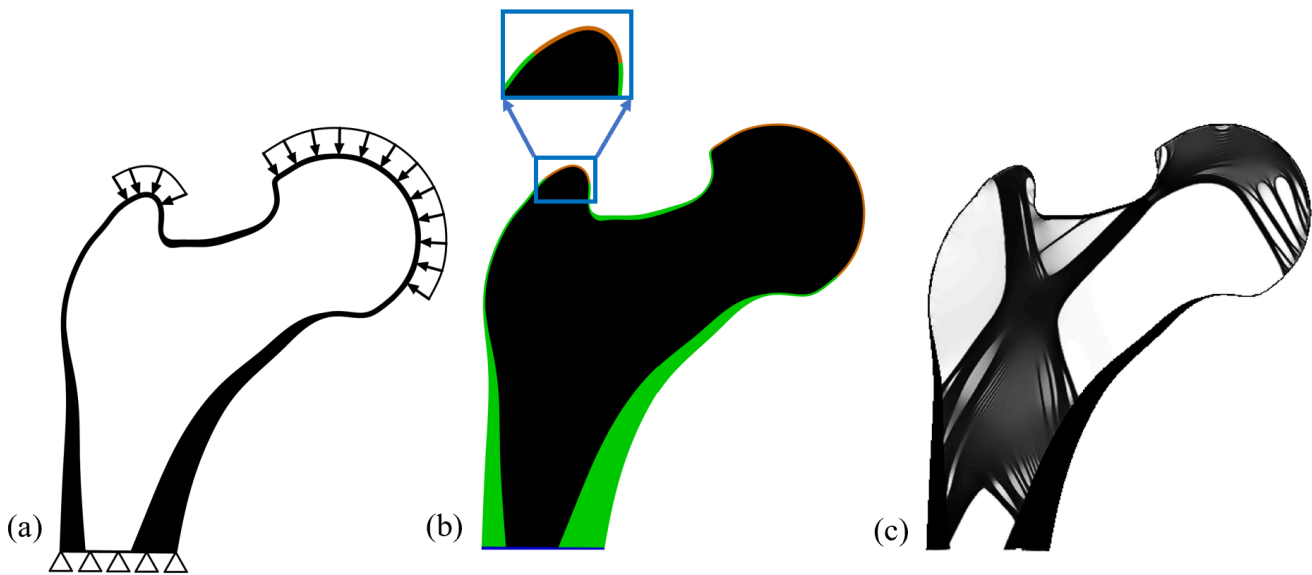

Figure 8.9: Topology optimization of a proximal femur model. (a) Design domain with load and boundary conditions, (b) input image for IbIPP, (c) optimized topology

8.4.4 Example 4

To implement the post-processing subroutine of IbIPP, two design problems are considered. The first is one half of a spanner design with the authors' lab acronym (MSAM) inscribed as shown in Figure 8.10(a). Half of the design is considered for optimization to save computational cost and time since a line of symmetry can be drawn in the middle. It is observed that additional regions are added as fixed regions in Figure 8.10(b) just to ensure some more material is distributed towards the head of the spanner. After the model is optimized in Figure 8.10(c), the post-processing subroutine `datatostl.m` receives

the density matrix and other data required for extrusion. By concatenating density matrix and its mirror matrix, and applying an extrusion length, the optimized model is obtained in Figure 8.10(d). For manufacturing purposes, such as printing the part, smoothening procedures might be required depending on the resolution of the optimization. Open-source codes such as MeshLab [204] can be used for smoothening and other mesh-related operations. Laplacian [226] and Taubin [227] Smooth operations were performed on the generated models in this example. The spanner model was printed using PLA via Fused Deposition Modeling (FDM) as shown in Figure 8.10(e). The user should recall that post-processing is only initiated when the name-value input 'modelName' is included as an input argument in the function declaration as shown below:

```
ibipp('half_spanner.png',500,0.5,'pressure',[1e6,1e6],'preserveSuppo
rt',1,'preserveLoad',2,'filter',3,'filterRadius',2,'YoungsModulus',1
90e9,'symmetry','right','modelName','spanner.stl','modelType','extru
de','extrudeLength',0.2)
```
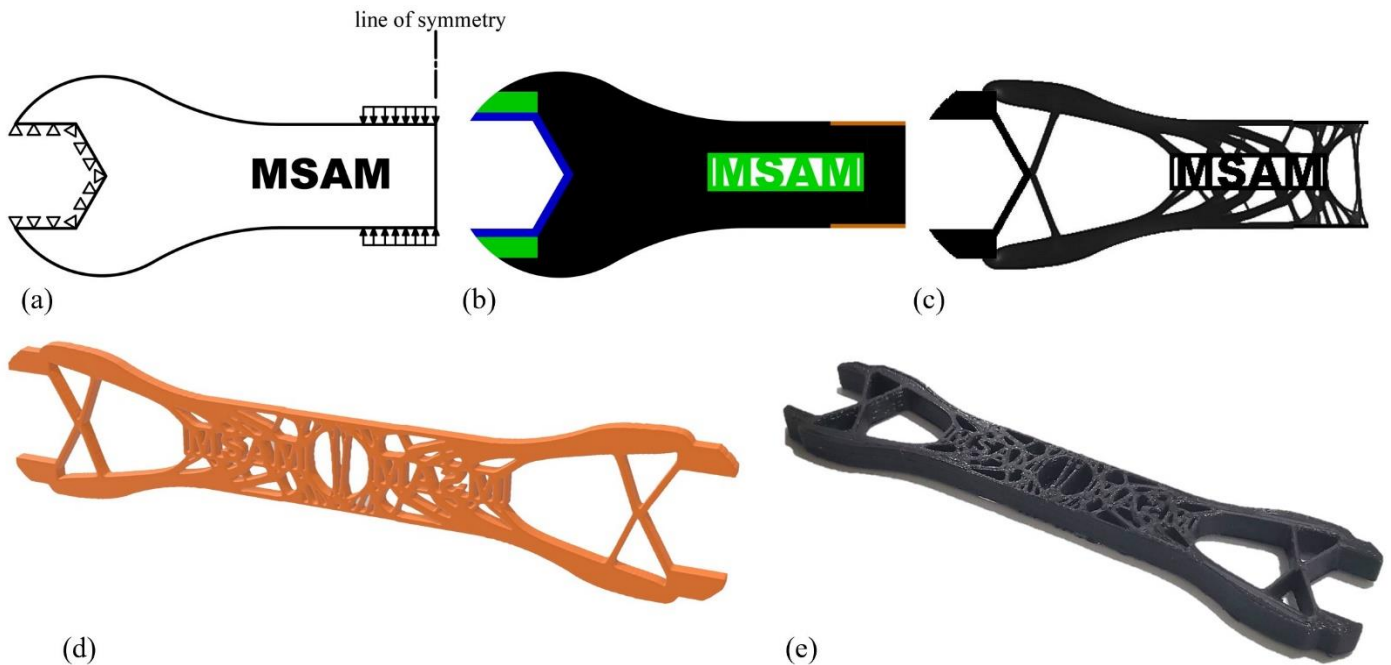

Figure 8.10: Workflow for generating an optimized spanner model using IbIPP. (a) The design problem with load and boundary conditions, (b) input image (c) optimized topology (d) generated model via symmetry and extrusion (e) printed spanner

The second design is a curved cantilever beam shown in Figure 8.11(a) intended for revolution. The workflow is similar to the previous example with a difference in the 'modelType' and inputs

'distancetoaxis' and 'revolutionAngle' in place of 'symmetry' and 'extrudeLength'. It should be noted that symmetry can also be applied to a model intended for revolution depending on the nature of the problem. However, care must be taken in applying the correct inputs. The inputs for 'Symmetry' are 'left', 'bottom', 'right', and 'top' as illustrated in Figure 8.6(c) and described in Table A in the Appendix. The optimized and revolved model are shown in Figure 8.11(c) and Figure 8.11(d) while the printed PLA part using FDM is shown in Figure 8.11(e). The function declaration for this design problem is:

```
ibipp('circularpart.png',450,0.4,1500,270,'YoungsModulus',190e9,'opt
imization','BESO','filterRadius',4,'modelName','circularpart.stl','m
odelType','revolve','revolutionAngle',100,'distancetoaxis',0.1)
```
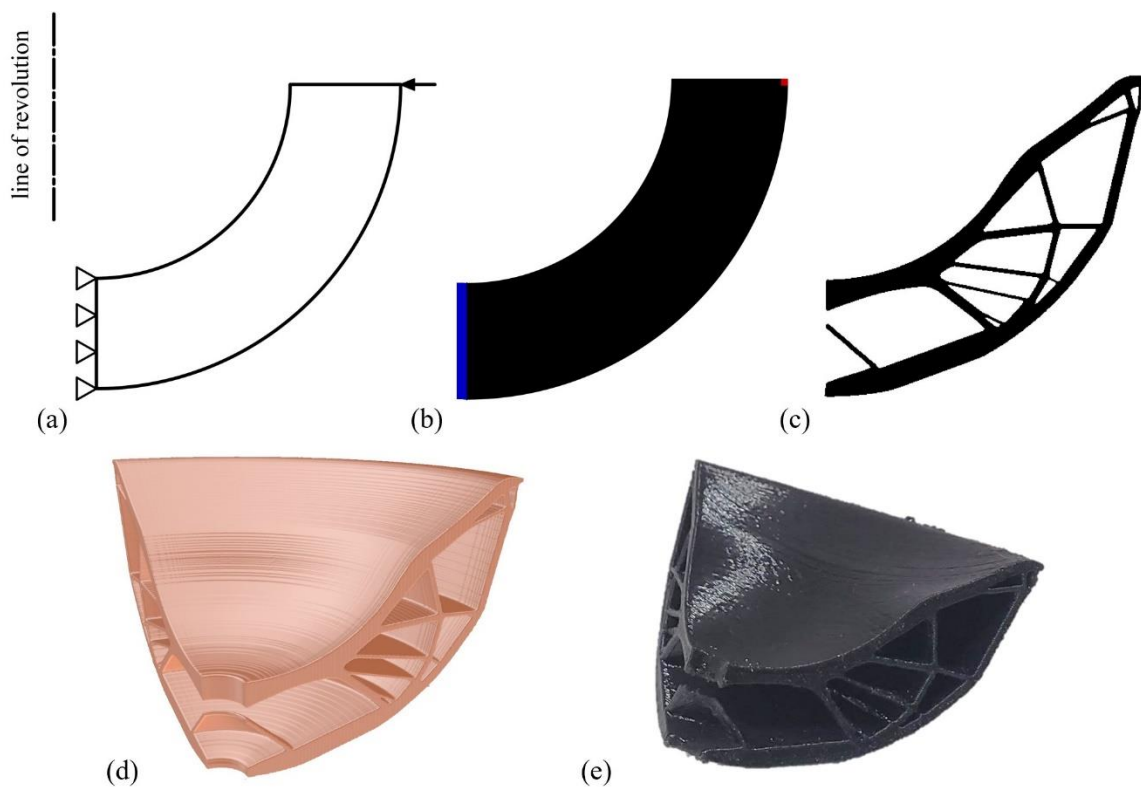

Figure 8.11: Workflow for optimizing a curved cantilever beam meant for revolution. (a) The design problem of the cantilever cross-section with load and boundary conditions, (b) input image (c) optimized topology (d) revolved model (e) printed part

8.5 Note on extensions

In the authors' best knowledge, IbIPP is the first open-source image-based initialization and post-processing code for topology optimization; therefore, there are many opportunities for enhancements. Some modifications and additions that can be made are not limited to the following:

a. The exclusion of non-design elements in the optimization process. Because an image is always a rectangular/square representation, intricate design problems such as the several numerical examples presented will leave an undesirable number of non-design elements, which will cause unnecessary entries in several matrices. This will also significantly influence the computational cost in computing the H-matrix in density-based approaches and increase storage requirements for pre-allocated matrices. To exclude non-design elements from the optimization process, the connectivity matrices for node numbers and DOFs in Lines 7 and 9 in `loadandsupport.m`, Lines 13 to 15 in `top88.m` and `esoL.m`, Lines 25 to 27 and 33 to 34 in `levelset88.m` should be modified to exclude these elements. This will potentially also necessitate changes in a few other sections in these functions.

b. Since IbIPP is suitable for discrete gradient-based topology approaches by utilizing finite elements, any new discrete approach can be easily included within Lines 63 and 73 in `ibipp.m` while ensuring the new approach is adapted accordingly with the discussion in Section 3.4 serving as a reference. Also, other efficient optimizers such as MMA, GCMMA can be used for density-based methods enabling multi-constraint problems and ensuring global optimums.

c. Other load types (such as heat fluxes, temperature constraints, voltages) and non-classical boundary conditions can be considered in `imageprocessor.m` subroutine. This will only involve expanding or modifying the color code rules in Table 8.1 according to the user's requirements. Consequently, `imageprocessor.m` and `loadandsupport.m` have to be modified to identify the new loads and/or boundary conditions. This is quite straightforward because the process of identifying these new entities should typically be the same as those already captured in IbIPP.

8.6 Summary

An image-based initialization and post-processing code for 2D topology optimization has been developed. It takes in an input image developed according to certain color code rules that correctly represent the features in a design problem for topology optimization. Depending on the user's choice, it can also obtain a printable model based on the optimized topology. It offers a variety of advantages for research and educational purposes:

a) It breaks the barrier of initializing arbitrary design domains and the flexibility in representing loads and boundary conditions.

b) It offers researchers the ability to test a variety of design problems without frequently modifying or writing new lines of code.

c) It deploys several topology optimization approaches ensuring that researchers, teachers, and students can use a variety of these approaches with relative flexibility. It also facilitates the addition of new approaches.

d) In many instances, the topological results might be required to undergo experimental tests. IbIPP provides a simplistic and easy platform to generate extruded, mirrored or revolved models. For low-resolution optimizations, the generated models might be composed of features with many jagged edges; open-source mesh-based tools can be employed to smoothen the features.

These capabilities have been demonstrated and further work to improve sections of this tool and translate the code into other languages will be done. This source code is available at https://github.com/CADmaniac/IbIPP.git and this chapter has been published [228].

Chapter 9: Conclusions and Future Work

9.1 Conclusions

In this work, methodologies have been established to address topology optimization of structures under design-dependent loads and additive manufacturing constraints. Design-dependent loads captured in this work are thermal stress, centrifugal, and pressure loads, while manufacturing constraints considered are overhang feature angle and minimum feature size. To accomplish these objectives, first, a load thresholding approach was adopted to analyze the design-dependent loads and select load type(s) for thresholding. Secondly, design-dependent pressure loads were resolved by a novel Boundary Identification and Load Evolution (BILE) model. Thirdly, sensitivity scaling was introduced in the weighted multiobjective optimization problem for bi- and tri-objective topology optimization. Fourthly, a novel post-topology optimization process was developed to eliminate overhanging features while restricting feature sizes, thereby ensuring the manufacturability of structures produced by AM technologies. Finally, experimental validation studies were carried out for the post-topology optimization methodology, while an open-source framework for initializing 2D topology optimization problems and post-processing density image maps to STL files was developed.

The following conclusions can be drawn from the frameworks developed:

1. Load thresholding can be applied to simplify design-dependent loads with a closely packed magnitude distribution and high directional randomness in the discretized domain. Thermal stress loads (TSLs) and centrifugal loads were analyzed for a case study and TSLs were found to match the aforementioned characteristics.
2. A simplistic and computationally efficient BILE model was developed to resolve design-dependent pressure loads for topology optimization.
3. The BILE model is simplistic and computationally efficient because it ensures insignificant differential changes of 'equivalent' forces with respect to the density design variable, thereby constraining the pressure load sensitivity to zero.
4. All the results for topology optimization problems presented using the BILE model were obtained under 80 seconds, and 100 iterations for several 2D problems discretized between 5,000 to 13,000 four-nodal square elements using an average desktop computer.
5. All the results obtained using the BILE model closely match those obtained by other recent and older methodologies in the literature.

166

6. Scale factors, in addition to weight factors, were introduced to load sensitivities for multiobjective topology optimization. This is to establish a balance in magnitude between all load sensitivities making it possible to use monotonic optimizers such as OCM and MMA for complex multiphysics and multiobjective topology optimization problems.

7. Some of the results of bi-objective topology optimization (for centrifugal loads and a point force) were compared with results from literature, and a good match was found. Also, the results of tri-objective topology optimization were compared with those obtained from Hypermesh®, although key features of the final topologies corresponded, variations were present due to the significant differences in the adopted optimization approach and the implementation of design-dependent pressure loads.

8. A novel post-topology optimization process has been developed to address a coupled overhang feature angle and feature size control, which are important AM constraints

9. Although the overhang elimination strategy is post-topology optimization, there is a seamless workflow from topology optimization because the type and number of design elements, density variables, feature size limit, and other controlling parameters are inputs in the strategy.

10. Data conversion or transformation is required in a previous post-topology optimization process in [196]; however, it is not necessary for this novel method, therefore, both tools (topology optimization and overhang elimination) can be deployed easily as one.

11. In the post-topology optimization method for overhang elimination, there is complete independence from several aspects of the topology optimization method, such as interpolation methods, optimizer types, parameter tuning, etc. However, the methodology is restricted to the use of 4-nodal square elements.

12. In the overhang elimination methodology, the user or designer can prescribe strict strut requirements such as thickness, orientation or angle, space between strut roots, and size of strut root (which in turn influences the number of struts added).

13. Post-topology optimization processes for overhang elimination can result in a volume increase of over 22%, and this new method can eliminate this by introducing a volume correction. Time analysis revealed that the stages of boundary identification and overhang elimination only took around 8% of the total time for the whole process. Using FDM and LPBF, this methodology was validated for manufacturability.

14. The effects of manufacturing constraints on surface residual stresses were observed to be negligible for optimized Hastelloy X parts.

15. The effects of manufacturing constraints on the performance of structures were experimentally investigated. A 30% decrease in the maximum force attainable (40% increase in compliance) was observed from a structure without overhang angle restriction to one with a 65° angle threshold. Also, an increase in the minimum feature size from $5a$ to $7a$ slightly decreased the height of the load-displacement curves.

16. The number and magnitude of manufacturing constraints on a design can reduce the performance of a structure; however, overhang angle restriction contributes to a lower performance than feature size control. In general, lower thresholds for manufacturing constraints are encouraged for performance optimality.

17. A simple image-based initialization and open-source post-processing code for 2D topology optimization has been written in Matlab for research and educational purposes.

The developed and implemented methodologies expand the capabilities of current topology optimization strategies for design for additive manufacturing as it bothers on design-dependent load considerations and AM manufacturability. These methodologies can be further developed into new software packages for topology optimization or plugins for existing CAD-related tools.

9.2 Future work

The several extensions of this work that can be done are:

1. A variety of design case studies can be investigated while considering other design-dependent loads, such as the effects of gravitational pull and fluid-flow for multi-objective topology optimization.

2. Even with the use of scaled sensitivities, the topology optimization process is not devoid of numerical instabilities, especially when high weight factors for TSLs and centrifugal loads are used. The use of other robust and non-monotonic optimizers such as the family of convex approximations like the Globally Convergent Method of Moving Asymptotes (GCMMA) [229], Gradient-Based Method of Moving Asymptotes (GBMMA) [230], Interior-Point Optimization (IPOPT) [181], and Method of Diagonal Quadratic Approximation (MDQA) [182], [231] should be explored.

3. The 3D extension of the BILE model for design-dependent pressure loads should be developed.

4. To tackle more practical design problems, the 3D extension of the multi-objective topology optimization should be developed and studied.

5. Robust experiments on the results from the multiphysics and multi-objective topology optimization model are recommended for validation and the provision of insights to possible enhancements.

6. Anisotropic material properties should be considered in the multiphysics and multiobjective topology optimization model.

7. The post-topology optimization overhang elimination process is currently developed in 2D, an extension should be made to 3D where it will be particularly useful.

8. Channel or void minimization/elimination should be considered as a constraint or filter in the AM-constrained topology optimization model.

9. The image-based initialization and post-processing code can be written in other languages such as Python and C++, this will ensure a wider adoption and versatility.

Letter of Copyright Permission
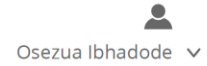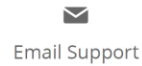
SPRINGER NATURE

Topology optimization of structures under design-dependent pressure loads by a boundary identification-load evolution (BILE) model

Author: Osezua Ibhadode et al

Publication: Structural and Multidisciplinary Optimization

Publisher: Springer Nature

Date: May 15, 2020

Copyright © 2020, Springer-Verlag GmbH Germany, part of Springer Nature

Order Completed

References

[1]   R. Ranjan, R. Samant, and S. Anand, "Integration of Design for Manufacturing Methods With Topology Optimization in Additive Manufacturing," vol. 139, no. June 2017, pp. 1–14, 2018, doi: 10.1115/1.4035216.

[2]   M. E. Orme *et al.*, "Designing for Additive Manufacturing : Lightweighting Through Topology Optimization Enables Lunar Spacecraft," pp. 1–6, 2018, doi: 10.1115/1.4037304.

[3]   ASTM, "Standard Terminology for Additive Manufacturing – General Principles – Terminology," *ASTM Int.*, vol. i, pp. 1–9, 2015, doi: 10.1520/F2792-12A.2.

[4]   M. F. Cruz and A. V. Borille, "Decision methods application to compare conventional manufacturing process with metal additive manufacturing process in the aerospace industry," *J. Brazilian Soc. Mech. Sci. Eng.*, vol. 39, no. 1, pp. 177–193, 2017, doi: 10.1007/s40430-016-0532-8.

[5]   R. Stolt, T. Heikkinen, and F. Elgh, "Integrating Additive Manufacturing in the Design of Aerospace Components," vol. 0, pp. 145–154, 2018, doi: 10.3233/978-1-61499-898-3-145.

[6]   K. V Fetisov and P. V Maksimov, "Topology optimization and laser additive manufacturing in design process of efficiency lightweight aerospace parts Topology optimization and laser additive manufacturing in design process of efficiency lightweight aerospace parts," 2018.

[7]   A. Gaymann, F. Montomoli, and M. Pietropaoli, "Design for Additive Manufacturing: Valves Without Moving Parts," pp. 1–8, 2018.

[8]   A. W. Gebisa and H. G. Lemu, "A case study on topology optimized design for additive manufacturing," *IOP Conf. Ser. Mater. Sci. Eng.*, vol. 276, no. 1, 2017, doi: 10.1088/1757-899X/276/1/012026.

[9]   M. Bici, G. B. Broggiato, and F. Campana, "Topological Optimization in Concept Design: starting approach and a validation case study," *Adv. Mech. Des. Eng. Manuf.*, pp. 289–299, 2017, doi: 10.1007/978-3-319-45781-9.

[10]   M. Abdi, I. Ashcroft, and R. D. Wildman, "Design optimisation for an additively manufactured automotive component," *Int. J. Powertrains*, vol. 7, no. 1/2/3, p. 142, 2018, doi: 10.1504/IJPT.2018.090371.

[11] S. N. K. Reddy, V. Maranan, T. W. Simpson, T. Palmer, and C. J. Dickman, "Application of Topology Optimization and Design for Additive Manufacturing Guidelines on an Automotive Component," *Proc. ASME 2016 Int. Des. Eng. Tech. Conf. Comput. Inf. Eng. Conf.*, pp. 1–10, 2018.

[12] H. Shahali, A. Jaggessar, and P. K. D. V. Yarlagadda, "Recent Advances in Manufacturing and Surface Modification of Titanium Orthopaedic Applications," *Procedia Eng.*, vol. 174, pp. 1067–1076, 2017, doi: 10.1016/j.proeng.2017.01.259.

[13] L. Jiang, S. Chen, C. Sadasivan, and X. Jiao, "Structural Topology Optimization for Generative Design of Personalized Aneurysm Implants: Design, Additive Manufacturing, and Experimental Validation," *2017 IEEE Healthc. Innov. Point Care Technol. HI-POCT 2017*, vol. 2017-Decem, pp. 9–13, 2017, doi: 10.1109/HIC.2017.8227572.

[14] C. A. G. Pérez, H. I. Medellín-castillo, R. Espinosa-castañeda, U. Autónoma, D. S. Luis, and S. L. Potosí, "Computer Assisted Design and Structural Topology Optimization of Customized Craniofacial Implants," *roceedings ASME 2017 Int. Mech. Eng. Congr. Expo.*, pp. 1–11, 2018.

[15] R. Hu, W. Chen, D. Ph, Q. Li, S. Liu, and P. Zhou, "Design optimization method for additive manufacturing of the primary mirror of a large-aperture space telescope," *J. Aerosp. Eng.*, vol. 30, no. 3, pp. 1–10, 2017, doi: 10.1061/(ASCE)AS.1943-5525.0000690.

[16] H. Herzog *et al.*, "Optical fabrication of lightweighted 3D printed mirrors," *Proc. SPIE*, vol. 9573, no. September 2015, p. 957308, 2015, doi: 10.1117/12.2188197.

[17] M. Pietropaoli, R. Ahlfeld, F. Montomoli, A. Ciani, and M. D'Ercole, "Design for Additive Manufacturing: Internal Channel Optimization," *Vol. 5B Heat Transf.*, vol. 139, no. October 2017, p. V05BT11A013, 2016, doi: 10.1115/GT2016-57318.

[18] J. Sepp and A. Hupfer, "Topology Optimization in Structural Design of a Lp Turbine Guide," *ASME Turbo Expo 2014 Turbine Tech. Conf. Expo.*, pp. 1–10, 2014, doi: 10.1115/GT2014-25637.

[19] M. E. Lynch *et al.*, "Design and topology/shape structural optimisation for additively manufactured cold sprayed components: This paper presents an additive manufactured cold spray component which is shape optimised to achieve 60% reduction in stress and 20% reduction in weigh," *Virtual Phys. Prototyp.*, vol. 8, no. 3, pp. 213–231, 2013, doi: 10.1080/17452759.2013.837629.

[20] R. Rezaie, M. Badrossamay, A. Ghaei, and H. Moosavi, "Topology optimization for fused deposition modeling process," *Procedia CIRP*, vol. 6, pp. 521–526, 2013, doi: 10.1016/j.procir.2013.03.098.

[21] F. Mezzadri, V. Bouriakov, and X. Qian, "Topology optimization of self-supporting support structures for additive manufacturing," *Addit. Manuf.*, vol. 21, no. April, pp. 666–682, 2018, doi: 10.1016/j.addma.2018.04.016.

[22] X. Guo, J. Zhou, W. Zhang, Z. Du, C. Liu, and Y. Liu, "Self-supporting structure design in additive manufacturing through explicit topology optimization," *Comput. Methods Appl. Mech. Eng.*, vol. 323, pp. 27–63, 2017, doi: 10.1016/j.cma.2017.05.003.

[23] Z. Li, D. Z. Zhang, P. Dong, I. Kucukkoc, and B. Peikang, "Incorporating draw constraint in the lightweight and self-supporting optimisation process for selective laser melting," *Int. J. Adv. Manuf. Technol.*, pp. 1–8, 2018, doi: 10.1007/s00170-018-2251-z.

[24] S. Liu, Q. Li, W. Chen, L. Tong, and G. Cheng, "An identification method for enclosed voids restriction in manufacturability design for additive manufacturing structures," *Front. Mech. Eng.*, vol. 10, no. 2, pp. 126–137, 2015, doi: 10.1007/s11465-015-0340-3.

[25] N. Meisel and C. Williams, "An Investigation of Key Design for Additive Manufacturing Constraints in Multimaterial Three-Dimensional Printing," *J. Mech. Des.*, vol. 137, no. 11, p. 111406, 2015, doi: 10.1115/1.4030991.

[26] Y. Mass and O. Amir, "Topology optimization for additive manufacturing : Accounting for overhang limitations using a virtual skeleton," *Addit. Manuf.*, vol. 18, pp. 58–73, 2017, doi: 10.1016/j.addma.2017.08.001.

[27] T. Gao and W. Zhang, "Topology optimization involving thermo-elastic stress loads," *Struct. Multidiscip. Optim.*, vol. 42, no. 5, pp. 725–738, 2010, doi: 10.1007/s00158-010-0527-5.

[28] D. LI, "Multi-objective Topology Optimization of Thermo-mechanical Compliant Mechanisms," *Chinese J. Mech. Eng.*, vol. 24, no. 06, p. 1123, 2011, doi: 10.3901/CJME.2011.06.1123.

[29] B. Zheng and H. C. Gea, "Topology Optimization Considering Gravitational and Centrifugal Forces," *Proc. IDETC2006 ASME 2006 Int. Des. Eng. Tech. Conf. Comput. Inf. Eng. Conf.*, 2006.

[30] E. C. Hooijkamp and F. van Keulen, "Topology optimization for linear thermo-mechanical

transient problems: Modal reduction and adjoint sensitivities," *Int. J. Numer. Methods Eng.*, vol. 113, no. 8, pp. 1230–1257, 2018, doi: 10.1002/nme.5635.

[31] Q. Li, G. P. Steven, and Y. M. Xie, "Thermoelastic topology optimization for problems with varying temperature fields," *J. Therm. Stress.*, vol. 24, no. 4, pp. 347–366, 2001, doi: 10.1080/01495730151078153.

[32] J. H. K. Haertel and G. F. Nellis, "A fully developed flow thermofluid model for topology optimization of 3D-printed air-cooled heat exchangers," *Appl. Therm. Eng.*, vol. 119, pp. 10–24, 2017, doi: 10.1016/j.applthermaleng.2017.03.030.

[33] J. H. Klaas, "Design of Thermal Systems Using Topology Optimization Jan Hendrik Klaas Haertel Department of Energy Conversion and Storage Ph . D . Thesis , December 2017," 2018.

[34] M. Attaran, "The rise of 3-D printing : The advantages of additive manufacturing over traditional manufacturing," *Bus. Horiz.*, vol. 60, no. 5, pp. 677–688, 2017, doi: 10.1016/j.bushor.2017.05.011.

[35] P. Stavropoulos and P. Foteinopoulos, "Modelling of additive manufacturing processes : a review and classi fi cation," *Manuf. Rev.*, vol. 5, no. 2, 2018.

[36] A. Busachi, J. Erkoyuncu, P. Colegrove, F. Martina, C. Watts, and R. Drake, "A review of Additive Manufacturing technology and Cost Estimation techniques for the defence sector," *CIRP J. Manuf. Sci. Technol.*, vol. 19, pp. 117–128, 2017, doi: 10.1016/j.cirpj.2017.07.001.

[37] K. V. Wong and A. Hernandez, "A Review of Additive Manufacturing," *ISRN Mech. Eng.*, vol. 2012, pp. 1–10, 2012, doi: 10.5402/2012/208760.

[38] M. K. Thompson *et al.*, "Design for Additive Manufacturing: Trends, opportunities, considerations, and constraints," *CIRP Ann. - Manuf. Technol.*, vol. 65, no. 2, pp. 737–760, 2016, doi: 10.1016/j.cirp.2016.05.004.

[39] A. W. Gebisa and H. G. Lemu, "Design for manufacturing to design for Additive Manufacturing: Analysis of implications for design optimality and product sustainability," *Procedia Manuf.*, vol. 13, pp. 724–731, 2017, doi: 10.1016/j.promfg.2017.09.120.

[40] M. Orquéra, S. Campocasso, and D. Millet, "Design for Additive Manufacturing Method for a Mechanical System Downsizing," *Procedia CIRP*, vol. 60, pp. 223–228, 2017, doi:

10.1016/j.procir.2017.02.011.

[41] U. Khaleeq uz Zaman, A. Siadat, M. Rivette, A. A. Baqai, and L. Qiao, "Integrated product-process design to suggest appropriate manufacturing technology: a review," *Int. J. Adv. Manuf. Technol.*, vol. 91, no. 1–4, pp. 1409–1430, 2017, doi: 10.1007/s00170-016-9765-z.

[42] E. Asadollahi-Yazdi, J. Gardan, and P. Lafon, "Integrated Design for Additive Manufacturing Based on Skin-Skeleton Approach," *Procedia CIRP*, vol. 60, no. 2212, pp. 217–222, 2017, doi: 10.1016/j.procir.2017.02.007.

[43] D. S. Nguyen and F. Vignat, "Topology Optimization as an Innovative Design Method for Additive Manufacturing," *Proc. 2017 IEEE IEEM*, pp. 304–308, 2017, doi: 10.1109/IEEM.2017.8289901.

[44] K. Salonitis and S. Al Zarban, "Redesign optimization for manufacturing using additive layer techniques," *Procedia CIRP*, vol. 36, pp. 193–198, 2015, doi: 10.1016/j.procir.2015.01.058.

[45] S. Hällgren, L. Pejryd, and J. Ekengren, "(Re)Design for Additive Manufacturing," *Procedia CIRP*, vol. 50, pp. 246–251, 2016, doi: 10.1016/j.procir.2016.04.150.

[46] S. Yang and Y. F. Zhao, "Additive manufacturing-enabled design theory and methodology: a critical review," *Int. J. Adv. Manuf. Technol.*, vol. 80, no. 1–4, pp. 327–342, 2015, doi: 10.1007/s00170-015-6994-5.

[47] M. Kumke, H. Watschke, and T. Vietor, "A new methodological framework for design for additive manufacturing," *Virtual Phys. Prototyp.*, vol. 11, no. 1, pp. 3–19, 2016, doi: 10.1080/17452759.2016.1139377.

[48] M. P. Bendsøe and O. Sigmund, *Topology optimization: theory, methods, and applications*, vol. 2nd Editio, no. 724. 2003.

[49] P. W. Christensen and A. Klarbring, *An Introduction to Structural Optimization*, vol. 153. 2009.

[50] G. I. N. Rozvany, "A critical review of established methods of structural topology optimization," *Struct. Multidiscip. Optim.*, vol. 37, no. 3, pp. 217–237, 2009, doi: 10.1007/s00158-007-0217-0.

[51] E. Meli and A. Rindi, "Innovative Structural Topology Optimization Approach for Rotodynamics Components using Innovative Materials and New Manufacturing Techniques," *Proc. ASME 2017 Int. Des. Eng. Tech. Conf. Comput. Inf. Eng. Conf.*, vol. V, pp. 1–11, 2017.

[52] J. Liu and Y. Ma, "A survey of manufacturing oriented topology optimization methods," *Adv. Eng. Softw.*, vol. 100, pp. 161–175, 2016, doi: 10.1016/j.advengsoft.2016.07.017.

[53] B. Hassani and E. Hinton, *Homogenization and Structural Topology Optimization*. 1999.

[54] E. Andreassen, A. Clausen, M. Schevenels, B. S. Lazarov, and O. Sigmund, "Efficient topology optimization in MATLAB using 88 lines of code," *Struct. Multidiscip. Optim.*, vol. 43, no. 1, pp. 1–16, 2011, doi: 10.1007/s00158-010-0594-7.

[55] K. Svanberg, "MMA and GCMMA – two methods for nonlinear optimization," *Kth*, vol. 1, pp. 1–15, 2007.

[56] T. Gao and W. Zhang, "Topology optimization involving thermo-elastic stress loads," *Struct. Multidiscip. Optim.*, vol. 42, no. 5, pp. 725–738, 2010, doi: 10.1007/s00158-010-0527-5.

[57] H. Rodrigues and P. Fernandes, "A material based model for topology optimization of thermoelastic structures," *Int. J. Numer. Methods Eng.*, vol. 38, no. 12, pp. 1951–1965, 1995, doi: 10.1002/nme.1620381202.

[58] J. Hou, J. H. Zhu, and Q. Li, "On the topology optimization of elastic supporting structures under thermomechanical loads," *Int. J. Aerosp. Eng.*, vol. 2016, 2016, doi: 10.1155/2016/7372603.

[59] J. D. Deaton and R. V Grandhi, "Stress-based Topology Optimization of Thermal Structures," *10 th World Congr. Struct. Multidiscip. Optim.*, pp. 1–10, 2013, doi: 10.2514/6.2013-1466.

[60] G. Vantyghem, V. Boel, M. Steeman, and W. De Corte, "Multi-material topology optimization involving simultaneous structural and thermal analyses," *Struct. Multidiscip. Optim.*, 2018.

[61] A. Takezawa and M. Kobashi, "Design methodology for porous composites with tunable thermal expansion produced by multi-material topology optimization and additive manufacturing," *Compos. Part B Eng.*, vol. 131, pp. 21–29, 2017, doi: 10.1016/j.compositesb.2017.07.054.

[62] Y. Du, Z. Luo, Q. Tian, and L. Chen, "Topology optimization for thermo-mechanical compliant actuators using mesh-free methods," *Eng. Optim.*, vol. 41, no. 8, pp. 753–772, 2009, doi: 10.1080/03052150902834989.

[63] R. Ansola, E. Vegueria, and J. Canales, "An element addition strategy for thermally actuated compliant mechanism topology optimization," *Eng. Comput. (Swansea, Wales)*, vol. 27, no. 6, pp. 694–711, 2010, doi: 10.1108/02644401011062090.

[64] S. A. Jahan *et al.*, "Implementation of Conformal Cooling & Topology Optimization in 3D Printed Stainless Steel Porous Structure Injection Molds," *Procedia Manuf.*, vol. 5, pp. 901–915, 2016, doi: 10.1016/j.promfg.2016.08.077.

[65] B. Chen and N. Kikuchi, "Topology optimization with design-dependent loads," *Finite Elem. Anal. Des.*, vol. 37, pp. 57–70, 2001.

[66] C. Niu, W. Zhang, and T. Gao, "Topology optimization of continuum structures for the uniformity of contact pressures," *Struct. Multidiscip. Optim.*, vol. 60, no. `, 2019.

[67] Z. mian Li, J. Yu, Y. Yu, and L. X. Xu, "Topology optimization of pressure structures based on regional contour tracking technology," *Struct. Multidiscip. Optim.*, vol. 58, no. 2, pp. 687–700, 2018, doi: 10.1007/s00158-018-1923-5.

[68] B. Zheng, C. C. Hae, and C. Gea, "Topology optimization with design-dependent pressure loading," *Struct. Multidiscip. Optim.*, pp. 535–543, 2009, doi: 10.1007/s00158-008-0317-5.

[69] C. Wang, M. Zhao, and T. Ge, "Structural topology optimization with design-dependent pressure loads," *Struct. Multidiscip. Optim.*, pp. 1005–1018, 2016, doi: 10.1007/s00158-015-1376-z.

[70] E. Lee, K. A. James, and J. R. R. A. Martins, "Stress-constrained topology optimization with design-dependent loading," *Struct. Multidiscip. Optim.*, vol. 46, no. 5, pp. 647–661, 2012, doi: 10.1007/s00158-012-0780-x.

[71] R. Picelli, R. van Dijk, W. M. Vicente, R. Pavanello, M. Langelaar, and F. van Keulen, "Topology optimization for submerged buoyant structures," *Eng. Optim.*, vol. 49, no. 1, pp. 1–21, 2017, doi: 10.1080/0305215X.2016.1164147.

[72] V. B. Hammer and N. Olhoff, "Topology optimization of continuum structures subjected to pressure loading," *Struct. Multidiscip. Optim.*, vol. 19, no. 2, pp. 85–92, 2000, doi: 10.1007/s001580050088.

[73] C. Wang, M. Zhao, and T. Ge, "Structural topology optimization with design-dependent pressure loads," *Struct. Multidiscip. Optim.*, vol. 53, no. 5, pp. 1005–1018, 2016, doi: 10.1007/s00158-015-1376-z.

[74] R. Picelli and A. N. H. A. Kim, "Topology optimization for design-dependent hydrostatic pressure loading via the level-set method," *Struct. Multidiscip. Optim.*, pp. 1313–1326, 2019.

[75] P. Kumar, J. S. Frouws, and M. Langelaar, "Topology optimization of fluidic pressure-loaded structures and compliant mechanisms using the Darcy method," *Struct. Multidiscip. Optim.*, vol. 61, no. 4, pp. 1637–1655, 2020, doi: 10.1007/s00158-019-02442-0.

[76] A. T. Gaynor and J. K. Guest, "Topology optimization considering overhang constraints: Eliminating sacrificial support material in additive manufacturing through design," *Struct. Multidiscip. Optim.*, vol. 54, no. 5, pp. 1157–1172, 2016, doi: 10.1007/s00158-016-1551-x.

[77] M. Langelaar, "An additive manufacturing filter for topology optimization of print-ready designs," *Struct. Multidiscip. Optim.*, vol. 55, no. 3, pp. 871–883, 2017, doi: 10.1007/s00158-016-1522-2.

[78] M. Langelaar, "Topology optimization of 3D self-supporting structures for additive manufacturing," *Addit. Manuf.*, vol. 12, pp. 60–70, 2016, doi: 10.1016/j.addma.2016.06.010.

[79] M. Leary, L. Merli, F. Torti, M. Mazur, and M. Brandt, "Optimal topology for additive manufacture : A method for enabling additive manufacture of support-free optimal structures," *Mater. Des.*, vol. 63, pp. 678–690, 2014, doi: 10.1016/j.matdes.2014.06.015.

[80] Y. Mass and O. Amir, "Topology optimization for additive manufacturing: Accounting for overhang limitations using a virtual skeleton," *Addit. Manuf.*, vol. 18, pp. 58–73, 2017, doi: 10.1016/j.addma.2017.08.001.

[81] Y. Kuo and C. Cheng, "Self-supporting structure design for additive manufacturing by using a logistic aggregate function," *Struct. Multidiscip. Optim.*, 2019.

[82] E. van de Ven, R. Maas, C. Ayas, M. Langelaar, and F. van Keulen, "Overhang control based on front propagation in 3D topology optimization for additive manufacturing," *Comput. Methods Appl. Mech. Eng.*, vol. 369, p. 113169, 2020, doi: 10.1016/j.cma.2020.113169.

[83] J. K. Guest, J. H. Prévost, and T. Belytschko, "Achieving minimum length scale in topology optimization using nodal design variables and projection functions," *Int. J. Numer. Methods Eng.*, vol. 254, no. July, pp. 238–254, 2004, doi: 10.1002/nme.1064.

[84] K. Mhapsekar, M. McConaha, and S. Anand, "Additive Manufacturing Constraints in Topology Optimization for Improved Manufacturability," *J. Manuf. Sci. Eng.*, vol. 140, no. May, pp. 1–16, 2018, doi: 10.1115/1.4039198.

[85] M. Zhou, B. S. Lazarov, F. Wang, and O. Sigmund, "Minimum length scale in topology optimization by geometric constraints," *Comput. Methods Appl. Mech. Eng.*, vol. 293, pp. 266–282, 2015, doi: 10.1016/j.cma.2015.05.003.

[86] J. Liu and Y. Ma, "A new multi-material level set topology optimization method with the length scale control capability," *Comput. Methods Appl. Mech. Eng.*, vol. 329, pp. 444–463, 2018, doi: 10.1016/j.cma.2017.10.011.

[87] X. Rong, J. Rong, S. Zhao, F. Li, J. Yi, and L. Peng, "New method for controlling minimum length scales of real and void phase materials in topology optimization," *Acta Mech. Sin. Xuebao*, no. 0123456789, 2020, doi: 10.1007/s10409-020-00932-9.

[88] Y. Xiong, S. Yao, Z. Zhao, and Y. Min, "A new approach to eliminating enclosed voids in topology optimization for additive manufacturing," *Addit. Manuf.*, vol. 32, no. December 2019, p. 101006, 2020, doi: 10.1016/j.addma.2019.101006.

[89] L. Zhou and W. Zhang, "Topology optimization method with elimination of enclosed voids," *Struct. Multidiscip. Optim.*, no. 2015, 2019, doi: 10.1007/s00158-019-02204-y.

[90] S. Liu, Q. Li, W. Chen, L. Tong, and G. Cheng, "An identification method for enclosed voids restriction in manufacturability design for additive manufacturing structures," *Front. Mech. Eng.*, vol. 10, no. 2, pp. 126–137, 2015, doi: 10.1007/s11465-015-0340-3.

[91] M. Langelaar, "Combined optimization of part topology, support structure layout and build orientation for additive manufacturing," *Struct. Multidiscip. Optim.*, vol. 57, pp. 1985–2004, 2018.

[92] M. P. Zwier and W. W. Wits, "Design for additive manufacturing : Automated build orientation selection and optimization," *Procedia CIRP*, vol. 55, pp. 128–133, 2016, doi: 10.1016/j.procir.2016.08.040.

[93] L. Cheng and A. To, "Part-Scale Build Orientation Optimization for Minimizing Residual Stress and Support Volume for Metal Additive Manufacturing : Theory and Experimental Validation," *Comput. Des.*, 2019, doi: 10.1016/j.cad.2019.03.004.

[94] R. Vaidya and S. Anand, "Optimum Support Structure Generation for Additive Manufacturing using Unit Cell Structures and Support Removal Constraint," *Procedia Manuf.*, vol. 5, pp. 1043–1059, 2016, doi: 10.1016/j.promfg.2016.08.072.

[95] A. B. Bogosel, "Optimizing supports for additive manufacturing," *Struct. Multidiscip. Optim.*, pp. 2493–2515, 2018.

[96] Z. D. Zhang *et al.*, "Topology optimization parallel-computing framework based on the inherent strain method for support structure design in laser powder-bed fusion additive manufacturing," *Int. J. Mech. Mater. Des.*, vol. 0123456789, 2020, doi: 10.1007/s10999-020-09494-x.

[97] G. Allaire and L. Jakabčin, "Taking into account thermal residual stresses in topology optimization of structures built by additive manufacturing," *Math. Model. Methods Appl. Sci.*, vol. 28, no. 12, pp. 1–45, 2017, doi: 10.1142/S0218202518500501.

[98] A. Garaigordobil, R. Ansola, J. Santamaría, and I. Fernández de Bustos, "A new overhang constraint for topology optimization of self-supporting structures in additive manufacturing," *Struct. Multidiscip. Optim.*, pp. 1–15, 2018, doi: 10.1007/s00158-018-2010-7.

[99] K. Zhang, G. Cheng, and L. Xu, "Topology optimization considering overhang constraint in additive manufacturing," *Comput. Struct.*, vol. 212, pp. 86–100, 2019, doi: 10.1016/j.compstruc.2018.10.011.

[100] X. Wang, C. Zhang, and T. Liu, "A Topology Optimization Algorithm Based on the Overhang Sensitivity Analysis for Additive Manufacturing," *IOP Conf. Ser. Mater. Sci. Eng.*, vol. 382, p. 032036, 2018, doi: 10.1088/1757-899X/382/3/032036.

[101] E. van de Ven, R. Maas, C. Ayas, M. Langelaar, and F. van Keulen, "Continuous front propagation-based overhang control for topology optimization with additive manufacturing," *Struct. Multidiscip. Optim.*, vol. 57, no. 5, pp. 2075–2091, 2018, doi: 10.1007/s00158-017-1880-4.

[102] D. Zhao, M. Li, and Y. Liu, "A novel application framework for self-supporting topology optimization," *Vis. Comput.*, 2020, doi: 10.1007/s00371-020-01860-2.

[103] M. Bi, P. Tran, and Y. M. Xie, "Topology optimization of 3D continuum structures under geometric self-supporting constraint," *Addit. Manuf.*, vol. 36, no. May, p. 101422, 2020, doi: 10.1016/j.addma.2020.101422.

[104] F. Mezzadri, V. Bouriakov, and X. Qian, "Topology optimization of self-supporting support structures for additive manufacturing," *Addit. Manuf.*, vol. 21, no. March, pp. 666–682, 2018, doi: 10.1016/j.addma.2018.04.016.

[105] W. Zhang and L. Zhou, "Topology optimization of self-supporting structures with polygon features for additive manufacturing," *Comput. Methods Appl. Mech. Eng.*, vol. 334, pp. 56–78, 2018, doi: 10.1016/j.cma.2018.01.037.

[106] X. Qian, "Undercut and overhang angle control in topology optimization: A density gradient based integral approach," *Int. J. Numer. Methods Eng.*, vol. 111, no. 3, pp. 247–272, 2017, doi: 10.1002/nme.5461.

[107] Z. Li, D. Z. Zhang, P. Dong, and I. Kucukkoc, "A lightweight and support-free design method for selective laser melting," *Int. J. Adv. Manuf. Technol.*, vol. 90, no. 9–12, pp. 2943–2953, 2017, doi: 10.1007/s00170-016-9509-0.

[108] F. Wang, B. S. Lazarov, and O. Sigmund, "On projection methods, convergence and robust formulations in topology optimization," *Struct. Multidiscip. Optim.*, vol. 43, no. 6, pp. 767–784, 2011, doi: 10.1007/s00158-010-0602-y.

[109] O. Sigmund, "Morphology-based black and white filters for topology optimization," *Struct. Multidiscip. Optim.*, vol. 33, no. 4–5, pp. 401–424, 2007, doi: 10.1007/s00158-006-0087-x.

[110] J. K. Guest, "Topology Optimization for Additive Manufacturing Considering Layer-Based Minimum Feature Sizes," *Proc. ASME 2017 Int. Des. Eng. Tech. Conf. Comput. Inf. Eng. Conf.*, pp. 1–8, 2018.

[111] L. N. S. Chiu, B. Rolfe, X. Wu, and W. Yan, "Effect of stiffness anisotropy on topology optimisation of additively manufactured structures," *Eng. Struct.*, vol. 171, pp. 842–848, 2018, doi: 10.1016/j.engstruct.2018.05.083.

[112] A. M. Mirzendehdel, B. Rankouhi, and K. Suresh, "Strength-based topology optimization for anisotropic parts," *Addit. Manuf.*, vol. 19, pp. 104–113, 2018, doi: 10.1016/j.addma.2017.11.007.

[113] J. Liu and A. C. To, "Deposition path planning-integrated structural topology optimization for 3D additive manufacturing subject to self-support constraint," *CAD Comput. Aided Des.*, vol. 91, pp. 27–45, 2017, doi: 10.1016/j.cad.2017.05.003.

[114] E. Ulu, E. Korkmaz, K. Yay, O. B. Ozdoganlar, and L. B. Kara, "Enhancing the Structural Performance of Additively Manufactured Objects Through Build Orientation Optimization," vol. 137, no. November 2015, pp. 1–9, 2018, doi: 10.1115/1.4030998.

[115] J. Robinson, I. Ashton, P. Fox, E. Jones, and C. Sutcliffe, "Determination of the effect of scan strategy on residual stress in laser powder bed fusion additive manufacturing," *Addit. Manuf.*, vol. 23, no. June, pp. 13–24, 2018, doi: 10.1016/j.addma.2018.07.001.

[116] A. S. Wu, D. W. Brown, M. Kumar, G. F. Gallegos, and W. E. King, "An Experimental Investigation into Additive Manufacturing-Induced Residual Stresses in 316L Stainless Steel," *Metall. Mater. Trans. A Phys. Metall. Mater. Sci.*, vol. 45, no. 13, pp. 6260–6270, 2014, doi: 10.1007/s11661-014-2549-x.

[117] C. Li, Z. Y. Liu, X. Y. Fang, and Y. B. Guo, "Residual Stress in Metal Additive Manufacturing," *Procedia CIRP*, vol. 71, pp. 348–353, 2018, doi: 10.1016/j.procir.2018.05.039.

[118] J.-H. Zhu, K.-K. Yang, and W.-H. Zhang, "Backbone cup – a structure design competition based on topology optimization and 3D printing," *Int. J. Simul. Multidiscip. Des. Optim.*, vol. 7, p. A1, 2016, doi: 10.1051/smdo/2016004.

[119] S. Li, S. Yuan, J. Zhu, C. Wang, J. Li, and W. Zhang, "Additive manufacturing-driven design optimization: Building direction and structural topology," *Addit. Manuf.*, vol. 36, no. June, p. 101406, 2020, doi: 10.1016/j.addma.2020.101406.

[120] A. Clausen, N. Aage, and O. Sigmund, "Exploiting Additive Manufacturing Infill in Topology Optimization for Improved Buckling Load," *Engineering*, vol. 2, no. 2, pp. 250–257, 2016, doi: 10.1016/J.ENG.2016.02.006.

[121] Z. Xiao, Y. Yang, R. Xiao, Y. Bai, C. Song, and D. Wang, "Evaluation of topology-optimized lattice structures manufactured via selective laser melting," *Mater. Des.*, vol. 143, pp. 27–37, 2018, doi: 10.1016/j.matdes.2018.01.023.

[122] L. Cheng, P. Zhang, E. Biyikli, J. Bai, J. Robbins, and A. To, "Efficient design optimization of variable-density cellular structures for additive manufacturing: Theory and experimental validation," *Rapid Prototyp. J.*, vol. 23, no. 4, pp. 660–677, 2017, doi: 10.1108/RPJ-04-2016-0069.

[123] P. Zhang *et al.*, "Efficient Design-Optimization of Variable-Density Hexagonal Cellular Structure by Additive Manufacturing: Theory and Validation," *J. Manuf. Sci. Eng.*, vol. 137, no. 2, p. 021004, 2015, doi: 10.1115/1.4028724.

[124] G. SHI, C. GUAN, D. QUAN, D. WU, L. TANG, and T. GAO, "An aerospace bracket designed

by thermo-elastic topology optimization and manufactured by additive manufacturing," *Chinese J. Aeronaut.*, vol. 33, no. 4, pp. 1252–1259, 2020, doi: 10.1016/j.cja.2019.09.006.

[125] Z. D. Ma, H. Wang, N. Kikuchi, C. Pierre, and B. Raju, "Experimental validation and prototyping of optimum designs obtained from topology optimization," *Struct. Multidiscip. Optim.*, vol. 31, no. 5, pp. 333–343, 2006, doi: 10.1007/s00158-005-0530-4.

[126] H. Zhang, A. S. Kumar, J. Y. H. Fuh, and M. Y. Wang, "Design and Development of a Topology-Optimized Three-Dimensional Printed Soft Gripper," *Soft Robot.*, vol. 5, no. 5, pp. 650–661, 2018, doi: 10.1089/soro.2017.0058.

[127] Y. Zhang, X. Wu, B. Guan, Z. Zhao, and M. Wan, "Application and practical validation of topology optimization technology for the frame of biaxial tensile testing machine," *Struct. Multidiscip. Optim.*, pp. 1519–1533, 2020, doi: 10.1007/s00158-020-02547-x.

[128] P. Wei, Z. Li, X. Li, and M. Y. Wang, "An 88-line MATLAB code for the parameterized level set method based topology optimization using radial basis functions," *Struct. Multidiscip. Optim.*, pp. 831–849, 2018.

[129] O. Sigmund, "A 99 line topology optimization code written in matlab," *Struct. Multidiscip. Optim.*, vol. 21, no. 2, pp. 120–127, 2001, doi: 10.1007/s001580050176.

[130] F. Ferrari and O. Sigmund, "A new generation 99 line Matlab code for compliance topology optimization and its extension to 3D," *Struct. Multidiscip. Optim.*, vol. 62, pp. 2211–2228, 2020, doi: 10.1007/s00158-020-02629-w.

[131] K. Suresh, "A 199-line Matlab code for Pareto-optimal tracing in topology optimization," *Struct. Multidiscip. Optim.*, vol. 42, no. 5, pp. 665–679, 2010, doi: 10.1007/s00158-010-0534-6.

[132] V. J. Challis, "A discrete level-set topology optimization code written in Matlab," *Struct. Multidiscip. Optim.*, vol. 41, no. 3, pp. 453–464, 2010, doi: 10.1007/s00158-009-0430-0.

[133] C. Talischi, G. H. Paulino, A. Pereira, and I. F. M. Menezes, "PolyMesher: A general-purpose mesh generator for polygonal elements written in Matlab," *Struct. Multidiscip. Optim.*, vol. 45, no. 3, pp. 309–328, 2012, doi: 10.1007/s00158-011-0706-z.

[134] L. Xia and P. Breitkopf, "Design of materials using topology optimization and energy-based homogenization approach in Matlab," *Struct. Multidiscip. Optim.*, vol. 52, no. 6, pp. 1229–1241,

2015, doi: 10.1007/s00158-015-1294-0.

[135] M. Otomori, T. Yamada, and K. Izui, "Matlab code for a level set-based topology optimization method using a reaction diffusion equation," *Struct. Multidiscip. Optim.*, pp. 1159–1172, 2015, doi: 10.1007/s00158-014-1190-z.

[136] M. Victoria, O. M. Querin, C. Díaz, and P. Martí, "liteITD a MATLAB Graphical User Interface (GUI) program for topology design of continuum structures," *Adv. Eng. Softw.*, vol. 100, pp. 126–147, 2016, doi: 10.1016/j.advengsoft.2016.07.012.

[137] E. D. Sanders, M. A. Aguiló, and G. H. Paulino, "Multi-material continuum topology optimization with arbitrary volume and mass constraints," *Comput. Methods Appl. Mech. Eng.*, vol. 340, pp. 798–823, 2018, doi: 10.1016/j.cma.2018.01.032.

[138] Q. Chen, X. Zhang, and B. Zhu, "A 213-line topology optimization code for geometrically nonlinear structures," *Struct. Multidiscip. Optim.*, vol. 59, no. 5, pp. 1863–1879, 2019, doi: 10.1007/s00158-018-2138-5.

[139] K. Liu and A. Tovar, "An efficient 3D topology optimization code written in Matlab," *Struct. Multidiscip. Optim.*, vol. 50, no. 6, pp. 1175–1196, 2014, doi: 10.1007/s00158-014-1107-x.

[140] O. Amir, N. Aage, and B. S. Lazarov, "On multigrid-CG for efficient topology optimization," *Struct. Multidiscip. Optim.*, vol. 49, no. 5, pp. 815–829, 2014, doi: 10.1007/s00158-013-1015-5.

[141] N. Aage, E. Andreassen, and B. S. Lazarov, "Topology optimization using PETSc: An easy-to-use, fully parallel, open source topology optimization framework," *Struct. Multidiscip. Optim.*, vol. 51, no. 3, pp. 565–572, 2015, doi: 10.1007/s00158-014-1157-0.

[142] S. Cai and W. Zhang, "Stress constrained topology optimization with free-form design domains," *Comput. Methods Appl. Mech. Engrg.*, vol. 289, no. October 2018, pp. 267–290, 2015, doi: 10.1016/j.cma.2015.02.012.

[143] Y. H. Chou and C. Y. Lin, "Improved image interpreting and modeling technique for automated structural optimization system," *Struct. Multidiscip. Optim.*, vol. 40, no. 1–6, pp. 215–226, 2010, doi: 10.1007/s00158-008-0352-2.

[144] J. F. Gamache, A. Vadean, É. Noirot-Nérin, D. Beaini, and S. Achiche, "Image-based truss recognition for density-based topology optimization approach," *Struct. Multidiscip. Optim.*, vol.

58, no. 6, pp. 2697–2709, 2018, doi: 10.1007/s00158-018-2028-x.

[145] K. Yaji, T. Yamada, S. Kubo, K. Izui, and S. Nishiwaki, "A topology optimization method for a coupled thermal-fluid problem using level set boundary expressions," *Int. J. Heat Mass Transf.*, vol. 81, pp. 878–888, 2015, doi: 10.1016/j.ijheatmasstransfer.2014.11.005.

[146] T. Wu *et al.*, "A Framework for Optimizing the Design of Injection Molds with Conformal Cooling for Additive Manufacturing," *Procedia Manuf.*, vol. 1, pp. 404–415, 2015, doi: 10.1016/j.promfg.2015.09.049.

[147] E. M. Dede, S. N. Joshi, and F. Zhou, "Topology Optimization, Additive Layer Manufacturing, and Experimental Testing of an Air-Cooled Heat Sink," *J. Mech. Des.*, vol. 137, no. 11, p. 111403, 2015, doi: 10.1115/1.4030989.

[148] A. Gaymann, F. Montomoli, and M. Pietropaoli, "International Journal of Heat and Fluid Flow Fluid topology optimization : Bio-inspired valves for aircraft engines," *Int. J. Heat Fluid Flow*, vol. 79, no. July, p. 108455, 2019, doi: 10.1016/j.ijheatfluidflow.2019.108455.

[149] N. Aage, T. H. Poulsen, A. Gersborg-Hansen, and O. Sigmund, "Topology optimization of large scale stokes flow problems," *Struct. Multidiscip. Optim.*, vol. 35, no. 2, pp. 175–180, 2008, doi: 10.1007/s00158-007-0128-0.

[150] N. Aage and B. S. Lazarov, "Parallel framework for topology optimization using the method of moving asymptotes," *Struct. Multidiscip. Optim.*, vol. 47, no. 4, pp. 493–505, 2013, doi: 10.1007/s00158-012-0869-2.

[151] R. Esmaeilizadeh *et al.*, "On the effect of laser powder-bed fusion process parameters on quasi-static and fatigue behaviour of Hastelloy X: A microstructure/defect interaction study," *Addit. Manuf.*, vol. 38, no. December 2020, p. 101805, 2021, doi: 10.1016/j.addma.2020.101805.

[152] W. G. Kim, S. N. Yin, W. S. Ryu, J. H. Chang, and S. J. Kim, "Tension and creep design stresses of the 'Hastelloy-X' alloy for high-temperature gas cooled reactors," *Mater. Sci. Eng. A*, vol. 483–484, no. 1-2 C, pp. 495–497, 2008, doi: 10.1016/j.msea.2006.12.184.

[153] S. Abotula, A. Shukla, and R. Chona, "Dynamic constitutive behavior of Hastelloy X under thermo-mechanical loads," *J. Mater. Sci.*, vol. 46, no. 14, pp. 4971–4979, 2011, doi: 10.1007/s10853-011-5414-y.

[154] D. Li, X. Zhang, Y. Guan, and J. Zhan, "Topology optimization of thermo-mechanical continuum structure," *IEEE/ASME Int. Conf. Adv. Intell. Mechatronics, AIM*, pp. 403–408, 2010, doi: 10.1109/AIM.2010.5695845.

[155] V. D. V. Emiel, H. Evert, L. Matthijs, and V. K. Fred, "Topology optimization of a transient thermo-mechanical problem using material penalization," in *Proceedings of the 11th World Congress of Structural and Multidisciplinary Optimization (WCSMO-11): Advances in Structural and Multidisciplinary Optimization*, 2015, pp. 966–971.

[156] G. P. Nikishkov, *Programming Finite Elements in Java(TM)*. Springer, 2010.

[157] S. Xu, Y. Cai, and G. Cheng, "Volume preserving nonlinear density filter based on heaviside functions," *Struct. Multidiscip. Optim.*, vol. 41, no. 4, pp. 495–505, 2010, doi: 10.1007/s00158-009-0452-7.

[158] Z. Kang and P. Liu, "Reliability-based topology optimization against geometric imperfections with random threshold model," *Int. J. Numer. Methods Eng.*, vol. 115, no. 1, pp. 99–116, 2018, doi: 10.1002/nme.5797.

[159] B. Zheng, C. J. Chang, and H. C. Gea, "Topology optimization with design-dependent pressure loading," *Struct. Multidiscip. Optim.*, vol. 38, no. 6, pp. 535–543, 2009, doi: 10.1007/s00158-008-0317-5.

[160] C. Liang, S. Shiah, C. Jen, and H. Chen, "Optimum design of multiple intersecting spheres deep-submerged pressure hull," *Ocean Eng.*, vol. 31, pp. 177–199, 2004, doi: 10.1016/S0029-8018(03)00120-3.

[161] D. A. Tortorelli and P. Michaleris, "Design sensitivity analysis: Overview and review," *Inverse Probl. Eng.*, vol. 1, no. 1, pp. 71–105, Oct. 1994, doi: 10.1080/174159794088027573.

[162] K. Dems and Z. Mroz, "Variational approach by means of adjoint systems to structural optimization and sensitivity analysis-i," *Int. J. Solids Struct.*, vol. 19, no. 8, pp. 677–692, 1983, doi: 10.1016/0020-7683(83)90064-1.

[163] J. Du and N. Olhoff, "Topological optimization of continuum structures with design-dependent surface loading – Part I : new computational approach for 2D problems," *Struct. Multidiscip. Optim.*, vol. 165, no. July 2003, pp. 151–165, 2004, doi: 10.1007/s00158-004-0379-y.

[164] C. Wang, M. Zhao, and T. Ge, "Structural topology optimization with design-dependent pressure loads," *Struct. Multidiscip. Optim.*, vol. 53, no. 5, pp. 1005–1018, 2016, doi: 10.1007/s00158-015-1376-z.

[165] M. Bruggi and C. Cinquini, "An alternative truly-mixed formulation to solve pressure load problems in topology optimization," *Comput. Methods Appl. Mech. Eng.*, vol. 198, no. 17–20, pp. 1500–1512, 2009, doi: 10.1016/j.cma.2008.12.009.

[166] O. Sigmund and P. M. Clausen, "Topology optimization using a mixed formulation: An alternative way to solve pressure load problems," *Comput. Methods Appl. Mech. Eng.*, vol. 196, no. 13–16, pp. 1874–1889, 2007, doi: 10.1016/j.cma.2006.09.021.

[167] R. T. Marler and J. S. Arora, "The weighted sum method for multi-objective optimization : new insights," *Struct. Multidiscip. Optim.*, pp. 853–862, 2010, doi: 10.1007/s00158-009-0460-7.

[168] P. Haleja and C. Shih, "Multiobjective Optimum Design in Mixed Integer and Discrete Design Variable Problems," *AIAA J.*, 1989.

[169] R. V. Grandhi, G. Bharatram, and V. B. Venkayya, "Multiobjective optimization of large-scale structures," *AIAA J.*, vol. 31, no. 7, pp. 1329–1337, 1993, doi: 10.2514/3.11771.

[170] Y. Chen, S. Zhou, and Q. Li, "Multiobjective topology optimization for finite periodic structures," *Comput. Struct.*, vol. 88, no. 11–12, pp. 806–811, 2010, doi: 10.1016/j.compstruc.2009.10.003.

[171] S. Arabnejad Khanoki and D. Pasini, "Multiscale design and multiobjective optimization of orthopedic hip implants with functionally graded cellular material," *J. Biomech. Eng.*, vol. 134, no. 3, 2012, doi: 10.1115/1.4006115.

[172] L. Wang, C. Zhang, and W. Gao, "A novel multiobjective topology optimization method for suppressing vibration," *Proc. 2018 IEEE Int. Conf. Mechatronics Autom. ICMA 2018*, no. 2, pp. 1750–1754, 2018, doi: 10.1109/ICMA.2018.8484468.

[173] D. J. Munk, T. Kipouros, G. A. Vio, G. T. Parks, and G. P. Steven, "Multiobjective and multi-physics topology optimization using an updated smart normal constraint bi-directional evolutionary structural optimization method," *Struct. Multidiscip. Optim.*, vol. 57, no. 2, pp. 665–688, 2018, doi: 10.1007/s00158-017-1781-6.

[174] M. Denk, K. Rot, and M. Denk, "Multi-Objective Topology Optimization of Heat Conduction

and Linear Elastostatic using Weighted Global Criteria Method," *DfX-Symposium*, 2020.

[175] J. Deng, J. Yan, and G. Cheng, "Multi-objective concurrent topology optimization of thermoelastic structures composed of homogeneous porous material," *Struct. Multidiscip. Optim.*, pp. 583–597, 2013, doi: 10.1007/s00158-012-0849-6.

[176] B. Wang, J. Yan, and G. Cheng, "Optimal structure design with low thermal directional expansion and high stiffness," *Eng. Optim.*, vol. 43, no. 6, pp. 581–595, 2011, doi: 10.1080/0305215X.2010.499941.

[177] Q. Yang, B. Gao, Z. Xu, W. Xie, and S. Meng, "Topology optimisations for integrated thermal protection systems considering thermo-mechanical constraints," *Appl. Therm. Eng.*, vol. 150, no. December 2018, pp. 995–1001, 2019, doi: 10.1016/j.applthermaleng.2019.01.067.

[178] G. Sun, D. Tan, X. Lv, X. Yan, Q. Li, and X. Huang, "Multi-objective topology optimization of a vehicle door using multiple material tailor-welded blank (TWB) technology," *Adv. Eng. Softw.*, vol. 124, no. July, pp. 1–9, 2018, doi: 10.1016/j.advengsoft.2018.06.014.

[179] Y. Sato, K. Yaji, K. Izui, T. Yamada, and S. Nishiwaki, "An optimum design method for a thermal-fluid device incorporating multiobjective topology optimization with an adaptive weighting scheme," *J. Mech. Des. Trans. ASME*, vol. 140, no. 3, 2018, doi: 10.1115/1.4038209.

[180] K. Svanberg, "MMA and GCMMA – two methods for nonlinear optimization," vol. 1. pp. 1–16, 2007.

[181] A. Wächter and L. T. Biegler, "On the implementation of an interior-point filter line-search algorithm for large-scale nonlinear programming," *Math. Program.*, vol. 106, no. 1, pp. 25–57, 2006, doi: 10.1007/s10107-004-0559-y.

[182] A. A. Groenwold and L. F. P. Etman, "A quadratic approximation for structural topology optimization," *Int. J. Numer. Methods Eng.*, no. November 2009, pp. 505–524, 2010, doi: 10.1002/nme.

[183] M. Bruyneel and P. Duysinx, "Note on topology optimization of continuum structures including self-weight," *Struct. Multidiscip. Optim.*, vol. 29, no. 4, pp. 245–256, 2005, doi: 10.1007/s00158-004-0484-y.

[184] F. Cangioli, S. Chatterton, P. Pennacchi, L. Nettis, and L. Ciuchicchi, "Tribology International

Thermo-elasto bulk- fl ow model for labyrinth seals in steam turbines," *Tribol. Int.*, vol. 119, no. November 2017, pp. 359–371, 2018, doi: 10.1016/j.triboint.2017.11.016.

[185] O. Ibhadode, Z. Zhang, P. Rahnama, A. Bonakdar, and E. Toyserkani, "Topology optimization of structures under design-dependent pressure loads by a boundary identification-load evolution (BILE) model," *Struct. Multidiscip. Optim.*, 2020.

[186] C. Methods, A. Mech, E. Lee, and J. R. R. A. Martins, "Structural topology optimization with design-dependent pressure loads," *Comput. Methods Appl. Mech. Eng.*, vol. 233–236, pp. 40–48, 2012, doi: 10.1016/j.cma.2012.04.007.

[187] E. Lee, K. A. James, and J. R. R. A. Martins, "Stress-constrained topology optimization with design-dependent loading," *Struct. Multidiscip. Optim.*, pp. 647–661, 2012, doi: 10.1007/s00158-012-0780-x.

[188] B. C. Chen and N. Kikuchi, "Topology optimization with design-dependent loads," *Finite Elem. Anal. Des.*, vol. 37, no. 1, pp. 57–70, 2001, doi: 10.1016/S0168-874X(00)00021-4.

[189] C. Paper, "A Modified Inherent Strain Method for Fast Prediction of Residual Deformation in Additive Manufacturing of Metal Parts," *Solid Free. Fabr. Symp.*, no. August, pp. 2539–2545, 2017.

[190] Y. Liu, Y. Yang, and D. Wang, "A study on the residual stress during selective laser melting (SLM) of metallic powder," *Int. J. Adv. Manuf. Technol.*, pp. 1–10, 2016, doi: 10.1007/s00170-016-8466-y.

[191] M. Matthews, J. Trapp, G. Guss, and A. Rubenchik, "Direct measurements of laser absorptivity during metal melt pool formation associated with powder bed fusion additive manufacturing processes," *J. Laser Appl.*, vol. 30, no. 3, p. 032302, 2018, doi: 10.2351/1.5040636.

[192] J. Kranz, D. Herzog, C. Emmelmann, J. Kranz, and D. Herzog, "Design guidelines for laser additive manufacturing of lightweight structures in TiAl6V4," *J. Laser Appl.*, vol. 14001, 2015, doi: 10.2351/1.4885235.

[193] J. C. Fox, S. P. Moylan, and B. M. Lane, "Effect of process parameters on the surface roughness of overhanging structures in laser powder bed fusion additive manufacturing," *Procedia CIRP*, vol. 45, pp. 131–134, 2016, doi: 10.1016/j.procir.2016.02.347.

[194] J. Allison, C. Sharpe, and C. C. Seepersad, "Powder bed fusion metrology for additive manufacturing design guidance," *Addit. Manuf.*, vol. 25, no. June 2018, pp. 239–251, 2019, doi: 10.1016/j.addma.2018.10.035.

[195] M. Leary, M. Babaee, M. Brandt, and A. Subic, "Feasible Build Orientations for Self-Supporting Fused Deposition Manufacture: A Novel Approach to Space-Filling Tesselated Geometries," *Adv. Mater. Res.*, vol. 633, pp. 148–168, 2013, doi: 10.4028/www.scientific.net/AMR.633.148.

[196] M. Leary, L. Merli, F. Torti, M. Mazur, and M. Brandt, "Optimal topology for additive manufacture: A method for enabling additive manufacture of support-free optimal structures," *Mater. Des.*, vol. 63, pp. 678–690, 2014, doi: 10.1016/j.matdes.2014.06.015.

[197] M. Langelaar, "An additive manufacturing filter for topology optimization of print-ready designs," *Struct. Multidiscip. Optim.*, vol. 55, no. 3, pp. 871–883, 2017, doi: 10.1007/s00158-016-1522-2.

[198] Y. Fu *et al.*, "Design and experimental validation of self-supporting topologies for additive manufacturing," *Virtual Phys. Prototyp.*, vol. 2759, 2019, doi: 10.1080/17452759.2019.1637023.

[199] K. Svanberg, "The method of moving asymptotes—a new method for structural optimization," *Int. J. Numer. Methods Eng.*, vol. 24, no. 2, pp. 359–373, 1987, doi: 10.1002/nme.1620240207.

[200] A. Alafaghani, A. Qattawi, and M. A. Ablat, "Design Consideration for Additive Manufacturing: Fused Deposition Modelling," *Open J. Appl. Sci.*, vol. 07, no. 06, pp. 291–318, 2017, doi: 10.4236/ojapps.2017.76024.

[201] L. Meng *et al.*, "From Topology Optimization Design to Additive Manufacturing : Today ' s Success and Tomorrow ' s Roadmap," *Arch. Comput. Methods Eng.*, no. 0123456789, 2019.

[202] X. Zhu, C. Zhao, X. Wang, Y. Zhou, P. Hu, and Z. D. Ma, "Temperature-constrained topology optimization of thermo-mechanical coupled problems," *Eng. Optim.*, no. January, 2019, doi: 10.1080/0305215X.2018.1554065.

[203] J. Liu and H. Yu, "Self-Support Topology Optimization with Horizontal Overhangs for Additive Manufacturing," *J. Manuf. Sci. Eng.*, vol. 142, no. September, 2020, doi: 10.1115/1.4047352.

[204] P. Cignoni, M. Callieri, M. Corsini, M. Dellepiane, F. Ganovelli, and G. Ranzuglia, "MeshLab: An open-source mesh processing tool," *6th Eurographics Ital. Chapter Conf. 2008 - Proc.*, no.

January, pp. 129–136, 2008, doi: 10.2312/LocalChapterEvents/ItalChap/ItalianChapConf2008/129-136.

[205] P. J. Withers and H. K. D. H. Bhadeshia, "Residual stress part 2 - Nature and origins," *Mater. Sci. Technol.*, vol. 17, no. 4, pp. 366–375, 2001, doi: 10.1179/026708301101510087.

[206] A. M. Driessen, "Overhang constraint in topology optimization for additive manufacturing: a density gradient based approach," 2016.

[207] G. I. N. Rozvany, M. Zhou, and T. Birker, "Generalized shape optimization without homogenization," *Struct. Optim.*, vol. 4, no. 3–4, pp. 250–252, 1992, doi: 10.1007/BF01742754.

[208] M. P. Bendsøe and O. Sigmund, "Material interpolation schemes in topology optimization," *Arch. Appl. Mech.*, vol. 69, no. 9–10, pp. 635–654, 1999, doi: 10.1007/s004190050248.

[209] R. Esmaeilizadeh *et al.*, "Customizing mechanical properties of additively manufactured Hastelloy X parts by adjusting laser scanning speed," *J. Alloys Compd.*, vol. 812, 2020, doi: 10.1016/j.jallcom.2019.152097.

[210] ASTM E8, "ASTM E8/E8M standard test methods for tension testing of metallic materials 1," *Annu. B. ASTM Stand. 4*, no. C, pp. 1–27, 2010, doi: 10.1520/E0008.

[211] J. Robinson, I. Ashton, P. Fox, E. Jones, and C. Sutcliffe, "Determination of the effect of scan strategy on residual stress in laser powder bed fusion additive manufacturing," *Addit. Manuf.*, vol. 23, pp. 13–24, 2018, doi: 10.1016/j.addma.2018.07.001.

[212] W. Chen *et al.*, "Microscale residual stresses in additively manufactured stainless steel," *Nat. Commun.*, vol. 10, no. 1, pp. 1–12, 2019, doi: 10.1038/s41467-019-12265-8.

[213] K. K. Yang, J. H. Zhu, C. Wang, D. S. Jia, L. L. Song, and W. H. Zhang, "Experimental validation of 3D printed material behaviors and their influence on the structural topology design," *Comput. Mech.*, vol. 61, no. 5, pp. 581–598, 2018, doi: 10.1007/s00466-018-1537-1.

[214] M. P. Bendsoe, "Optimal Shape Design as a Material Distribution Problem," *Struct. Optim.*, vol. 202, pp. 193–194, 1989.

[215] H. Lin, A. Xu, A. Misra, and R. Zhao, "An ANSYS APDL code for topology optimization of structures with multi-constraints using the BESO method with dynamic evolution rate (DER-BESO)," *Struct. Multidiscip. Optim.*, pp. 2229–2254, 2020, doi: 10.1007/s00158-020-02588-2.

[216] Y. Liang and G. Cheng, "Further elaborations on topology optimization via sequential integer programming and Canonical relaxation algorithm and 128-line MATLAB code," *Struct. Multidiscip. Optim.*, vol. 61, no. 1, pp. 411–431, 2020, doi: 10.1007/s00158-019-02396-3.

[217] H. Smith and J. A. Norato, "A MATLAB code for topology optimization using the geometry projection method," *Struct. Multidiscip. Optim.*, pp. 1579–1594, 2020, doi: 10.1007/s00158-020-02552-0.

[218] C. Solomon and T. Breckon, *Fundamentals of digital image processing - A Practical Approach with Examples in Matlab*. Wiley-Blackwell, 2011.

[219] R. C. Gonzalez, R. E. Woods, and B. R. Masters, *Digital Image Processing, Third Edition*, vol. 14, no. 2. 2009.

[220] G. Blanchet and C. Charbit, *Digital Image Processing for MATLAB*. Antony Rowe Ltd, 2001.

[221] L. Xia, Q. Xia, X. Huang, and Y. M. Xie, "Bi-directional Evolutionary Structural Optimization on Advanced Structures and Materials: A Comprehensive Review," *Arch. Comput. Methods Eng.*, no. November, 2016, doi: 10.1007/s11831-016-9203-2.

[222] B. E. Treeby and B. T. Cox, "k-Wave : MATLAB toolbox for the simulation and reconstruction of photoacoustic wave fields," *J. Biomed. Opt.*, vol. 15, no. 2, pp. 1–12, 2010, doi: 10.1117/1.3360308.

[223] Sven, "stl write - write ASCII or Binary STL files," *Matlab Central File Exchange*, 2020. https://www.mathworks.com/matlabcentral/fileexchange/20922-stlwrite-write-ascii-or-binary-stl-files (accessed Oct. 14, 2020).

[224] A. T. Gaynor, J. K. Guest, and C. D. Moen, "Reinforced concrete force visualization and design using bilinear truss-continuum topology optimization," *J. Struct. Eng. (United States)*, vol. 139, no. 4, pp. 607–618, 2013, doi: 10.1061/(ASCE)ST.1943-541X.0000692.

[225] P. Wei, Y. Liu, and Z. Li, "A multi-discretization scheme for topology optimization based on the parameterized level set method," *IInternational J. Simul. Multidiscip. Des. Optim.*, vol. 3, 2020.

[226] O. Sorkine, "Laplacian Mesh Processing," *Eurographics - State Art Reports*, vol. 24, no. 4, pp. 53–70, 2005.

[227] G. Taubin, "Signal processing approach to fair surface design," *Proc. ACM SIGGRAPH Conf.*

Comput. Graph., pp. 351–358, 1995, doi: 10.1145/218380.218473.

[228] O. Ibhadode, Z. Zhang, A. Bonakdar, and E. Toyserkani, "IbIPP for Topology Optimization - An Image-Based Initialization and Post-Processing Code Written in MATLAB," *SoftwareX*, vol. 14, p. 100701, 2021, doi: 10.1016/j.softx.2021.100701.

[229] K. Svanberg, "MMA and GCMMA – two methods for nonlinear optimization," vol. 1, pp. 1–15, 2007.

[230] M. Bruyneel and P. Duysinx, "Note on topology optimization of continuum structures including self-weight," *Struct. Multidiscip. Optim.*, vol. 29, no. 4, pp. 245–256, 2005, doi: 10.1007/s00158-004-0484-y.

[231] A. A. Groenwold, D. W. Wood, L. F. P. Etman, and S. Tosserams, "Convex Separable Diagonal Quadratic Approximations," *AIAA J.*, vol. 47, no. 11, 2009, doi: 10.2514/1.41975.

Appendix

Table A: Table of Name-Value Input Parameters

Name-value input	Description	Value	Default value
pressure	Pressure loads		1
optimization	Topology optimization approach	Density, BESO, Level Set	Density
densityType	Type of density-based method	SIMP, RAMP	SIMP
preserveSupport	Preserve elements within the support region(s) in the image	0 – none 1 – Only completely fixed elements 2 – Only elements fixed in the $x-axis$ 3 – Only elements fixed in the $y-axis$ 4 – the union of 1 and 2 5 – the union of 1 and 3 6 - the union of 2 and 3 7 – the union of 1, 2, and 3	0
preserveLoad	Preserve elements within the load region(s) in the image	0 – none 1 – elements in the force region 2 – elements in the pressure region 3 – the union of 1 and 2	0
filterRadius	Specify filter radius for density-based and BESO approaches	> 1	2
Filter	Specify filter type for density-based approaches	1 – density 2 – sensitivity 3- Heaviside projection	2

Beta	Regolarization parameter for Heaviside projection	> 1	2
penaltySIMP	Penalty value for SIMP density-based approach	> 1	3
penaltyRAMP	Penalization factor for RAMP density-based approach	> 1	10
ER	Evolution ratio for BESO	> 0	0.15
Tau	Regularization parameter for level set method (reaction diffusion)	> 0	2×10^{-4}
YoungsModulus	Youngs Modulus material property	≥ 1	
PoissonRatio	Poisson Ratio material property	> 0	0.3
modelName	Name given to model obtained by extrusion or revolution of the optimized topology. Must end in .stl		
modelType	Modeling by extrusion or revolution	Extrude or revolve	extrude
extrudeLength	Length for extrusion. It is a factor multiplied by the minimum of nelx and nely to obtain the length of the 3rd dimension	> 0	0.1
Symmetry	Specifies the position of the line of symmetry for symmetry-based modeling	None, Left, bottom, right, and top	None
Distancetoaxis	Distance between the optimized topology and its center of revolution to the	≥ 0	0

	left for revolution-based modeling		
revolutionAngle	The angle of revolution for revolution-based modeling	≥ 0	360